UNCLASSIFIED

AD NUMBER
AD841834
LIMITATION CHANGES
TO: **Approved for public release; distribution is unlimited.**
FROM: **Distribution authorized to U.S. Gov't. agencies and their contractors; Critical Technology; JUL 1968. Other requests shall be referred to Air Force Avionics Laboratory, Attn: AVTL, Wright-Patter son AFB, OH 45433. This document contains export-controlled technical data.**
AUTHORITY
AFAL ltr, 30 Jul 1973

THIS PAGE IS UNCLASSIFIED

AFAL-TR-68-227

00097

AD841834

GASEOUS ION LASER RESEARCH

A.S. Halsted, W.B. Bridges, and G.N. Mercer

HUGHES RESEARCH LABORATORIES
Malibu, California

TECHNICAL REPORT AFAL-TR-68-227

JULY 1968

D D C
OCT 29 1968

THIS DOCUMENT IS SUBJECT TO SPECIAL EXPORT CONTROLS AND EACH TRANSMITTAL TO FOREIGN GOVERNMENTS OR FOREIGN NATIONALS MAY BE MADE ONLY WITH PRIOR APPROVAL OF AIR FORCE AVIONICS LABORATORY (AVTL) WRIGHT-PATTERSON AFB, OHIO 45433.

AIR FORCE AVIONICS LABORATORY
AIR FORCE SYSTEMS COMMAND
WRIGHT-PATTERSON AIR FORCE BASE, OHIO

191

Best
Available
Copy

CFSTI WHITE SECTION
DDC BUFF SECTION
UNANNOUNCED
JUSTIFICATION
BY
DISTRIBUTION/AVAILABILITY CODES
DIST. AVAIL. and/or SPECIAL
2

NOTICES

When Government drawings, specifications, or other data are used for any purpose other than in connection with a definitely related Government procurement operation, the United States Government thereby incurs no responsibility nor any obligation whatsoever; and the fact that the Government may have formulated, furnished, or in any way supplied the said drawings, specifications, or other data, is not to be regarded by implication or otherwise as in any manner licensing the holder or any other person or corporation, or conveying any rights or permission to manufacture, use, or sell any patented invention that may in any way be related thereto.

Copies of this report should not be returned unless return is required by security considerations, contractual obligations, or notice on a specific document.

ABSTRACT

The results of a program to improve the reliability and operating characteristics of argon ion lasers are reported. This work on laser technology is a continuation of the earlier studies on excitation mechanisms, scaling laws, plasma properties, and laser technology which was described in a previous final report of the same title.* Emphasis of the present work has been on life testing of cathodes and bore materials, evaluation of bore construction techniques (continuous, segmented, and disk bore structures), and improvement of operational characteristics. Both oxide and impregnated tungsten cathodes were evaluated under typical ion laser conditions in extended life tests. Extensive data were gathered on gas cleanup rate and on the amount of additional cathode heating which occurs when discharge current is drawn from the cathode. Promising laser bore materials were evaluated to determine resistance to ion sputtering, cleanliness as a vacuum material, gas cleanup properties, and thermal characteristics. Materials tested and reported upon are pyrolytic graphite, graphite overcoated with pyrolytic graphite, graphite overcoated with tungsten, tungsten, quartz, and beryllia. The characteristics of lasers having bores constructed of thin disks spaced many disk-thicknesses apart are described. The output power, efficiency, resistance to erosion, and large heat dissipation capability demonstrated by tungsten disk-bore structures make this method of bore construction very attractive. The operation of argon ion lasers using periodic permanent magnets (PPM) to replace the conventional solenoid magnet was investigated. A comparison is reported of the performance of a laser when operated in a solenoid and in a PPM assembly. Severe bore erosion occurred at the field reversals with PPM confinement. The theory of segmented bore lasers with internal gas return paths is considered. Very large areas in the bore segments or disks must be allocated to gas return path holes to provide an adequate gas return path because of the high gas temperature within the bore structure. Modulation of the output beam by power supply ripple and discharge fluctuations was investigated. The quantitative relationship between laser light modulation and the ripple amplitude of the several power supplies used to run a laser is given and was confirmed experimentally. Less than 1% total peak-to-peak beam modulation can be obtained. Characteristics are given of a discharge instability in the hundred kilohertz range which is present under certain discharge conditions and which increases the beam modulation level.

---

*W.B. Bridges and A.S. Halsted, "Gaseous Ion Laser Research," Technical Report No. AFAL-TR-67-89, Hughes Research Laboratories, Malibu, California, May 1967 (DDC No. AD 814897).

AFAL-TR-68-227

GASEOUS ION LASER RESEARCH

A.S. Halsted
W.B. Bridges
G.N. Mercer

This document is subject to special export controls and each transmittal to foreign governments or foreign nationals may be made only with prior approval of Air Force Avionics Laboratory (AVTL), Wright-Patterson AFB, Ohio 45433.

FOREWORD

This is the Final Report on Contract F33615-67-C-1435, Project No. 5237, Task No. 523708. The work reported herein was accomplished by Hughes Research Laboratories, 3011 Malibu Canyon Road, Malibu, California 90265. This report covers the period 1 January 1967 through 30 June 1968. The Air Force program monitor was Donald R. Nordstrom. This report was submitted by the authors on 30 June 1968.

Principal investigator was A.S. Halsted. Other members of the technical staff who contributed were W.B. Bridges; G.N. Mercer, who conducted impregnated cathode and noise studies; and R.J. Freiberg, who assisted in the periodic permanent magnet evaluation. Very able technical assistance was supplied by D.F. Sobieralski.

This technical report has been reviewed and is approved for publication.

Donald R Nordstrom

DONALD R. NORDSTROM
ACTING CHIEF, Laser Technology Branch
Electronic Technology Division

TABLE OF CONTENTS

SECTION		PAGE
I	INTRODUCTION	1
II	CATHODE STUDIES	3
	A. Discussion of Cathode Types	3
	B. Oxide Cathode Tests	5
	C. Impregnated Tungsten Cathode Tests	21
	D. Summary and Conclusions	40
III	BORE MATERIAL STUDIES	43
	A. Summary of Experiments	43
	B. Tube Design and Test Apparatus	43
	C. Evaluation of Pyrolytic Graphite	48
	D. Evaluation of Graphite with a PG Overcoat (Tube No. B-133)	57
	E. Evaluation of Pyrolytic Graphite in a Ceramic Envelope (Tube No. B-138-C)	64
	F. Evaluation of Tungsten-Overcoated Graphite	72
	G. Evaluation of a Quartz-Bore Tube (Tube No. F-29)	82
	H. Evaluation of Beryllium Oxide (Tube No. B-155)	85
IV	EVALUATION OF DISK-BORE TUBES	97
	A. Experiments with a Graphite-Disk Tube (No. B-136)	97
	B. Experiments with a Tungsten-Disk Tube (No. B-146)	102
	C. Additional Test Results with Tungsten Disk-Bore Tubes	108

SECTION		PAGE
V	PERIODIC PERMANENT MAGNET STUDIES	113
	A. Theoretical Considerations	113
	B. Experimental Considerations	120
	C. Summary and Conclusions	131
VI	GENERAL LASER DESIGN CONSIDERATIONS	135
	A. Gas Return Path Design	135
	B. Cathode Throat Studies	140
VII	NOISE STUDIES	147
	A. Power Supply Modulation of the Light Output	147
	B. Other Noise Sources	157
	C. Conclusions	162
VIII	CONCLUSIONS	165
	REFERENCES	167
	APPENDIX I – Heat Transfer Characteristics of a Disk-Bore Tube	169

LIST OF ILLUSTRATIONS

FIGURE		PAGE
1	Emission current density versus surface temperature for different cathode types	4
2	Hughes ion laser oxide cathode with front heat shielding removed	6
3	Photograph of cathode evaluation apparatus	8
4	Schematic representation of experimental apparatus used to monitor the gas cleanup rate of a laser cathode	9
5	Pressure variation with time for oxide cathode B-132 at 20 A	10
6	Gas cleanup rate versus gas pressure during successive gas fills, tube B-132	12
7	Gas pressure versus time showing variation in pressure with discharge current, tube B-132	13
8	Photograph of oxide cathode after 1700 hours of operation	15
9	Pressure variation with time for oxide cathode B-136	16
10	Power dissipated in the cathode as a function of discharge current	19
11	Current emission density versus operating temperature for impregnated tungsten cathodes	22
12	Instantaneous evaporation rate of barium as a function of time for a cathode at 1190°C	24
13	Evaporation rate of barium as a function of temperature for a cathode 200 hours old	25
14	Photograph showing the three indirectly heated impregnated tungsten cathodes	26

FIGURE		PAGE

15	Photograph of directly heated, impregnated tungsten cathode, B-151	27
16	Average gas cleanup rate during each gas fill as a function of total hours of cathode operation	31
17	Temperature difference developed between the front and back coils of the cathode as a function of discharge current and heater bias	33
18	Photograph of directly heated helical cathode inside a single-layer heat shield	35
19	Cathode temperature versus heater power and current with and without a heat shield in place	36
20	Resistance of cathode heater with the discharge off as a function of cathode temperature	37
21	Average temperature of heat-shielded cathode versus discharge current with constant heater power	38
22	Photograph of an assembled segmented bore tube	45
23	Potential variation along the axis of the tube and from segment to segment in a segmented bore tube	46
24	Photograph of pyrolytic graphite segments	50
25	Gas pressure and power output characteristics of tube B-131 versus time	51
26	Gas cleanup rate as a function of gas pressure during successive runs in tube B-131	52
27	Multiline output power versus discharge current for tubes B-131, B-133, and B-138-C at end of test	53
28	Appearance of quartz envelope and bore segments at the cathode end of tube B-131 after 225 hours	55

FIGURE PAGE

29 Appearance of quartz envelope and bore segments at the anode end of tube B-131 after 225 hours . . . 55

30 Appearance of PG segments from B-131 after 225 hours (6x magnification) 56

31 Photographs of PG overcoated segments 58

32 Cross section view of PG overcoated segments . . . 59

33 Gas pressure and power output characteristics of tube B-133 versus time 62

34 Gas cleanup rate in tube B-133 as a function of gas pressure during successive runs 63

35 Appearance of quartz envelope and bore segments at cathode end of tube B-133 after 230 hours 65

36 Appearance of quartz envelope and bore segments at the anode end of B-133 after 230 hours 65

37 Appearance of overcoated segments from tube B-133 after 230 hours (10x magnification) 66

38 Gas pressure and power output characteristics of tube B-138-C versus time 68

39 Photographs of cross section of a pyrolytic graphite segment after 400 hours of operation . . . 70

40 End view of segment showing bore, gas return path, and support rod holes with a spacer ring in place 71

41 Photograph of alumina spacers after test 71

42 Graphite bore segment with a 0.005 in. overcoating of tungsten on the bore, i.d., and end surfaces 71

43 Cross sectional view of overcoated segments which exhibited erosion 74

44 High magnification photographs of coating on segment 6 75

FIGURE PAGE

45 Curves showing sputtering yield versus ion energy for argon ions striking at normal incidence 77

46 Photographs of sputtering damage to porous tungsten throat segments 79

47 Photograph of anode end of segment 6 (left) and cathode end of segment 7 (right) 80

48 Gas pressure versus time for quartz bore tube F-29 at 20 A 83

49 Average gas cleanup rate in quartz bore tube F-29 for each gas fill as a function of total hours of tube operation 84

50 BeO bore assembly with weld rings 87

51 Sketch showing dimensions of beryllia bore 88

52 BeO bore with cathode, anode, and coolant jacket assemblies in place 89

53 Experimental arrangement for testing BeO bore tube 90

54 Output power versus discharge current for different gas filling pressure 92

55 Appearance of braze joints of the BeO bore assembly 93

56 Power output characteristics of the BeO bore tube at high discharge currents 95

57 Photograph of the graphite disk bore assembly . . . 98

58 Output power versus discharge current for different cold filling pressures for the disk tube 100

59 Dependence of the power output on magnetic field for three different filling pressures 101

FIGURE		PAGE

60	Photographs of tungsten disks assembled in a quartz envelope	103
61	Output power versus discharge current for different cold filling pressures	104
62	Appearance of disk structure after 517 hours of operation	106
63	Photographs of a tungsten disk	107
64	Output power characteristics of a 2.5 mm aperture tungsten disk tube	109
65	Over-all tube efficiency versus discharge current at different gas filling pressures for a 2.8 mm aperture tungsten disk tube	110
66	Schematic diagram of a periodic permanent magnet assembly	113
67	Trajectory of a charged particle in a magnetic cusp at a field reversal	119
68	Disassembled PPM laser system	121
69	Anode portion of laser discharge tube	122
70	Assembled PPM laser system	123
71	View of solenoid and PPM laser system	124
72	Axial variation of PPM field	125
73	Axial variation of PPM field	126
74	Axial variation of PPM field	127
75	Current dependence of the argon ion laser output power	129
76	Tube voltage versus discharge current	130
77	Bore damage at the cathode end of the discharge tube	132

FIGURE		PAGE

78	Cross-sectional view of laser bore illustrating the damage which occurred at the field reversals	133
79	Bore segments with (a) three off-axis holes for gas flow, and (b) the same segment with six additional slots machined on the o.d.	136
80	Output power versus discharge current for different cold filling pressures and with the external gas return path open and closed	138
81	Apparatus for measuring temperature of segments in a segmented-bore tube	142
82	Variation of magnetic field strength along the axis of the solenoid with and without pole pieces	143
83	Dependence of segment temperature on field strength	144
84	Dependence of segment temperature on the position of the throat in the converging magnetic field	146
85	Dependence of laser output power on magnetic field at constant discharge current . . .	149
86	(a) Equivalent circuit showing the relation of the power supply, ballast resistor, and discharge tube	151
	(b) Equivalent circuit expressed as a current source	151
87	Dependence of tube voltage V_T on magnetic field for two different values of discharge current	152
88	Tube voltage versus discharge current at two different gas pressures for the 4 mm diameter tube	153
89	Spectrum analyzer display for random fluctuation of laser output	161
90	Spectrum analyzer display of laser output spectrum	163

SECTION I

INTRODUCTION

This report contains the results of a 15-month program to investigate and improve the reliability and operating characteristics of argon ion lasers. The technical effort of the program may be divided into three activities:

1. Life testing of critical discharge tube elements (cathode, bore) to determine the failure modes of the most practical materials and configurations

2. Evaluation of bore designs to minimize erosion and/or localized damage

3. Measurement and improvement of operational characteristics.

The studies performed under this contract drew heavily upon the results of an earlier 15-month Air Force contract (AF 33(615)-3077) of the same title and sponsorship as the present program. The 300 page final report of this earlier contract (Ref. 1) reported in detail on the basic mechanisms, scaling laws, performance, and plasma properties of argon ion lasers. Gas pumping in ion lasers, and mirror damage and mode distortion effects were also investigated in detail. At the outset of the present program, the scaling laws which predict the tradeoffs among power output, size, and efficiency were reasonably well understood, and all of the problem areas associated with ion laser construction were clearly identified. The goal of the present program was to provide solutions to these problems and to improve the operational characteristics of the laser. This goal has been attained in large part.

Highlights of the work performed during the present program are the following: determination of the behavior of oxide and impregnated cathodes in ion lasers (life, gas cleanup, discharge heating); evaluation of the important ion laser bore materials (graphites, quartz, tungsten, and beryllia); and development of a tungsten disk bore structure which provides long life and high efficiency. Also studied were the use of a periodic permanent magnet structure to confine the discharge, and noise modulation of the output beam.

In Section II, studies of oxide and impregnated cathode for use in ion lasers are reported. Life test data for two oxide cathodes run 1700 hours and an impregnated cathode run 2500 hours are reported. Gas cleanup was closely monitored during these tests to determine what fraction of the gas cleanup rate in lasers is attributable to the cathode and what fraction must be attributed to the bore. Quantitative measurements are reported of the amount of additional cathode heating which occurs when current is drawn from the cathode in the discharge.

Section III describes experiments to evaluate various ion laser bore materials. A typical test of each bore material consisted of fabricating a 3 mm diameter laser bore of the material and operating the laser for approximately 200 hours. Properties of interest were resistance to ion sputtering, cleanliness as a vacuum material, gas cleanup properties, and thermal characteristics. Materials tested and reported upon are pyrolytic graphite, graphite overcoated with pyrolytic graphite, graphite overcoated with tungsten, tungsten, quartz, and beryllia.

One of the most important developments during this contract was the excellent operating performance of lasers using a disk-bore structure (i.e., thin disks, widely spaced), as described in Section IV. The efficiency and resistance to sputtering damage of this structure are the best of any laser construction method we have tested to date. The heat transfer properties of the disk-bore structure are analyzed in Appendix A.

Section V is concerned with the operation of argon ion lasers using periodic permanent magnets (PPM) to replace the solenoidal magnet. The design of a PPM assembly to confine the plasma with special emphasis on the parameters which minimize electron loss to the walls at the field reversals is discussed. Results are presented which compare the performance of an argon ion laser when operated in a solenoid and in a PPM assembly. While the output characteristics were similar, severe bore erosion occurred at the field reversals with PPM confinement.

Two topics which were also studied briefly during the program — the design of internal gas return paths in segmented-bore tubes and the magnetic field dependence of localized power dissipation in the cathode throat — are discussed in Section VI. The general problem of unwanted modulation of the output beam by power supply ripple and discharge fluctuations is considered in Section VII. The quantitative relationship between laser light modulation and the ripple amplitude of the several power supplies used to run a laser is given and was confirmed experimentally. Less than 1% peak-to-peak total beam modulation could be obtained. Characteristics of a discharge instability in the hundred kHz range are given. The physical source of this oscillation was not determined but it could always be eliminated by a proper choice of operating conditions.

Section VIII summarizes briefly the important results and conclusions of this program.

SECTION II

CATHODE STUDIES

The objective of this effort has been the measurement of the operating characteristics of cathodes which are suitable for use in ion lasers. The operating characteristics of interest are the lifetime, efficiency, current capability, gas cleanup rate, and resistance to poisoning. Two 1700-hour life tests of oxide cathodes and a 2400 hour life test of an impregnated tungsten cathode are reported.

A. DISCUSSION OF CATHODE TYPES

The basic equation for the rate of thermal emission of electrons from a heated solid is given by the Richardson-Dushman equation

$$J = AT^2 \exp(-\phi/kT) \tag{1}$$

where J is the thermionic emission in amperes per square centimeter, A is a fundamental constant equal to 120 A/cm^2, k is the Boltzmann constant, T is the temperature (^oK), and ϕ is the potential barrier that the electrons must overcome to go from the Fermi level inside to the vacuum level outside of the solid. Emission properties of a surface depend critically on ϕ; typical values of ϕ are 1.5 eV for oxide cathodes, 2.0 eV for tungsten matrix cathodes, 2.6 to 3.2 eV for refractory coated cathodes (Gd_2O_3, LaB_6, ThO_2), 3.1 eV for thoriated tungsten, and 3.4 to 5 eV for metal cathodes. Figure 1 shows the emission characteristics of thermionic cathode types which are capable of emitting a sufficiently high current density (> 1 A/cm^2) to be of interest for ion laser use (Ref. 2).

The major advantage of oxide cathodes is, of course, the low operating temperature, and therefore low heater power, required per emitted ampere. We have used this type of laser extensively in our ion laser program. Two successful 1700 hour life tests of this type of cathode have been conducted under this program. One disadvantage of the oxide surface is that when high current densities (> 2 A/cm^2) are drawn from the cathode, particles of the coating may flake off from the supporting mesh.

Nickel matrix cathodes, the second most efficient type, act essentially as patchy oxide cathodes and have no particular advantage over oxide cathodes unless intricate shapes are required (Ref. 2).

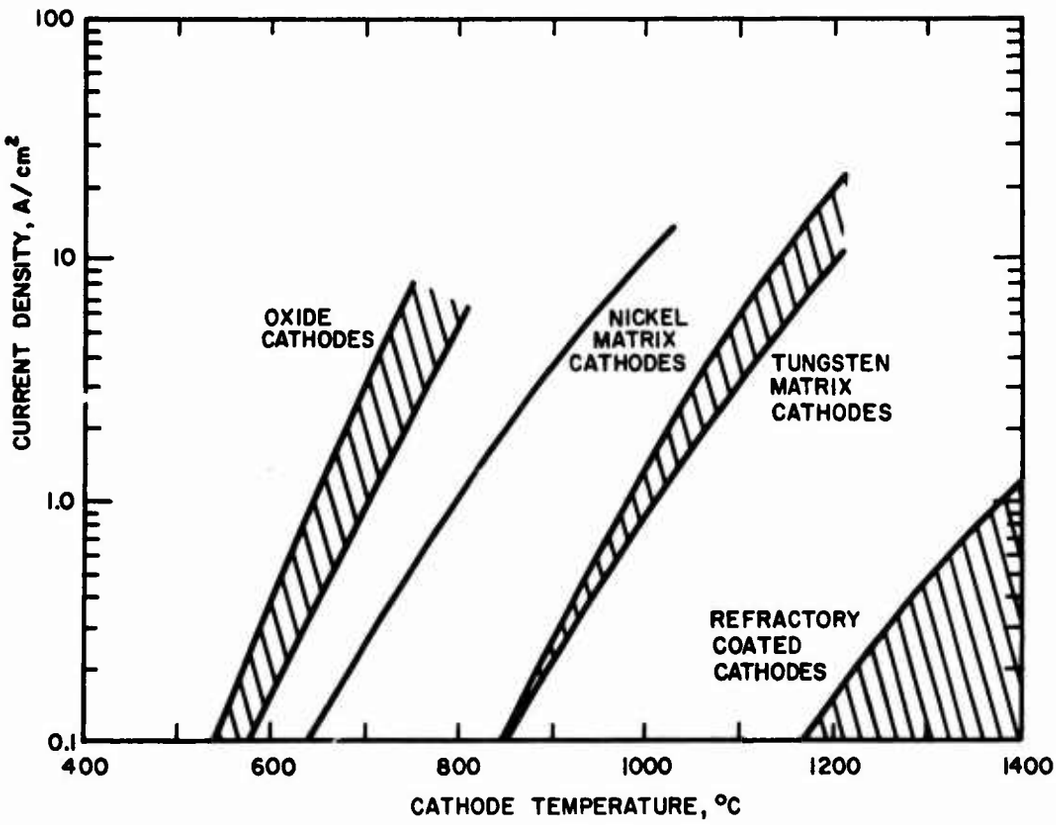

Fig. 1. Emission current density versus surface temperature for different cathode types.

Many different types of tungsten matrix cathodes (L cathodes, impregnated cathodes, dispenser cathodes, etc.) have been discussed in the literature. In all of these cathode types, barium diffuses through porous tungsten to form an emitting layer on the tungsten surface. The higher operating temperature of this cathode makes it inherently less efficient than the oxide cathode at a given current density; for an emission current of 1 A/cm^2, the oxide cathode requires one-fifth the heater power. The advantages of tungsten matrix cathodes are (1) mechanical ruggedness and (2) ability to supply continuously high current densities (5 to 10 A/cm^2). Four different configurations of impregnated tungsten cathodes have been evaluated under this program.

B. OXIDE CATHODE TESTS

1. Description of the Hughes Ion Laser Oxide Cathode

The cathodes widely used in our laser programs are directly heated, oxide-coated nickel mesh structures such as that shown in Figure 2. The completed cathode has a triple heat shield with a 1/2 in. diameter hole in the front for electron extraction. Another hole in the rear allows passage of the laser beam so that the cathodes may be mounted coaxially with the beam.

These cathodes were developed specifically for ion lasers and were initially fabricated at the Research Laboratories. They are now built as a product by the Hughes Electron Dynamics Division (EDD). The flower-shaped mesh shown in Figure 2 has an area of 24 cm^2 and is coated with the two-carbonate ($BaCO_3$, $SrCO_3$) coating used at EDD for space-qualified TWT's; in this application the cathode is maintained at 725°C and emits 250 mA/cm^2 for > 20,000 hours.

In ion laser applications, which require high current densities, the cathode temperature is maintained at 850°C. The input power to the cathode to maintain this temperature is approximately 60 W (25 A at 2.4 V).

Evaporation of the oxide coating starts to occur above 800°C. Evaporation and/or ion sputtering of the oxide coating should be the life-limiting cathode processes.

We find these oxide cathodes to be very resistant to poisoning in argon lasers. The cathodes may be let down to an argon, helium, or dry nitrogen atmosphere repeatedly for minor tube repairs (such as window replacement) without impairing their operation. This is in agreement with the results of Haas and Jensen (Ref. 3), who have shown that cathode poisoning is largely caused by the absorption of water vapor, and that good emission will be maintained if the cathode is kept at 150°C during exposure to air.

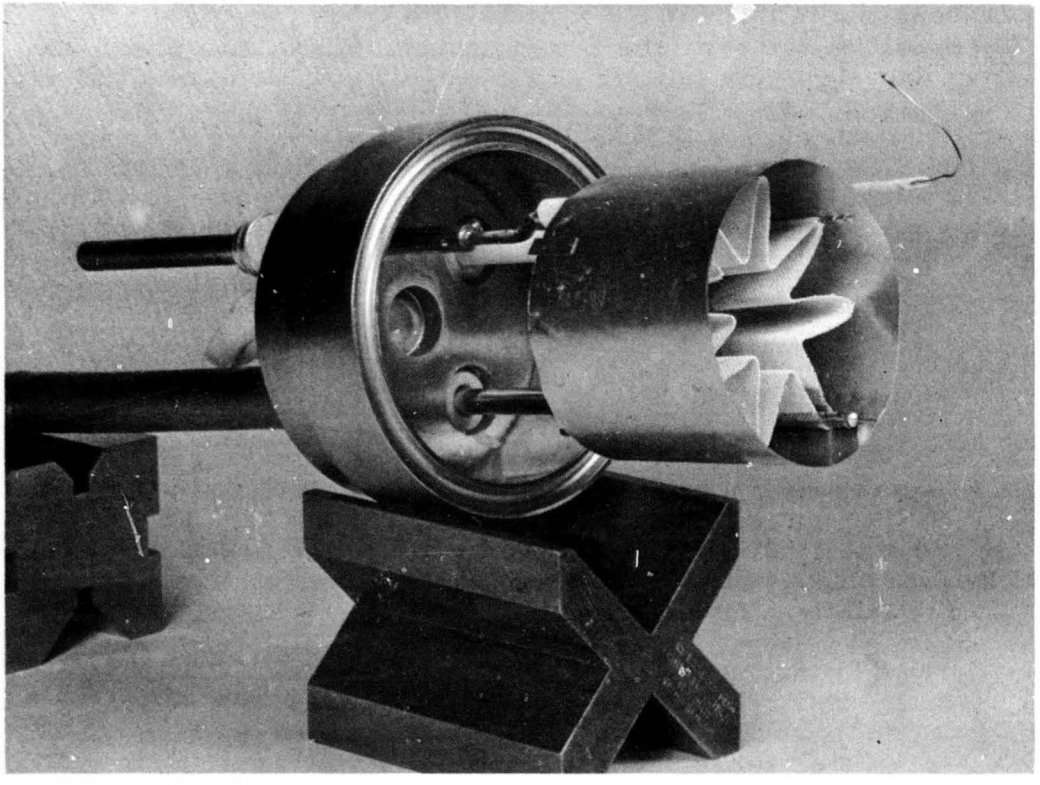

Fig. 2. Hughes ion laser oxide cathode with front heat shielding removed.

2. Cathode Test Apparatus

The experimental apparatus used to evaluate cathode performance is shown in Figure 3. Figure 4 is a schematic representation. The cathode and anode are separated by a 1-1/2 in. diameter, 5 in. long quartz bore. This configuration reproduces the electrodes and approach arms, but not the bore or constrictions, of quartz and segmented bore tubes. A thermocouple gauge, getter, gas leak valve, and high pressure argon reservoir are located on a side arm. The Hasting thermocouple gauge was calibrated for argon using a McLeod gauge. The volume of the tube is 0.7 liter.

3. Results of First Oxide Cathode Tests (No. B-132)

An oxide cathode was operated for 1700 hours before being disassembled for inspection. The discharge current was 20 A for the first 1100 hours, and was varied between 10 and 20 A during the last 600 hours to determine the dependence of gas cleanup rate (GCR) on current. Particular attention was paid to the GCR throughout the run since we wished to determine what fraction of the GCR measured in bore material experiments is attributable to the bore material and what part to the cathode and anode.

a. Gas Cleanup Rate

Figure 5 shows the variation in gas pressure during the first 1050 hours of operation at 20 A. The tube was operated in 8-hour and then 23-hour increments. The gas pressure was recorded both while the discharge was on (solid line) and when the tube was shut off; this provided a measurement under uniform, cold conditions. When the cold filling pressure fell to 0.1 Torr, gas was added to obtain a pressure of 0.28 Torr, and the test continued.

It is clear from Figure 5 that there is a continual aging process going on with each successive run exhibiting a lower gas cleanup rate. The average GCR was 3.5 μ-liter/hour for the first run (10 to 40 hours) and 0.46 μ-liter/hour for the last complete run (790 to 1066 hours). This decrease was not caused by contamination or leaks in the tube; the getter (which remained shiny and appeared unused throughout the run) was reflashed at 1025 hours, and no change in the gas pressure or GCR was observed.

The effect of gas pumping is evident from the difference in the hot and cold pressure readings at high and low filling pressures. The pressure gauge was mounted on the cathode bottle. In our gas pumping studies (Ref. 1), it was determined that the anode to cathode pressure

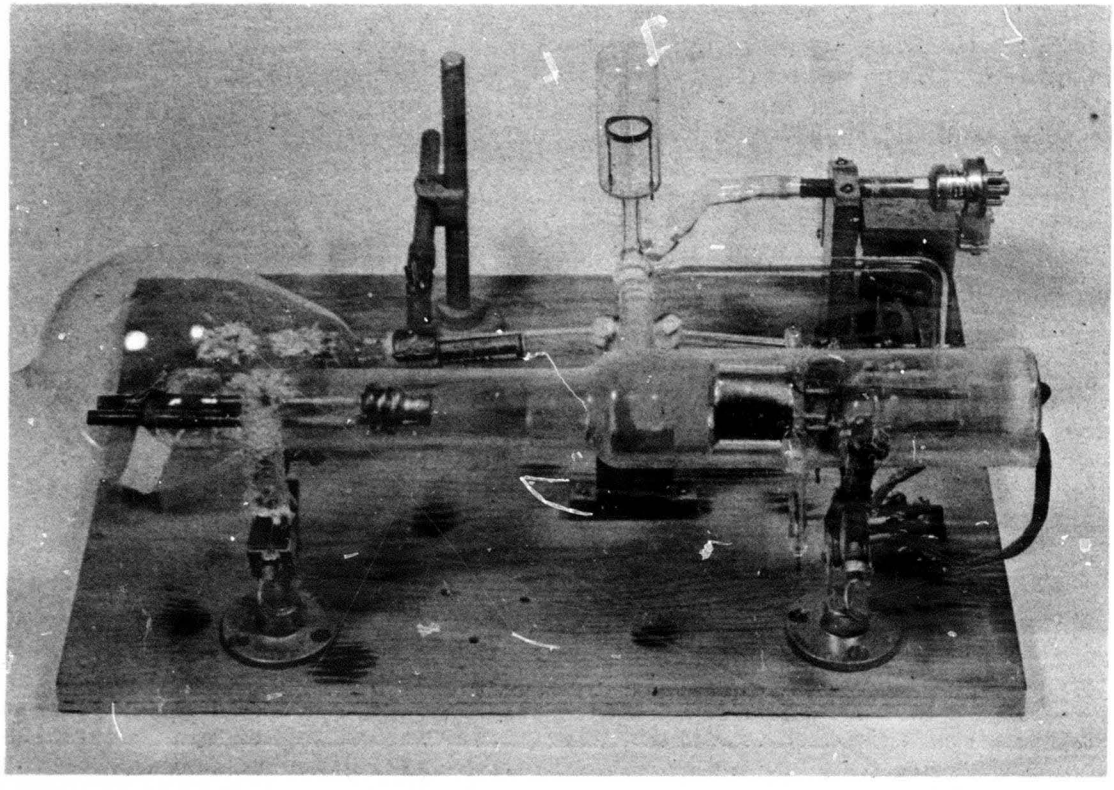

Fig. 3. Photograph of cathode evaluation apparatus.

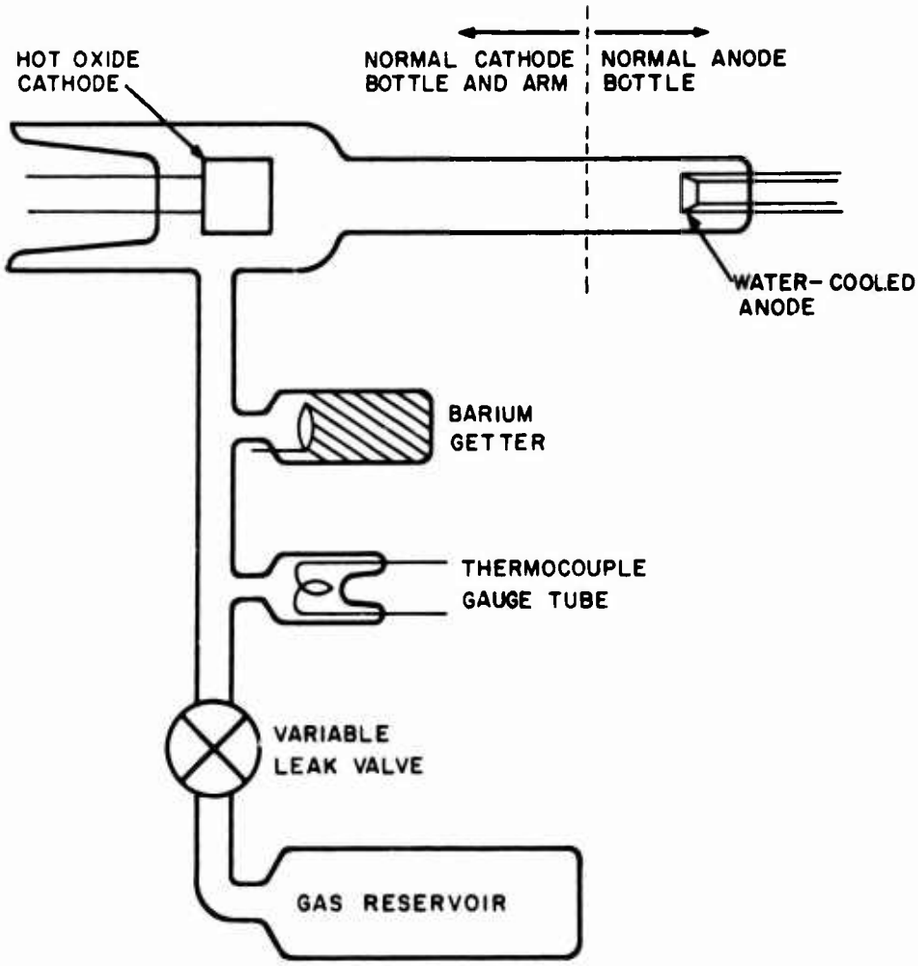

Fig. 4. Schematic representation of experimental apparatus used to monitor the gas cleanup rate of a laser cathode.

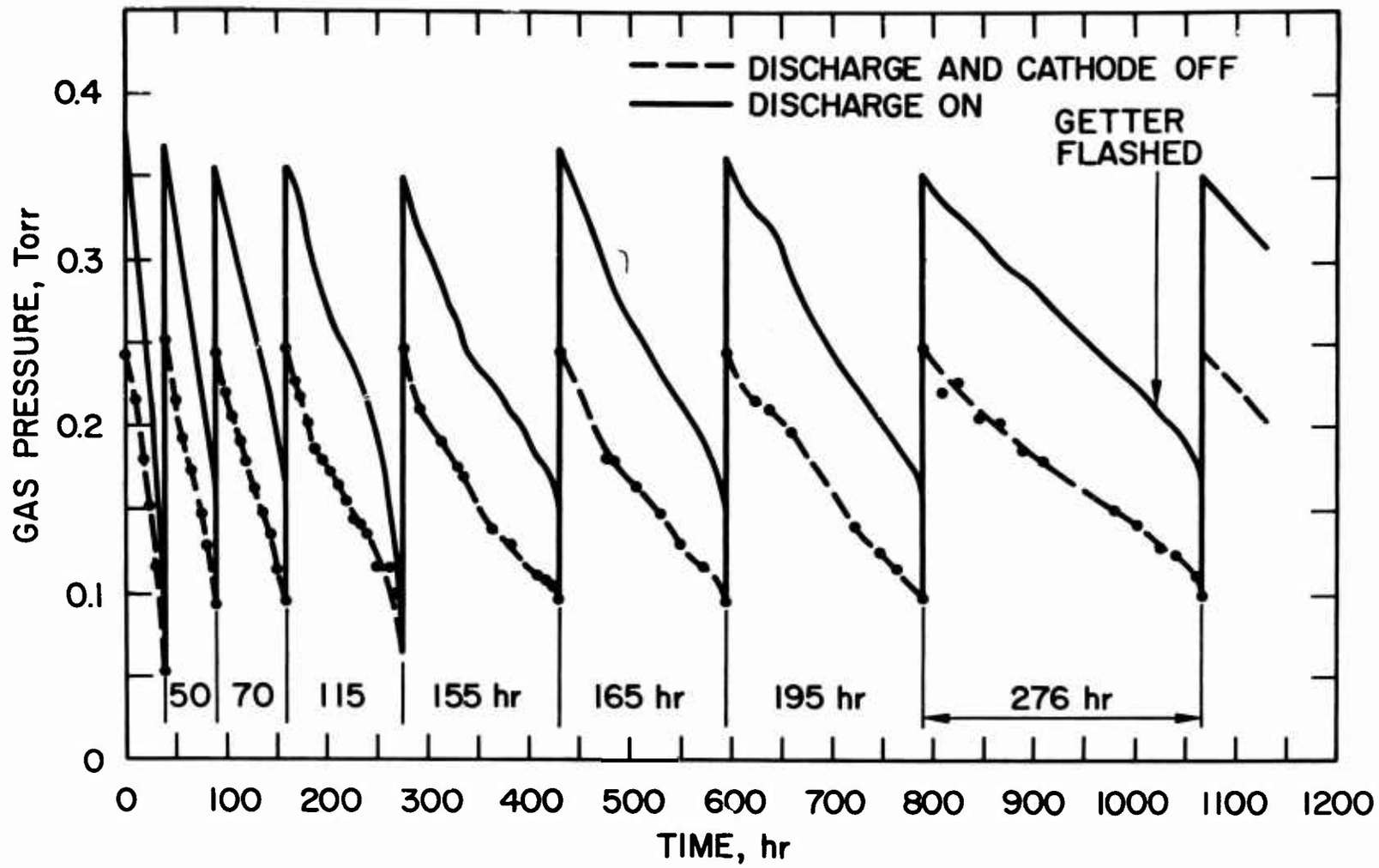

Fig. 5. Pressure variation with time for oxide cathode B-132 at 20 A.

differential decreases as the gas pressure is reduced at constant I. This accounts for the observation in our cathode test that the hot tube pressure is ~ 0.11 Torr greater than the cold pressure at high pressures, and only ~ 0.06 Torr greater at low pressures.

We have based our calculation of GCR on changes in the cold pressure to avoid errors caused by gas pumping. The variation in GCR with pressure during each run is shown in Figure 6. These curves were calculated from the daily change in cold gas pressure. For the sake of clarity, data have not been shown for the two runs between 430 and 790 hours; the GCR during these two runs fell between that of the preceding and following runs.

The gas cleanup behavior during the last 600 hours of the test is shown in Figure 7. After the arbitrary requirement of 1000 hours at 20 A was satisfied, the discharge current was varied to observe the effect on the GCR.

The discharge was run at 10 A for 240 hours (1125 to 1365 hours). During this time the gas pressure decreased only 12 μ, yielding a GCR of 0.033 μliter/hour, less than one tenth of the rate at 20 A. The strong dependence of GCR on I makes it clear that it is meaningful to compare the cleanup rates of different materials only if the discharge current is specified.

Another important observation is that large amounts of gas are absorbed in the walls and then re-emitted as the discharge current is varied. Note in Figure 7 that the cold pressure after the tube has been operated at 10 A is 45 to 60 μ lower than after operation at 20 A. When the tube is again operated at 20 A, the gas is re-emitted and the cold gas pressure increases to the value previously recorded after operation at 20 A.

Measurements show that approximately 5 hours of operation at 10 A is required for the walls to absorb the gas and become saturated. The gas is all re-emitted in about 25 min when the current is increased to 20 A.

Approximately 20% of the gas in the tube can appear or disappear into the walls under different operating conditions. Additional data on this phenomenon are reported in Section III-G, which describes a life test of a quartz-bore laser.

b. Voltage Current Characteristics

At the start of the experiment, the discharge voltage was 25 V and the filament was operated at 26 A ac and 2.1 V ac. During the test the tube voltage increased to a maximum of 35 V; when the electrical

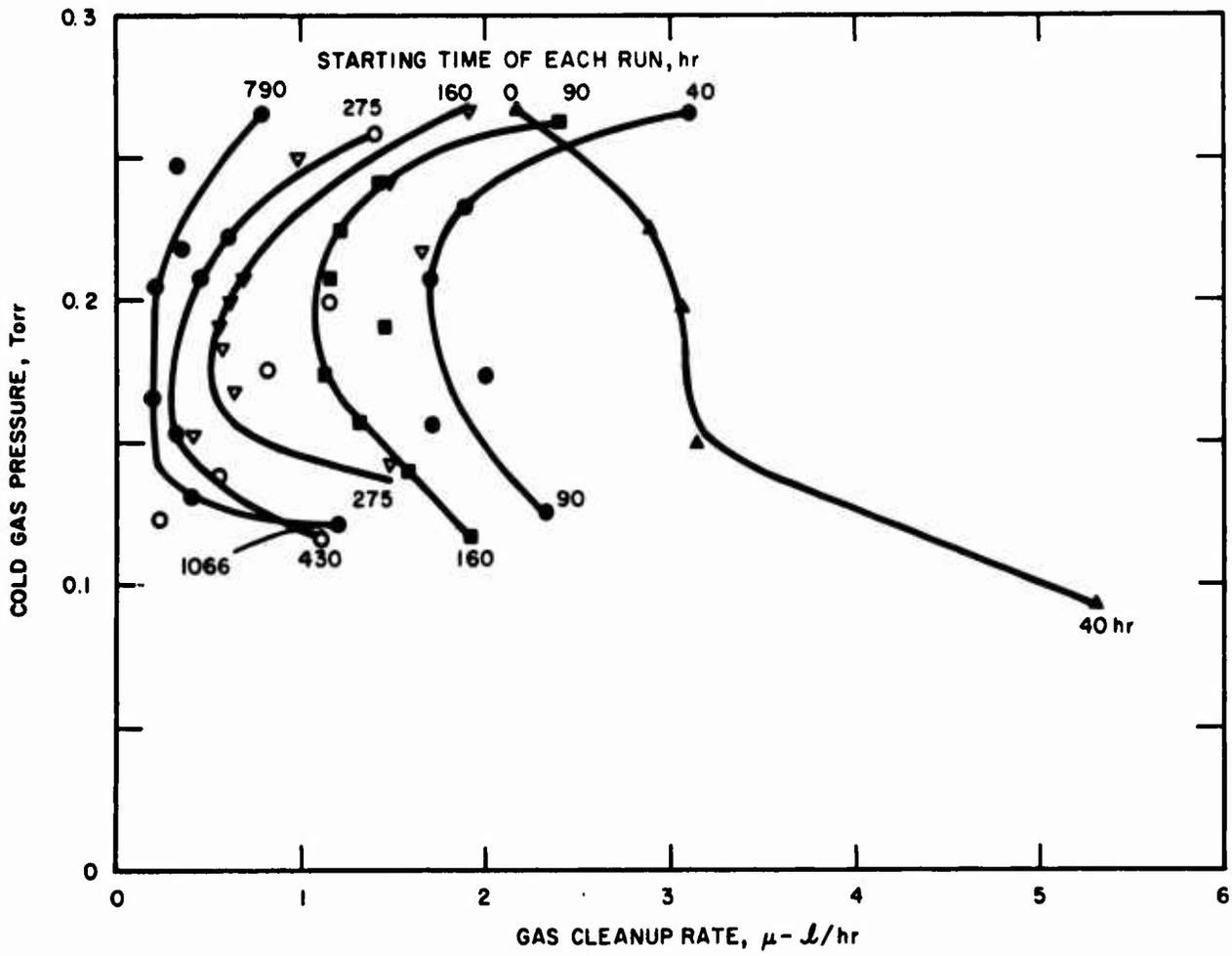

Fig. 6. Gas cleanup rate versus gas pressure during successive gas fills, tube B-132.

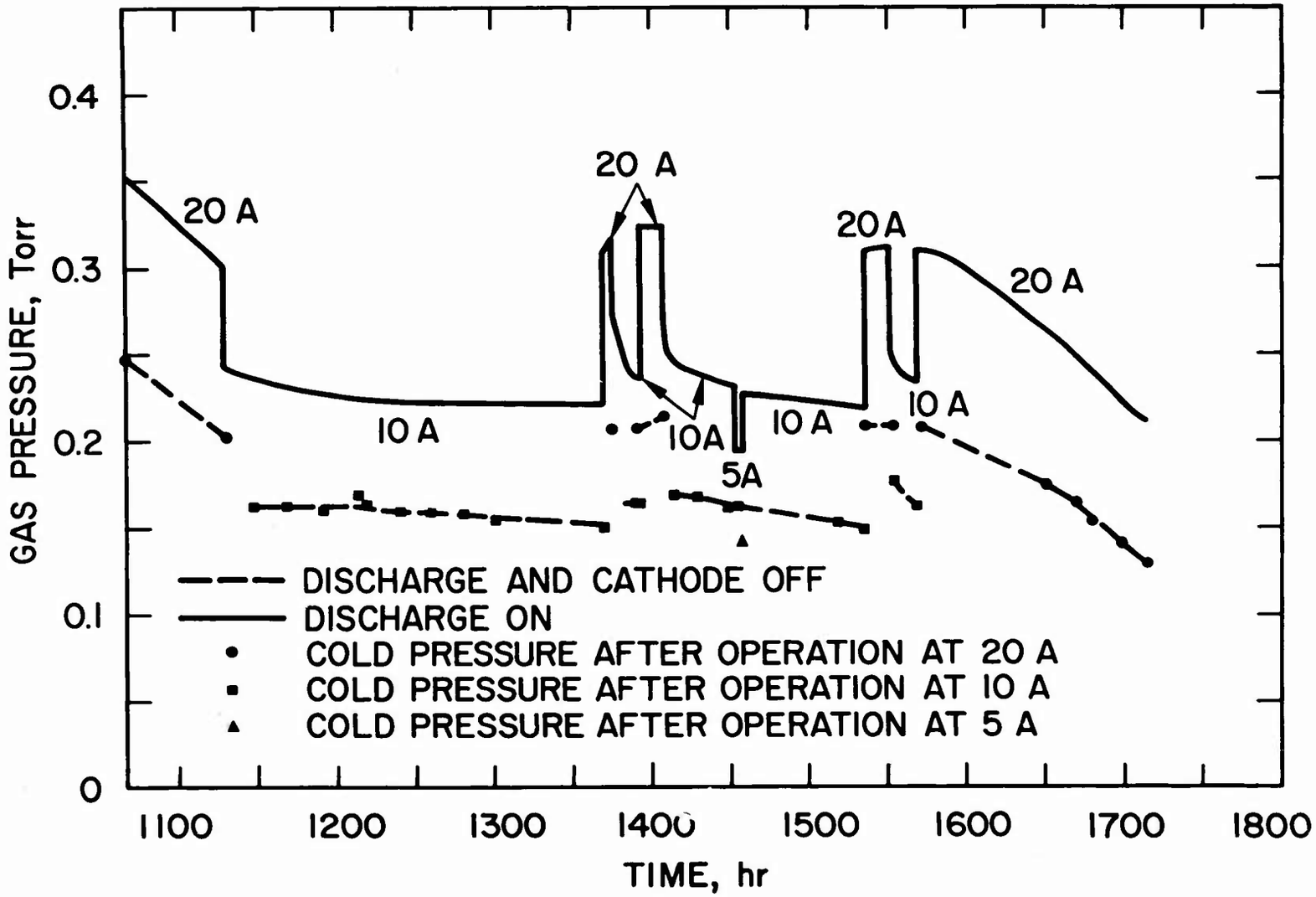

Fig. 7. Gas pressure versus time showing variation in pressure with discharge current, tube B-132.

contacts were cleaned of oxidation, the voltage decreased to 27 and remained in the range of 27 to 29 V. The filament current was maintained at 26 A throughout the experiment; this required a gradual increase in the cathode voltage from 2.1 to 2.5 V ac.

c. Appearance of Cathode at End of Test

After 1715 hours of operation the test was terminated and the cathode inspected. The cathode was still operating satisfactorily at 20 A at the end of the test.

Figure 8 is a photograph of the front of the cathode with part of the heat shield cut away to expose the oxide coated mesh. Several observations may be made:

- The oxide coating is completely removed from the inner points of the mesh which are closest to the discharge. The mesh is still intact.
- Only a thin oxide coating is left on the mesh at the outer points.
- Ion sputtering has feathered the edge of the nickel heat shield. The edge of the innermost heat shield showed more damage than the edge of the outermost shield.

4. Results of Second Oxide Cathode Test (No. B-136)

A second oxide cathode was run on life test for 1810 hours. Two changes were made in the second cathode test; a thermocouple was attached to the cathode mesh to monitor cathode temperature, and a separate connection was made to the cathode heat shield (which normally floats with respect to the cathode mesh) to monitor the potential of the heat shield during operation.

The test schedule and apparatus were the same as those described in detail for the first test. The tube was operated in 23 hour increments. When the cold gas pressure (discharge current and filament off) fell to 0.1 Torr, gas was added to obtain a pressure of 0.28 Torr, and the test continued.

a. Gas Cleanup Rate Results

Figure 9 shows the variation in gas pressure during operation at 20 A discharge current (0 to 1130 hours) and at 25 A (from 1130 hours on). The duration of successive runs was 68, 183, 593,

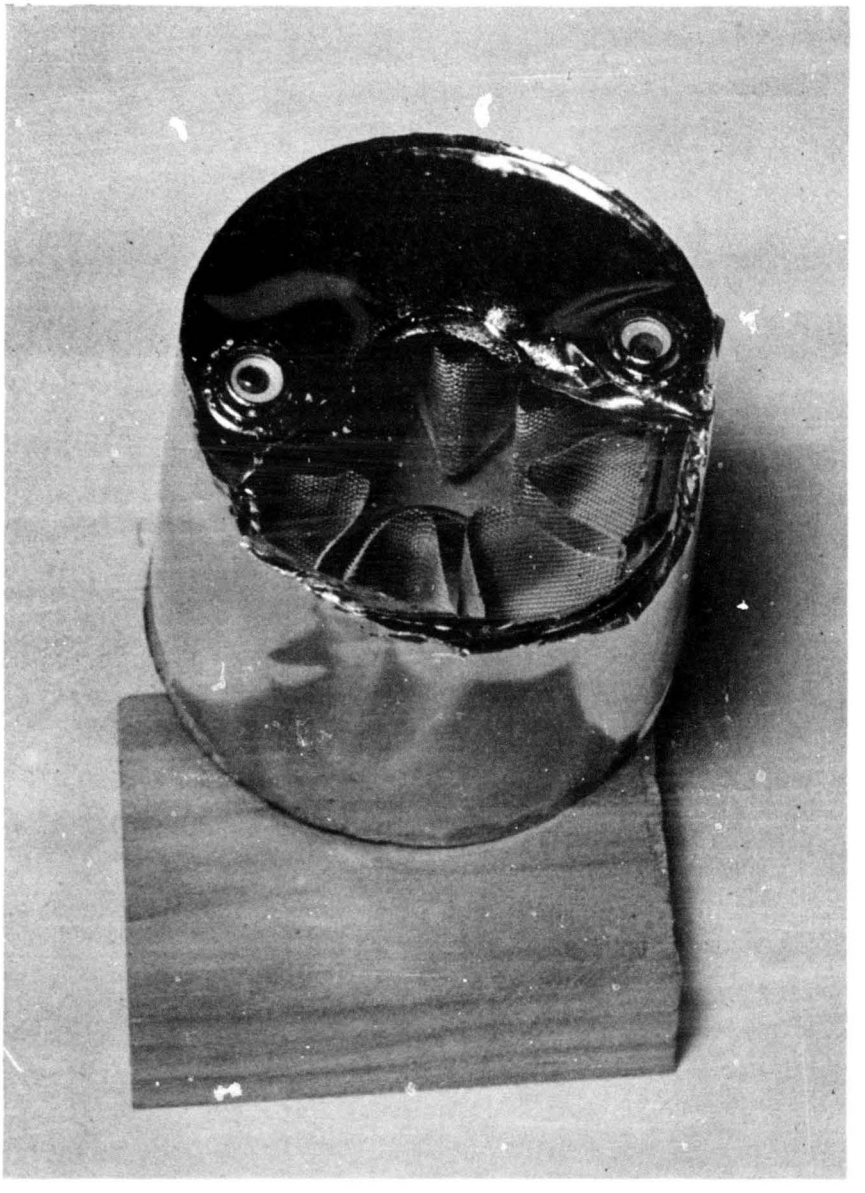

Fig. 8. Photograph of oxide cathode after 1700 hours of operation. Heat shield has been partially cut away to expose the nickel mesh.

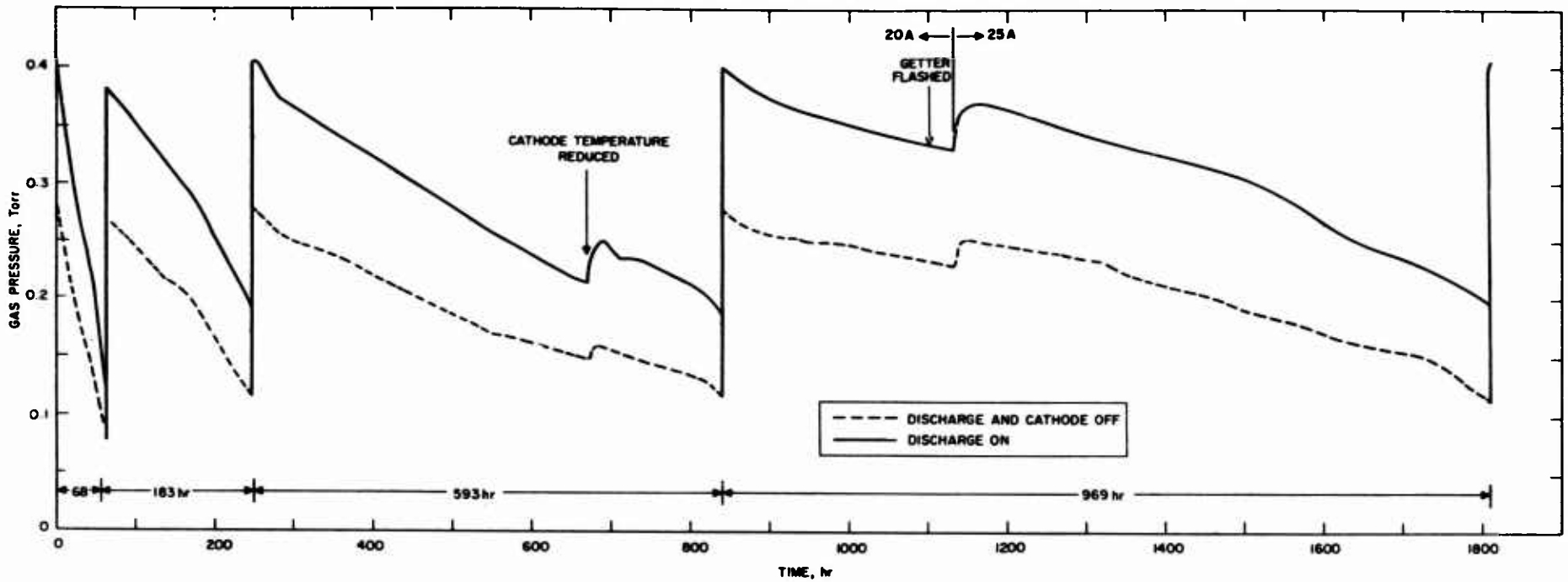

Fig. 9. Pressure variation with time for oxide cathode B-136.

and 969 hours, yielding average gas cleanup rates (GCR) for the 0.6 liter volume of 1.8, 0.53, 0.16, and 0.10 μliter/hour. These runs are two to three times longer, and the GCR proportionately lower, than the runs recorded during the same period of the previous cathode life test.

To insure that the low GCR was not caused by a gas leak, the barium getter was reflashed at 1100 hours. No change in gas pressure or operating characteristics occurred.

In our GCR measurements with different bore and vacuum envelope materials, we have found that quartz exhibits a high and extremely variable gas cleanup rate. It is likely, therefore, that the factor of three difference in the measured GCR during the two life tests is caused by differences in the surface properties of the quartz envelope; the same quartz envelope was used in the second test as the first and this was "aged."

The tube voltage cycled during each run between 20 V at low gas pressures (0.13 Torr) and 17 V at high gas pressures (0.25 Torr). The test was terminated after 1810 hours when the tube cracked at an anode pin. The cathode was emitting satisfactorily at this time.

b. Cathode Temperature Data

It was noted while operating lasers in the laboratory that the cathode temperature increased when the discharge was operating; in fact, once the discharge was started, satisfactory emission could be obtained even when filament power was removed. In this second experiment, a Pt:Pt-Rh thermocouple was spot welded directly to the cathode mesh to provide more complete temperature data.

Readings of cathode temperature were taken at the beginning of the test using the thermocouple and an optical pyrometer for comparison. The pyrometer readings were about 15°C higher.

When the tube was filled to 0.2 Torr, the cathode temperature dropped 40°C. An input power of 60 W (2.2 V ac at 27 A) was required to maintain the cathode mesh at the recommended temperature of 850°C. As expected, the cathode temperature (in degrees Kelvin) varied as the fourth root of the input power.

Thermocouple temperature readings taken during the first few hundred hours of operation indicated that an increased amount of filament power was required to maintain a temperature of 850°C. After 670 hours of operation, thermocouple data indicated that an input of 90 W resulted in a temperature of only 720°C. However, a temperature of 910°C was recorded with an optical pyrometer at this input level.

This higher temperature reading agreed with the power input-temperature data taken at the beginning of the test. It was clear that the thermocouple characteristics had changed in the discharge and operation was resumed at 60 W input which, from pyrometer readings, yielded 850°C. The change in gas pressure shown in Figure 9, which occurred when the cathode temperature was reduced, is surprising; no such dependence of cold gas pressure on cathode temperature was observed during the previous cathode test.

Discharge noise and spontaneous emission prevented the recording of the cathode temperature while the discharge was operating. However, the cooling rate of the cathode was sufficiently slow that an accurate reading could be taken immediately after an interruption of the discharge current. Table I contains data taken at 1130 hours on cathode temperature T_c as a function of discharge current I. The total power input to the cathode P_c has been calculated using as a basis the facts that (1) the radiated power varies as the fourth power of the absolute temperature, and (2) a 60 W input produces a cathode temperature of 850°C. The incremental power ΔP_c is the additional power delivered to the cathode from the discharge with the discharge on. P_c has been plotted as a function of discharge current in Figure 10; P_c is closely approximated by the expression

$$P_c = P_{co} + 1.25\ I \text{ watts} \qquad (2)$$

where P_{co} = 60 W in this case, and ΔP_c = 1.25 I. The reason for the linear dependence on I is not obvious; one would expect ΔP_c to increase as I^2 because of resistive I^2R losses in the cathode mesh and coating. Heating caused by ion bombardment, which would vary as I, should be a negligible contribution (< 4 W at 20 A).

As a final measurement, the dependence of ΔP on the initial temperature of the cathode was measured at I = 20 A. These data are shown in Table II. The fact that ΔP_c is constant for T_c (I = 0) ≥ 760°C is consistent with space-charge-limited operation. The value of 30 W for ΔP_c for T_c (I = 0) = 720°C may be in error because of difficulties in reading temperatures lower than 750° with an optical pyrometer.

c. Potential of the Heat Shield

A lead attached to the heat shield was brought out through the vacuum envelope to an electrometer. With the cathode operating at T_c(I = 0) = 850°C, the potential of the heat shield with respect to the cathode varied from 0.3 V to 1.0 V when the discharge current was increased from 5 A to 20 A. For different operating pressures and initial cathode temperatures, the shield potential at 20 A remained in the range 0.8 to 1.2 V.

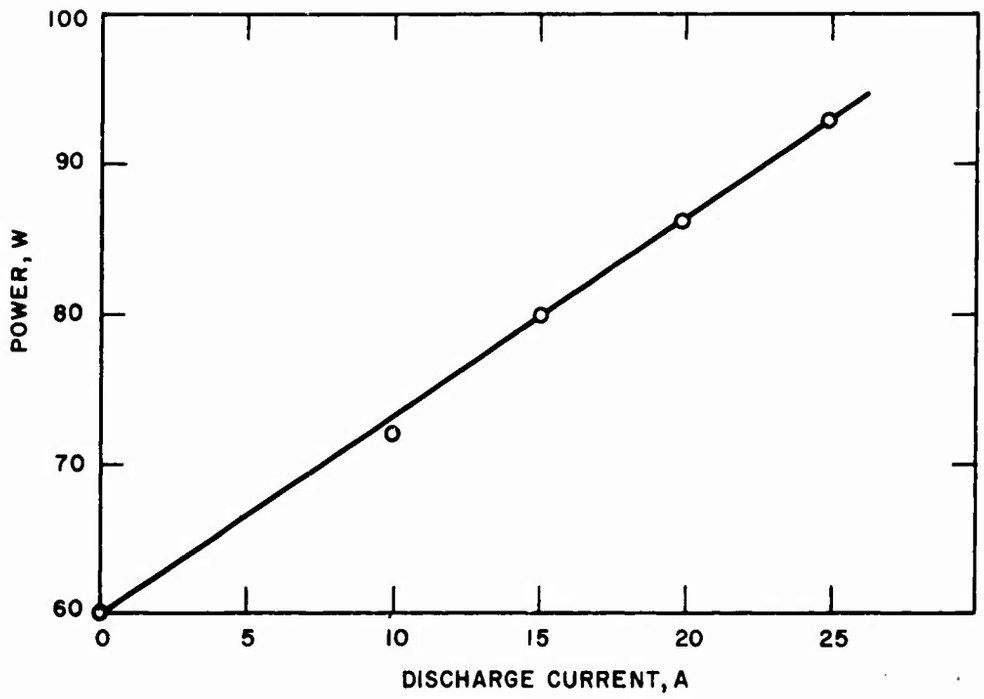

Fig. 10. Power dissipated in the cathode as a function of discharge current.

TABLE I

Dependence of Cathode Temperature on Discharge Current

I, A	T_c, °C	P_c, W	ΔP_c, W
0	850	60	0
10	905	72	12
15	933	80	20
20	960	86	26
25	980	93	33

TABLE II

Dependence of Cathode Operating Temperature on Initial Temperature

$T_c(I = 0)$, °C	$T_c(I = 20\ A)$, °C	ΔP_c, W
850	960	26
818	930	26
760	892	26
720	885	30

The requirement which determines the potential of the conducting heat shield is that the sum of the total ion and electron currents to the conductor must be zero. (This condition need not be satisfied at every point on the conducting surface, but only for the entire surface.) When the shield was connected to the cathode, an ion current of ~ 1 A was drawn. This condition must correspond to the same ion current being collected on the shield in both cases, but with a reduced electron current reaching the shield when it is grounded to the cathode.

When the shield is grounded, ions collected at the shield will have ~ 1 eV more kinetic energy than when the shield is floating. Increased heating and sputtering of the heat shield should occur, therefore, when it is connected to the cathode mesh. In an experiment conducted a year ago, it was noted that increased heating of the cathode (evidenced by increased incandescence) occurred when the cathode mesh and heat shield were connected. For this reason, all cathodes are now constructed so that the heat shield is not connected electrically to the cathode mesh.

C. IMPREGNATED TUNGSTEN CATHODE TESTS

1. Description of Cathodes

The impregnated tungsten cathodes tested in this program consist of a porous tungsten matrix with a barium compound dispersed throughout. During activation, a thin film of barium diffuses to the emitting surface and decreases the work function. Figure 11 is a plot of emission current density versus operating temperature for this type of cathode. Although such cathodes have been operated at temperatures from 800 to 1250°C, the usual operating range is from 1025 to 1125°C. The emission current values given in Figure 11 are for vacuum conditions. The current density obtained at a given temperature in a gas discharge is less because the barium layer is continually being damaged by ion bombardment. Recommendations from manufacturers of this type of cathode (Philips Metalonics, Spectra-Mat, Inc.) are that the cathode emission in the gas discharge be derated 50% from the values shown in Figure 11.

The operating lifetime of the cathode will be dependent on the operating temperature, which controls the barium evaporation rate. Values quoted by a manufacturer are 1000 hours at 1200°C, 10,000 hours at 1120°C, and 100,000 hours at 1050°C. These figures are for vacuum tube conditions; as in the case of the emission current, the operating lifetime values must be derated for operation in a gas discharge. The amount of degradation of the cathode operating characteristics in the gas discharge is dependent on the gas used, the pressure, and other parameters, and no one value can be specified for all situations.

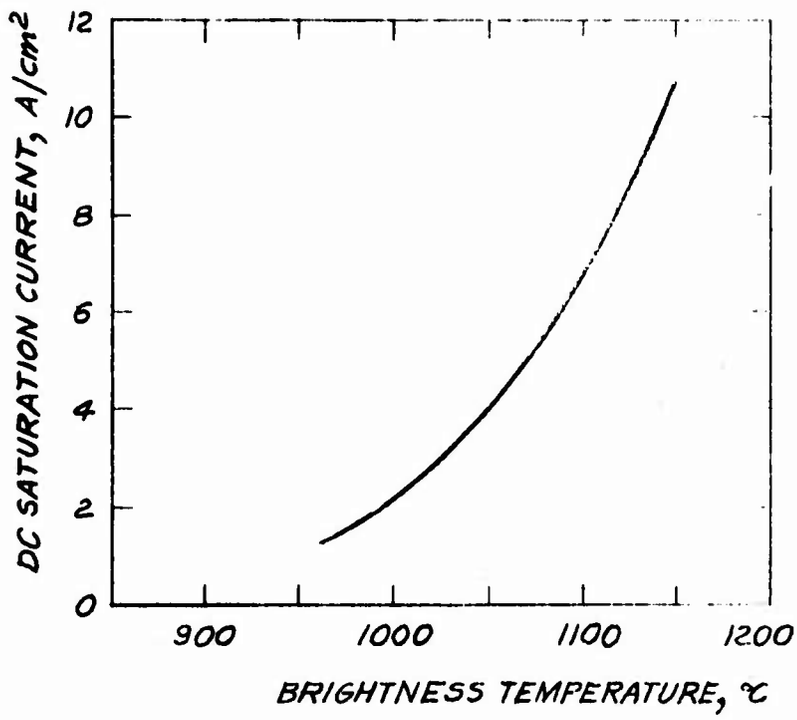

Fig. 11. Current emission density versus operating temperature for impregnated tungsten cathodes (data from Spectra-Mat, Inc.).

Another important factor to consider in employing impregnated tungsten cathodes is the evaporation rate of barium from the cathode surface. Unless precautions are taken, barium may degrade laser performance by depositing on Brewster angle windows or internal mirror surfaces. Figure 12 shows the dependence of the evaporation rate of barium from the cathode surface as a function of temperature. The evaporation rate also varies greatly during the life of the cathode, as shown in Figure 13. To estimate the magnitude of the evaporation problem, consider the time required to deposit a 100 Å thick film on a 1 cm^2 area, assuming that all of the evaporated barium from a 1 cm^2 area of the cathode deposits on this surface. Since the density of barium is 3.8 g/cm^3, a film 100 Å thick on a 1 cm^2 area weighs 3.8 μg. From Figure 13, barium will evaporate at a rate of about 0.4 $\mu g/cm^2$-hour from a cathode at 1050°C. Therefore, the barium deposition rate for the example chosen would be ~10 Å/hour, or 10 hours to deposit a 100 Å film. Since films on the laser optical surfaces of > 100 Å thickness would seriously degrade performance, the necessity for shielding optical surfaces either by heat shielding or geometric orientation of the impregnated cathode surface is clear.

Three indirectly heated impregnated tungsten cathodes purchased from Spectra-Mat, Inc., for evaluation are shown in Figure 14. They are designated B-137, B-140, and B-144. Cathode B-137 is a 1 in. diameter disk cathode with a 5 cm^2 emitting area. B-140 and B-144 are annular cathodes which emit from the i.d., o.d., and front face. B-140 is 0.40 in. long, with a 0.44 in. o.d., 0.25 in. i.d., and an emitting area of 6 cm^2. B-144 is 1 in. long, with a 1 in. o.d., 0.25 in. i.d., and an emitting area of 28 cm^2. All cathodes have potted heaters; B-137 and B-144 have isolated heater leads and B-140 has one heater lead common to the emitting surface.

Two directly heated impregnated cathodes as pictured in Figure 15 were purchased from Philips Metalonics. The impregnated tungsten surface in these cathodes is heated by passing current through the tungsten helix, rather than through a separate heater. These cathodes have a surface area of 10 cm^2.

2. Description of Test Apparatus

The test apparatus used for the impregnated tungsten cathode experiments is similar to that shown in Figures 3 and 4 for the oxide cathode life test. The anode, quartz envelope, barium getter, and thermocouple pressure gauge were the same. In order that the pressure at the cathode might be monitored more closely during processing and breakdown of the cathode, an ionization gauge tube was located on the discharge envelope.

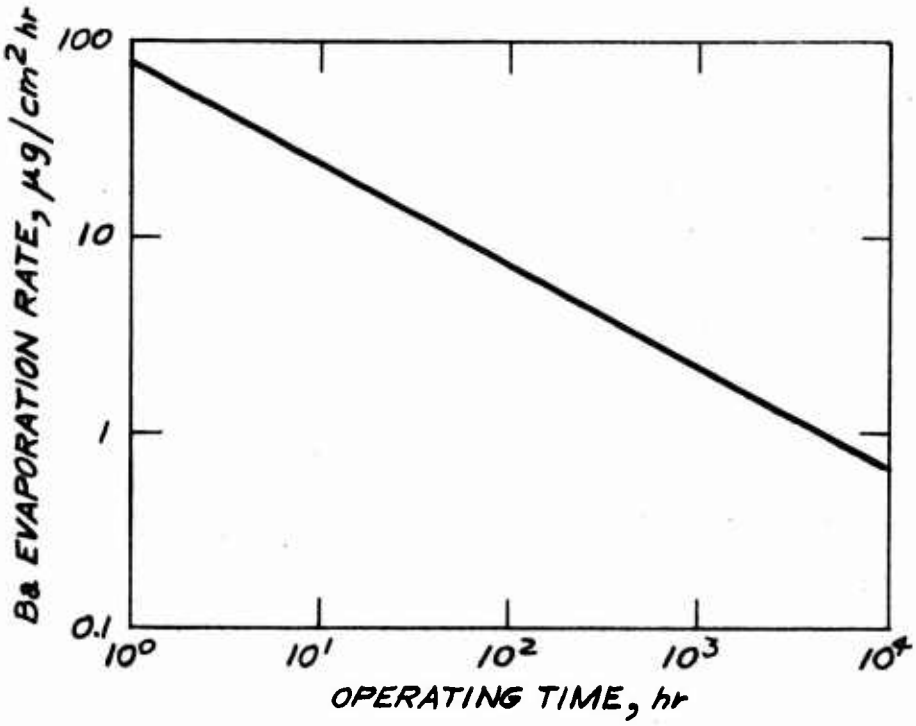

Fig. 12. Instantaneous evaporation rate of barium as a function of time for a cathode at 1190°C (Ref. 3).

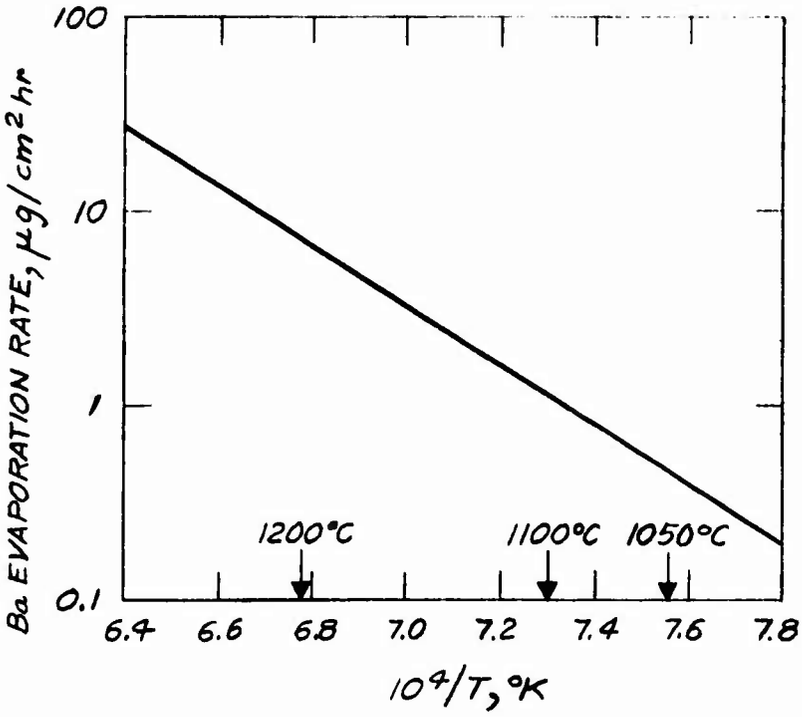

Fig. 13. Evaporation rate of barium as a function of temperature for a cathode 200 hours old (Ref. 3).

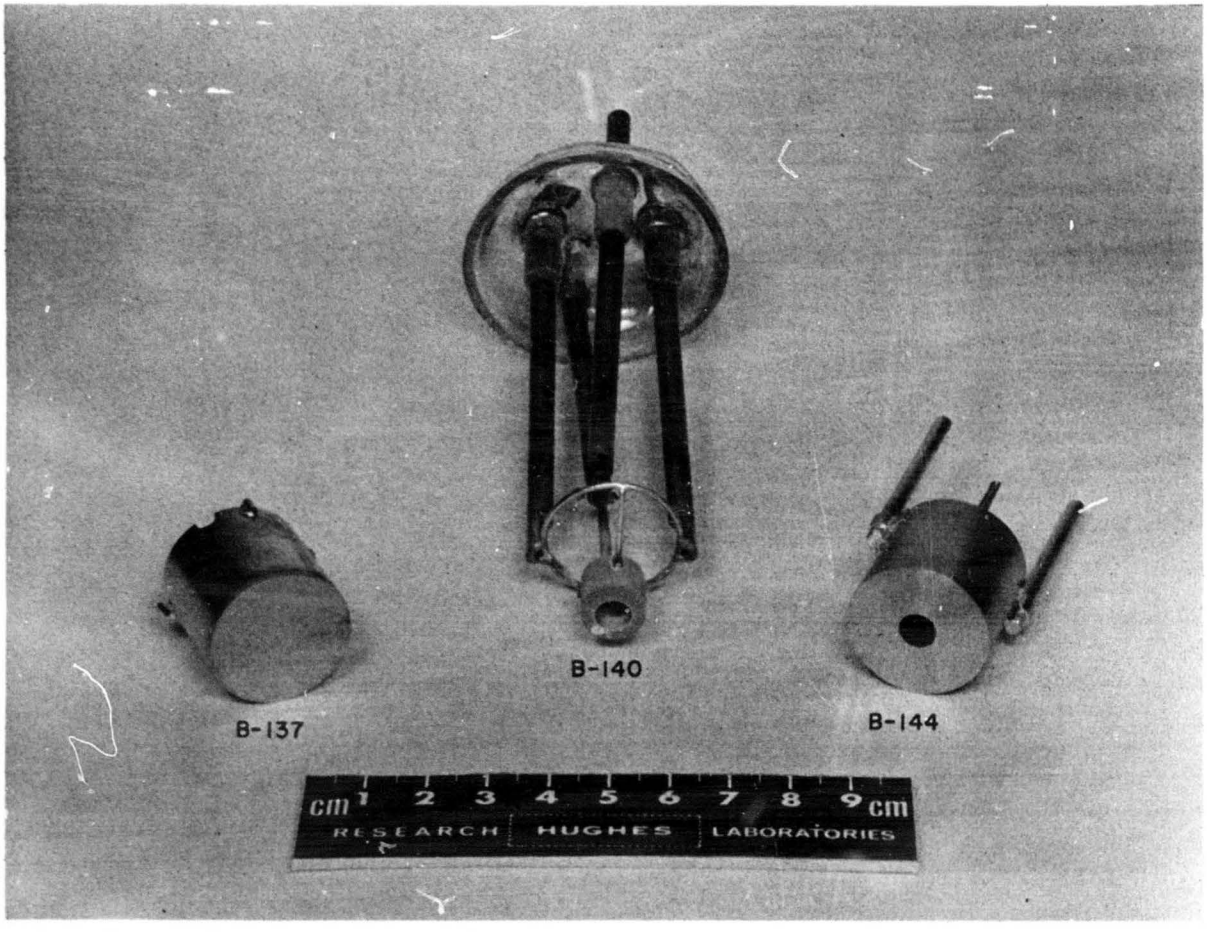

Fig. 14. Photograph showing the three indirectly heated impregnated tungsten cathodes.

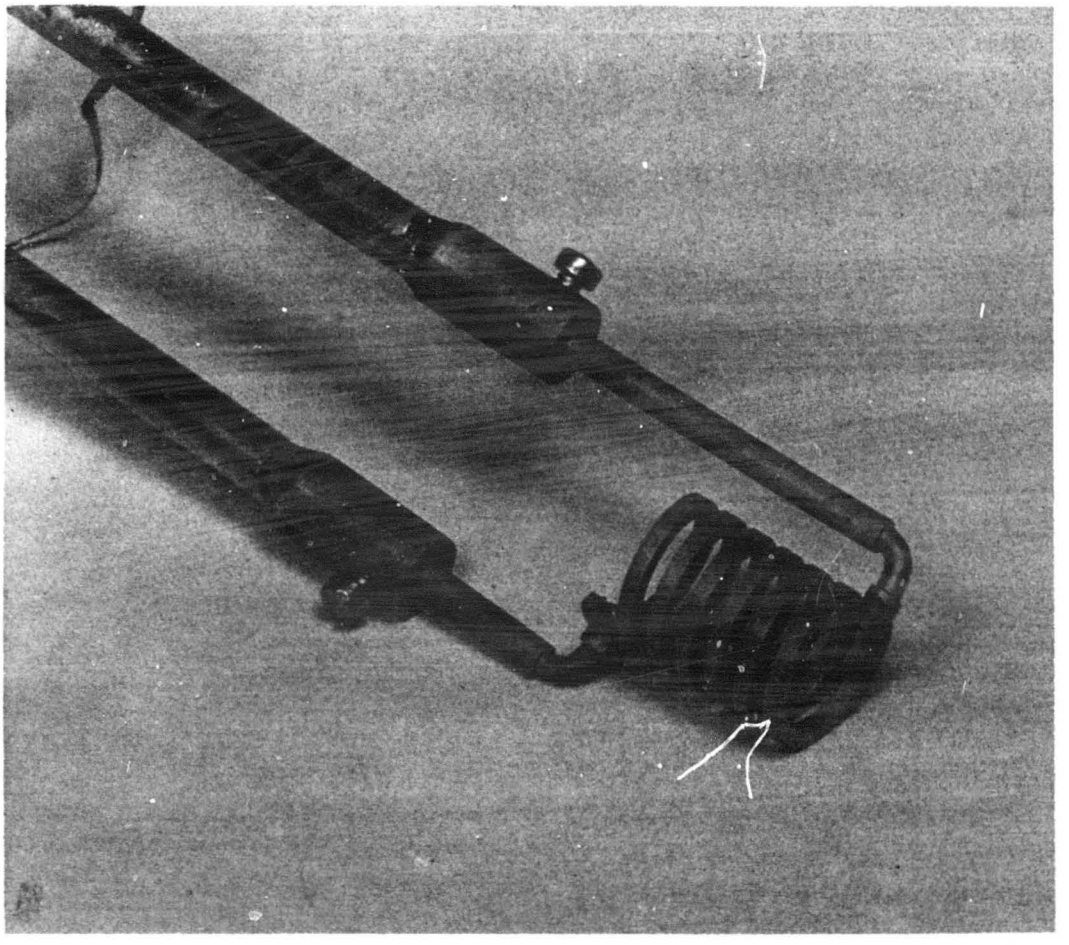

Fig. 15. Photograph of directly heated, impregnated tungsten cathode, B-151. The six-turn helix has a total emitting area of 10 cm^2.

In addition, after the second impregnated tungsten cathode test, a radiation-cooled anode was substituted for the previous water-cooled design. This was done in order to allow operation of the entire life-test apparatus without requiring cooling water. The anode was a 1-in. diameter, 2-in. long tube of 0.020 in. tantalum with external fins to improve cooling efficiency.

3. Evaluation of Indirectly Heated Cathodes

a. Cathode B-137

Results obtained from the first two tests of impregnated cathodes were disappointing. Problems which arose during these tests are reviewed below, however, to provide information on difficulties which can be encountered with this type of cathode. The first cathode (B-137 in Figure 14) was processed while maintaining the pressure below 10^{-5} Torr. The tube envelope was not completely baked out in the usual sense, but was heated only with a heat gun. Three days were required to process the cathode to 1185°C.

A small leak developed while the cathode was hot. The tube pressure remained below 10^{-3} Torr until the leak was sealed, however. When first operated, only 5 A could be drawn from the cathode without rapid contamination of the discharge. After 50 cycles of filling, operating the cathode, and pumping out the tube, the cathode could be operated satisfactorily at 20 A. The tube was then opened and cleaned. Attempts to reactivate the cathode were unsuccessful. Current emission > 10 A could not be sustained without the occurrence of localized heating of the emitting surface and discharge instabilities, and the test was terminated.

The cathode's failure to emit properly probably can be attributed to (1) oxidation of the tungsten surface during initial processing when a gas leak occurred while the cathode was at 1150°C, (2) contamination from the vacuum envelope, or (3) poisoning of the cathode surface by nickel from the support pins used in the reassembly.

b. Cathode B-140

The second cathode (B-140 in Figure 14) was processed in one day to 1138°C on the o.d. and 1240°C on the i.d., and 2 A emission current was successfully obtained. The glass envelope broke as a result of stresses while the cathode was cold. An attempt at cathode reactivation was unsuccessful, as evidenced by the fact that the discharge jumped around the cathode to the support pins, eventually destroying the one heater lead.

c. Cathode B-144

Testing of the large annular cathode B-144 indicated a much greater resistance to poisoning and a much easier reactivation than the impregnated cathodes tested previously. This cathode has an emitting area of 28 cm^2, which is more than four times that of the two cathodes tested previously. The cathode was processed using standard high-vacuum techniques. The vacuum envelope was baked for 3 hours at 300°C, and a vacuum of 5×10^{-7} Torr was achieved prior to activation. During activation, the pressure was held below 4×10^{-4} Torr. The cathode temperature was raised to 1190°C on the front face (1360°C on the inside surface) for 20 min. The temperature was then lowered to 1150°C on the front face (1255°C on the inside surface). After activation, the getter was flashed and the discharge was run for 10 min. After the cathode was cooled and the tube pumped out, a pressure of 1.7×10^{-7} Torr was observed; the pressure rose to about 3×10^{-4} Torr after the tube was valved off for 60 hours.

After discharges were run intermittently at 20 A for about 13 hours at a cathode temperature of 1100°C, a dark deposit was formed on the inside of the quartz envelope surrounding the cathode. The tube was opened and samples of the deposits were scraped from the tube walls for x-ray analysis. The Laue pattern of the samples indicated that the primary constituent was alumina, with trace impurities. Known sources of alumina in the tube are the potting compound encasing the cathode heater, and barium aluminate, which is the substance impregnated into the tungsten.

Because this deposit also covered much of the emitting surface, the cathode was sandblasted with clean alumina grit and ultrasonically cleaned in pure methanol. This is the cleaning procedure recommended by the manufacturer. The tube was reassembled and replaced on the vacuum station.

The cathode was reactivated at 1190°C for 20 min, and then reduced to 1150°C. Ten-minute discharges were run at 2 A, 4 A, 6 A, . . . , 20 A as the cathode temperature was slowly reduced to 1025°C. At no time was there any evidence of contamination. The tube was then operated intermittently for about 45 min at 20 A at 1025°C. At this temperature the required heater power was 196 W (19.0 A at 10.3 V). This is 3.5 times the power required by the Hughes oxide cathode; however, the power requirements can certainly be reduced by the use of suitable heat shielding. This cathode has been life-tested for a total of 2464 hours, longer than any other cathode tested. It was operated in 23-hour increments. For the first 671 hours, 20 A emission current was drawn. The emission current was then increased to 25 - 30 A, running approximately 8 hours at 30 A, 16 hours at 25 A, 8 hours at 30 A, etc.

Figure 16 shows data on the average gas cleanup rate during each of the 17 successive gas fills. During the first 600 hours of operation at 20 A, the GCR decreased from 1 μ-liter/hour to 0.8 μ-liter/hour. The cathode was operated at an average current of 25 A during the next 1900 hours. The GCR rate decreased from 1.5 μliter/hour at 600 hours to 0.3 μliter/hour at 2460 hours. These rates are similar to the cleanup rates measured at 25 A during the second life test of an oxide cathode.

4. Evaluation of Directly Heated Cathodes

During the evaluation of these cathodes, particular attention was paid to the heater and cathode biasing connections and the resulting cathode temperature distributions. Since the discharge current as well as the heater current is drawn through the cathode body itself, temperature control under a wide range of discharge currents presents more of a problem than with the indirectly heated type.

a. Cathode Test B-152-A

A directly heated helix cathode was mounted in a cathode test apparatus such as that described previously. The discharge tube was first prepared by heating to 350°C for 3 hours under vacuum. Cathode activation was then quite rapid, requiring about 1 hour. The cathode operated satisfactorily at 5 A emission current; the current was increased gradually after several gas refills to 20 A after 50 min of operation.

The cathode was operated at 20 A discharge current in 23-hour increments for a total of 91 hours. A small area on the second turn from the front of the cathode appeared to stop emitting after 88 hours. Small spots in this area were observed to become quite hot (estimated at 1600°C) when the discharge was operated at 20 A.

A uniform coating of barium appeared on the discharge tube walls surrounding the cathode during the 91 hours of operation. We had measured the temperature of the cathode as a function of current before this film was present. By measuring the apparent temperature with the film present as a function of current, we were able to establish that the transmission of the barium film was approximately 20%. Corrections were made for the transmission of the film in subsequent measurements.

A series of temperature measurements was made to determine the uniformity of heating and the required heater power at different discharge currents. These measurements were made using both ac and dc for heating the cathode.

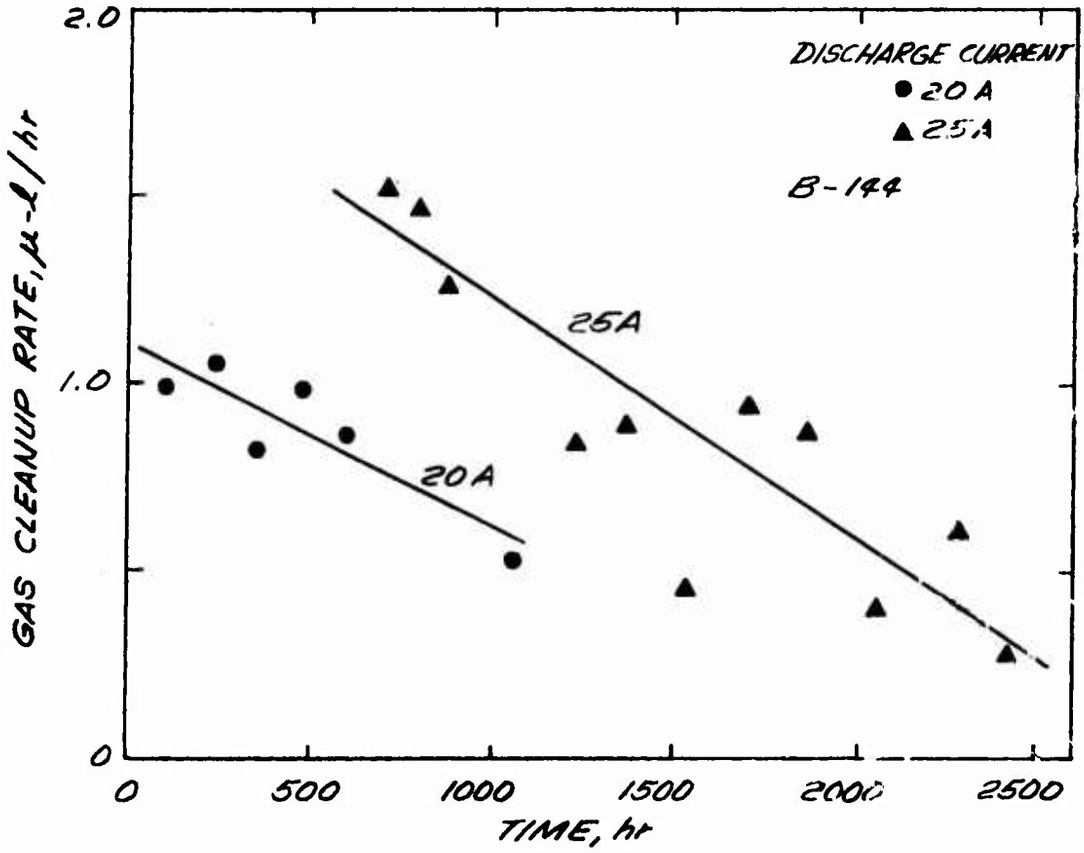

Fig. 16. Average gas cleanup rate during each gas fill as a function of total hours of cathode operation.

In order to measure the cathode temperature with the discharge running, it is necessary to distinguish between thermal radiation entering the pyrometer from the cathode and spontaneous emission from the discharge. To do this, a relay switching mechanism was employed which allowed the discharge to be turned off and on rapidly. The pyrometer was then read immediately after the discharge was switched off, before the cathode temperature decreased noticeably.

The cathode temperature is always increased with the discharge on, as is the case with oxide cathodes. Under some conditions the cathode temperature is quite nonuniform along its length, particularly at high discharge currents. This effect is clearly shown in Figure 17. The temperature difference between the front and back of the cathode is plotted as a function of discharge current. Data are shown for three different heater and cathode bias arrangements. These are indicated in the figure; the cathode connection is to ground and the discharge current I flows from the anode, located to the right of the cathode.

In the upper curve the cathode connection is to the rear pin (away from the anode), as is the positive heater connection. The potential drop across the cathode due to the heater current is about 2 V. The front of the cathode is overheated because it is (a) closest to the anode and (b) the most negative point in the discharge.

In the lower trace the polarity of the heater supply is reversed, and the back of the cathode is overheated from effect (b) above. However, since the negative part of the cathode is farthest from the anode, current emission is more uniform over the cathode and localized heating is decreased considerably.

In the middle trace, using ac on the heater, the ends of the cathode are heated more equally, with the front end slightly hotter because of its position closer to the anode.

At this point the cathode test apparatus was disassembled for modification. While the cathode was being removed from its mounting a small torque was applied to one pin, snapping off the cathode at the middle of its first coil. This experience emphasizes the well-known fact that tungsten becomes quite brittle after heating. The directly heated cathodes are thus quite brittle after operation and must be handled with care. The more rugged indirectly heated design does not exhibit this problem.

b. Cathode Test B-152-B

In an effort to eliminate the nonuniform heating described above, a cylindrical heat shield of tantalum was fabricated to provide an equipotential and isothermal surrounding to the cathode. A slit was provided in the side of the can so that the cathode could be viewed with a

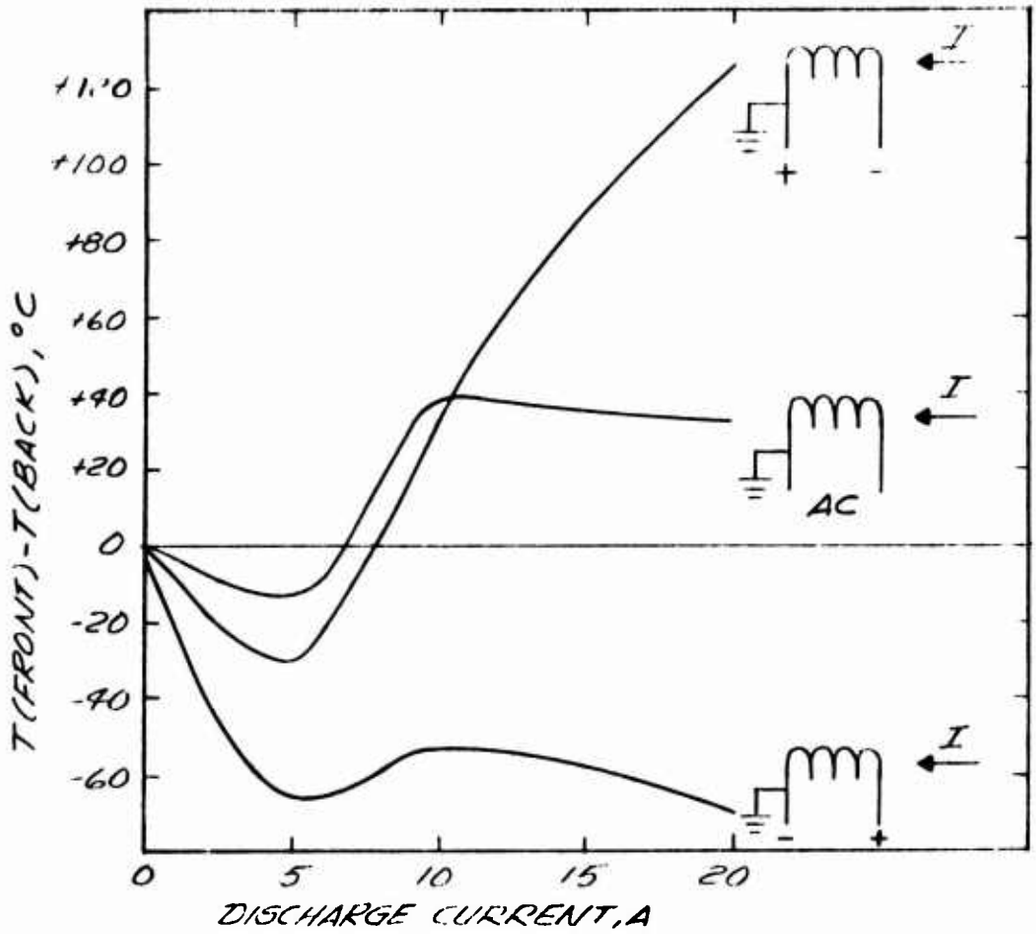

Fig. 17. Temperature difference developed between the front and back coils of the cathode as a function of discharge current and heater bias.

pyrometer, as shown in Figure 18. A second directly heated cathode was used, identical to the first. The efficacy of the heat shield in reducing the heater power required to maintain a given cathode temperature with the discharge off is illustrated in Figure 19. With the heat shield in place, the heater power required to maintain the cathode at 1050°C was reduced from 65 W to 35 W.

The cathode activated in 1 hour, following a 2 hour vacuum bakeout of the assembly at 300°C. The discharge current was gradually increased to 25 A. At this time a glass-to-metal seal broke, and the entire assembly was exposed to air while hot.

The badly oxidized cathode was removed from the tube and heat shield and fired in dry hydrogen for 30 min at 1000°C, but the visible oxide coating persisted. The cathode was sandblasted using clean alumina grit and then ultrasonically cleaned in pure (electronic grade) methanol. The cathode was reprocessed and emitted satisfactorily.

Attempts to monitor the cathode temperature, however, immediately indicated an anomaly. The observed temperature appeared to have decreased by as much as 150°C at the same heater power since the initial processing. The cathode resistance as a function of power was unchanged, however. Examination of Figure 20, where we have plotted cathode resistance versus temperature, indicates that a shift of even 20° in temperature would be accompanied by a substantial change in cathode resistance. We conclude that the temperature change was only an apparent one, resulting from deposition of metallic film on the tube walls since the initial processing. This effect was corrected for in the analysis of the temperature data.

The increased thermal efficiency of the heat-shielded assembly proved to be a problem when operating in the discharge. The additional heating from the discharge heated the cathode far beyond its optimum operating temperature unless the heater power was drastically reduced. Figure 21 illustrates this effect clearly. The heater power was held constant at 50 W as the discharge current was increased from 0 to 20 A. Operation within the recommended temperature range could not be achieved at high discharge currents even by reducing the filament power. At a discharge current of 25 A the heat-shielded cathode operated at an average temperature of 1300°C, even with the heater power completely removed. Continuous operation at such a high temperature would drastically reduce cathode life.

The uniformity of heating of the cathode was considerably improved by the heat shield, at least for certain bias conditions. Temperature data were recorded on the front, middle, and back surfaces of the cathode for different bias connections. Values obtained for the temperature difference between the front and back turns of the cathode helix at a discharge current of 25 A are summarized in Table III.

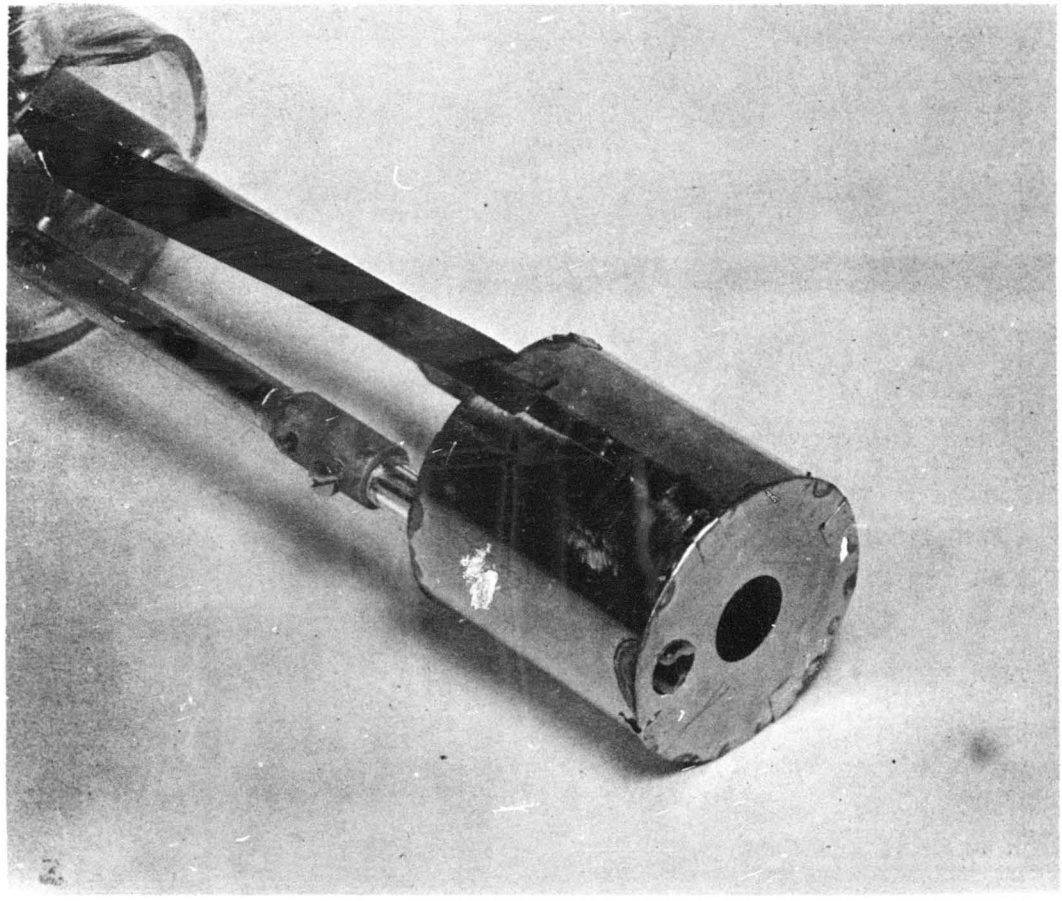

Fig. 18. Photograph of directly heated helical cathode inside a single-layer heat shield.

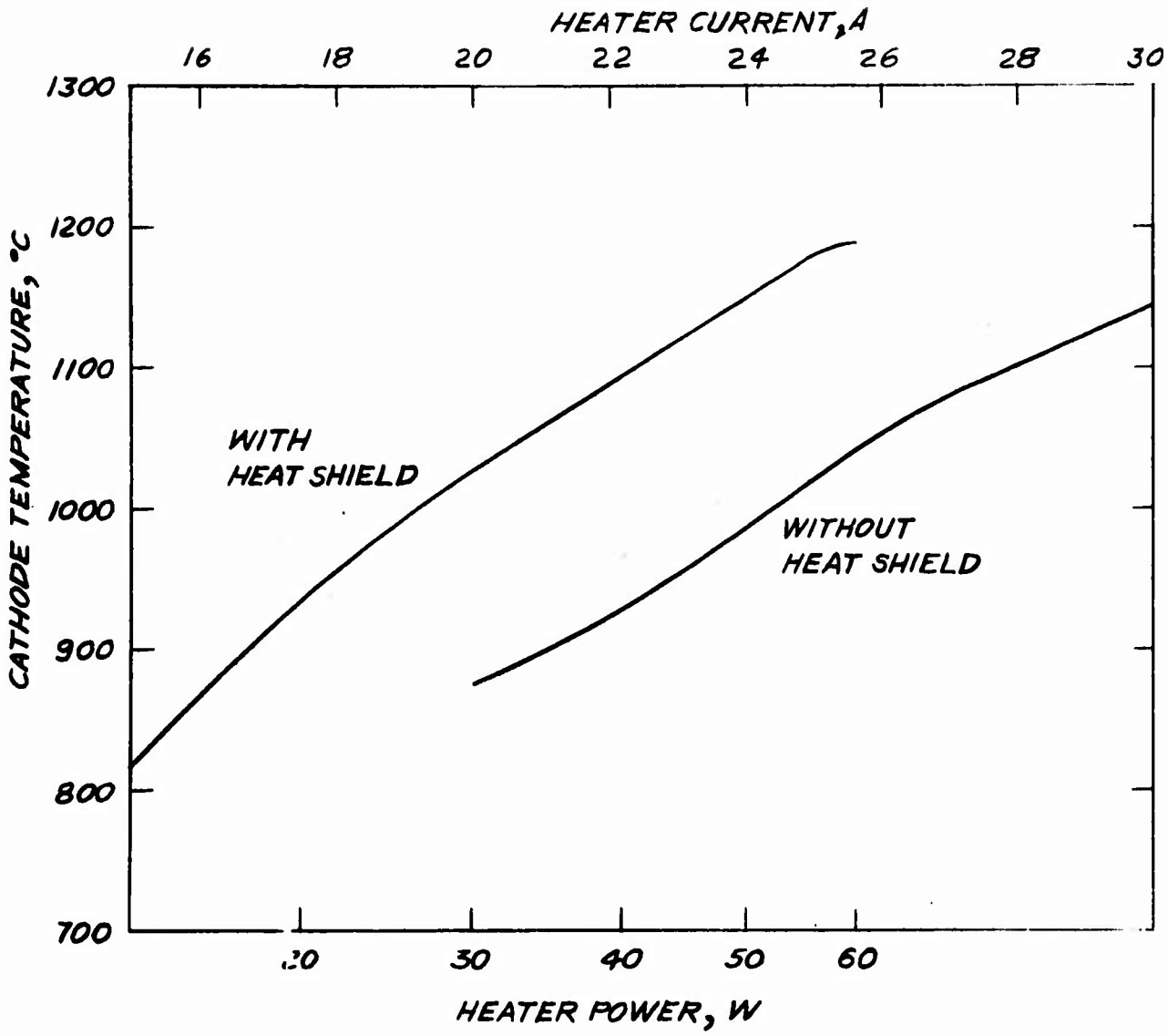

Fig. 19. Cathode temperature versus heater power and current with and without a heat shield in place.

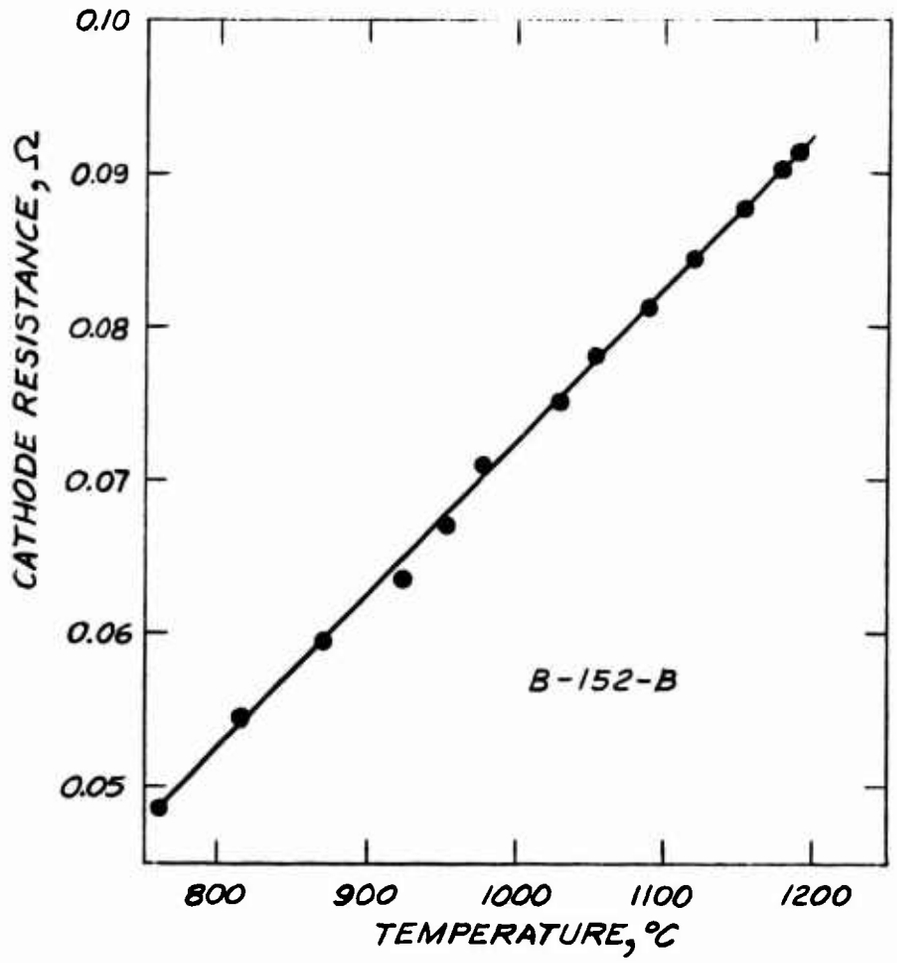

Fig. 20. Resistance of cathode heater with the discharge off as a function of cathode temperature.

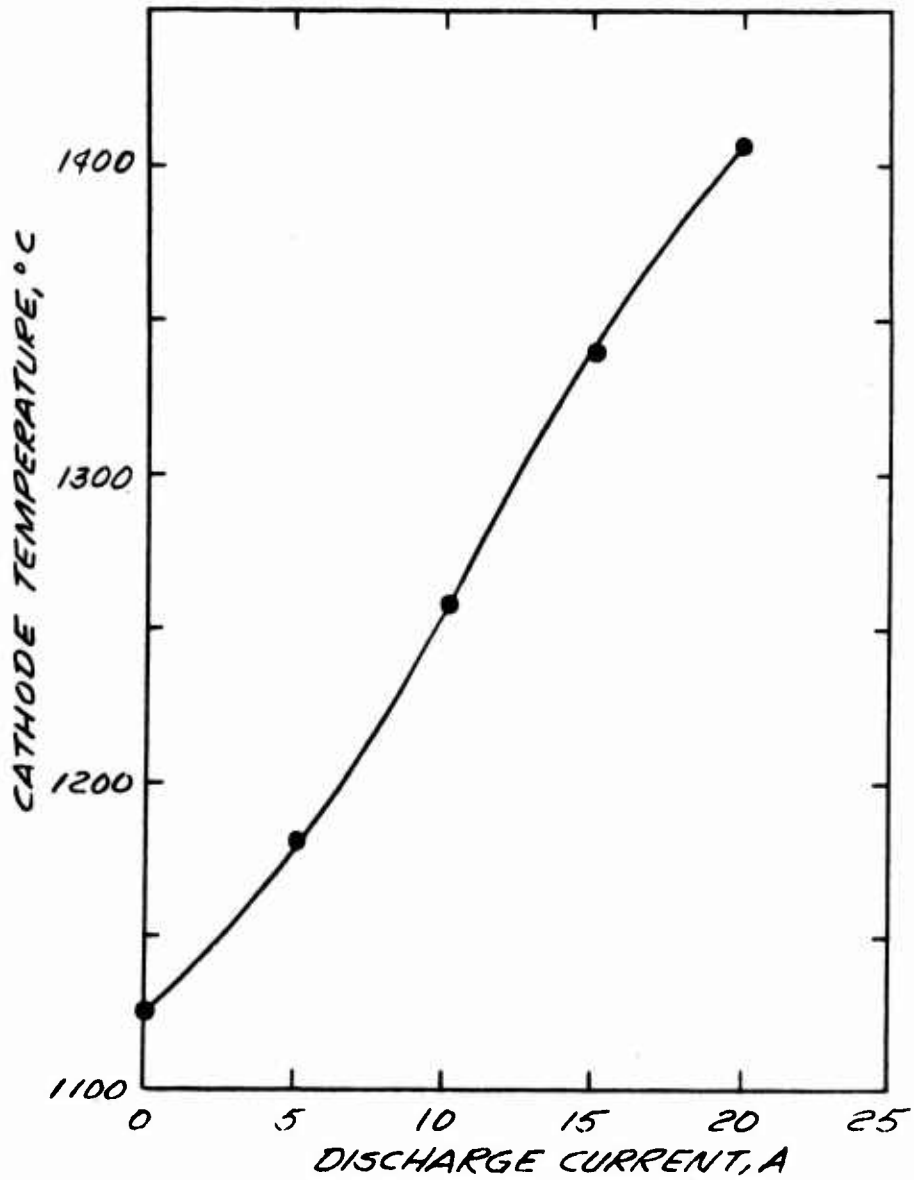

Fig. 21. Average temperature of heat-shielded cathode versus discharge current with constant heater power.

TABLE III

Cathode Temperature Difference for Different Heater and Cathode Bias Connections

Configuration	T(front)-T(back)	Comment
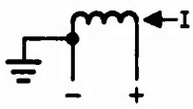	-4°C	Best configuration with dc heater
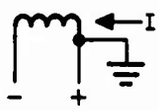	40°C	
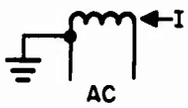	80°C	Best configuration with ac heater
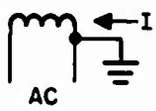	150°C	
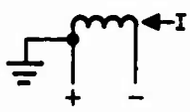	255°C	
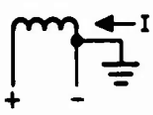	281°C	Worst configuration with dc heater

The best bias configuration (i.e., that which gave the most uniform cathode temperature distribution) occurred with the cathode and the heater negative leads connected to the cathode pin farthest from the anode. Philips Metalonics, the manufacturer of the helical cathode, recommends that when the cathode is dc heated, the negative heater lead be connected to the cathode turn closest to the anode. The data of Table III indicate that under our experimental conditions, connection of the negative heater lead to the opposite end of the cathode is preferable.

We conclude that heat shielding offers a solution to the nonuniform heating problem. However, even the simple heat shield which we designed is too efficient; that is, it does not allow enough heat dissipation through radiation. Consequently, the power dissipated in the cathode by the passage of the discharge current (which must be drawn through the cathode coils themselves) and by ion bombardment from the discharge causes the cathode to become overheated, even without the application of any heater power. One possible solution would be to use a somewhat less efficient heat shield, perhaps one as pictured in Figure 18 but with more slots cut parallel to the longitudinal axis. This may still result in uniform heating while allowing sufficient radiation to avoid overheating. The exact number and size of the slits would depend on the maximum discharge currents at which the cathode would be run. At lower discharge currents, of course, the self-heating of the cathode would have to be supplemented with heater power.

D. SUMMARY AND CONCLUSIONS

Both oxide and impregnated tungsten cathodes were evaluated under typical ion laser conditions in extended life tests. A conservative value for the expected lifetime of the type of cathodes tested, which had emitting areas of approximately 25 cm^2, is 2000 hours at a discharge current of 25 A.

Extensive data were gathered on the gas cleanup rate (GCR) of cathodes operating in a large-diameter quartz envelope. During the first 1000 hours of operation, the GCR at 20 A decreased from approximately 2 μliter/hour to 0.5 μliter/hour. However, a large part of the gas absorption probably occurs in the quartz surfaces of the envelope rather than at the cathode. Gas cleanup was found to depend strongly on the discharge current. Measurements of the reversible absorption and evolution of gas were made under different conditions of discharge current and gas pressure; an appreciation of these phenomena is beneficial in designing a gas replenishment system.

The dependence of cathode temperature on discharge current has been studied in detail. In all cases the temperature of the cathode surface increases when discharge current is drawn. The operating characteristics of directly heated, helical tungsten cathodes of the type now advertized for use in ion lasers were measured. Temperature control was determined to be a serious problem with this type of cathode. The polarity of heater and cathode connections made to this type of cathode was determined to have a critical effect on the spatial uniformity of the cathode temperature. Specific recommendations for biasing the cathode have been given.

As a result of the experience with various cathode types gained during this program, a rugged indirectly heated impregnated tungsten cathode for use in airborne lasers has been designed, assembled, and tested to 60 A discharge current. An impregnated tungsten cathode was selected over an oxide cathode to avoid any possibility of window contamination by flaking or powdering of the cathode surface at high discharge currents. Indirect heating of the cathode surface was adopted to minimize temperature control problems and to avoid modulation of the light output by heater power supply ripple. This topic is considered in detail in Section VII.

SECTION III

BORE MATERIAL STUDIES

A. SUMMARY OF EXPERIMENTS

The objective of this task was to evaluate promising ion laser bore materials. Properties of interest are resistance to ion sputtering, cleanliness as a vacuum material, gas cleanup properties, and thermal characteristics.

Initial experiments using continuous quartz and alumina bore discharge tubes and segmented molybdenum, tungsten, and graphite bore discharge tubes were conducted during the period covered by the previous contract. Our conclusions regarding normal graphite were that although it was desirable from the standpoint of cost, resistance to localized damage, machinability, emissivity, and thermal properties, it was not suitable for use in high power lasers because it lacks mechanical integrity (i.e., it powders). Graphite dust which gradually collects between the segments of the tube does not affect the operation of the discharge itself. However, the dust would create a serious window contamination problem if the tube were tilted from the horizontal or shaken, as it would be during shipment and field use other than in a quiet laboratory environment.

The different bore material experiments conducted during the period covered by the present contract are listed in Table IV. The results of each of these experiments are described below. Data on the last two tubes, which employed a disk-bore structure, are contained in Section IV.

B. TUBE DESIGN AND TEST APPARATUS

With the exception of the tests of quartz and BeO bores, experimental tubes were constructed using a water-cooled quartz envelope to support and maintain the alignment of the bore segments. A photograph of a typical segmented bore tube is shown in Figure 22. Each segment is electrically isolated from the next so that it may float at the average potential appropriate to the wall of the positive column at that position, as indicated in Figure 23. Heat transfer from the segments is partly by conduction to the wall and partly by radiation. Approximately 75% of the power radiated by the segments is absorbed in the water jacket. (Water begins to absorb strongly at wavelengths greater than 1.5 μ, while the peak radiation intensity of segments at 1200°C is at 2 μ.) Radiation at visible wavelengths is not appreciably

TABLE IV

Bore Material Experiments

Tube No.	Description
B-131	Pyrolytic graphite (PG) segments in a quartz envelope
B-133	Graphite segments overcoated with PG in a quartz envelope
B-138-C	PG segments in an alumina ceramic envelope
B-141	Tungsten-overcoated graphite (TOG) in a quartz envelope
B-145-A	TOG (B-141) with porous tungsten segments in the cathode throat
B-145-B	TOG (B-141) with pure tungsten segments in the cathode throat
B-145-C	TOG (B-141) with Poco graphite disks in the cathode throat
F-29	Quartz-bore tube
B-155	BeO bore, metal-ceramic tube
B-136	Graphite disk in a quartz envelope (see Section IV)
B-146	Tungsten disks in a quartz envelope (see Section IV)

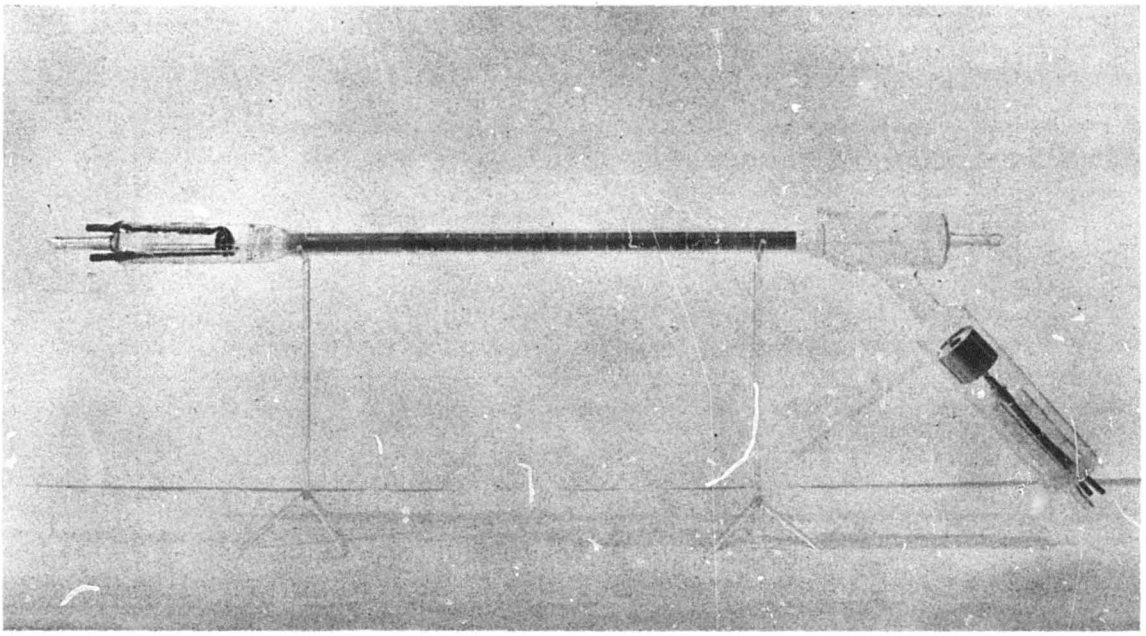

Fig. 22. Photograph of an assembled segmented bore tube.

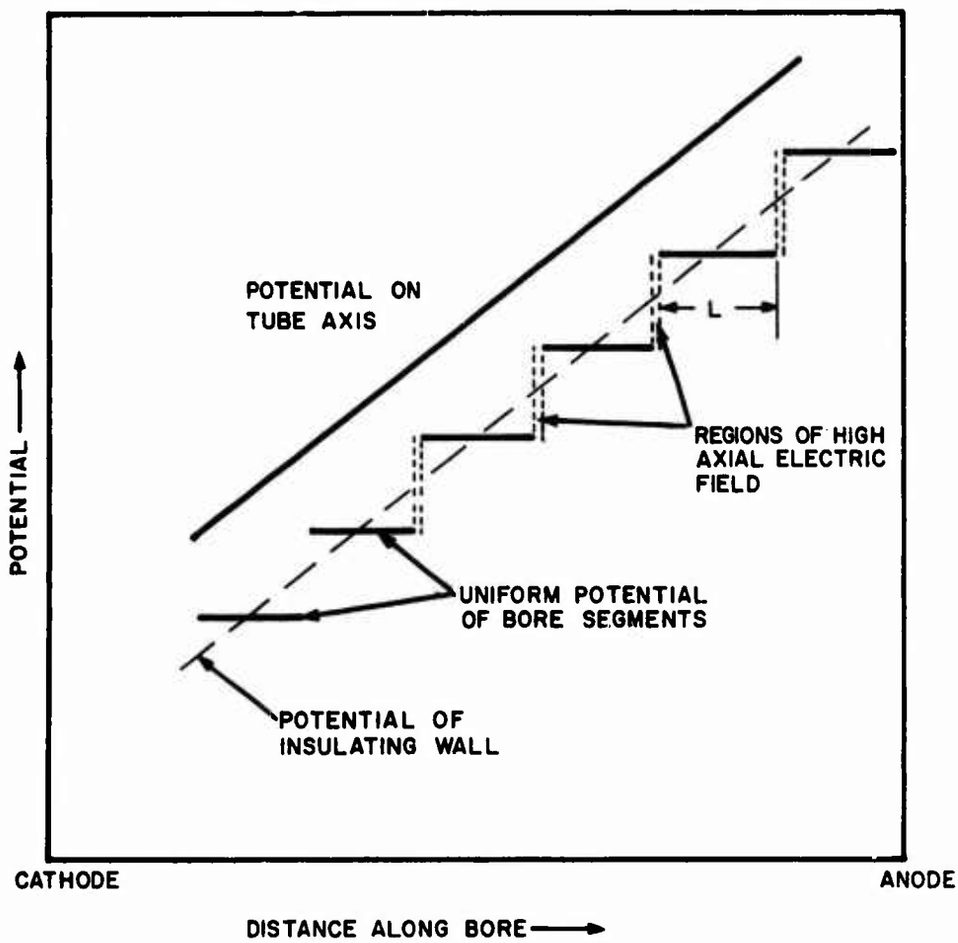

Fig. 23. Potential variation along the axis of the tube and from segment to segment in a segmented metal-bore tube.

absorbed in the thin water filled section. The major advantages of the segmented bore tube which encouraged us to investigate this design approach in depth are listed below.

1. A variety of low sputtering, refractory materials is available.

2. There is no fundamental limitation on power dissipation per unit length by radiation; the most promising materials have very high melting points ($>2500^{\circ}C$).

3. Thermal expansion strain and thermal shock are not problems with the bore materials of interest.

4. The o.d. of the segments may be as large as necessary to provide an adequate cooling surface. (Power dissipation per unit length increases linearly with diameter).

5. The power density incident on the large diameter quartz or ceramic envelope is less by the ratio of the envelope diameter to the bore diameter than on a continuous-bore quartz or ceramic discharge tube.

6. The quartz or ceramic envelope is protected from the discharge by the large-heat-capacity segments, thus avoiding thermal shock problems in the envelope materials.

7. A radiation-cooled anode may be conveniently inserted in the envelope as the final segment.

8. Different throat shapes and bore sizes are easily fabricated.

9. Internal gas return paths may be included in the segments (provided the segment diameter is reasonably large, see Section VI-A).

10. The bore material does not have to be the vacuum seal, thus allowing a wider choice of materials.

Each evaluation of a bore material consisted of constructing a discharge tube bore of the material and operating the tube as a laser for approximately 200 hours. Parameters of particular interest were the gas cleanup rate, output power, and durability of the material.

The lasers were sealed off from the vacuum station during operation by a Granville-Phillips leak valve. A barium getter and a Hastings thermocouple gauge tube were connected to the laser. Gas replenishment to maintain the gas pressure within the desired operating range was carried out by opening the leak valve and adding gas to the existing gas fill whenever a lower pressure limit was reached. The vacuum envelopes were constructed with graded glass or metal-ceramic seals (i.e., without O-ring, ball joint, Swagelok, etc., seals).

Unless otherwise noted, all tubes had a uniform 3 mm diameter bore region 46 cm long. The bore constriction at each end of the bore was 1.4 in. long and consisted of three 0.375 in.-long segments tapered to approximate an exponential decrease in bore diameter from 0.300 in. to 3 mm. Each bore segment was 0.500 in. long and had a 0.500 in. o.d. and 3 mm i.d. The segments were spaced 0.062 in. apart by sapphire balls. The segments were made nonreentrant so that sputtering or powdering of the segments could be observed through the quartz envelope. The oxide cathode was located in a side arm, as shown in Figure 22. The over-all length of the tubes from window to window was 90 cm. A 120 cm radius of curvature high reflectance mirror on a 5% flat output mirror was used.

C. EVALUATION OF PYROLYTIC GRAPHITE (TUBE No. B-131)

1. Description of the Material

Pyrolytic graphite is formed by deposition of carbon atoms on a hot (2000°C) substrate from hot flowing methane gas. The material has a layered structure similar to mica, and is highly anisotropic in its thermal, electrical, and mechanical properties. The c-axis of PG is normal to the planar structure, so that the material is uniform and closely bound in the a-b plane, and layered along the c-axis. The density is 2.2 g/cm, the theoretical maximum for carbon, compared with a density of 1.8 to 1.9 g/cm for ultrapure forms of graphite. The thermal conductivity in the a-b plane is excellent, while along the c-axis the conductivity is comparable to that of firebrick. Pyrolytic graphite was evaluated with the hope that the higher density and tighter bonding of its carbon atoms might prevent the material from powdering. A set of bore segments fabricated from 1/2 in. thick sheet PG was purchased from Super Temp Corporation, a commercial manufacturer of PG. The c-axis of the material was aligned along the segment axis. Some of the

characteristics of this material are apparent in the photographs shown in Figure 24. Note the difference in the structure of the material when viewed along the a-b plane (Figure 24(b)) and normal to this plane (Figures 24(c) and (d)).

2. Operating Characteristics

The operating characteristics of the laser during the 220 hour test at 20 A discharge current are summarized in Figure 25. The gas pressure and output power are plotted as a function of time. These data were taken over a 10 week period.

The change in the pressure versus time characteristic at 145 hours was caused by air introduced (by mistake) into the tube during gas replenishment. Even though the tube was immediately pumped out, the getter was used up. The laser was operated for another 55 hours before the problem was diagnosed. Normal operating characteristics were again obtained at 200 hours when the getter was reflashed and the tube refilled.

At 90 hours the filament supply power failed while the discharge was operating. The discharge tube continued to operate without heater power for 8 hours. No change in the tube voltage was noted. The filament supply was purposely turned on and off several times to verify this behavior. It was determined that once the tube is operating, heating of the oxide coating by the passage of the discharge current, or by ion bombardment, is sufficient to heat the coating to emission temperature.

Gas cleanup data, calculated from the change in cold gas pressure, are plotted in Figure 26. Two trends are evident: (1) the GCR (gas cleanup rate) increases with decreasing pressure (with roughly a $1/p^3$ dependence), and (2) the GCR decreases with each gas fill (the cleanup rate during run 2 was roughly 2.5 times that of run 4).

The cleanup rate of the oxide cathodes was found to range between 0.5 and 3 μ-liter/hour during the first 160 hours of operation (see Section II), so that a significant fraction of the cleanup in the PG tube may actually have occurred at the cathode or anode rather than in the PG bore.

The lower curve of Figure 27 shows the output power versus current as measured at the end of the experiment. At 35 A, 5.9 W was obtained. No window contamination problems were encountered.

The temperature of the radiation-cooled segments in the uniform bore was 1145°C at 20 A and 1365°C at 35 A. The hottest segment, in the cathode throat, was 1220°C at 20 A and 1436°C at 35 A. The low

(a)

(b)

(c)

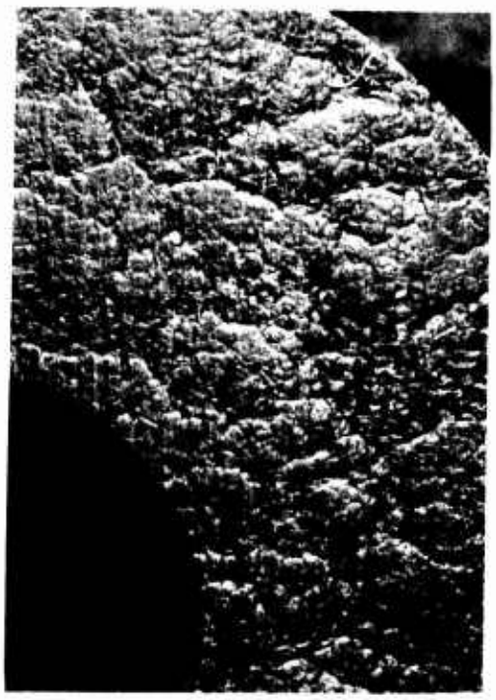

(d)

Fig. 24. Photographs of pyrolytic graphite segments. (a) Over-all segment appearance, (b) appearance of segment viewed along a-b planes, and (c) and (d) normal to a-b plane at 15x magnification.

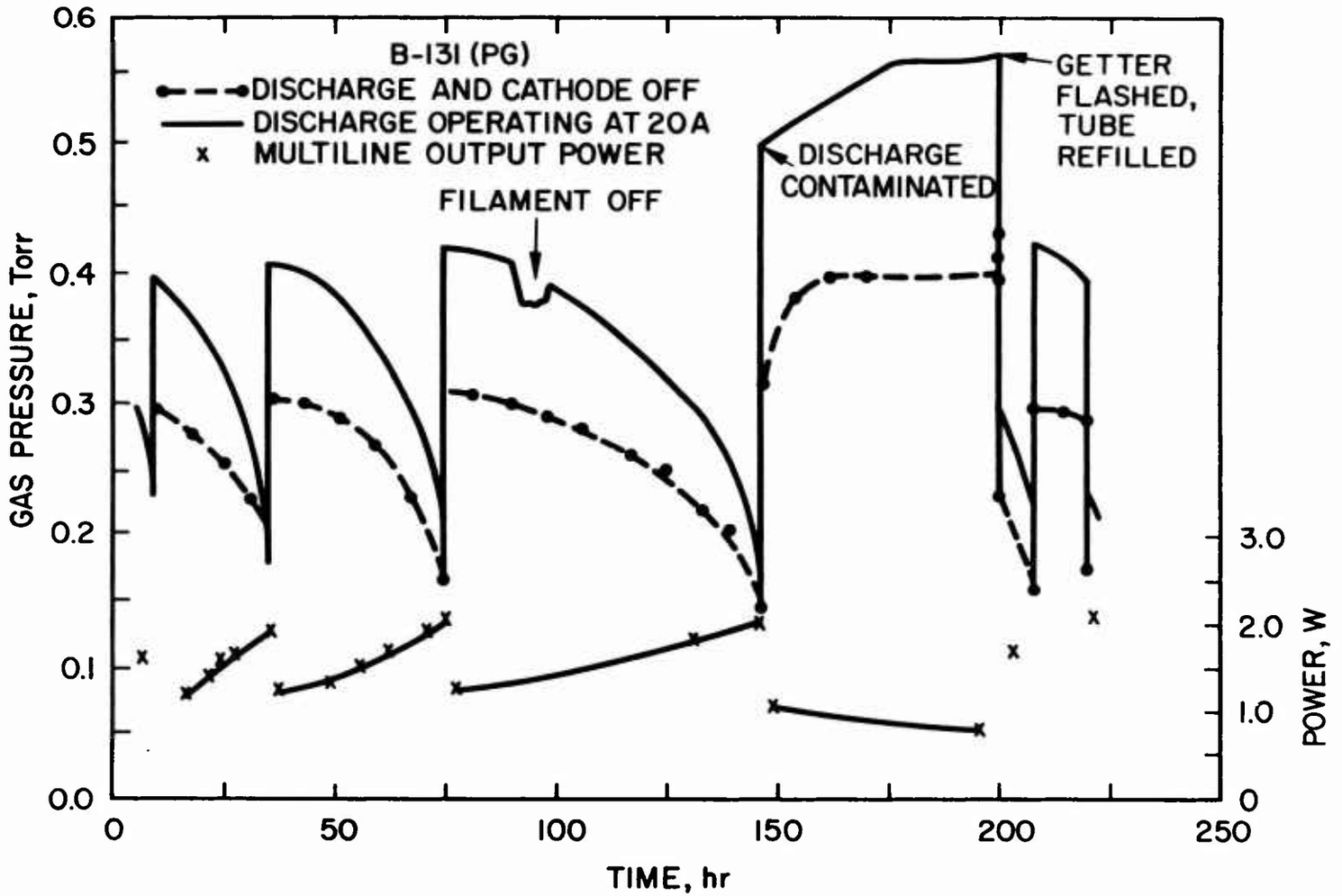

Fig. 25. Gas pressure and power output characteristics of tube B-131 versus time.

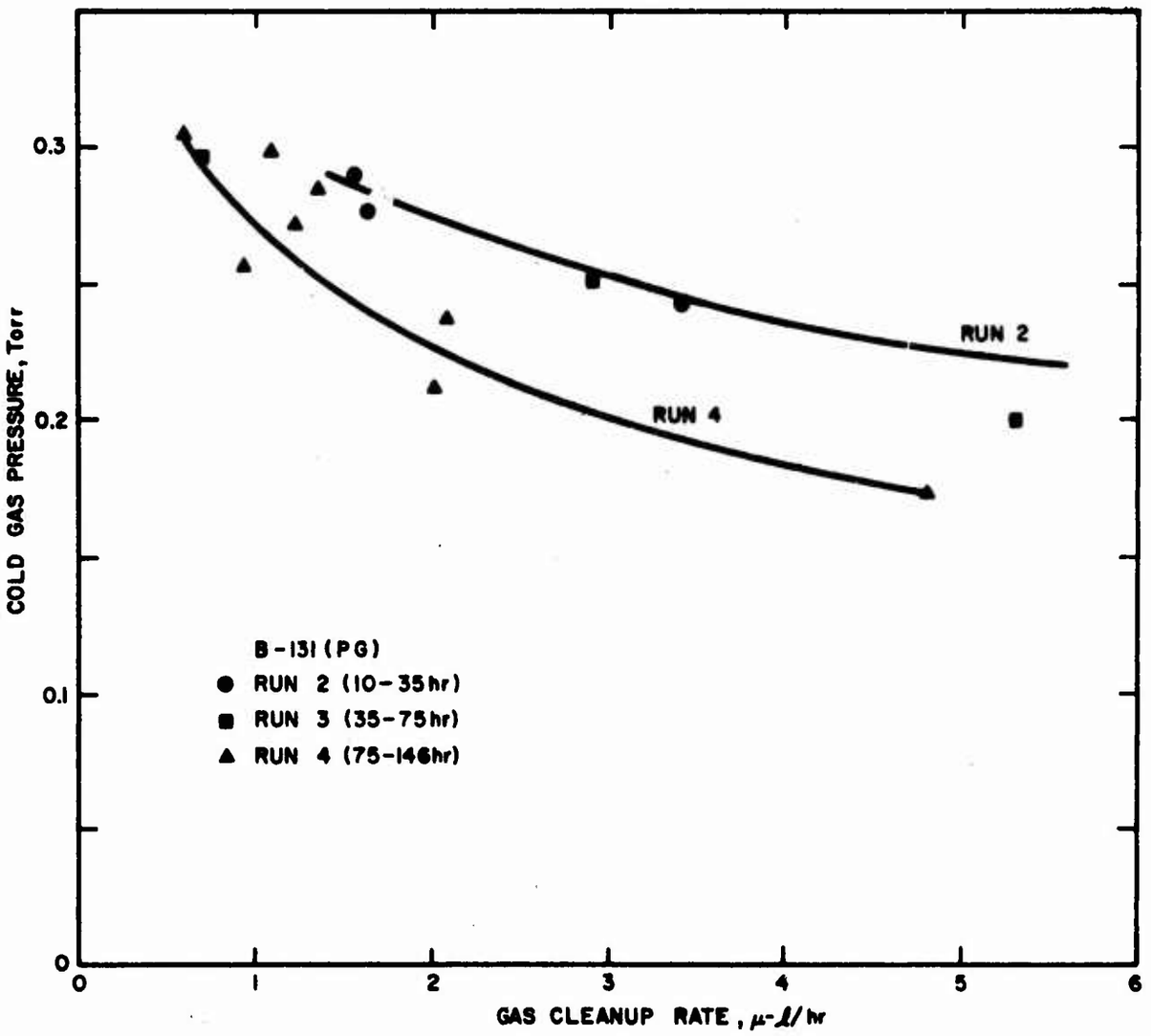

Fig. 26. Gas cleanup rate as a function of gas pressure during successive runs in tube B-131.

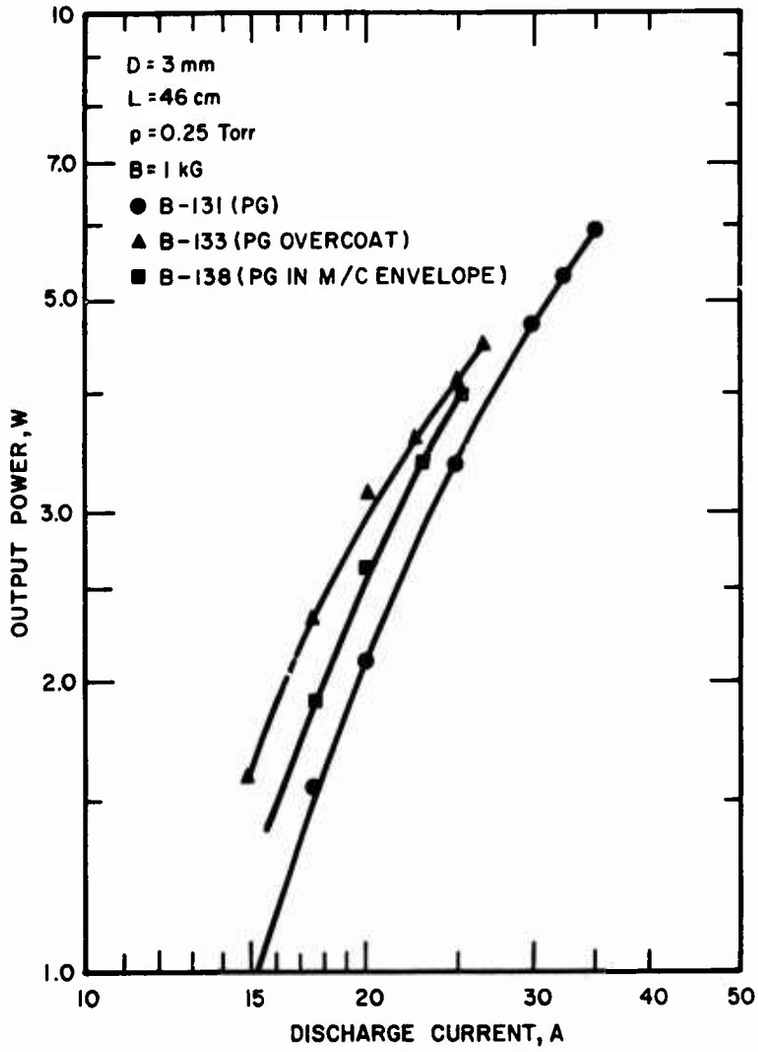

Fig. 27. Multiline output power versus discharge current for tubes B-131, B-133, and B-138-C at end of test.

axial thermal conductivity of the PG was obvious from the temperature gradient in the throat segments which undergo nonuniform axial heating; the temperature of the anode end of one segment was $> 100^{\circ}C$ more than the cathode end of the same segment!

The tube voltage of the segmented PG tube ranged from 220 V at low pressures to 250 V at high pressures. This is approximately 40 V higher than the tube voltage of quartz bore tubes of the same length.

3. Resistance of the Material to Sputtering and Erosion

After 225 hours the tube was disassembled and the parts inspected for damage. Figure 28 is a photograph showing the appearance of the segments and the quartz envelope near the cathode end. The 1/16 in. diameter sapphire ball spacers are on the bottom of the tube. The first segment on the left is the first tapered segment in the cathode throat; experiments with molybdenum have shown that this segment is always the most severely damaged by sputtering. A buildup of graphite on the cathode end of the two segments on the right may be seen; the growth has fallen away from one of the segments. Figure 29 is a similar photograph of segments near the anode end of the tube.

Photographs illustrating features of the PG segments are shown in Figure 30. Figure 30(a) and (b) show the anode and cathode ends of typical bore segments. A buildup of graphite occurs on the cathode end of the segment. Figure 30(c) shows exfoliation of the layers of the throat segment which reached the highest temperature. The layers were not separated on the far side of the segment where the sapphire ball pressed against the surface; we would not expect such layer separation to occur if there were a uniform pressure on the end of the segment.

The greatest deposit of carbon occurred at the anode end of the tube, as illustrated in Figure 30(d) and Figure 29. From our earlier experiments with quartz-bore and molybdenum segment tubes, we know that wall damage is not appreciable in the bore near the anode, yet this is where the greatest accumulation of carbon is noted in all types of graphite bore tubes. Probable explanations for this are that either carbon particles become negatively charged and drift toward the anode, or gas flow carries the particles toward the anode.

All the discoloration and carbon buildup on the segments, such as is shown in Figures 30(a), (b), and (d), could be wiped off, leaving a clean surface such as is shown in Figures 24(c) and (d). The corners of the bore were not eroded. The material in the carbon growths must therefore come from the inside bore surface. This hypothesis was verified by observations made on tube B-138-C (Section III-E).

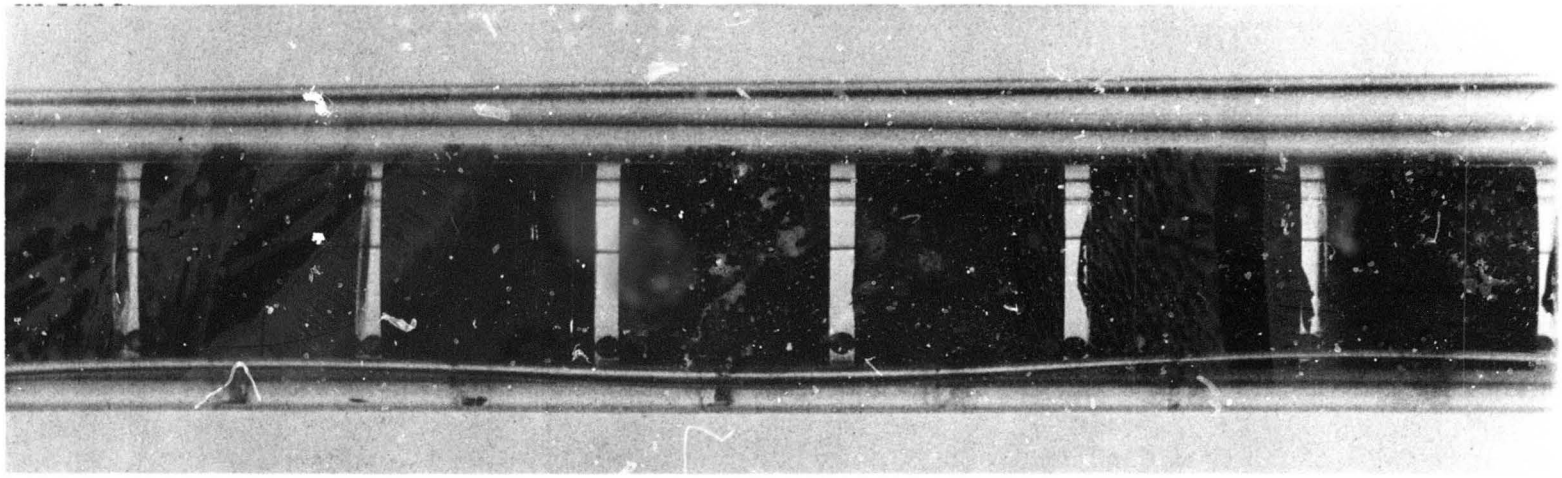

Fig. 28. Appearance of quartz envelope and bore segments at the cathode end of tube B-131 after 225 hours.

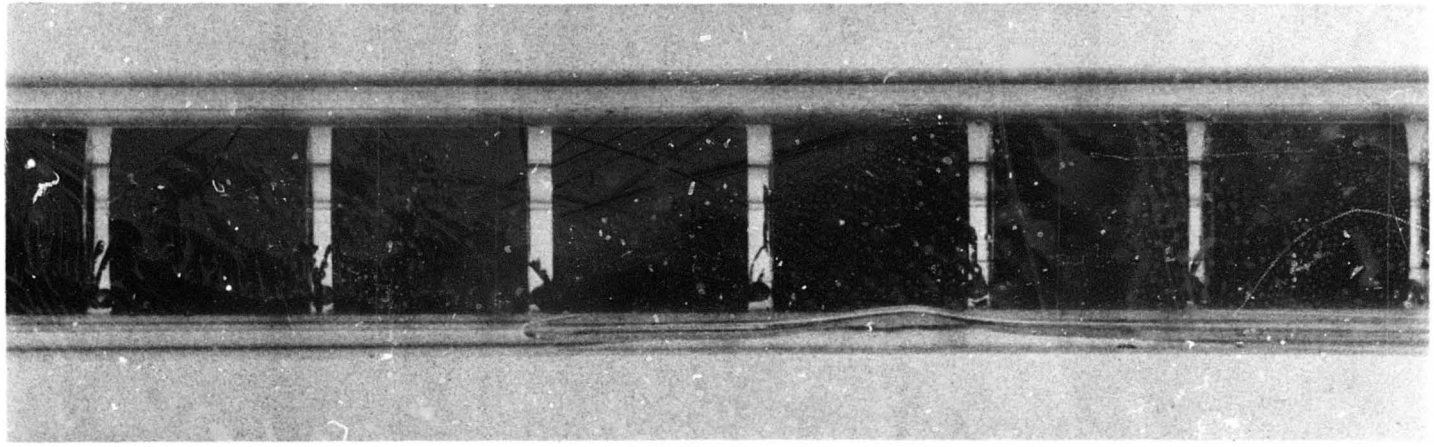

Fig. 29. Appearance of quartz envelope and bore segments at the anode end of tube B-131 after 225 hours. (The wavy line along the bottom of each picture is residual water in the water jacket.)

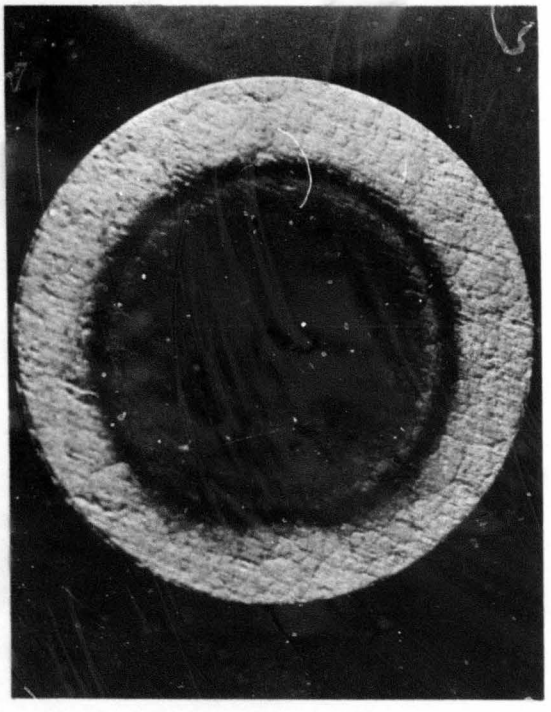

(a)

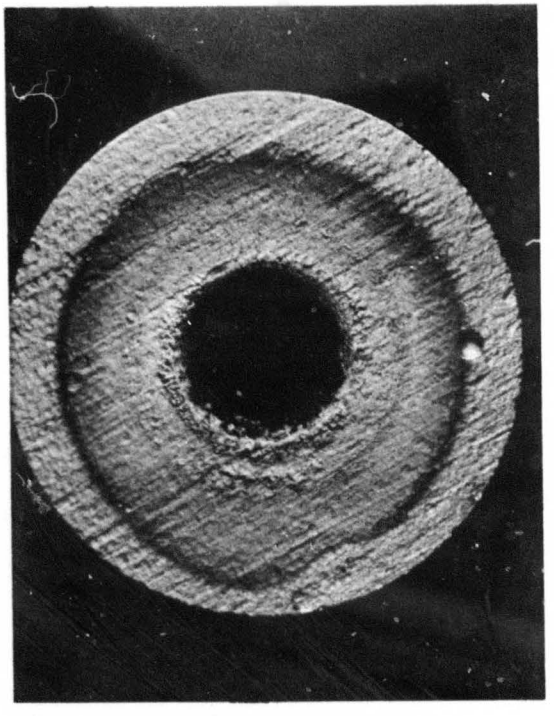

(b)

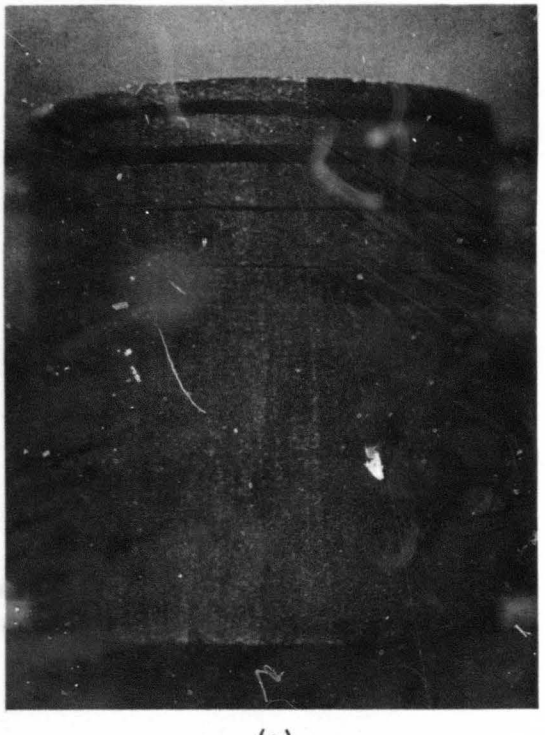

(c)

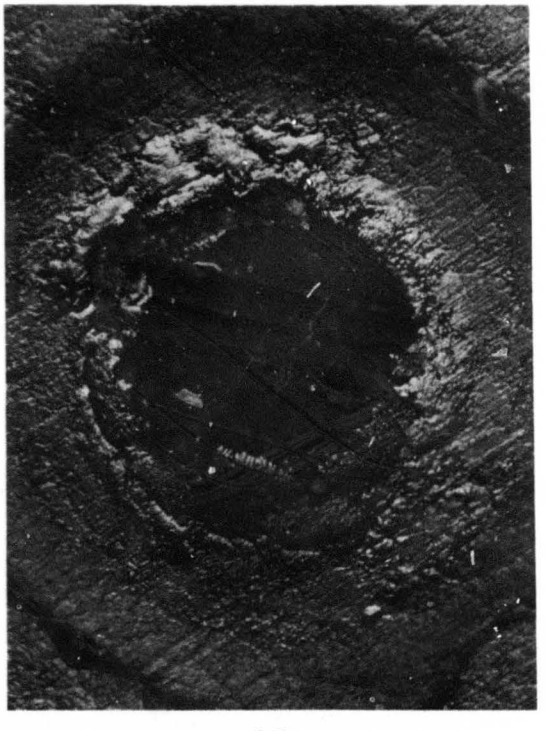

(d)

Fig. 30. Appearance of PG segments from B-131 after 225 hours (6x magnification). (a) Anode end, and (b) cathode end of typical bore segment. (c) Cathode throat taper segment showing exfoliation. (d) Cathode end of anode throat taper segment.

Our conclusions regarding pyrolytic graphite as a bore material are as follows:

- PG does not sputter or evaporate; there is no indication of material deposited on the walls by sputtering

- Comparing the amount of graphite powder generated during 10 and 40 hour tests of normal graphite with that observed in the PG tube after 225 hours, we estimate PG powders at less than one tenth the rate of graphite.

D. EVALUATION OF GRAPHITE WITH A PG OVERCOAT (TUBE No. B-133)

1. Description of the Material

A second approach to improving the surface properties of graphite is to overcoat graphite with PG This is done by heating the graphite segment to 2000°C and passing low pressure methane gas over the part. Pyrolytic graphite layers form, first infiltrating the existing surface, and then forming a thin PG overcoat. The PG structure is deposited with the C-axis normal to the surface, so that the layers follow the surface. The main advantage of this approach should be that the discharge bears upon a uniform surface in which each atom is tightly bound, rather than on the edge of the layers.

A set of bore segments was fabricated by overcoating spectroscopic grade graphite with a 0 005 ± 0 001 in PG coating. The appearance of the surface is shown in Figure 31 The grooved texture of the o.d. resulted from a poor machine finish of the graphite. The i.d., which was reamed, was smooth.

The way in which the overcoat bonds to the segment may be seen from the sectioned segment shown in Figure 32. Figure 32(a) shows an over-all view of the segment, the PG layer is just visible as a dark border. Figure 32(b) through (e) show the coating on different surfaces of the segments as viewed with polarized light at 400x magnification. The coating thickness is 0.0045 in. The homogeneity of the PG compared with the graphite is evident Note the formation of growth cones in Figure 32(d); the tops of these cones appear as bumps on the surface as shown in Figure 31(b) and (c)

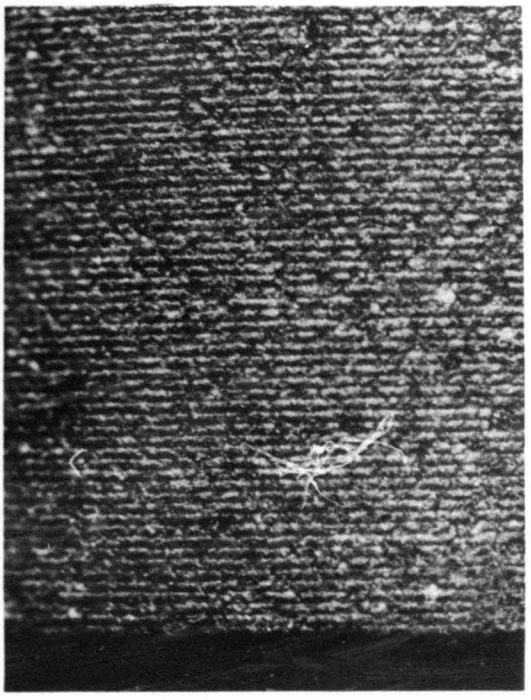

(a)

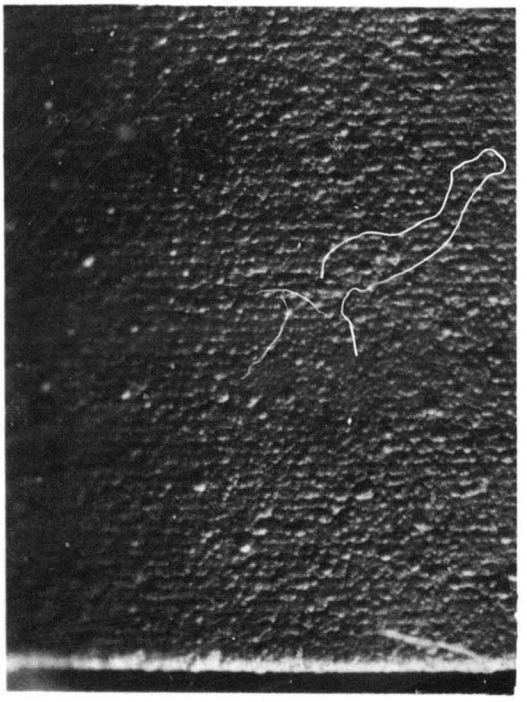

(b)

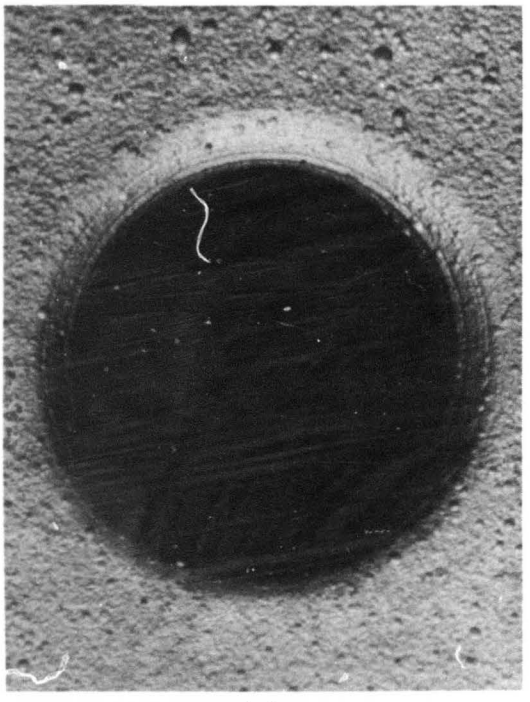

(c)

Fig. 31. Photographs of PG overcoated segments. (a) Side view of uncoated segment (15x magnification). Lines are machine marks. (b) Side view of overcoated segment. (c) End view of overcoated segment.

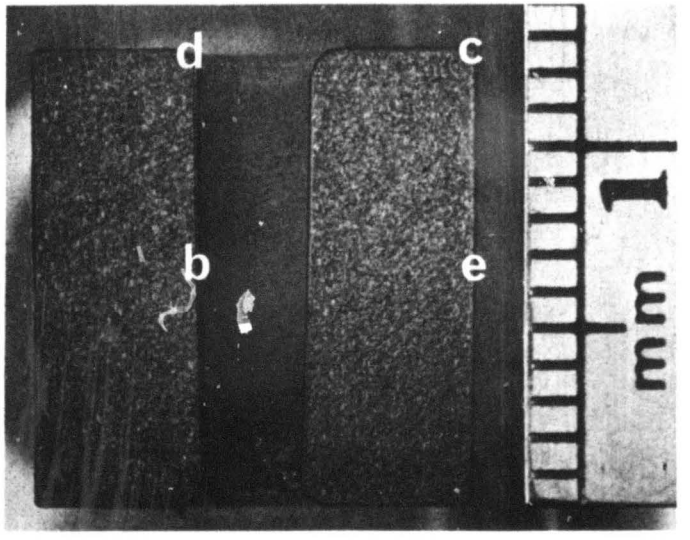

(a)

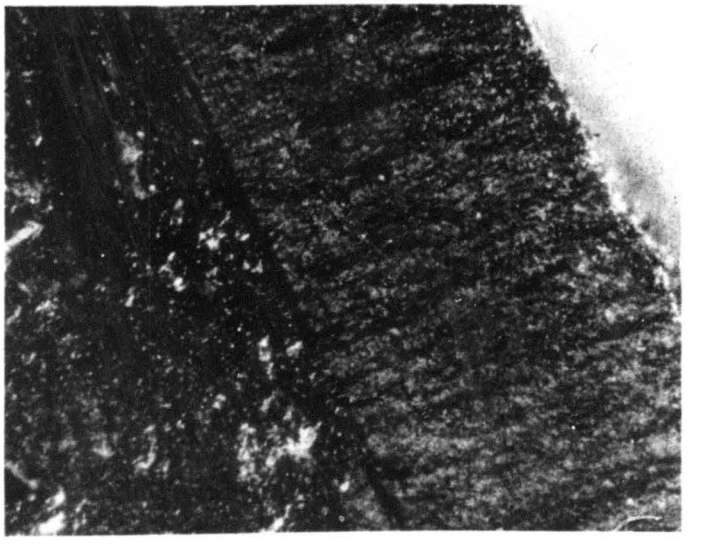

(b)

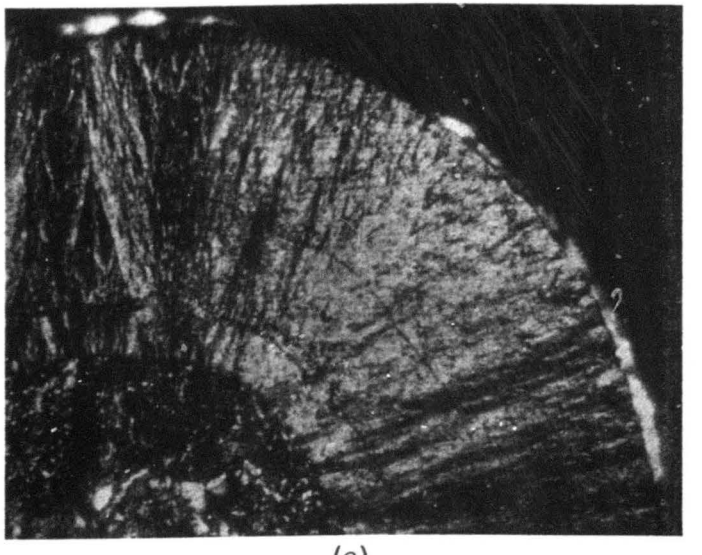

(c)

Fig. 32.
Cross section view of PG overcoated segments. (a) Cross section of segment at 5x magnification. Letters indicate regions shown in the higher magnification photographs which follow. (b) Cross section of coating in bore, 400x magnification. (c) Outside corner.

(d)

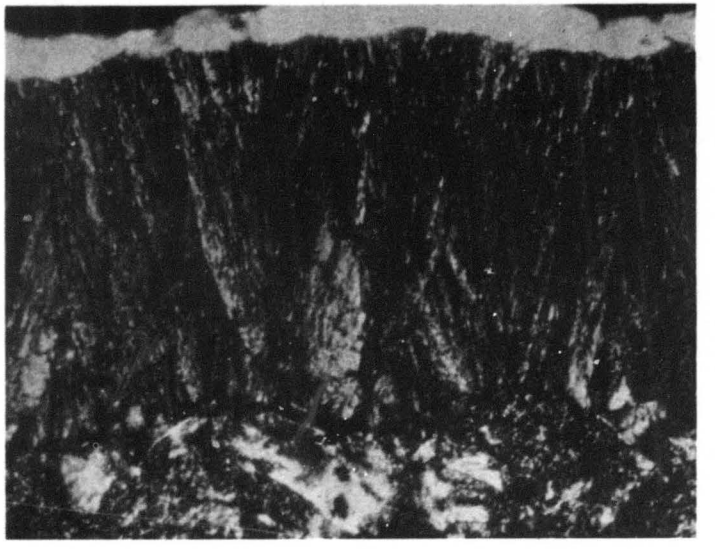

(e)

Fig. 32 (cont'd). Cross section view of PG overcoated segments.
(d) Inside corner. (e) Outside surface.

2. Operating Characteristics

The operating characteristics of the tube are summarized in Figure 33. The tube was operated at 20 A for 205 hours over a two month period.

The GCR characteristics of the tube are plotted in Figure 34. A comparison of the cleanup rate of tubes B-131 (Figure 26) and B-133 shows that the rates are very similar during the same period of operation.

The tube was operated for 7 hours at 10 A midway through the test. The same type of gas absorption and emission from the walls at different current levels was observed in the laser as in the cathode life test (see Figure 7). Approximately 40 μ-liter of gas was absorbed into the walls during operation at 10 A. This gas was re-emitted when the tube was again operated at 20 A.

The output power cycled with pressure between 1.3 and 3.1 W at 20 A. At t = 38 hours the power was disappointingly low. The windows were sparked with a Tesla coil to see if performance could be improved. In the past, we have found that this sparking technique, which draws a glow discharge to the inside surface of the window, removes residue films which reduce output power or cause mode distortion. The films are presumably removed by bombarding ions from the glow discharge; this is a well-known technique of cleaning mirror substrate before coating. (Sparking does not remove particles from the window; in fact, it is likely to drive particles resting near the window up onto the windows.) A marked improvement in power was obtained, as indicated by the arrow at t = 38 hours in Figure 33.

During the last 40 hours of the experiment the laser was being used as a source to study the beam divergence of low order transverse modes. After 205 hours the life test experiment was terminated and a new set of windows put on because a dust particle on the cathode window made it difficult to obtain TEM_{00} operation. The tube was run for an additional 25 hours at 20 A while additional beam divergence data were gathered. The power output characteristics of the tube at the end of test are shown in Figure 27. The power output was 3.1 W at 20 A and 4.1 W at 25 A.

The tube voltage during the test cycled with pressure between 200 and 220 V.

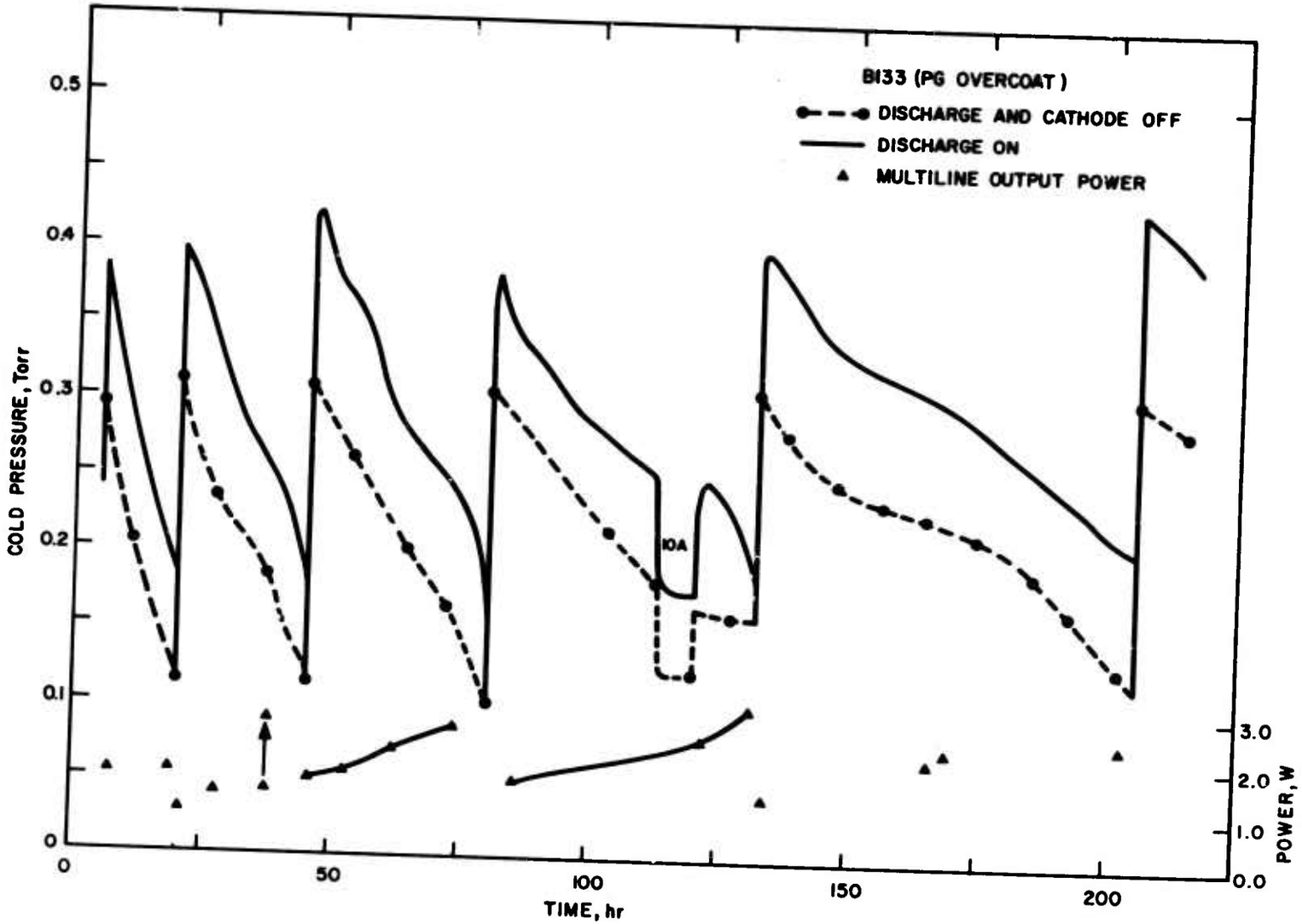

Fig. 33. Gas pressure and power output characteristics of tube B-133 versus time.

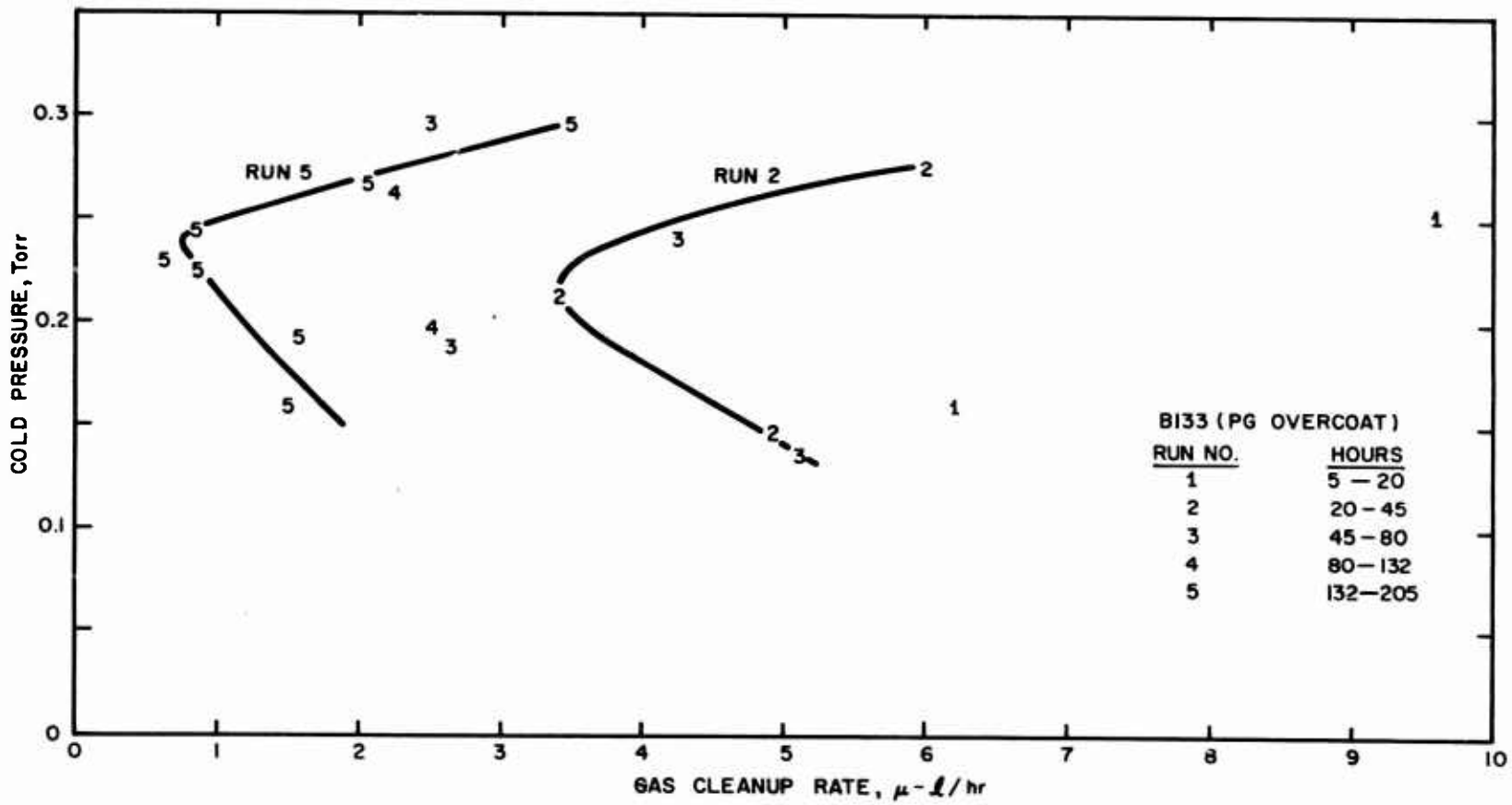

Fig. 34. Gas cleanup rate in tube B-133 as a function of gas pressure during successive runs.

3. Resistance of the Material to Sputtering and Erosion

The tube was disassembled and the parts inspected after 230 hours of operation at 20 A. Figures 35 and 36 shows the appearance of the quartz envelope in the center of the tube and at the anode end. (The spring and tungsten wire arrangement shown in Figure 36 allows longitudinal expansion of the segments toward the anode.) There was a slight discoloration of the envelope in the center of the tube, but otherwise this region was free of carbon dust. The concentration of carbon powder toward the anode end, which was mentioned earlier, is clearly evident in Figure 36.

Photographs of typical segments are shown in Figure 37. There is some discoloration of the ends of the segments in the middle of the bore, as shown in Figure 37(a) and (b), but there is no buildup of material. Figure 37(c) shows the segment at the anode end which had the largest accumulation of dust. All the carbon could be scraped from the segment, down to the original surface.

Measurement of the i.d. of the segments revealed no erosion of the bore. The photographs of the PG overcoated segment shown in Figure 32 are actually of a segment after it was run in the tube for 230 hours. The overcoating is of uniform thickness on all surfaces; erosion of as little as 0.0005 in. could have been detected easily if it had occurred. (The apparent axial change in the i.d. of the segment in Figure 32(a) is caused by the sectioned plane being slightly tilted with respect to the axis, rather than by erosion.)

Our conclusions regarding the PG overcoated segments are similar to our comments on PG. Both materials are much better than regular graphite. Some difficulty with window contamination was noted with overcoated PG. The contaminating film could be removed by "sparking" the window, and did not appear to be carbon dust. Carbon dust and films were detected on the segments and envelope.

E. EVALUATION OF PYROLYTIC GRAPHITE IN A CERAMIC ENVELOPE (TUBE No. B-138-C)

A 422 hours evaluation of PG segments supported in a metal-ceramic (M/C) vacuum envelope was conducted which yielded additional information on the characteristics of PG as a bore material.* This

*The experiment was carried out under a continuing Company-funded effort on metal-ceramic ion laser development. Experimental results are quoted here which are pertinent to an understanding of the properties of bore materials.

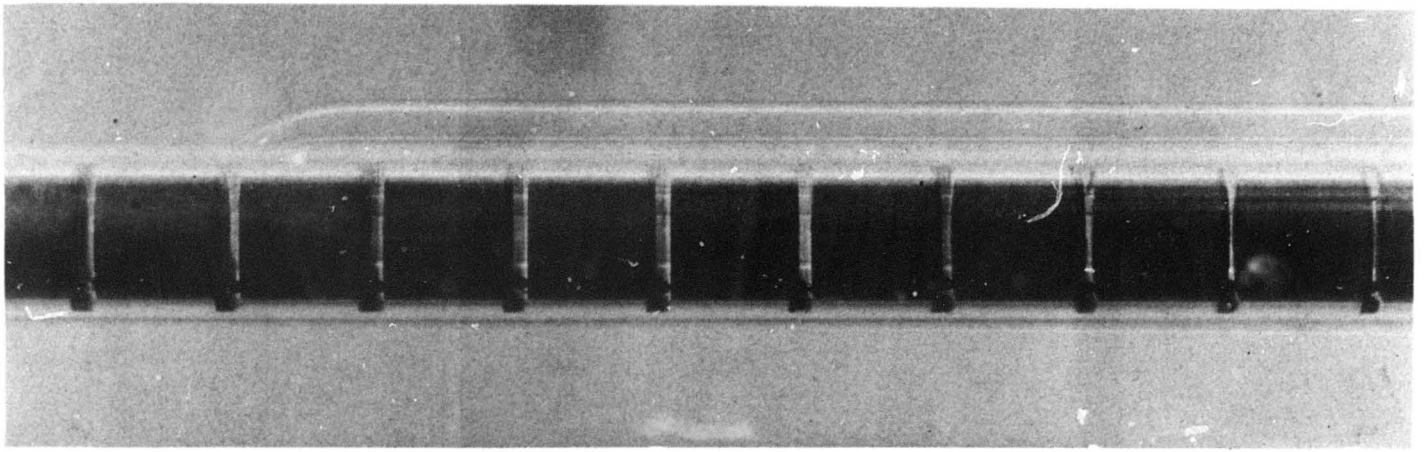

Fig. 35. Appearance of quartz envelope and bore segments at cathode end of tube B-133 after 230 hours.

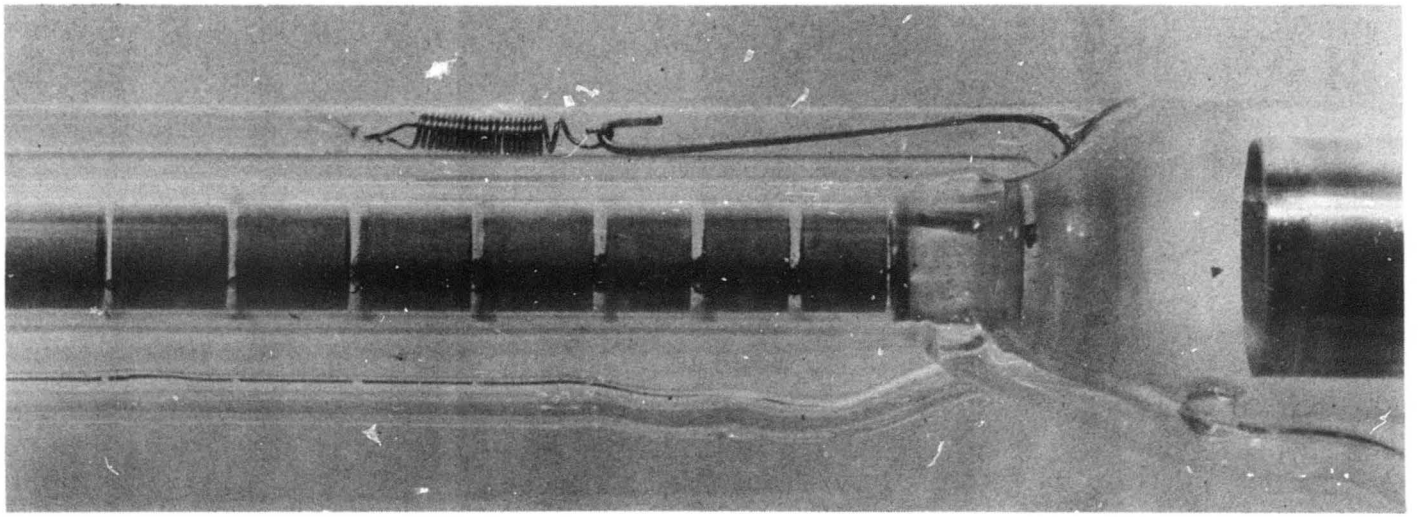

Fig. 36. Appearance of quartz envelope and bore segments at the anode end of tube B-133 after 230 hours.

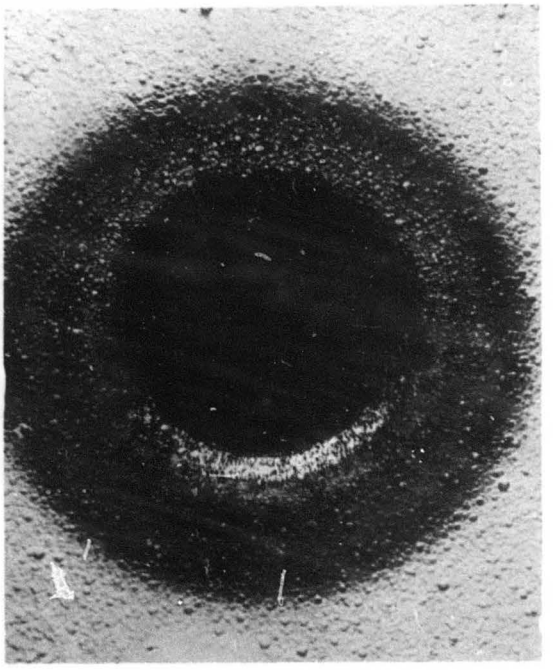

(a)

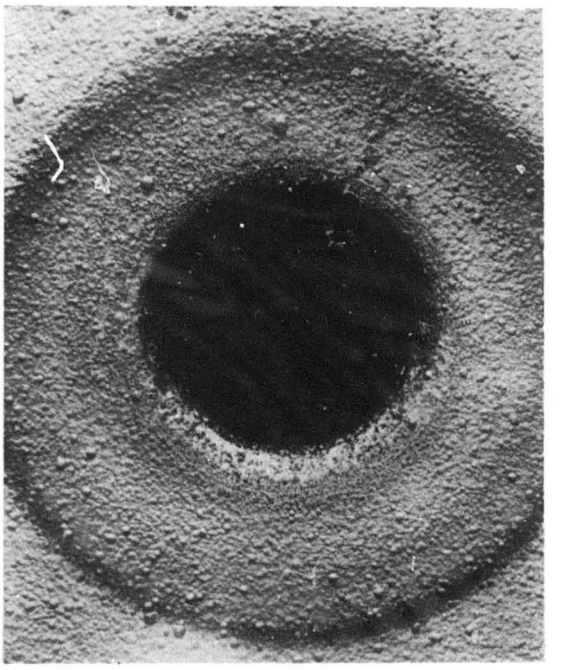

(b)

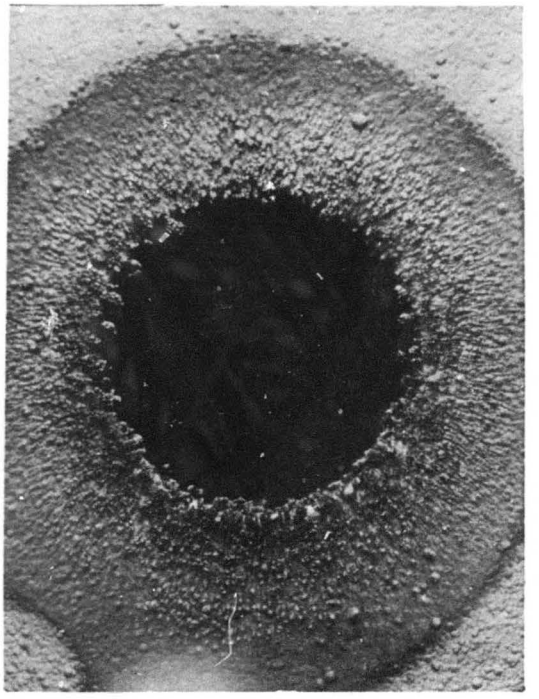

(c)

Fig. 37. Appearance of overcoated segments from tube B-133 after 230 hours (10x magnification). (a) Anode end and (b) cathode end of typical bore segment. (c) Cathode end of segment in the anode constriction.

experiment has also yielded data on the efficacy of internal and external gas return paths in segmented-bore tubes. This topic is discussed in Section VI-A.

The metal-ceramic structure consisted of a 0.75 in. i.d. water-cooled alumina tube which supported the radiation-cooled PG segments and anode, and a stainless steel assembly which housed the cathode. Except for the M/C envelope and larger segment diameter, the tube construction duplicated that of the earlier quartz envelope experiment (i.e., same 3 mm bore size, 1/16 in. segment spacing, throat shape, bore length). The gas volume of the metal-ceramic tube, B-138-C, was 0.3 liter, which was one-half that of the earlier quartz-envelope test.

Curves of the variation of gas pressure and output power throughout the test are shown in Figure 38. As usual, the output power increased with decreasing gas pressure during each gas fill. Comparison of the gas cleanup rates (GCR) of tube B-131 (quartz envelope) and B-138-C (M/C envelope) during the first 150 hours of operation shows that the GCR of the latter varies between 0.2 and 2 μliter/hour, which is roughly one-third that of the quartz envelope tube. This is consistent with our conclusion that large amounts of argon are adsorbed on the quartz walls. Unfortunately, the gas replenishment procedure in the ceramic envelope experiment was somewhat different from that used in the previous life tests; the M/C tube was thoroughly pumped out each time before being refilled for all but the last gas fill at 177 hours. For the last run, gas was added to the existing fill as in previous tests. Some gas was undoubtedly removed from the segments and walls during evacuation; this would not have occurred if gas were simply added. The basic cleanup rate of PG and alumina may therefore be lower than that calculated from the data of Figure 38.

Graphite dust accumulated between the segments and at the anode end during operation of the tube. Roughly 0.3 cm^3 of dust was collected from the tube at the end of the test. The concentration of dust toward the anode end apparently may be accounted for by gas motion in the tube, even at the very low operating gas pressure. Evidence that graphite dust is moved about by gas flow in the tube was obtained from examination of the distribution of dust at the anode end. In one place, gas flowing through the gas return path holes in one tapered segment exited directly onto the tapered surface of the adjacent segment. The surface of the segment in line with these gas return holes was free of dust, while the surface which was not in line with the holes was covered with graphite powder.

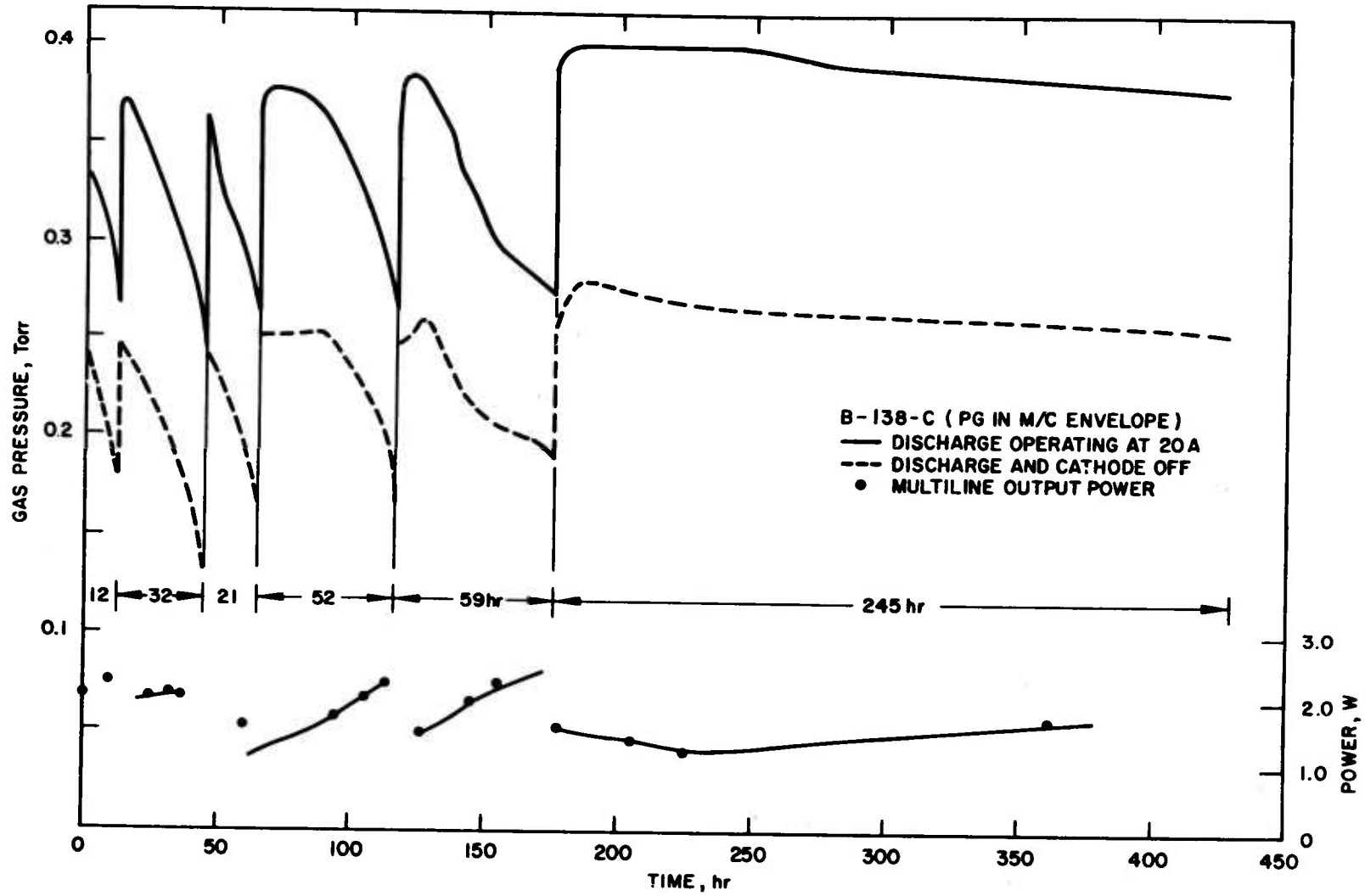

Fig. 38. Gas pressure and power output characteristics of tube B-138-C versus time.

Despite the generation of graphite powder in the tube, no localized erosion of the bore segments was evident by visual inspection or by measurement of the bore diameter with gauge pins. This lack of measurable erosion has been the rule in all our graphite tubes However, examination of a segment in cross section has yielded information on the probable source of the powder. Figure 39 shows photographs of the o.d., corner, and i.d. edges of a segment at 100x magnification. The c-axis of the PG lies along the axis of the tube, with the isotropic layers normal to the axis. The smooth end-surface, parallel to these layers, is seen at the top of Fig. 39(a) and (b). On the inner diameter, small pieces of graphite are seen to have been removed from the edges of the layer, leaving a serrated surface. The distance from the crests and valleys on this surface is 0.002 in. Therefore, it appears that the source of powder in these tubes is graphite particles picked from the inner surface where the edges of the layers are exposed. When measured with a gauge pin, the dimension of the i.d. does not appear to be changed because the pin rests on the peaks along the surface.

Figure 40 is an end view of a 3/4 in. o.d. segment showing the arrangement of the bore, three gas return path holes, and holes with the three sapphire support rods in place. A 1/16 in. long alumina ring was placed around one of these rods as a spacer between the segments, as shown. The innermost edge of the spacer was 1/16 in. from the bore aperture.

Figure 41 is a photograph of three of the alumina spacers at the end of test. One spacer, located in the uniform bore region, is unchanged. The other two, located near the cathode throat, are badly flattened on the side exposed to the discharge. The maximum temperature of the segments in the tube was 1250°C, well below the 1900°C melting point of high purity alumina. We conclude, therefore, that the ceramic surface has been eroded by ion sputtering, rather than by melting.

In our early experiments with alumina bore tubes, failure always occurred within a few tens of hours as a result of thermal shock; therefore, no data were obtained on the resistance of the ceramic to sputtering and erosion. Based on the amount of erosion illustrated in Figure 41, we would conclude that alumina is not a suitable ceramic to be used in contact with the discharge, even if thermal shock were not a problem.

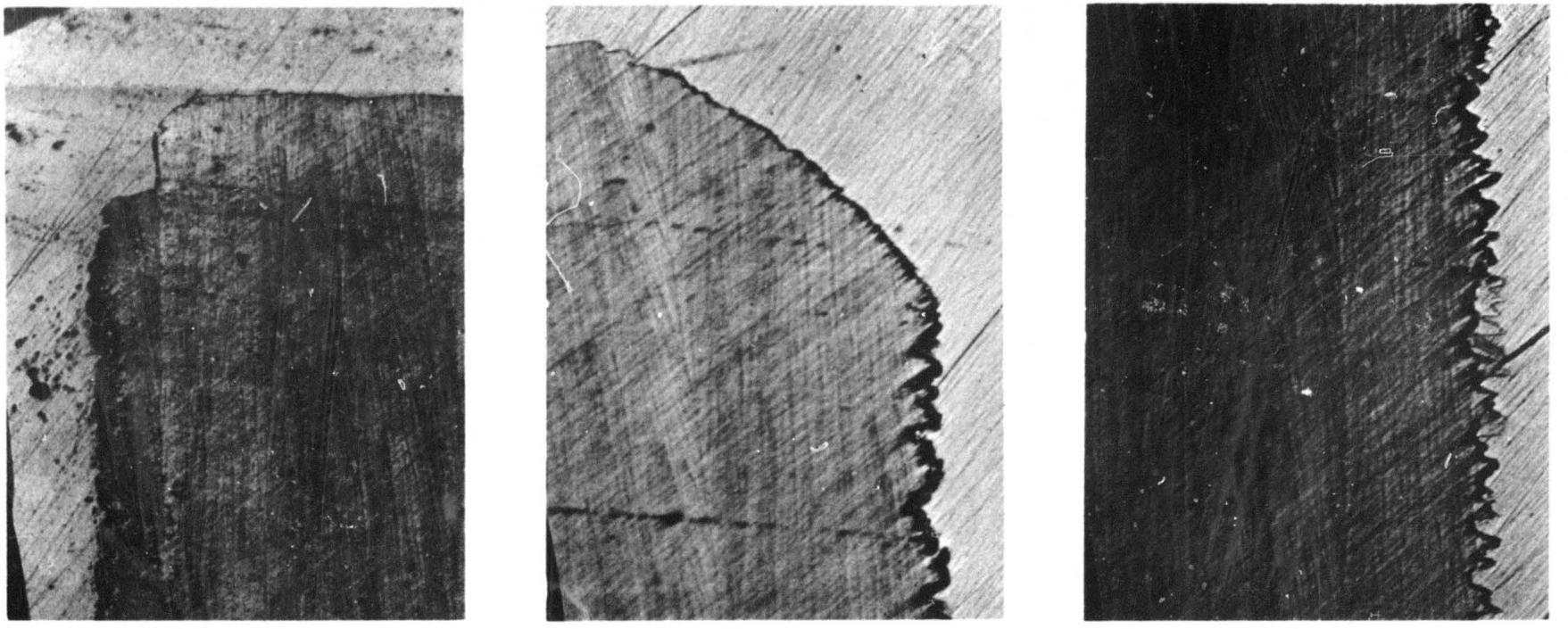

(a) (b) (c)

Fig. 39. Photographs of cross section of a pyrolytic graphite segment after 400 hours of operation. (a) Edge on o.d. (b) Corner on i.d. (c) Edge on i.d.

Fig. 40.
End view of segment showing bore, gas return path, and support rod holes with a spacer ring in place.

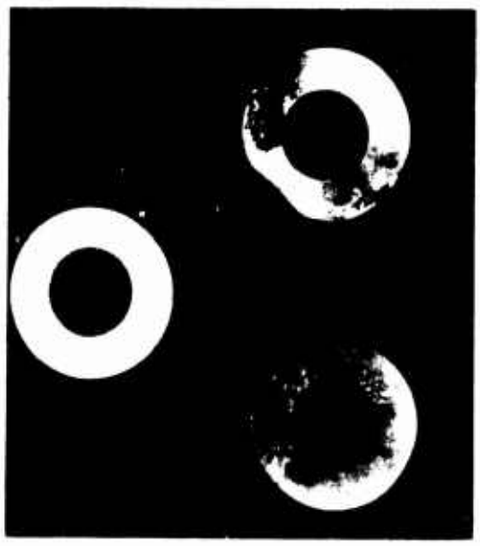

Fig. 41.
Photograph of alumina spacers after test.

Fig. 42.
Graphite bore segment with a 0.005 in. overcoating of tungsten on the bore, i.d., and end surfaces.

F. EVALUATION OF TUNGSTEN-OVERCOATED GRAPHITE

1. Discussion

In an effort to eliminate powdering of graphite bore segments, segments were fabricated with a 0.005 in. overcoat of tungsten vapor-deposited on the i.d. and ends of graphite segments. The deposition is achieved by passing WF_6 gas over the segments at 600°C. A set of graphite segments was machined here, and then overcoated with tungsten at San Fernando Laboratories, Inc.

The motivation for this approach is to combine the refractory, sputter-resistant properties of tungsten which were noted in earlier experiments with the low cost, easy machining, low weight, and high emissivity properties of graphite. (Tungsten-overcoated graphite segments have only one-tenth the weight of solid tungsten segments; this is an important consideration since the laser must survive mechanical shock in field use when these segments are used in a quartz or ceramic envelope.)

A simple calculation shows that, ideally, an 0.005 in. thick tungsten coating should not be removed by sputtering with 33 eV ions for >6000 hours. For a 3 mm diameter bore, the volume of tungsten per centimeter of bore length is 1.2×10^{-2} cm^3, or 7.5×10^{20} tungsten atoms/cm. The sputtering threshold for argon ions on tungsten, defined by Wehner as the ion energy which produces a yield of 10^{-5} atoms/ion, is 33 eV (Ref. 4). For a 3 mm tube operating at 20 A with a fill pressure of 0.25 Torr, the number of ions striking the wall per linear centimeter may be calculated to be 3.3×10^{18} ions/sec (Ref. 5). Based on these values, we may estimate the time in hours required to sputter away the coating to be

$$T = \frac{(7.5 \times 10^{20} \text{ atoms})}{(10^{-5} \text{ atoms/ion})(3.3 \times 10^{18} \text{ ions})(3.6 \times 10^{3} \text{ sec/hour})} = 6300 \text{ hours.}$$

A uniform bore segment (after 400 hours run time) is shown in Figure 42. The bore segments are 0.5 in. long with a 0.5 in. o.d. and 3 mm i.d. The outer diameter of the segment, which is not exposed to the discharge, is not coated with tungsten in order to retain a high emissivity on the outer surface.

We have run four separate experiments with the tungsten-overcoated segments using throat segments of different materials, as listed in Table IV and discussed below.

2. Tests Using Tungsten-Overcoated Graphite Throughout the Tube (Tube No. B-141)

The 0.5 in. long segments were assembled in the same 0.5 in. i.d. water-cooled quartz envelope used in earlier bore material studies. The active, uniform bore length was 46 cm.

At 25 A and a fill pressure of 0.28 Torr, the power output was 3.4 W and the tube voltage 200 V. The operating temperature of the segments in the bore was 1100°C; the temperature of solid tungsten segments of the same o.d. would have been ~1380°C because of their lower emissivity.

Evaporated tungsten in the vicinity of the cathode throat constriction was noted after only 10 hours of operation at 20 A. A glass-to-quartz seal failed after 20 hours of operation, and the segments were removed and examined.

The cathode throat constriction is formed by three segments, each 0.375 in. long, spaced 0.062 in. apart. Each segment is machined to a different taper which approximates an exponential decrease in diameter from 12 mm to 3 mm when the three segments are assembled. Numbering the segments starting at the cathode, segments 1, 2, and 3 are 0.375 in. long tapered segments; segments 4 through 35 are 0.5 in. long uniform bore segments; and segments 36, 37, and 38 are 0.375 in. long segments tapering to a 12 mm diameter at the anode.

Examination of the segments showed that the tungsten layer was sputtered from the anode end of segments 3, 4, 5, and 6. No change in the dimensions of other segments could be detected. Segments 3, 5, and 6 were encapsulated in plastic, cross-sectioned, and polished so that the erosion of the tungsten layer could be studied in detail. An over-all view of these segments at 5x magnification is shown in Figure 43. The overcoating has been completely removed from the anode end of each segment. The uniformity in thickness of the original coating was quite good, as seen in Figure 43(a). The variation in thickness of the film in the bore and ends of segments 5 and 6 is caused by the deposition of material sputtered from the anode end. This is shown clearly by the photographs in Figure 44, which were taken at 100x magnification. In Figure 44(b) the transition between the original 0.010 in. thick coating and a 0.003 in. layer of sputtered material may be clearly seen. In Figure 44(c), a 0.004 in. thick layer is seen to have accumulated on the original 0.008 in. thick layer.

The clear diameter of segments 4, 5, and 6 was reduced from 0.125 in. to 0.114, 0.116, and 0.114 in., respectively. The diameter of segment 7 was 0.125 in.

(a) (b) (c)

Fig. 43. Cross sectional view of overcoated segments which exhibited erosion. (a) Segment 3. (b) Segment 5. (c) Segment 6.

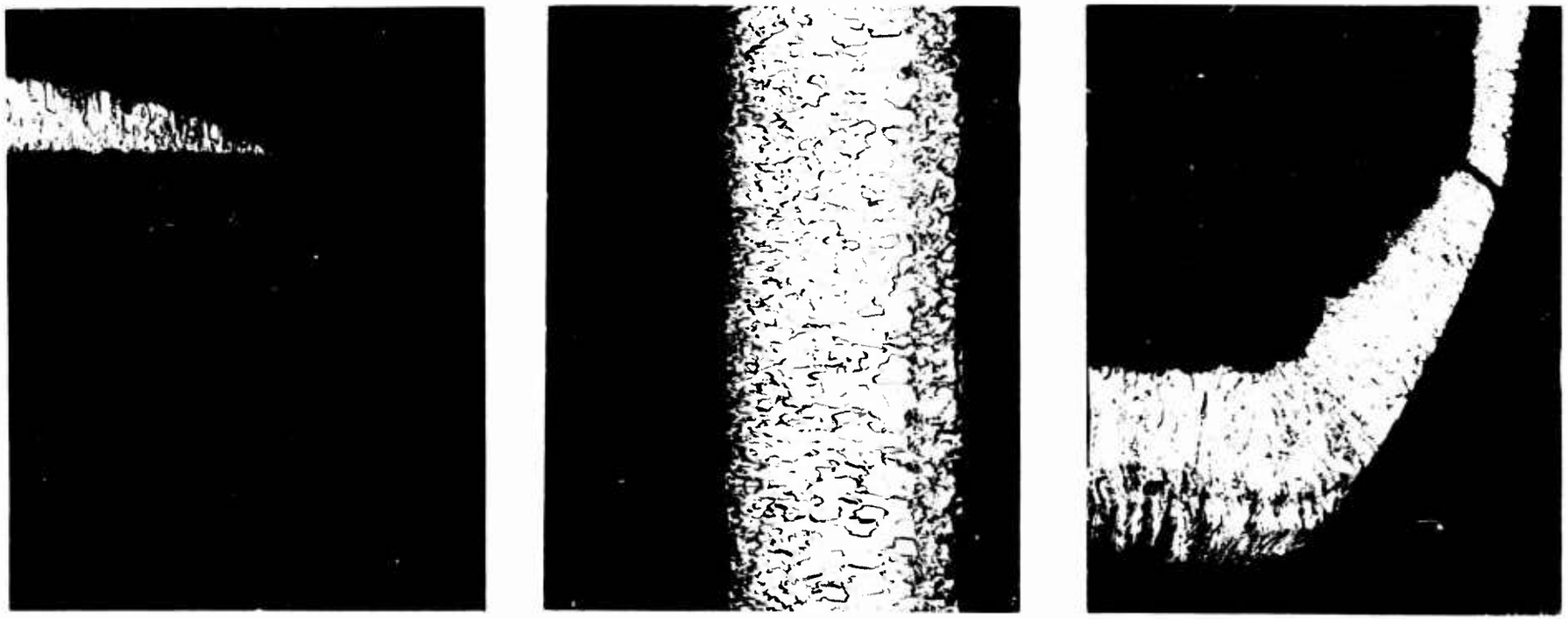

(a) (b) (c)

Fig. 44. High magnification photographs of coating on segment 6. (a) Corner of i.d., anode end. (b) i.d. midway in the segment. (c) Corner of i.d., cathode end.

It was calculated previously that the time necessary to sputter away a 0.005 in. thick tungsten coating from the uniform bore region of a 3 mm diameter tube should be 6000 hours. This estimate was based upon an ion flux of 3.3×10^{18} ions/sec/linear cm striking the wall, each with a kinetic energy of 33 eV. Sputtering rate data for argon ions striking tungsten at normal incidence are plotted in Figure 45 (Ref. 4). Data on quartz (Ref. 6) are also plotted for comparison. The sputtering yield for quartz is approximately 100 times greater. At the sputtering threshold of 33 eV, the yield for a tungsten surface is 10^{-5} atoms/sec. Assuming the same 3.3×10^{18} ions/sec flux in the throat, removal of the tungsten layer in 20 hours implies a yield of 3×10^{-3} atoms/sec, which correspond to 55 eV ions impinging on the surface in the throat region. This gives a relative idea of the steepness of the yield curves for low energy ions. In fact, the presence of doubly ionized atoms and the striking of the ions at nonnormal incidence can account for a yield of $> 10^{-3}$ atoms/ion for an average ion energy of < 55 eV.

3. Tests Using Porous Tungsten Throat Segments and a Gradual Cathode Constriction (Tube No. B-145-A)

To reduce the localized bore damage which occurred in B-141, the cathode throat was redesigned with a more gradual taper. The constriction from 12 mm to 3 mm was formed in five tapered segments rather than three, so that the taper extended over 2.2 in. instead of 1.3 in. The linear taper of each segment was chosen to approximate an exponential decrease in diameter over the five segments.

The new throat segments and the first three uniform bore segments were machined of porous tungsten.* The segments were processed in vacuum at 1800°C to remove the copper added for free-machining.

The tube was assembled and operated at 20 A for 165 hours. During the experiment, additional copper diffused out of the segments (which operated at 1200°C) and coated the quartz walls. The copper film eventually caused a successive electrical short between the tungsten segments. This of course impressed a common potential upon the shorted segments and accelerated the erosion of the segments.

The test was terminated after 165 hours when shorting among the throat segments made the discharge unstable. No graphite dust was present in the tube at the end of test.

---

*Porous tungsten was chosen for ease of machining. The material is made by powder metallurgy techniques with a composition of 80% tungsten and 20% copper. After machining, the copper is removed from the material by baking under vacuum, leaving the pure tungsten matrix.

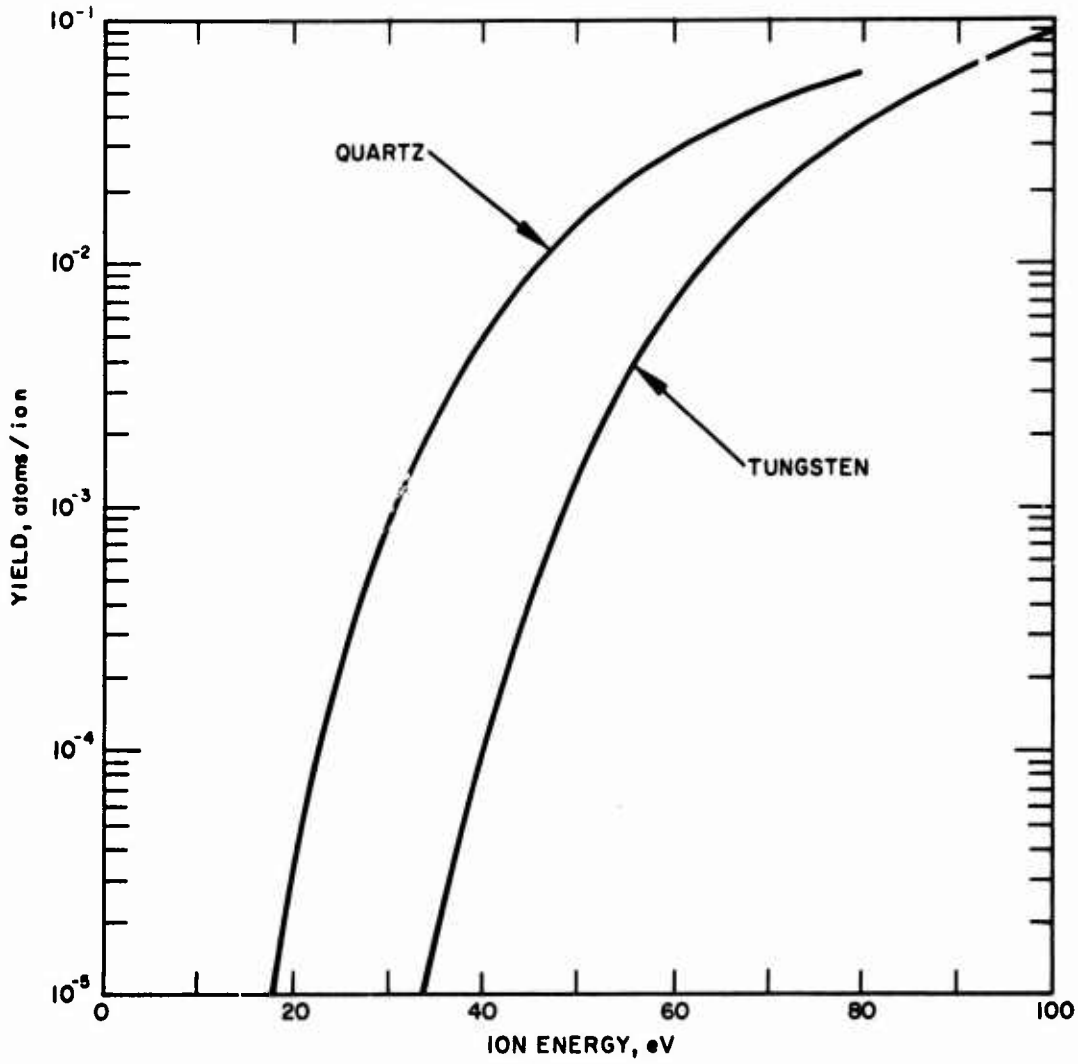

Fig. 45. Curves showing sputtering yield versus ion energy for argon ions striking at normal incidence. Data from Stuart and Wehner (Ref. 4) and Jorgenson and Wehner (Ref. 6).

Examination of the tungsten segments revealed massive sputtering damage caused by the shorting together of the segments. No erosion of the tungsten overcoated segments occurred. Figure 46(a) is an over-all view of the segment arrangement at the cathode end. Pieces of the copper-covered quartz envelope are also shown; the copper coating was 0.002 in. thick. Figure 46(b) shows the anode and cathode ends of segments 6 and 7. These segments were actually joined together on the i.d. at the end of test, as may be seen in Figure 46(a). Figure 46(c) is a similar view of segments 8 and 9. The clear diameters of segments 7 and 8 were reduced from 0.125 to 0.065 and 0.090 in., respectively, by sputtered tungsten.

In enlarging the i.d. of the anode end of segment 8 from 3 mm to 6.3 mm (see Figure 46(c)), tungsten was removed at a rate of 2.5 x 10^{16} atoms/sec/linear cm of length. This assumes a uniform erosion rate throughout the test; actually, the erosion was much worse toward the end of test, when more segments were shorted. For an incident ion flux of 10^{18} to 10^{19} ions/cm, this corresponds to sputtering yield of 10^{-2} to 10^{-3} atoms/ion, and ion energies at normal incidence of 50 to 64 eV.

4. Test Using Solid Tungsten Throat Segments (Tube No. B-145-B)

The quartz envelope was rebuilt and the bore was reassembled with solid (nonporous) tungsten segments in the throat and first 1 in. of uniform bore. A thin tungsten film formed on the quartz walls opposite these segments after 45 hours of operation at 20 A, and the test was terminated. Inspection of the segments showed slight erosion at the anode end of segments 3 and 4 in the throat and the two adjacent uniform bore segments. Figure 47 shows the anode and cathode ends of segments 6 and 7, respectively; segment 7 was the only one which showed any buildup of material. No noticeable erosion of the tungsten layer occurred on the overcoated segments in the uniform bore region.

5. Test Using Graphite Disks in the Throat (Tube No. B-145-C)

The tungsten overcoated graphite segments were reassembled in a tube using 0.08 in. thick Poco graphite disks with a 1/8 in. spacing in the throat and first 2 in. of uniform bore. This configuration was selected for three reasons:

1. Good laser performance had been obtained previously in a graphite disk tube (see Section IV).

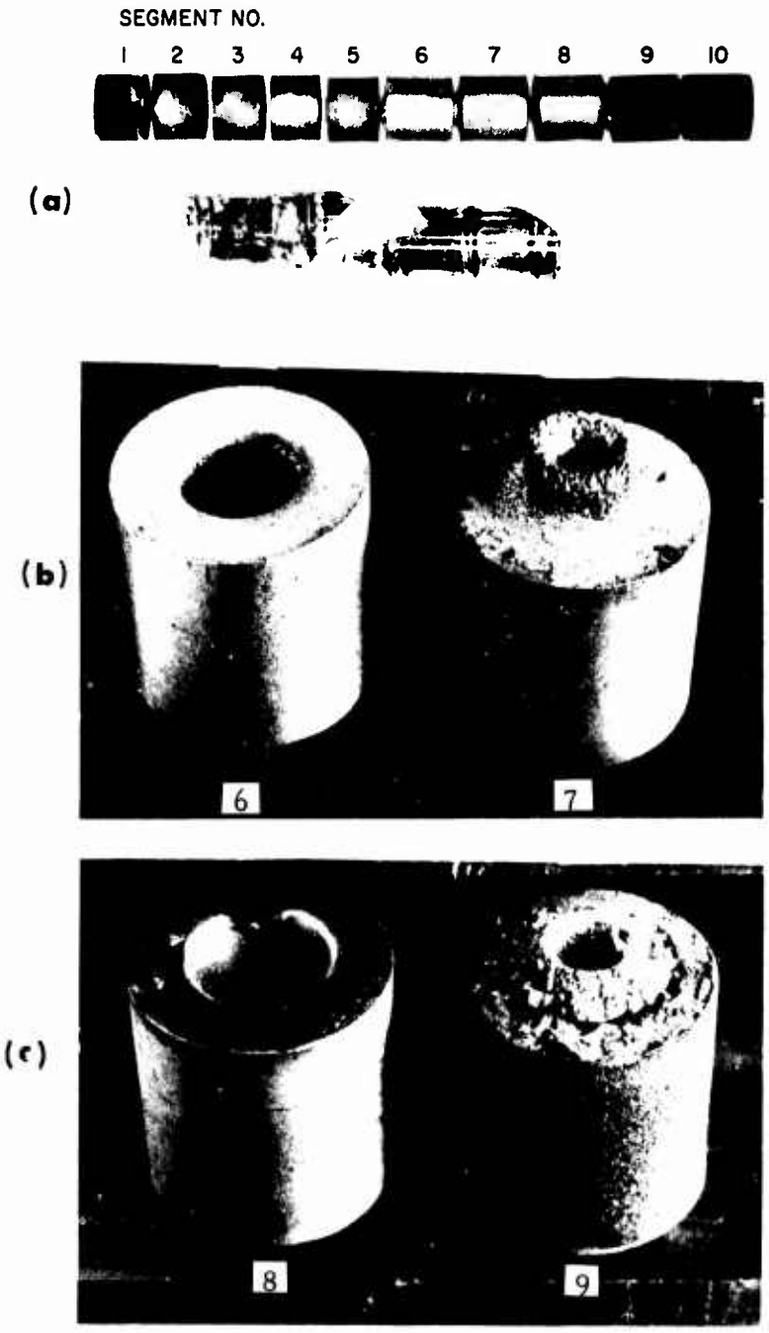

Fig. 46. Photographs of sputtering damage to porous tungsten throat segments.

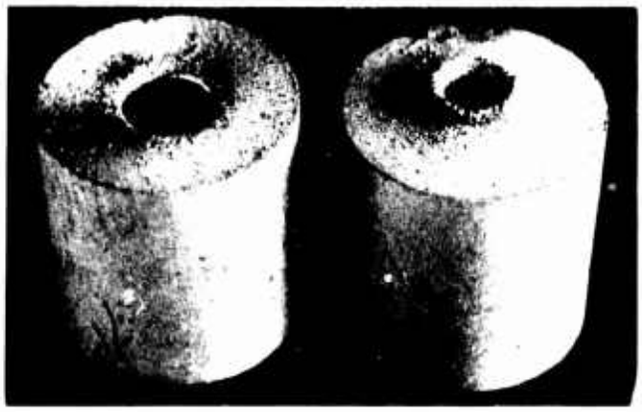

Fig. 47. Photograph of anode end of segment 6 (left) and cathode end of segment 7 (right).

2. 3 mm bore disk structures had been found to prefer a lower gas pressure than 3 mm long-segment tubes, presumably because there is less severe gas pumpout in the disk structure. Operating the laser at the optimum pressure for the long-segment region would result in higher-than-optimum pressure for the disk region. We reasoned that this should reduce the sputtering rate in the disk region.

3. In previous experiments using normal graphite, Ultra Carbon grade XUT-31 and Graphite Specialties Graph-i-tite G grade had been used. In this experiment Poco Graphite, Inc., grade AXF-5Q1 was used; this has a higher density and more uniform structure than the other graphites. The propensity of graphites to powder was checked by heating a sample of each to incandescence, and plunging it into the water. (This is a process used in commercial vacuum tube practice to free carbon anodes of dust. Steam formed at the surface of the material blows off loose particles from the surface.) Unlike the results with the Ultra-Carbon and Graphite Specialties graphite, the water remained dust-free when Poco graphite or PG was tested.

The tube was operated for 80 hours at 20 A. The maximum laser output was obtained at the usual optimum pressure for long-segment tubes. At the end of test, carbon dust was present in the tube from the graphite disks in the throat. No erosion of the tungsten overcoat had occurred.

6. Conclusions Regarding Tungsten Overcoated Graphite

The same set of tungsten overcoated graphite segments was used in four experiments over a four month period, and operated for a total of 450 hours at 20 A No erosion of the tungsten coating occurred for segments located in the uniform bore region. We judge that the use of a tungsten coating on the graphite to eliminate powdering of the graphite is successful for the region of the tube.

The problem of erosion in the throat region was demonstrated in these experiments. It is clear that graphite forms powder, and tungsten segments are sputtered badly in this region. Use of the tungsten disk structure, described in Section IV, is one method to avoid erosion. Additional data on the throat region problem are given in Section VI.

G. EVALUATION OF A QUARTZ BORE TUBE (TUBE No. F-29)

1. Operating Characteristics

A 3 mm diameter, 46 cm long quartz bore tube was tested for comparison with segmented-bore tubes of the same dimensions. The tube was sealed off and included a getter bottle, thermocouple gauge, gas leak valve, and high-pressure argon reservoir. The optimum magnetic field was 1 kG and the power output was 2.5 W at 20 A, which is typical of quartz or segmented bore tubes. Over the gas filling pressure range of interest (0.1 to 0.3 Torr), the tube voltage at 20 A varied between 164 V and 190 V. This is approximately 40 V lower than the tube voltage of segmented-bore tubes of the same diameter and length.

2. Gas Cleanup Behavior

Figure 48 shows the variation of the gas pressure with time throughout the run. Gas was added to the laser 12 times. Three important observations may be made:

- Quartz bore tubes have a high gas cleanup rate (GCR)
- The GCR decreases with increased tube life
- After 30 hours of operation, the absorption and release of gas from the walls under different discharge conditions make it difficult to control the gas pressure.

Figure 49 is a plot of the average GCR during each run versus hours of tube operation. The cleanup rate decreased sharply from 52 μ-liter/hour for the first fill to rates in the range of 5 to 15 μ-liter/hour at 100 hours. Within each run, the GCR is lowest at high gas pressures, and increases monotonically with decreasing pressure. Average cleanup rates in graphite tubes under identical conditions are 8 μ-liter/hour during the first run, and 2 μ-liter/hour during later runs.

As shown in Figure 48, with each successive run the amount of gas absorbed in the walls at low pressure and released at high pressure (after adding more gas) became greater and greater. After the tube was filled to a cold pressure of 0.29 Torr at 82 hours, the cold pressure rose to 0.42 Torr after 15 hours of operation. This represents an increase of 90 μ-liter, which is approximately one half the amount of gas originally in the tube. Attempts were made to control the pressure rise by filling to a lower pressure; these were not particularly successful.

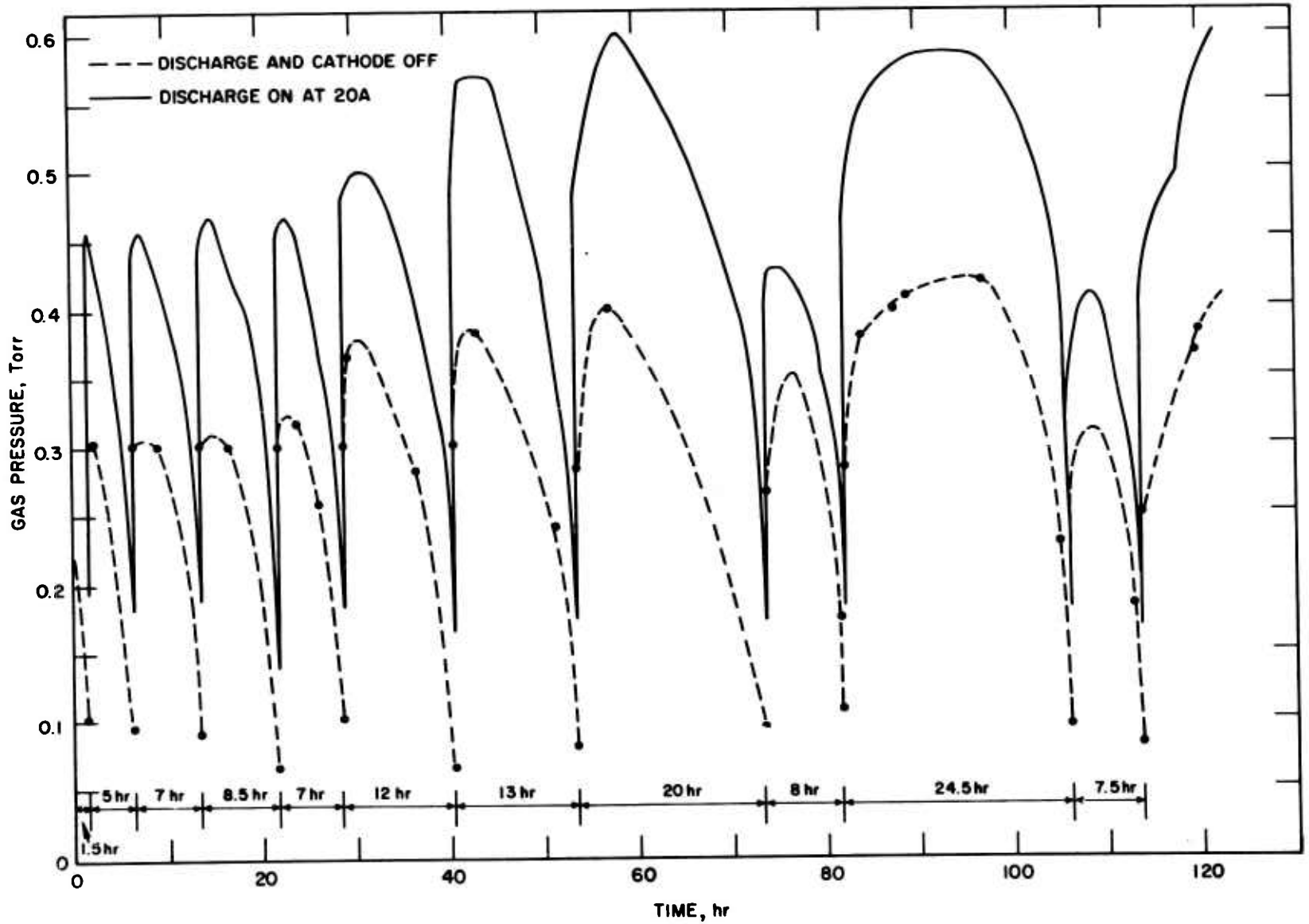

Fig. 48. Gas pressure versus time for quartz bore tube F-29 at 20 A.

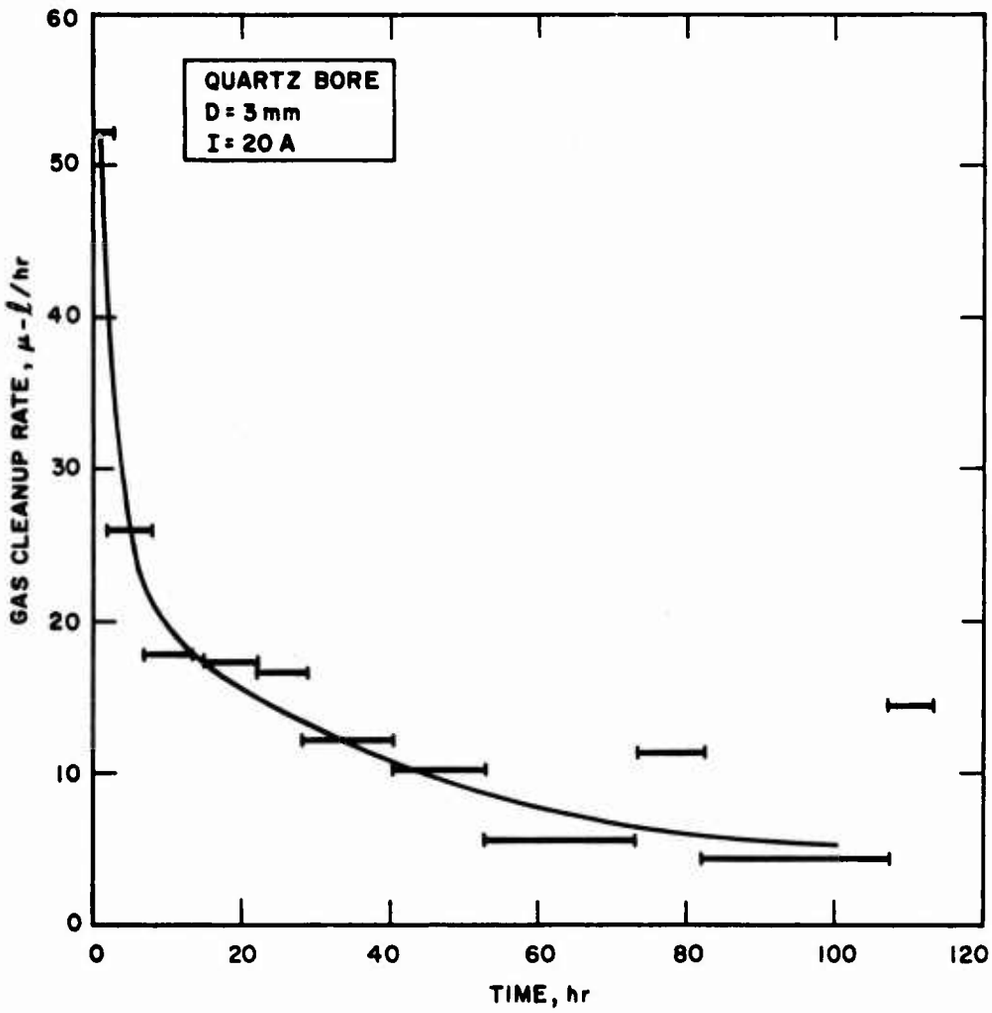

Fig. 49. Average gas cleanup rate in quartz bore tube F-29 for each gas fill as a function of total hours of tube operation.

In the past we have received reports of erratic and increasing gas pressure from other users of quartz tubes. We had not observed this behavior in tubes operated under experimental laboratory conditions, where operation was for periods of a few hours on a given gas fill. Reports of suddenly increasing gas pressure in sealed-off tubes can now, in retrospect, be accounted for by the behavior shown in Figure 48.

Operation at high gas pressures is undesirable because laser power is reduced, starting the discharge is more difficult, and the operating voltage, and therefore the input power, is higher (216 V at 0.41 Torr, compared with ~170 V at the optimum pressure for lasing).

Compounding the difficulty of maintaining the pressure in the desired range in quartz tubes is the dependence of the operating pressure on discharge current, and of the cold filling pressure on the value of discharge current at which the tube was last operated. This dependence was described in previous sections. We may summarize the basic pressure control problem by the statement that gas is absorbed in the walls at low gas pressures and low discharge currents, and released at high gas pressures and high discharge currents.

H. EVALUATION OF BERYLLIUM OXIDE (TUBE NO. B-155)

1. Description of the Material

Beryllia is a ceramic material which has a thermal conductivity seven times larger than that of high purity alumina and one-half that of copper. The high thermal conductivity, resistance to thermal shock, and good vacuum properties of this material make it an excellent candidate as a bore material. Two manufacturers have advertised argon ion lasers using BeO as a directly cooled bore material.

One disadvantage of the material at present is its relative non-availability in long length, low camber pieces. A recent survey of domestic manufacturers indicated that tubing which could meet the specification of a 90% clear bore diameter when viewed along the axis of the tube was available only up to a maximum length of 16 in. For this reason, users of BeO have had to adopt methods of joining several shorter lengths of tubing together to obtain a long, straight tube (see below). Control of the quality of the material is still not as universally good as desired. Care must be taken to select a manufacturer whose material will metallize well. Tubing which has been formed by extrusion has been found to be more subject to failure from thermal shock along planes of weakness than the isostatically pressed material (Ref. 7).

Beryllia is classed as an acutely toxic substance which, if inhaled or ingested, "may cause death or permanent injury after very short exposure to small quantities" (Ref. 8). Special facilities are therefore required for forming and grinding the material. No data have been published regarding whether toxic amounts of powdered beryllia are present in BeO discharge tubes after extended high power operation.

2. Experimental Apparatus

Two identical BeO bore samples as pictured in Figure 50 were purchased for evaluation from Monolith, Inc., Mountain View, California. The bore is formed by metallizing and brazing together three sections of tubing. (Monolith did the grinding, metallizing, and brazing of BeO stock obtained from National Beryllia Corp.) Figure 51 is a sketch showing the dimensions of the part; the uniform bore region is 0.080 in. i.d. and 10 in. long. The large diameter weld ring is welded into a water-cooled stainless steel cathode housing; a water-cooled anode is welded onto the opposite end.

Figure 52 shows the completed tube assembly with the cathode and anode assemblies attached. The coolant jacket covers the BeO bore section; the coolant flows around the double-walled cathode assembly and between the o.d. of the bore and the i.d. of the coolant jacket before emerging near the anode. The arrangement of the tube in the 12 in.-long solenoid is shown in Figure 53. A 1 liter volume ballast reservoir, getter assembly, and thermocouple gauge may be seen on the left. A 3 mm diameter external gas return path is connected from the anode window tubulation to the reservoir.

3. Operating Characteristics

The two BeO bore assemblies were ordered in September 1967 for delivery by 7 December 1967. Unfortunately, delivery was not made until 15 March 1968, which did not allow time for an extended life test.

No difficulties with outgassing from the bore material were encountered during the initial operation of the tube. The amount of contaminants observed to be released into the discharge was similar to the contaminant level observed in quartz-bore tubes. After eight short periods of operation at low discharge currents, each followed by complete evacuation of the tube, the discharge could be operated at 10 A without any sign of additional contamination. The 2 mm diameter bore tube yielded maximum power output at a magnetic field of 1.4 kG, a gas pressure of ~0.5 Torr, and an axial electric field of ~4 V/cm. These are the same values which are observed in 2 mm

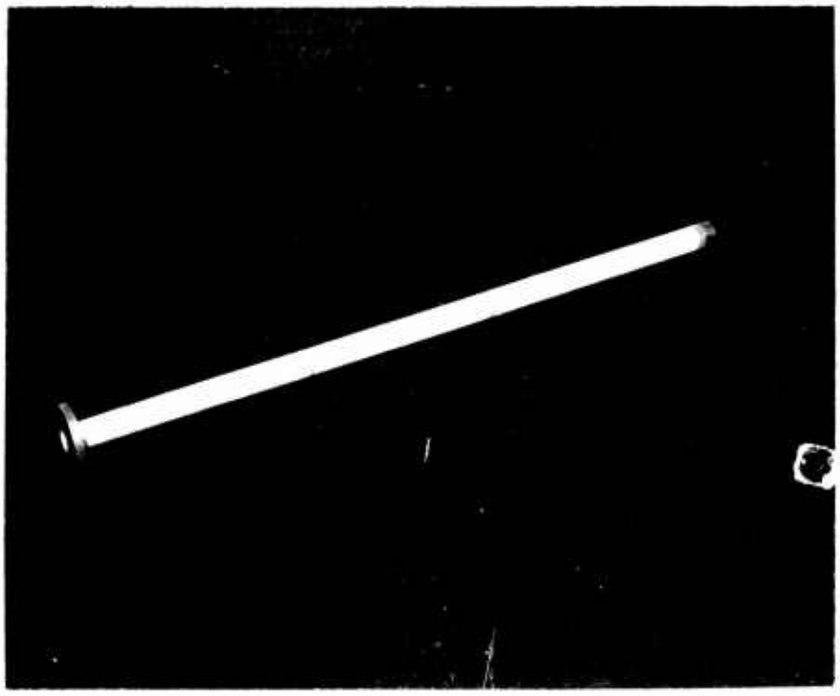

Fig. 50. BeO bore assembly with weld rings. The bore is formed from three sections of tubing which are brazed together.

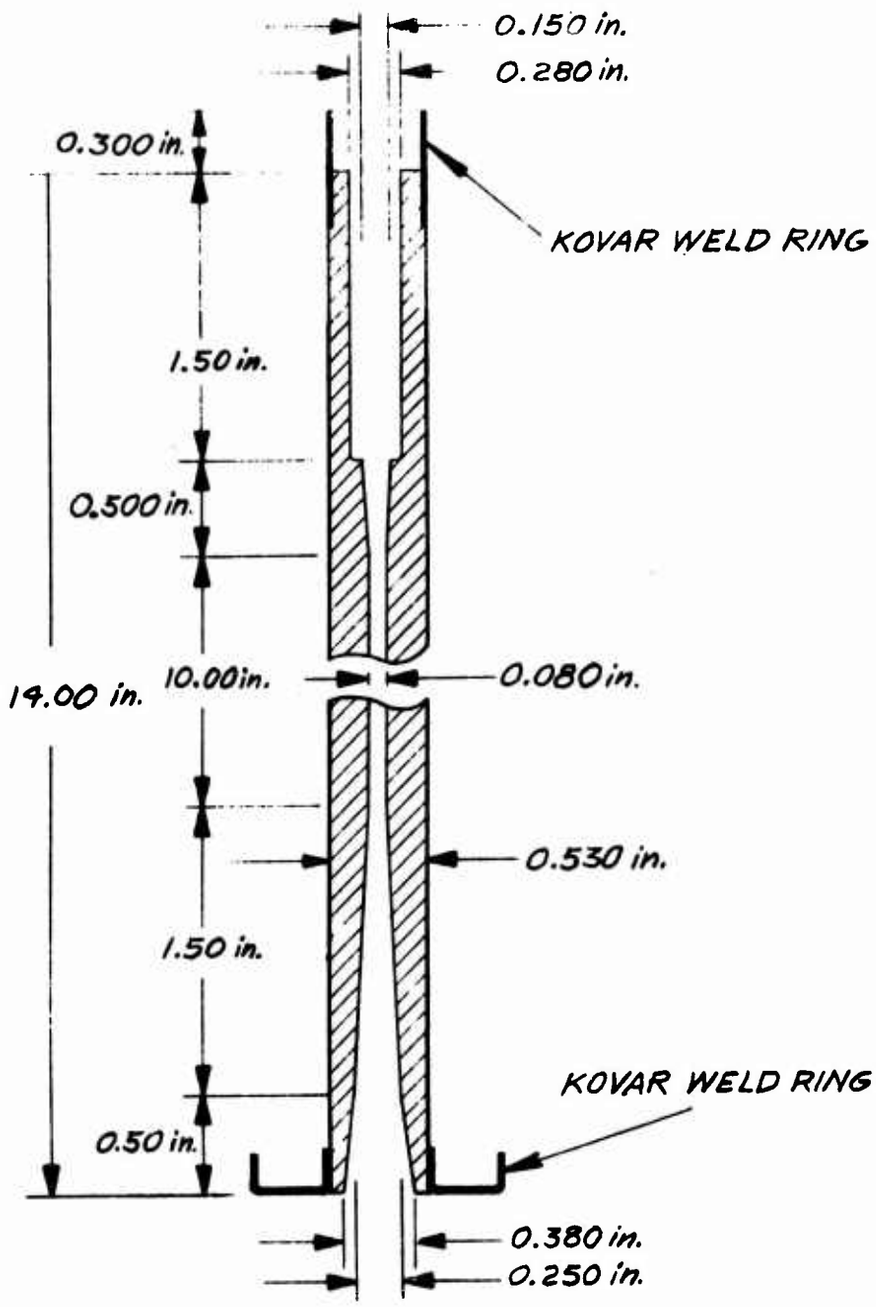

Fig. 51. Sketch showing dimensions of beryllia bore.

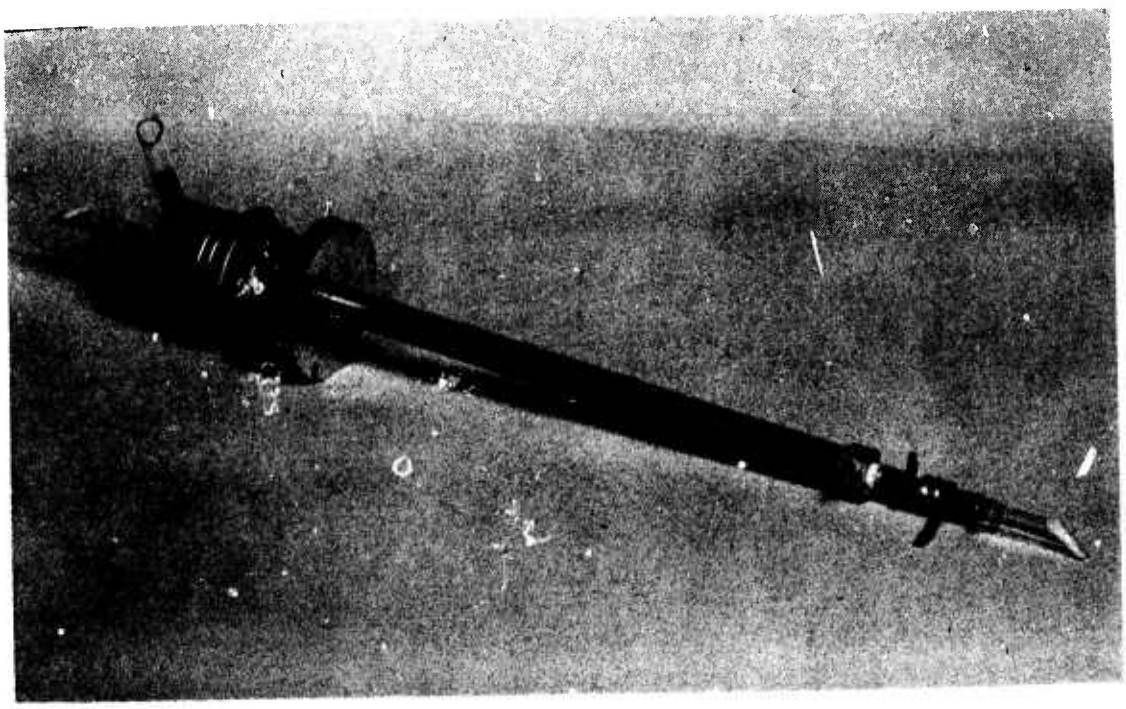

Fig. 52. BeO bore with cathode, anode, and coolant jacket assemblies in place.

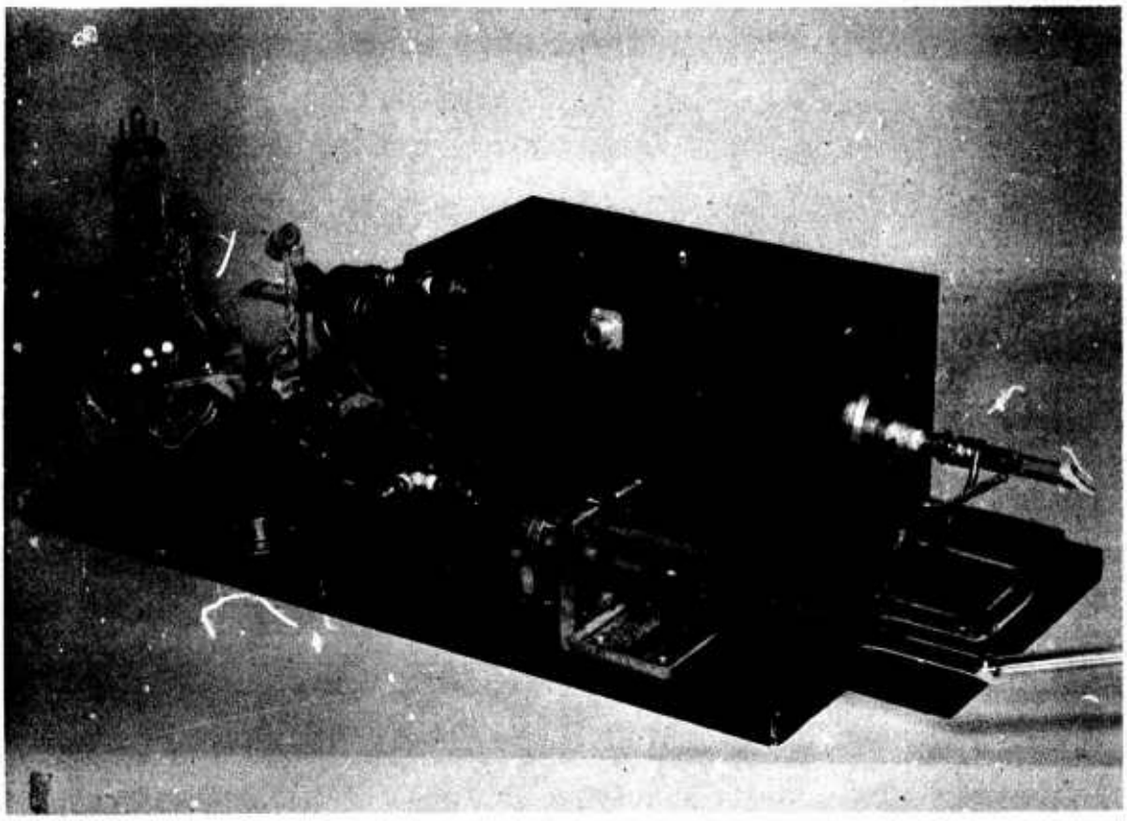

Fig. 53. Experimental arrangement for testing BeO bore tube. Reservoir getter, and thermocouple gauge tube are at left near the cathode assembly.

quartz-bore tubes, as expected. Curves of output power versus discharge current as a function of gas pressure are shown in Figure 54. At 14 A, the maximum current at which the bore was tested, the output power was 1.13 W at 138 V across the discharge tube, yielding an over-all tube efficiency of 0.059%.

The tube had been operated for approximately 5 hours when the above measurements were made. Before additional data could be gathered, failure of a ceramic-to-ceramic seal in the bore assembly terminated the test. Inspection of the bore showed that failure occurred because of electrolytic erosion of the brazed joints of the bore assembly. The conductivity of the water in the laboratory coolant system was great enough to allow electrolysis to occur between the grounded water jacket and the brazed ceramic joints. This is illustrated in Figure 55. Figure 55 (a) shows deposits on the o.d. of the joint near the cathode. The joint near the anode, which failed, is pictured in Figure 55 (b). This second joint was biased by the discharge at a higher potential with respect to ground than the joint pictured in Figure 55(a).

The vendor had originally stated that the braze joint was only made near the o.d. and was isolated from the 2 mm diameter discharge capillary. Inspection of the braze joint confirmed that the metallized joint extended all the way into the bore i.d. As shown in Figure 55(b), the braze was eroded on the i.d. by ion sputtering an on the o.d. by electrolysis.

The laser was reconstructed using the second BeO bore assembly. In order to avoid electrolysis problems, a dielectric coolant (Coolanol 25) was used to cool the bore.

The power output characteristics of the laser are shown by the solid-line curves in Figure 56. An output of 3.05 W was recorded at 24 A discharge current. The tube was not operated at higher currents in order to avoid possible damage to the bore.

Two other BeO bore assemblies identical to the bores described here were purchased for evaluation by the Electron Dynamics Division (EDD) of Hughes. One of these bores has been tested by EDD to 35 A. Experimental data recorded with this tube are plotted as the dashed line in Figure 56. At 35 A and a fill pressure of 1.3 Torr, an output of 5 W was obtained at a tube voltage of 200 V. This corresponds to an over-all tube efficiency of 0.071%. The 3.05 W output recorded at 24 A corresponds to an efficiency of 0.076%. The saturation in efficiency is caused by the increase in tube voltage with discharge current at very high current densities. The performance of this short 2 mm bore tube is very impressive. At 35 A, corresponding to a current density of $J = 1110$ A/cm^2, the linear power dissipation in the bore was 220 W/cm and the specific power output 6.25 W/cm^2.

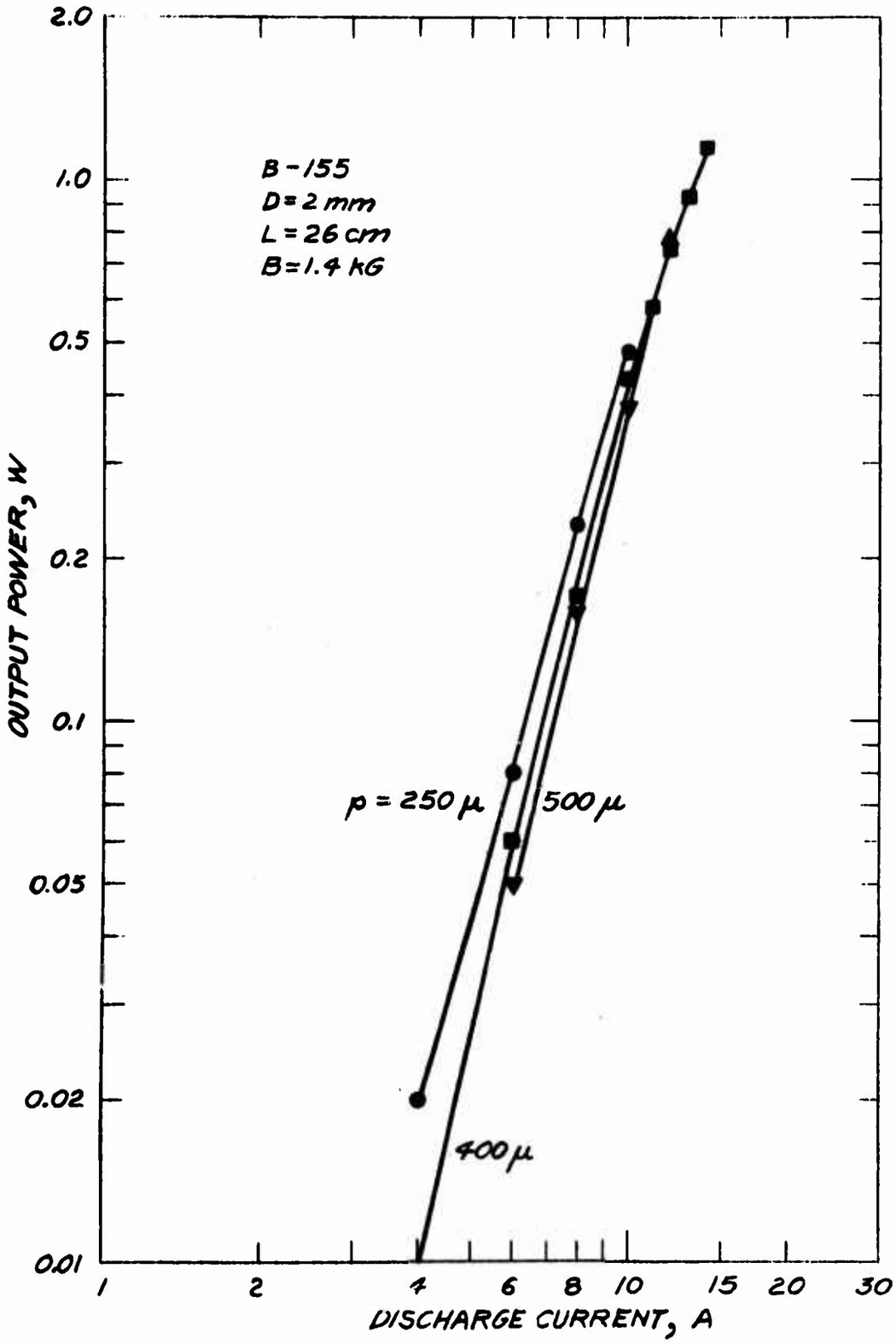

Fig. 54. Output power versus discharge current for different gas filling pressure.

(a) Joint near the cathode.

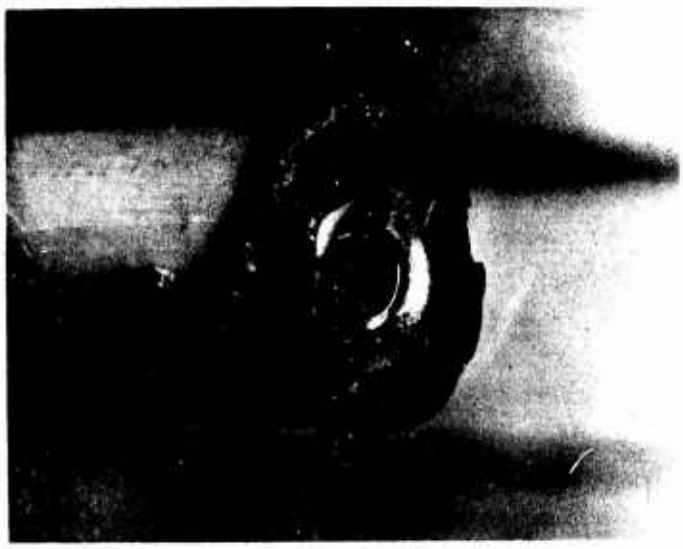

(b) Joint which failed near the anode. The braze washer originally extended from the i.d. to the o.d.

Fig. 55. Appearance of braze joints of the BeO bore assembly.

The second BeO bore tube (B-155-B) was operated to obtain life and gas cleanup data. The tube was operated at 20 A discharge current and with a 0.54 Torr gas fill while sealed off from the vacuum station. The test was terminated by burnout of the oxide cathode after 54 hours of operation (~7 hours/day for 8 days). No change in the cold gas pressure was observed during the test. Even allowing for possible drift in the thermocouple gauge tube or meter, it is clear that the gas cleanup rate was < 0.1 μ-ℓ/hour.

Following the short life test, the tube was inspected for traces of ceramic powder. The bore was flushed with alcohol and the solution collected for examination. No precipitant could be observed, and no residue remained after the alcohol was evaporated. We conclude that powdering of BeO is not a serious problem.

4. Conclusions

Two beryllia bore assemblies have been tested as laser bore capillaries. The material is very clean in vacuum and exhibited no outgassing, window contamination, or powdering. Two different bores have been tested at linear power dissipation levels in the bore of > 100 W/cm without failure.

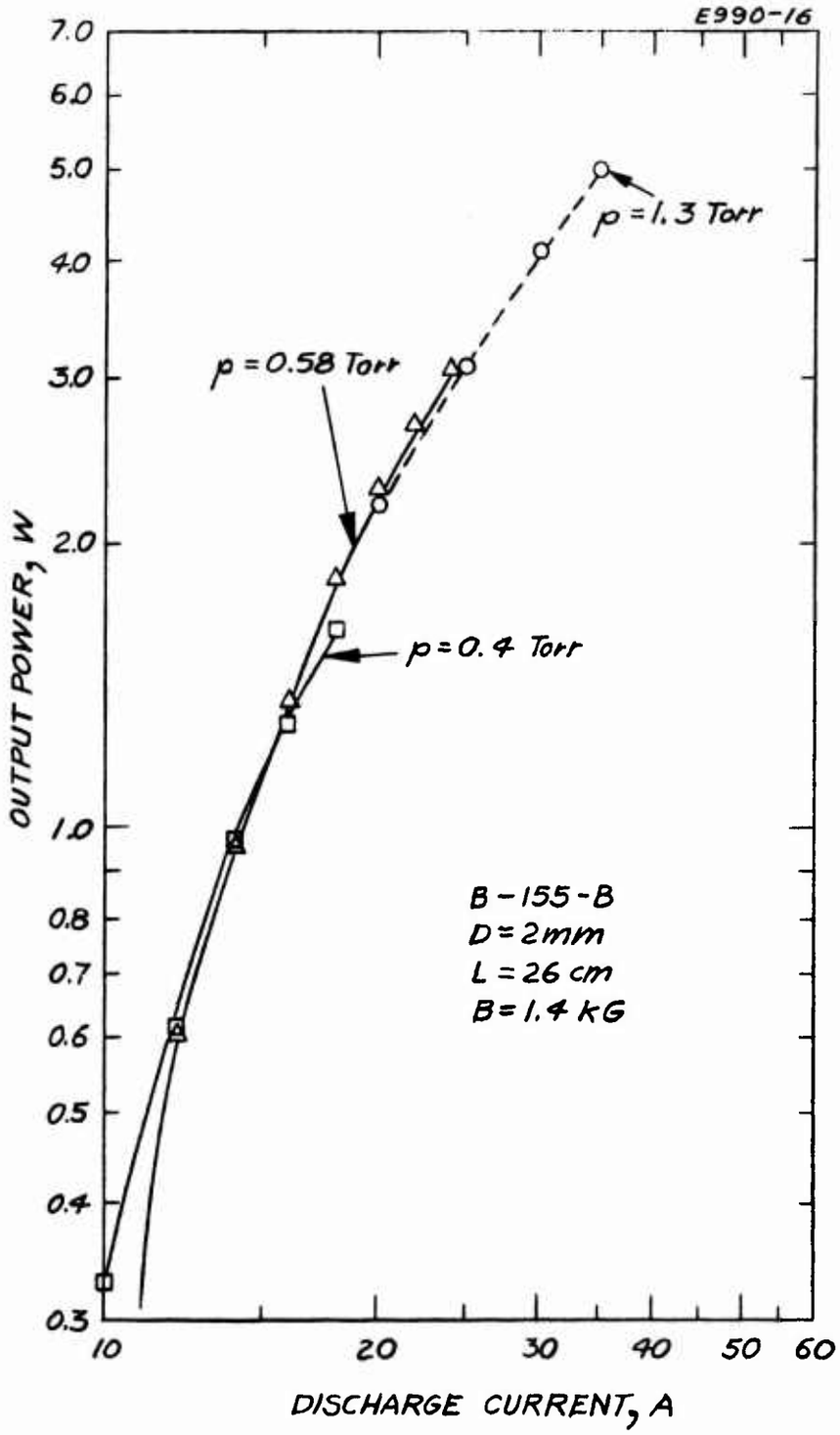

Fig. 56. Power output characteristics of the BeO bore tube at high discharge currents.

SECTION IV

EVALUATION OF DISK-BORE TUBES

The operating characteristics, durability, and heat transfer characteristics of lasers constructed using a disk-bore structure have been investigated. The efficiency and resistance to sputtering damage of this structure are the best of any laser construction method we have tested to date, and this method of tube construction is considered extremely promising. Results obtained by Parker (Ref. 9) using this tube structure have also been encouraging.

The distinction between "disk" and "segmented" bores may appear somewhat artificial, since we can vary the dimensions in order to go continuously from one to the other. By "disk bore" we will mean one in which the length of the small-diameter region is shorter than the spacing between segments; by "segmented bore" we mean one in which the length is large compared with the intersegment spacing. A typical disk bore used in this study has segments ("disks") 0.020 in. thick and 0.75 to 1.3 in. in diameter, with an interdisk spacing of 0.125 to 0.375 in.

A. EXPERIMENTS WITH A GRAPHITE-DISK TUBE (No. B-136)

1. Description of the Discharge Tube

This first experiment was designed to investigate the general characteristics of the disk configuration, e.g., the V-I characteristics, the dependence of the laser output and discharge properties on pressure and magnetic field, the degree of discharge confinement between disks, etc. A tube was assembled using a 3/4 in. i.d. quartz envelope with an external gas return path and disks made of graphite.

Details of the bore assembly are shown in Figure 57. Three ceramic rods maintain the alignment of the disks, with quartz sleeves acting as spacers. Starting from the cathode end, the 20 in. long bore consisted of (1) a "normal" tapered construction using four 1/2 in. long segments, (2) twenty-two 1/8 in. thick disks separated by a 1/4 in. gap, (3) four 1/8 in. thick segments separated by a 3/8 in. gap, (4) sixteen 1/16 in. thick disks separated by a 1/4 in. gap, and (5) an anode throat containing three 1/2 in. long segments.

During operation, the discharge between the disks could be examined through the water-cooled quartz envelope.

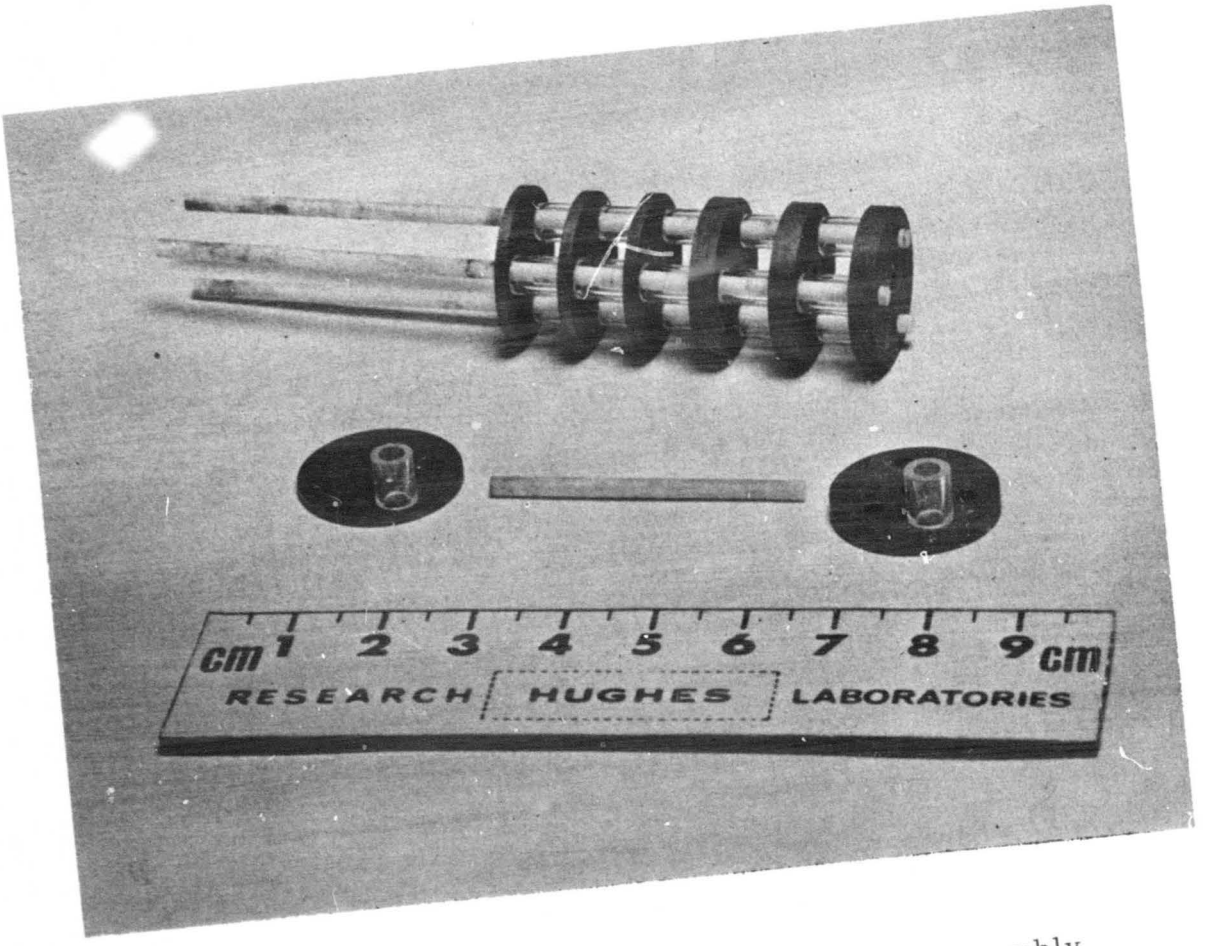

Fig. 57. Photograph of the graphite disk bore assembly.

2. Operating Characteristics

In the gaps between the disks the discharge appeared as a 3 mm diameter cylinder (the aperture diameter) emitting the intense blue Ar II spectrum, surrounded by a 2 mm thick pink glow which is characteristic of the lower energy neutral spectrum. The discharge appeared to be the same diameter in both the 3/8 in. and 1/4 in. gaps. When the axial magnetic field was decreased from 1 kG to zero, the discharge increased in diameter less than 1 mm.

The graphite-disk tube operated in the same voltage range (210 to 230 V) as long-segment tubes of the same bore length.

Curves of the power output versus current as a function of filling pressure are shown in Figure 58. The optimum pressure for a continuous-bore 3 mm tube at 20 A is approximately 0.2 Torr; the graphite-disk tube operated best at about one-half this pressure. At p = 0.1 Torr, the output power was 2.9 W at 20 A and 3.9 W at 25 A, with over-all tube efficiencies of 0.067% and 0.086%. Parametric study data on 3 mm quartz bore tubes (Ref. 1) yielded efficiencies of 0.063% and 0.075% at 20 A and 25 A. Discharge currents above 25 A could not be reached because of a discharge instability at the anode; the discharge extended through the cylindrical anode at these low pressures. This difficulty can be overcome easily by changing the anode shape and position in the magnetic field.

The dependence of the power output on magnetic field is shown in Figure 59. The optimum field clearly increases with decreasing pressure. For a continuous bore tube, B_{opt} is about 1.0 kG.

The gas cleanup rate at 20 A during 8 hours of sealed-off operation at low gas pressures averaged 20 μ-liter/hour. Since the low pressure discharge was contained by quartz walls in the cathode support arm, this high cleanup rate was probably caused by sputtering of the quartz walls rather than by processes in the graphite disk bore.

3. Interpretation of Experimental Results

It is to be expected that the discharge will remain well confined while in the gaps between the segments. The probability P_c of elastic collision between electrons and neutrals is 20 for 3 eV electrons (Ref. 10). The electron mean free path may be estimated from the relation

$$\lambda_e = \frac{1}{P_c p_o}$$

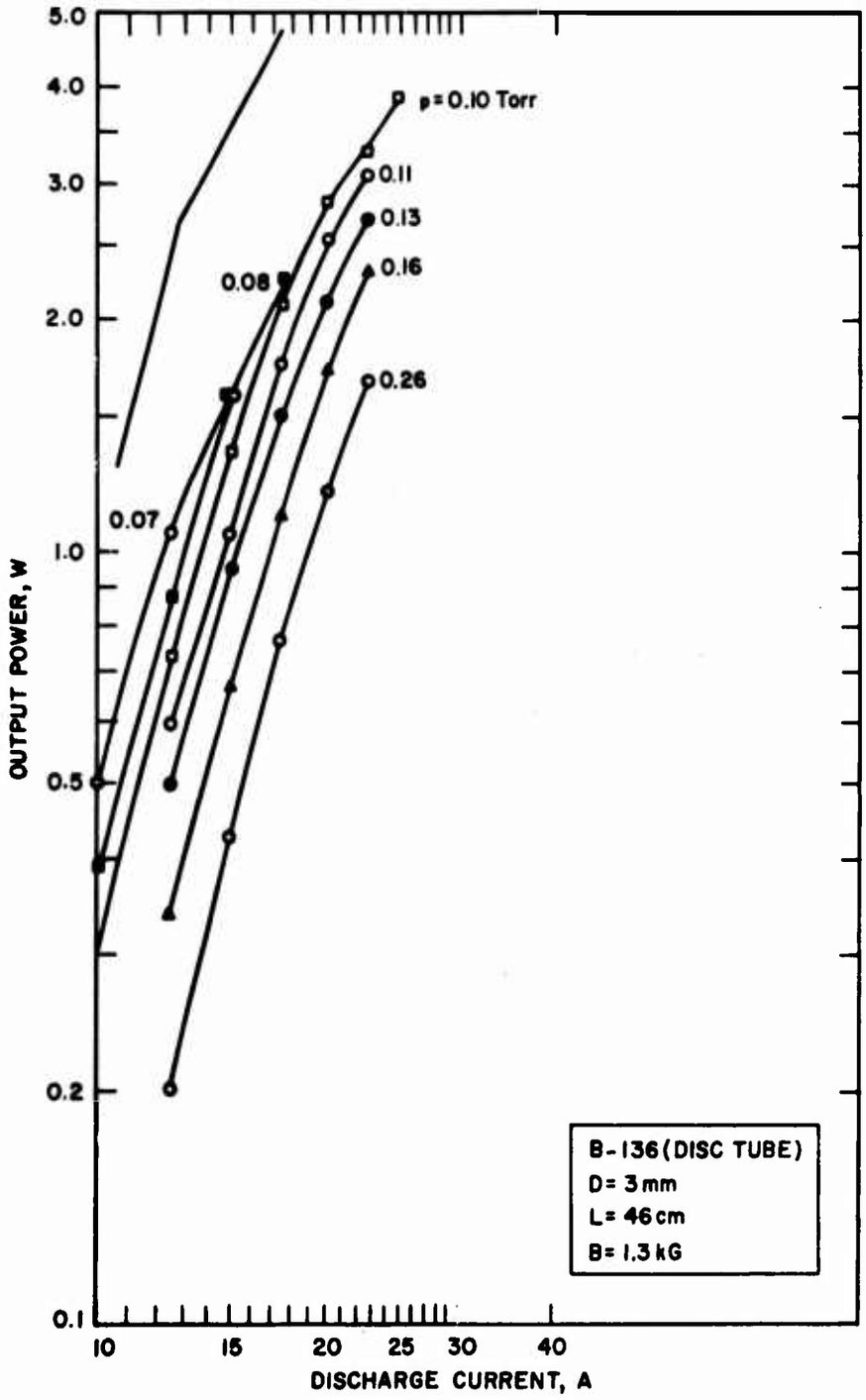

Fig. 58. Output power versus discharge current for different cold filling pressures for the disk tube.

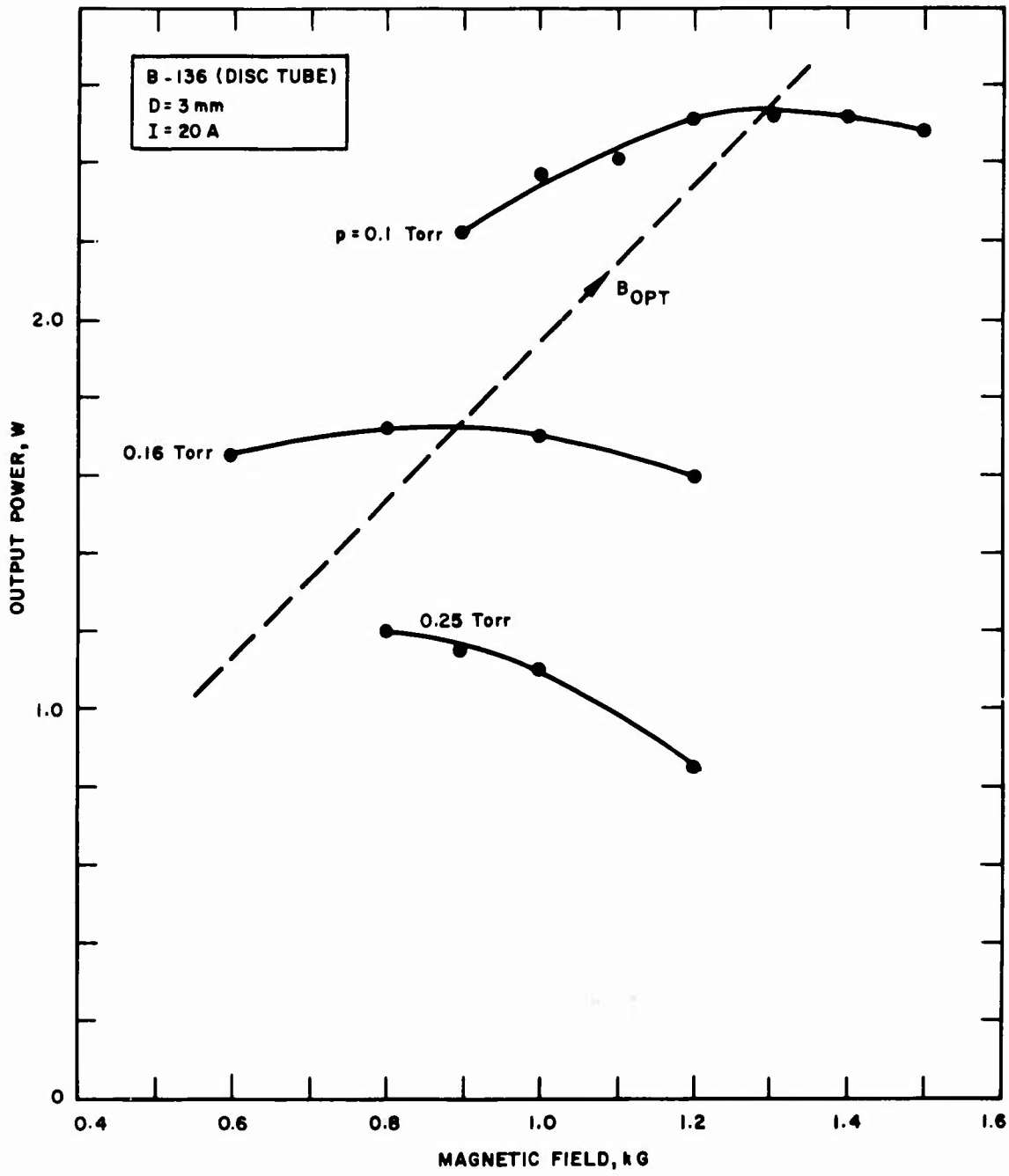

Fig. 59. Dependence of the power output on magnetic field for three different filling pressures.

where p_o is the reduced pressure. (For a discussion of the relation of p_o to filling pressure, see Section IV-B of Ref. 1. The reduced pressure represents the density of the gas in the bore after gas heating and pumpout occur.) For p_o = 0.05 Torr, λ_e = 1 cm, so that the disk spacing is less than λ_e.

The graphite-disk tube operated with roughly half the value of optimum gas pressures of continuous-bore and "long" (i.e., 1/2 in.) segment tubes. The strong dependence of magnetic field on gas pressure shown in Figure 59 also is not observed in other tubes. The characteristics of the tungsten-disk tube described in the next subsection and of three other disk tubes (subsequently constructed under different programs) are almost identical to those of quartz-bore and long-segment tubes. We have concluded, therefore, that the low gas pressure and pressure-magnetic field dependence exhibited by this tube are not characteristics of the disk-bore structure. It is more likely that they are caused by insufficient gas return path.

B. EXPERIMENTS WITH A TUNGSTEN-DISK TUBE (No. B-146)

1. Description of the Discharge Tube

A discharge tube was assembled using a 3.3 cm i.d. water-cooled quartz envelope with an external gas return path, and disks made of tungsten sheet. The 46 cm long active bore was defined by 2.3 mm diameter holes in 0.020 in. thick tungsten disks. The disks were spaced 1 cm apart by quartz spacer rings. The cathode was in line with and 1 in. away from the first segment. Photographs of the assembly in the throat and uniform bore region are shown in Figure 60.

2. Operating Characteristics

The operating characteristics of the disk-bore tube are almost identical with those of a continuous bore tube. The tube voltage fell in the usual range of 190 to 220 V, which corresponds to an axial electric field of 3.3 to 4 V/cm (assuming a 40 V drop at the electrodes and bore constrictions). The optimum magnetic field for maximum power output was 1.25 kG.

Curves of the output power as a function of discharge current for different filling pressures are shown in Figure 61. The maximum power obtained was 4.9 W at 30 A. Attempts were not made to operate at higher currents because one purpose of the experiment was to obtain extended life-test data.

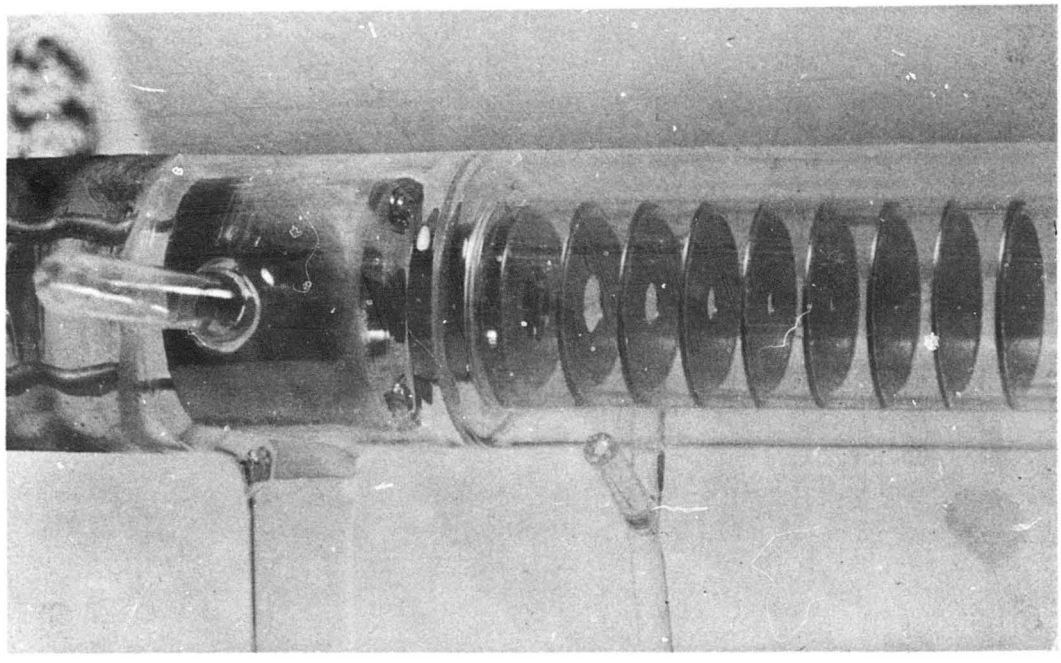

(a) Cathode throat constriction

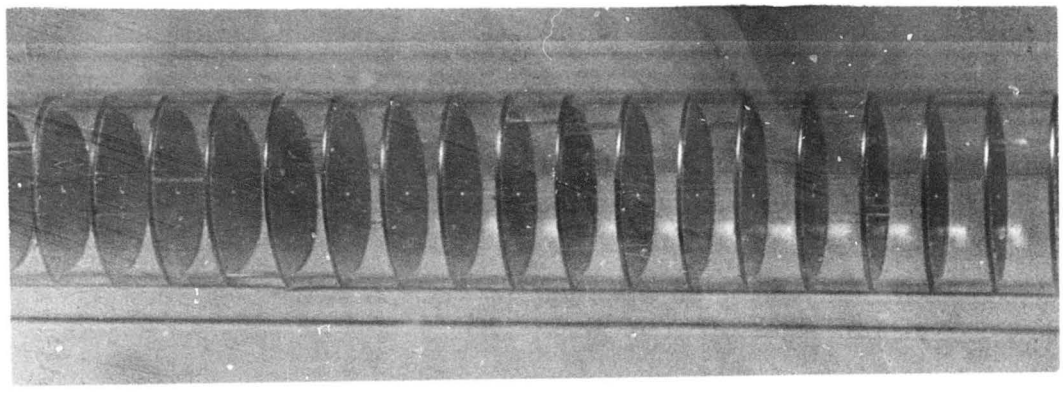

(b) Uniform bore region.

Fig. 60. Photographs of tungsten disks assembled in a quartz envelope.

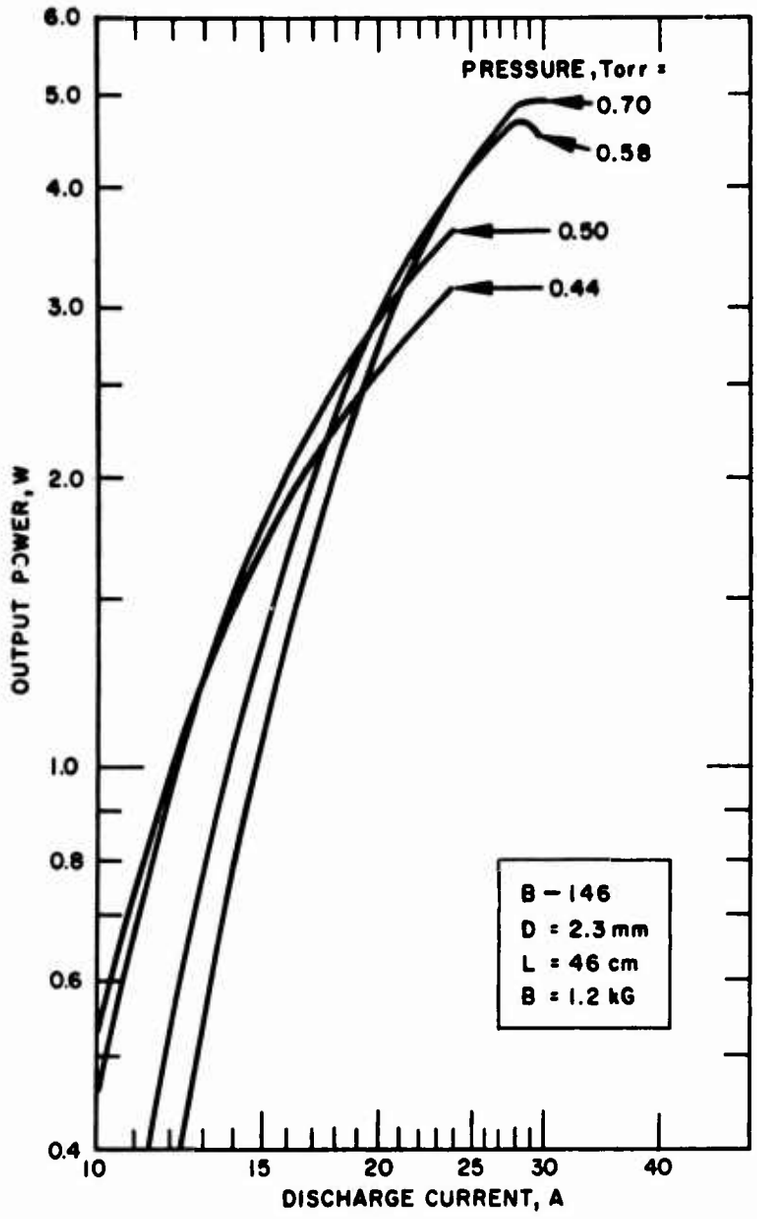

Fig. 61. Output power versus discharge current for different cold filling pressures.

As shown in Figure 61, the optimum gas filling pressure increases with increased discharge currents. This is the normal dependence which is observed in argon ion lasers. The optimum filling pressures for the 2.3 mm disk tube are the same as, or perhaps 20% higher than, those for quartz-bore tubes.

3. Life Test Data

The disk tube was operated on life test for 517 hours at 20 A. A gas cleanup rate of 0.5 μ-liter/hour was measured during the last 300 hours of the life test. However, this value is suspect because of the presence of a very slow leak in the vacuum envelope. The leak was from the water jacket or water-cooled anode into the tube, and strong hydrogen lines could be observed spectroscopically in the discharge.

Figure 62 shows photographs of the tube envelope at the end of test. The tungsten films on the walls were partially transparent, indicative of a film thickness of 200 to 500 Å. The film did not appear to be sputtered material; it was of approximately uniform thickness between the segments, and a blue-black film existed adjacent to the segments and behind the quartz spacer rings.

The formation of the wall films and the appearance of the segments themselves may be explained by the chemical reaction of the hot tungsten disks with the water vapor from the leak. The chemical transport of tungsten from a hot surface to a cold surface in the presence of water vapor is, in fact, the classic method used to refine tungsten. Hot tungsten at temperatures greater than 500°C reacts with water vapor to form WO_3 by the process

$$W + 3H_2O \rightleftarrows WO_3 + 3H_2,$$

liberating H_2 into the discharge. WO_3 has a high vapor pressure and evaporates from the hot disks, depositing onto the cold tube walls. Tungsten is then formed on the cold walls by the reduction of WO_3 by H_2, the above reaction being driven from right to left at temperatures < 400°C. Tungsten is thus transported chemically from the disks to the walls. Right at the segments, where the wall is hottest, WO_3 is reduced to the blue-black oxide W_4O_{11} instead of to W.

Photographs of a typical tungsten disk at the end of test are shown in Figure 63. The chemical etching of the tungsten surface may be seen near the bore aperture where the tungsten was hottest (~ 1150°C).

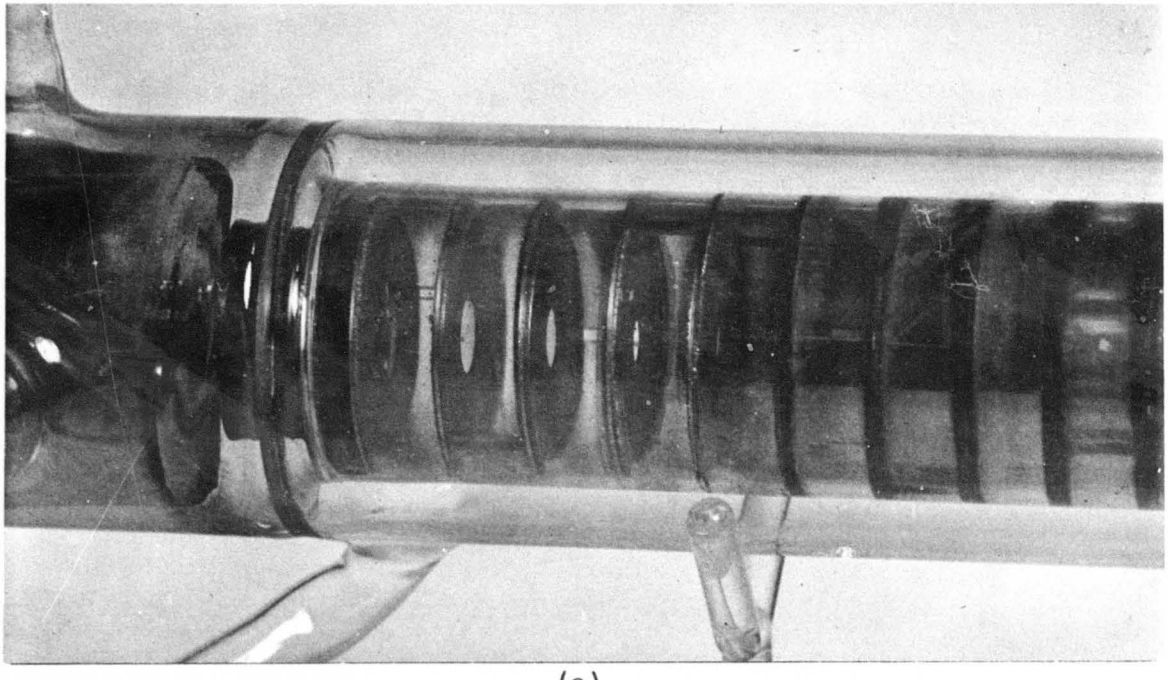

(a)

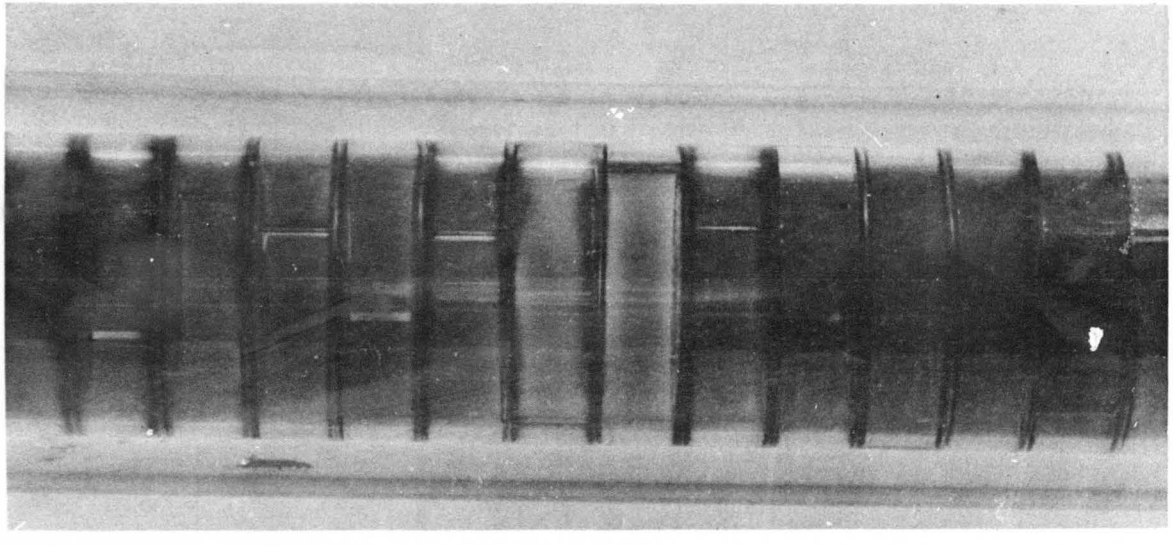

(b)

Fig. 62. Appearance of disk structure after 517 hours of operation. (a) Cathode throat constriction. (b) Uniform bore region. The tungsten coating on the walls is partially transparent.

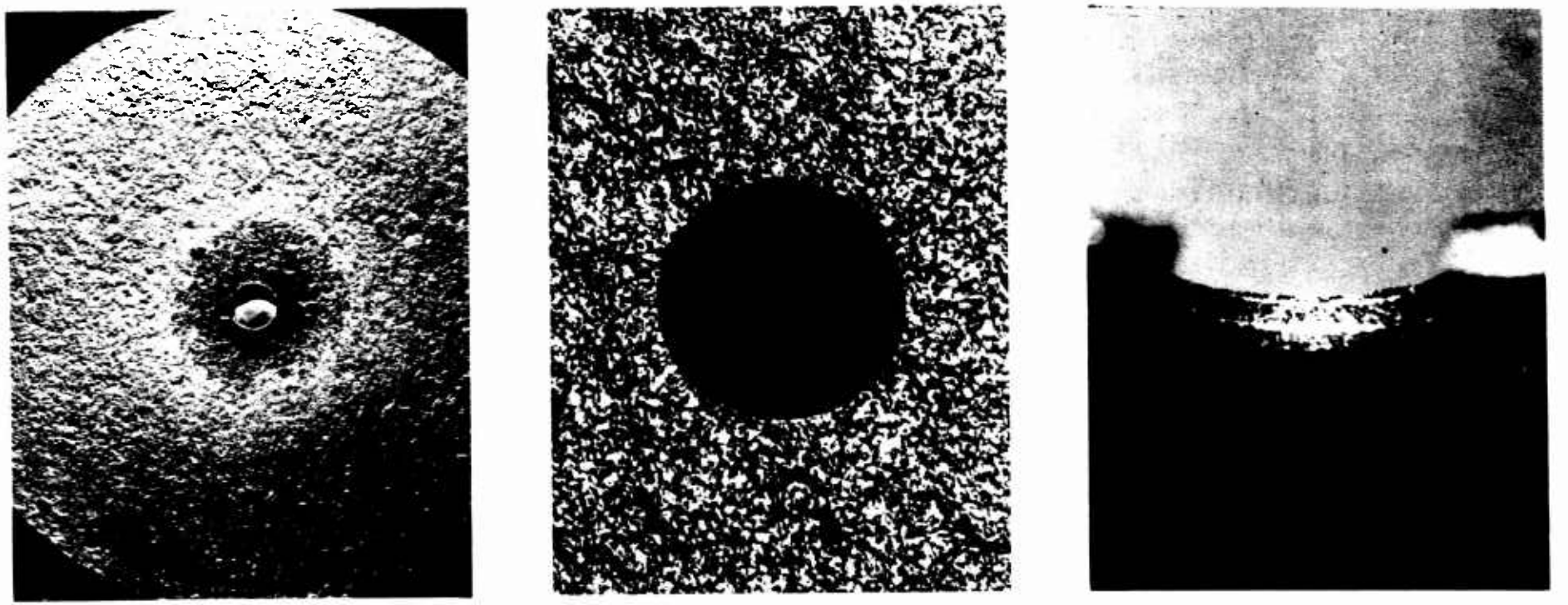

(a) (b) (c)

Fig. 63. Photographs of a tungsten disk. (a) Chemical etching around bore. (b) Detail of bore showing clean hole. (c) Side view showing sharp corners and original machining marks.

Figures 63(b) and (c) illustrate the sharp edges of the bore aperture. Gauging and inspection of all the segments in the tube failed to show any sign of sputtering damage after 520 hours at 20 A ($J \approx 500$ A/cm^2).

C. ADDITIONAL TEST RESULTS WITH TUNGSTEN DISK-BORE TUBES

The operating characteristics, resistance to erosion, and large heat dissipation capability exhibited by the tungsten disk-bore structure make this method of bore construction very attractive. Powdering of the bore material is obviously not a problem. Additional work to develop a compact rugged tungsten bore structure has been carried out under company and other government funded programs. To date, metal-ceramic envelope lasers employing a tungsten disk bore have been fabricated for four different programs.

The output power characteristics of a 2.5 mm aperture tungsten disk tube* are shown in Figure 64. The tube had a uniform bore length of 46 cm and an over-all tube length of 82 cm. Multiline outputs of 3.6 W at 20 A and 4.9 W at 25 A were obtained at tube voltages of 193 and 197 V, respectively. These values correspond to an over-all tube efficiency of 0.093% and 0.10%, respectively.

The efficiency at comparable power levels in larger-aperture tubes is greater than 0.1%. The over-all tube efficiency of a 2.8 mm aperture tungsten disk tube is plotted in Figure 65. Extensive measurements made during the previous contract on quartz-bore tubes have shown that the efficiency of small bore tubes (2 to 4 mm diameter) saturates at a value of < 0.09% (see Section III-B of Ref. 1). The higher efficiency of the disk-bore structure and the continuing increase in efficiency with increasing discharge current (provided the optimum gas pressure is maintained) are important assets of the disk-bore structure.

Under another program, we have been able to run 55 A discharge current through a 2 mm bore tungsten disk tube; the specific power input to the bore region was approximately 400 W/cm steady state, with no noticeable damage to the tungsten disks.

The spacing between adjacent disks does not appear to be a critical parameter affecting laser performance; structures with a spacing as small as 1/16 in. and as large as 3/8 in. between disks

*Delivered to NASA under Contract NAS 8-20806.

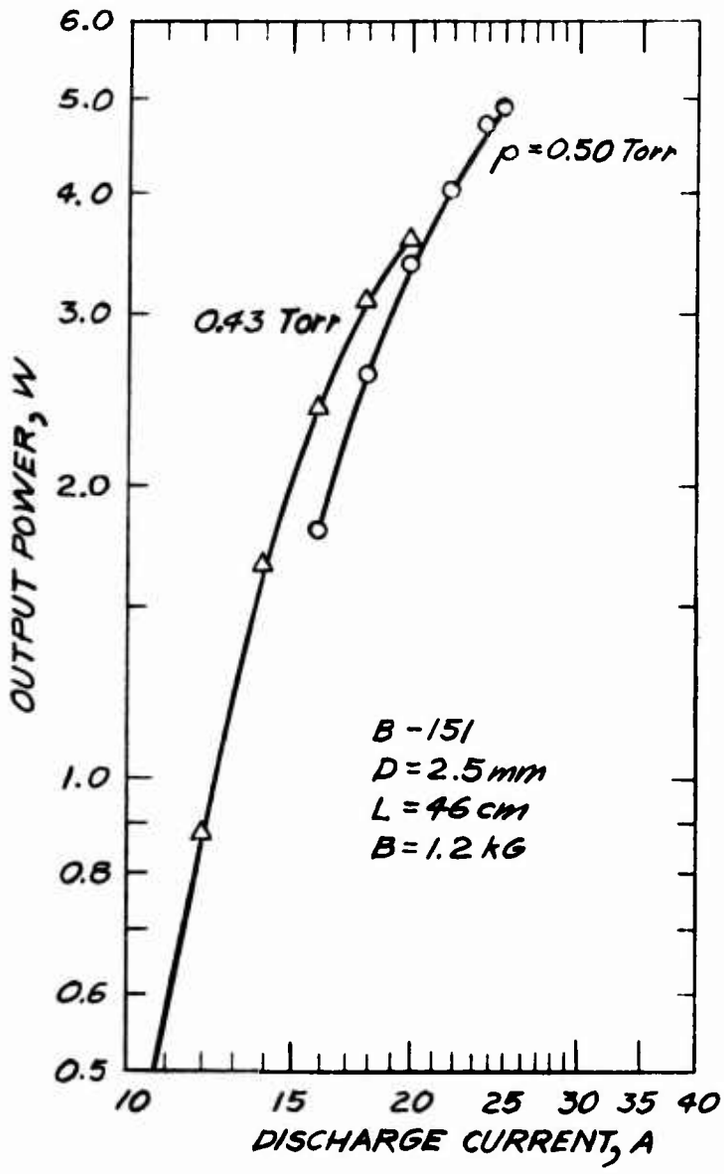

Fig. 64. Output power characteristics of a 2.5 mm aperture tungsten disk tube.

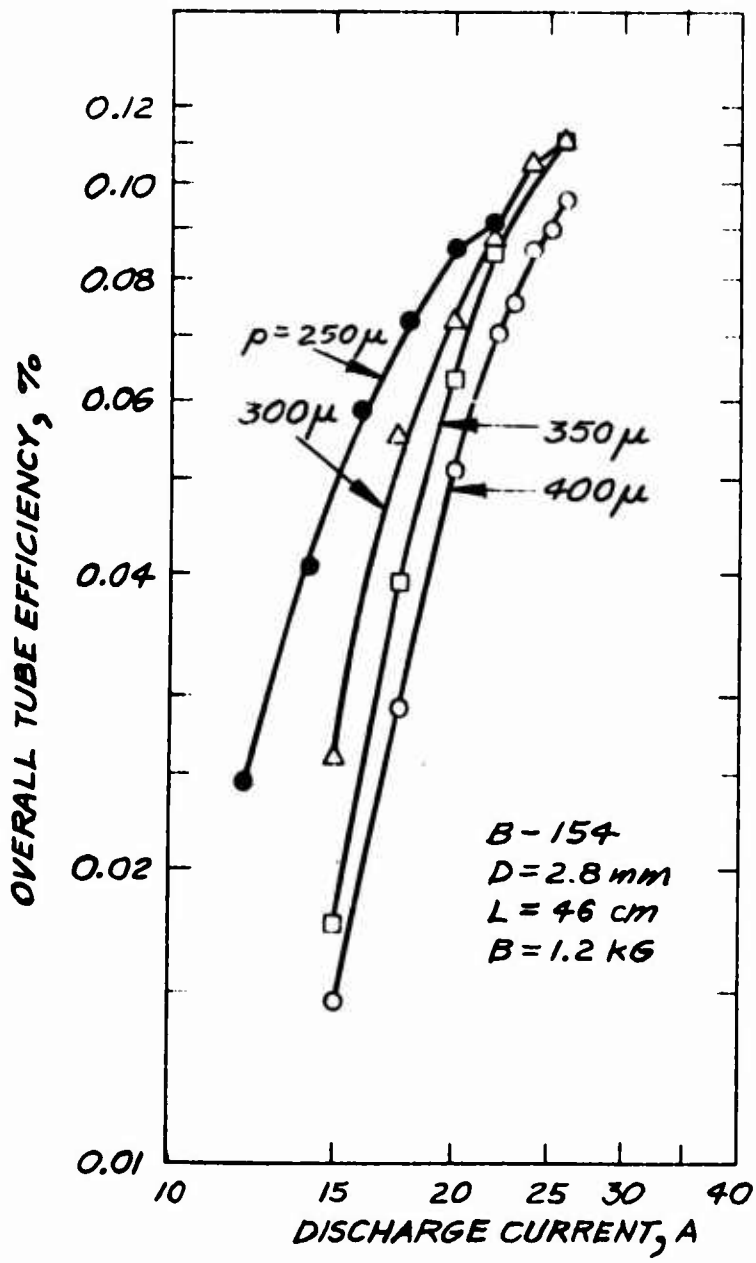

Fig. 65. Over-all tube efficiency versus discharge current at different gas filling pressures for a 2.8 mm aperture tungsten disk tube.

have been made with no noticeable effect on confinement or efficiency of the arc. However, the operating temperature of the radiation-cooled disk structure is strongly dependent on the disk spacing. For example, if the average power dissipation in the uniform bore region is 200 W/cm, this power will be divided evenly among the number of disks per centimeter of bore length. In order to predict the operating temperature of the disks in a given configuration, the heat transfer characteristics of the disk structure have been analyzed as a function of disk diameter, spacing, and emissivity. This analysis is presented in Appendix I.

SECTION V

PERIODIC PERMANENT MAGNET STUDIES

Periodic permanent magnet (PPM) structures have been used successfully for the focusing of electron beams in vacuum devices and have several advantages over solenoids. They weigh substantially less, eliminate the need for a power supply, and require no cooling. Because of these advantages, we have investigated the practicability of replacing the solenoid around the argon ion laser with a periodic permanent magnet stack.

In the following sections a brief development of the theory and the pertinent parameters associated with periodic permanent magnet design will be presented. The problem of electron loss to the wall at the magnetic field reversals is discussed.

In Section V-B, the design of an experimental laser tube utilizing coaxial gas return and water cooling paths is described. The design of this tube allowed comparative measurements of tube performance to be made, using a normal solenoid and then a PPM stack. Axial magnetic probe measurements were made for the solenoid and for various periodic permanent magnet stacks. Laser operation employing a periodic permanent magnet field is compared with that using conventional solenoidal fields. The problem of bore erosion associated with the field reversals of the PPM assembly is discussed.

A. THEORETICAL CONSIDERATIONS

In this section the relations which determine the axial magnetic fields within a periodic permanent magnet stack are outlined briefly. The high particle loss rate characteristic of cusped magnetic field geometry is considered and the pertinent design parameters for optimum laser operation are discussed.

1. Periodic Permanent Magnet Characteristics

Figure 66 is a diagram of a typical periodic permanent magnet assembly which consists of ring shaped magnets separated by thin shims at the field reversals. The magnetic rings are made of a high coercive force magnetic material, magnetized axially. Magnetic rings within a given section are aligned with the field in the same direction. Adjacent

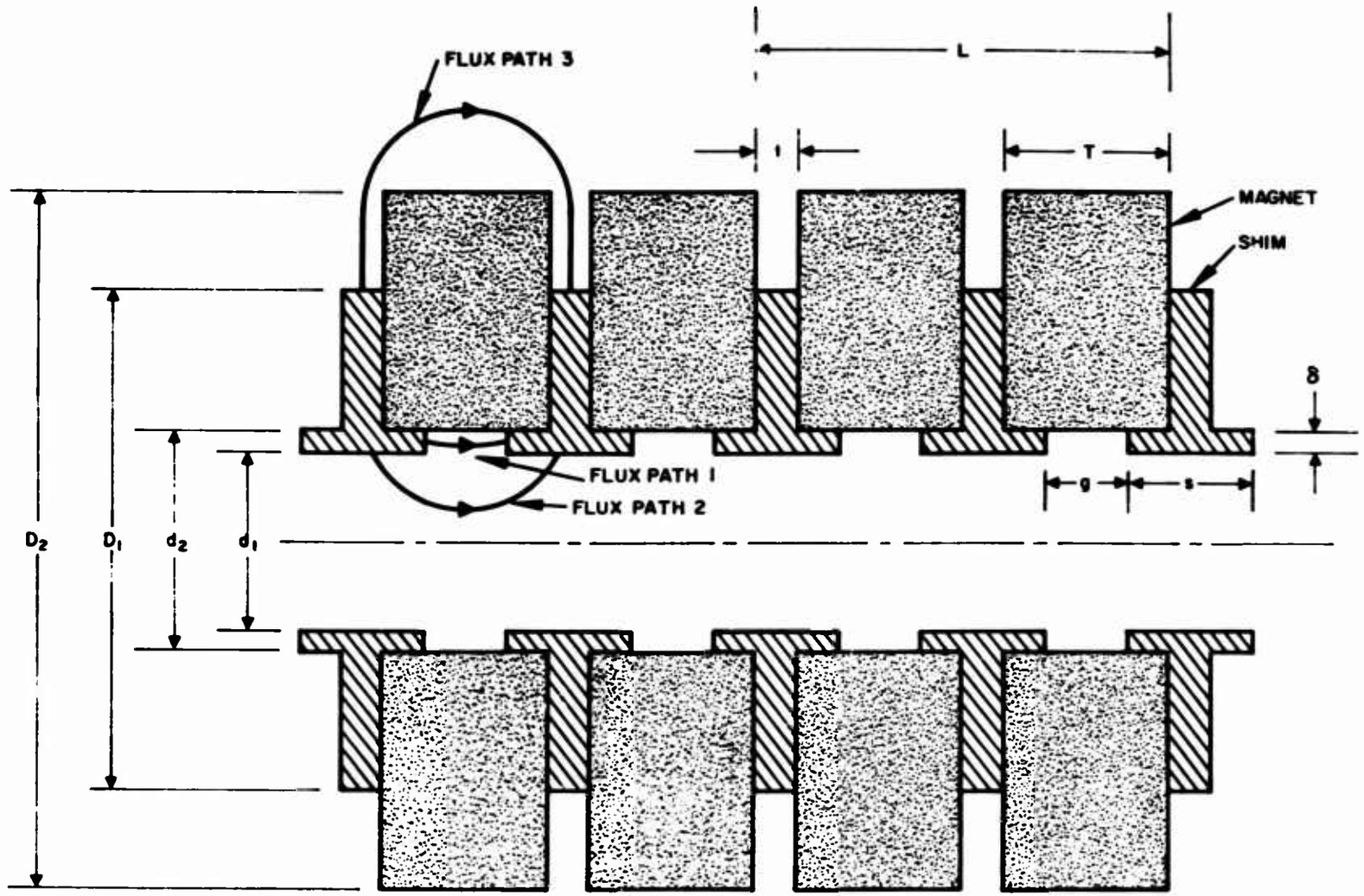

Fig. 66. Schematic diagram of a periodic permanent magnet assembly.

magnetic sections, which are separated by magnetic shims, are polarized in opposite directions. The shims are made of a high-permeability material which serves to reduce the permeance of the flux paths between adjacent magnetic sections. As indicated in Figure 66 the magnetic rings have an o.d. denoted by D_2, an i.d. denoted by d_2, and a thickness T. The parameters D_1, d_1, t_1, s, and δ denote the o.d., i.d., shim thickness, shoe length, and shoe thickness of the magnetic shims.

The design of a permanent magnet structure involves a rather complicated tradeoff among the dimensions of the magnets and shims and the properties of the magnetic material. The magnetic properties are summarized in the B versus H magnetization curve for the material. The operating point on this on the curve is selected by the magnetic permeance of the magnetic circuit, as discussed below.

In the region $0 \leq r \leq d_1/2$, the magnetic field can be expressed in series form (Ref. 11)

$$B_z(z, r) = \sum_{m=1}^{\infty} \frac{4B_g \sin\left(\frac{n\pi g}{L}\right)}{I_o\left(\frac{n\pi d_1}{L}\right) n\pi} I_o\left(\frac{2n\pi r}{L}\right) \cos\left(\frac{2n\pi z}{L}\right) . \qquad (3)$$

where the radial variation is described by the zero order modified Bessel function of the first kind, I_o, and the axial variation is cosinusoidal. B_g is the flux density in the region of the air gap and is related to the magnetic intensity H_d in the magnetic material by

$$B_g g = H_d T \qquad (4)$$

where g is the air gap length and T is the thickness of the magnetic ring. The period of the magnetic field variation in the Z direction is denoted by L where

$$L = 2(T + t) . \qquad (5)$$

The maximum magnetic field on the axis of the magnet structure is, from (3),

$$B_m = \frac{H_d T}{g} \sum_{n=1,3,5}^{\infty} \frac{1}{m} \frac{4}{\pi I_o\left(\frac{\pi n d_1}{L}\right)} \sin\left(\frac{n\pi g}{L}\right) . \tag{6}$$

In most cases terms for which $n > 1$ are very small compared with the first order term and can be neglected. From Eq. (6), to obtain a large value of B_m one desires to design a magnetic circuit which gives an operating point on the magnetization curve with a large value of H_d.

In order to determine the value of H_d, the magnetic intensity within the magnetic material, it is necessary to evaluate the total permeance P_T of the three external flux paths shown in Figure 66.

$$P_T = P_1 + P_2 + P_3 \tag{7}$$

where

$$P_1 = \frac{0.785\left(d_2^2 - d_1^2\right)}{g} , \tag{8}$$

$$P_2 = \sum_{n=1,3,5}^{\infty} \frac{L d_1}{n^2 g} \frac{2}{\pi} \left[\frac{I_1\left(\frac{n\pi d_1}{L}\right)}{I_o\left(\frac{n\pi d_1}{L}\right)}\right] \sin\left(\frac{n\pi g}{L}\right) , \tag{9}$$

where I_1 is the first order modified Bessel function of the first kind, and

$$P_3 = \sum_{n=1,3,5}^{\infty} \frac{L D_2}{T n^2} \frac{2}{\pi} \left[\frac{K_1\left(\frac{n\pi D_2}{L}\right)}{K_o\left(\frac{n\pi D_2}{L}\right)}\right] \sin\left(\frac{n\pi T}{L}\right) , \tag{10}$$

where K_1 and K_o are the first and zero order modified Bessel functions of the second kind. From the basic relation for the magnetic circuit that

$$\frac{B_d}{H_d} = - \frac{T}{A'} P_T , \tag{11}$$

where A' is the cross-sectional area of the magnets, it is apparent that in order to maximize H_d, the total permeance P_T must be minimized. The value of H_d can be obtained from the demagnetization characteristics of the magnetic material (B_d versus H_d) and (11).

In designing a PPM assembly for a particular application, several parameters must be considered. In order to minimize the volume and hence the weight of the magnet assembly, the i.d. of the shims d_1 should be as small as possible. Furthermore, the permeance P_2 expressed by (9) decreases with decreasing d_1, thereby increasing the axial magnetic field. For a given value of H_d, the required magnetic field is obtainable in a magnetic assembly of minimum volume when a magnetic material of high coercive force is used. Ceramic magnetic materials having the approximate composition $BaFe_{12}O_{19}$ (such as Indox and Genox) are ideally suited for periodic permanent magnets because of their high coercive force demagnetization characteristics. The thickness of the shoe of the shim $(d_2 - d_1)/2$ should be as small as possible without saturating in order to minimize the permeance P_1 expressed by (8). Likewise, the shim thickness t of the pole piece should be as thin as possible to minimize the permeance P_3 expressed by (10). Consequently, the shim material must have a high magnetic permeability at high magnetic flux densities; soft iron is commonly used for pole piece construction.

The choice of d_1 is obviously limited by the outside diameter of the discharge tube. The magnetic properties of the shim material determine δ and t. The values of B_m and L are governed by the plasma conditions required for optimum laser operation. Once these parameters have been determined, the outside diameter D_2 and the air gap g can be calculated for the particular magnetic material being used.

2. Charged Particle Losses in a Cusp Geometry

A magnetic field reversal exists at each pole piece in the periodic permanent magnet stack. The most serious disadvantage of a cusped

magnetic field configuration is the high charged particle loss rate in the region of the cusps. Assuming no collisions, the total kinetic energy of a charged particle moving in a magnetic field is an invariant.

$$W_T = W_{||} + W_{\perp} \tag{12}$$

where W_T, $W_{||}$, and $W_{\perp}$ denote the total energy, parallel energy component, and perpendicular energy component with respect to the magnetic field. Consider two locations a and b in the magnetic field configuration shown in Figure 67. From this energy invariance

$$W_{\perp_a} + W_{||_a} = W_{\perp_b} + W_{||_b} . \tag{13}$$

For a charged particle moving in a magnetic field, the quantity $W_{\perp}/B$ is an adiabatic invariant. (See, for example, Ref. 12.) We may therefore write for the particle at locations a and b

$$\frac{W_{\perp_a}}{B_a} = \frac{W_{\perp_b}}{B_b} . \tag{14}$$

Using the previous two equations, we obtain

$$W_{||_b} = W_{||_a} - W_{\perp_a}\left(\frac{B_b}{B_a} - 1\right) . \tag{15}$$

Therefore, if $B_b > B_a$, the velocity component along the field lines will be reduced. Furthermore, the longitudinal motion of the particle along the field lines will be stopped and the particle turned back if

$$\frac{W_T}{W_{\perp_a}} < \frac{B_b}{B_a} . \tag{16}$$

In this case no charged particle loss will result. Hence, only the very energetic particles escape if the mirror ratio $B_b/B_a \gg 1$.

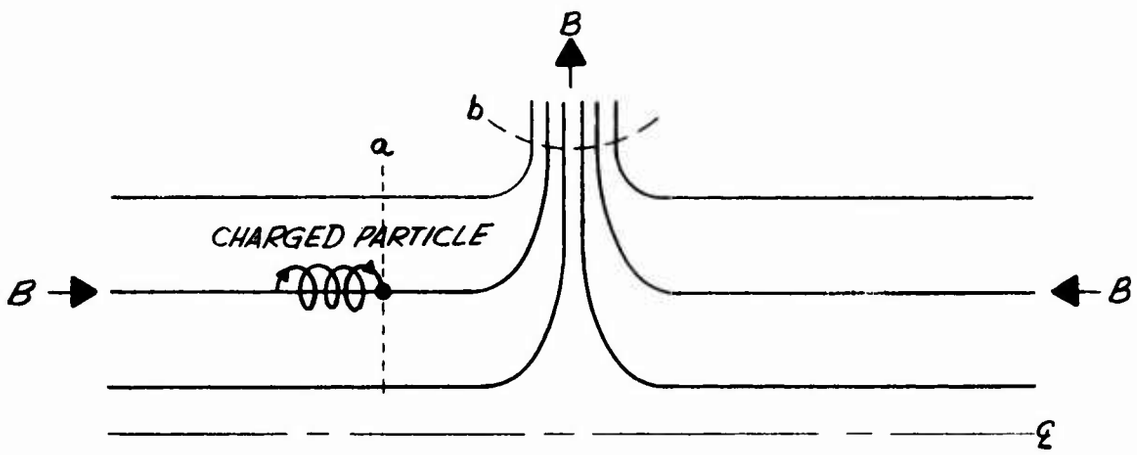

Fig. 67. Trajectory of a charged particle in a magnetic cusp at a field reversal.

B. EXPERIMENTAL CONSIDERATIONS

1. Laser Tube Design

A special discharge tube was fabricated which could be inserted both into various small-diameter permanent magnet assemblies and into a conventional solenoid without opening the vacuum envelope. The complete discharge tube is shown in Figure 68; a PPM assembly is in the foreground. The tube had a 28 cm long, 2 mm bore. Special provisions were made to provide a coolant path and external gas return path within a 0.6 in. over-all o.d. of the tube. The bore coolant was extracted from the coolant jacket through a small hole near the anode. A removable brass sleeve with two O-rings, which may be seen in Figure 68, was positioned over the hole after the PPM stack was in place to connect the coolant jacket and the external line. A radiation-cooled molybdenum anode was employed, the surface of which was sand-blasted to improve its emissivity. Electrical contact was made to the anode by two platinum wires welded to a Kovar ring, as shown in Figure 69. The water coolant outlet hole in the outer wall appears just to the right of the anode.

The external gas return path was constructed as a cylindrical path surrounding the coolant jacket. The connection from the bore through the water jacket to the triaxial gas return path may be seen in Figure 69. The complete tube assembly with magnets in place is shown in Figure 70.

2. Periodic Permanent Magnets and Solenoid

Permanent magnets were used which consist of 1/4 in. thick Indox rings with a 3 in. o.d. and a 0.7 in. i.d. Soft iron pole pieces having a 2.5 in. o.d., 0.625 in. i.d., with a 0.080 in. thick, 0.60 in. long shoe, were used at the field reversals.

A periodic permanent magnet stack with a period of L = 3.58 in. and an over-all length of 12 in. is shown in Figures 70 and 71. Each section consisted of seven Indox rings. A plot of the axial magnetic field within the structure is shown in Figure 72. Only the variation in the first 7 in. of the assembly is plotted. The peak axial magnetic field was approximately 1100 G.

For comparison, Figures 73 and 74 show the axial magnetic field variation for structures with periods of 0.58 in. and 5.58 in. Note the higher values of peak magnetic field and the more rapid field reversal which occur as the period is shortened.

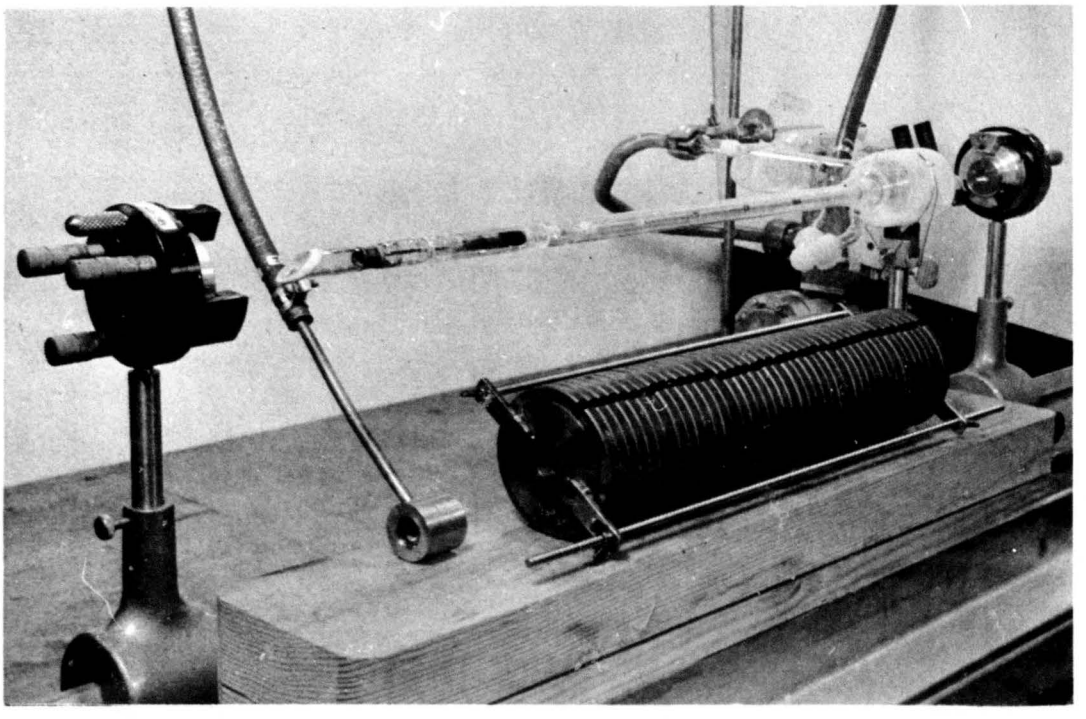

Fig. 68. Disassembled PPM laser system.

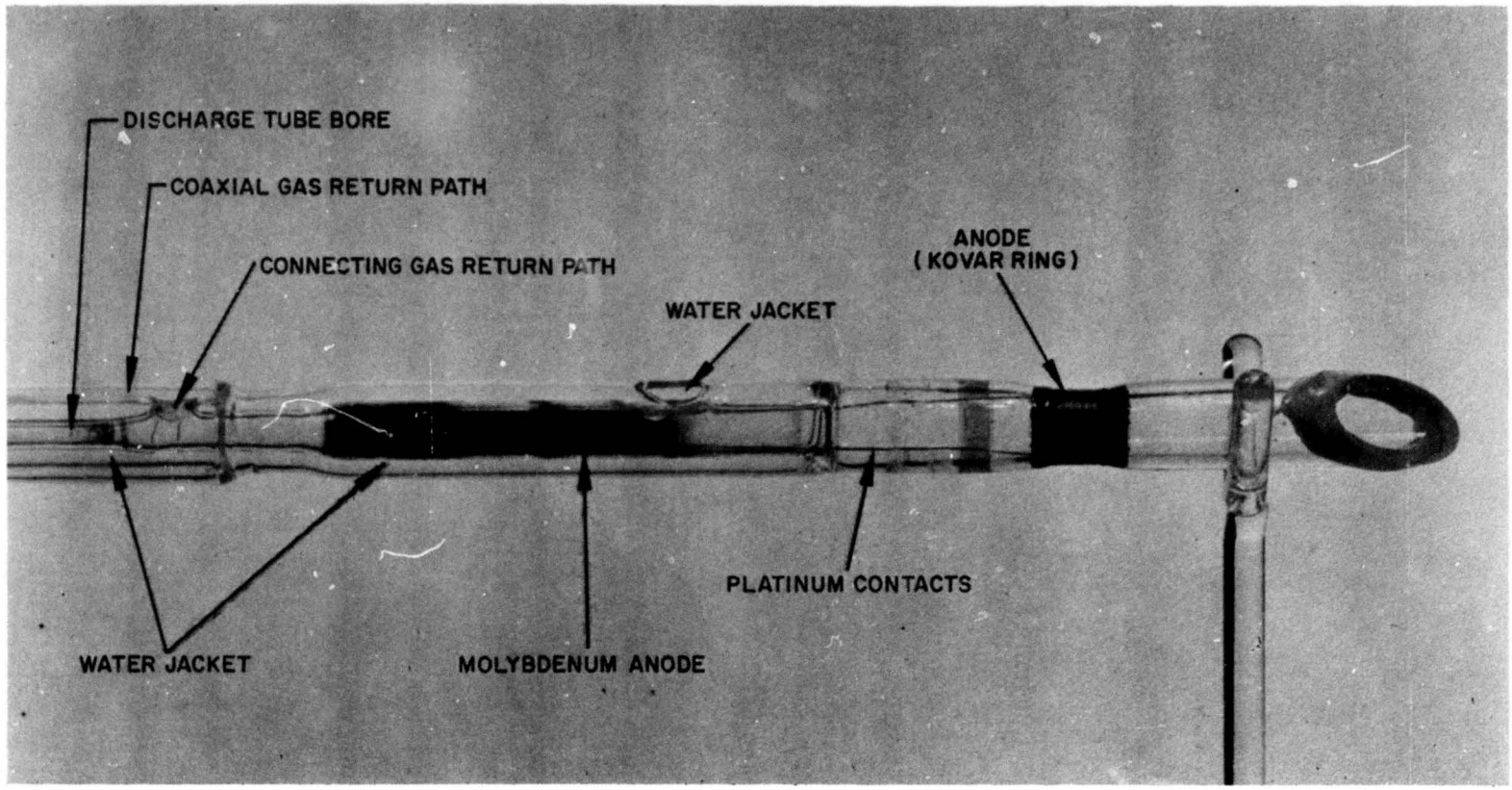

Fig. 69. Anode portion of laser discharge tube.

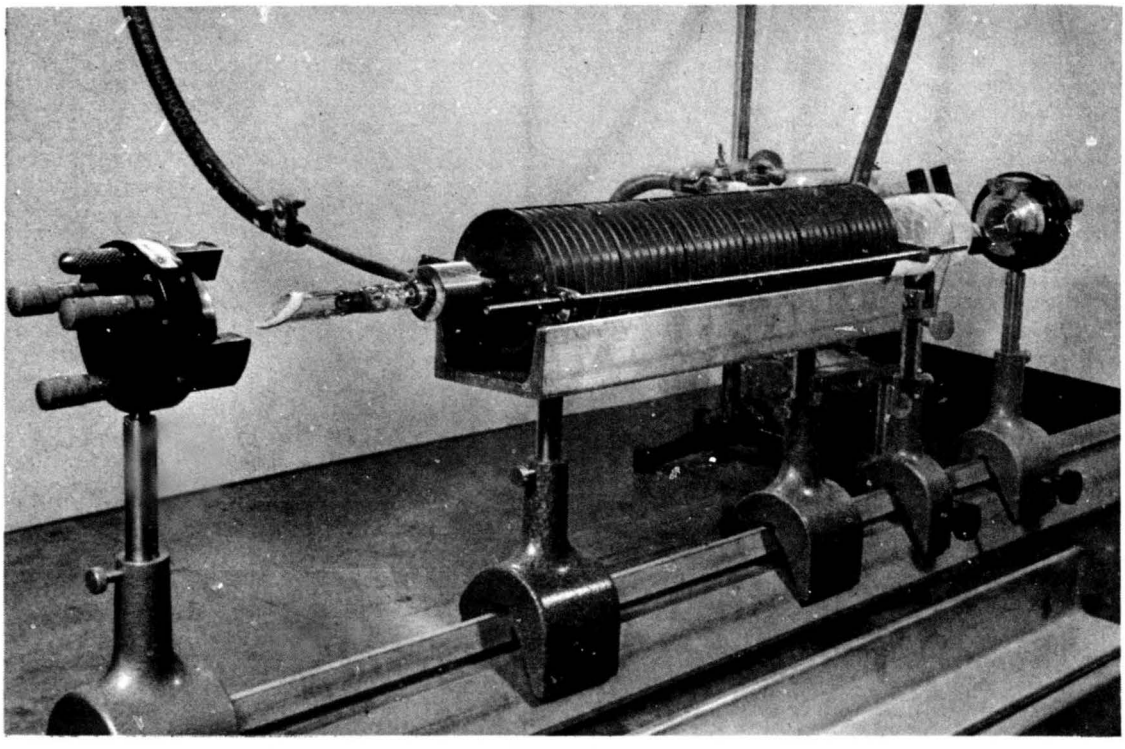

Fig. 70. Assembled PPM laser system.

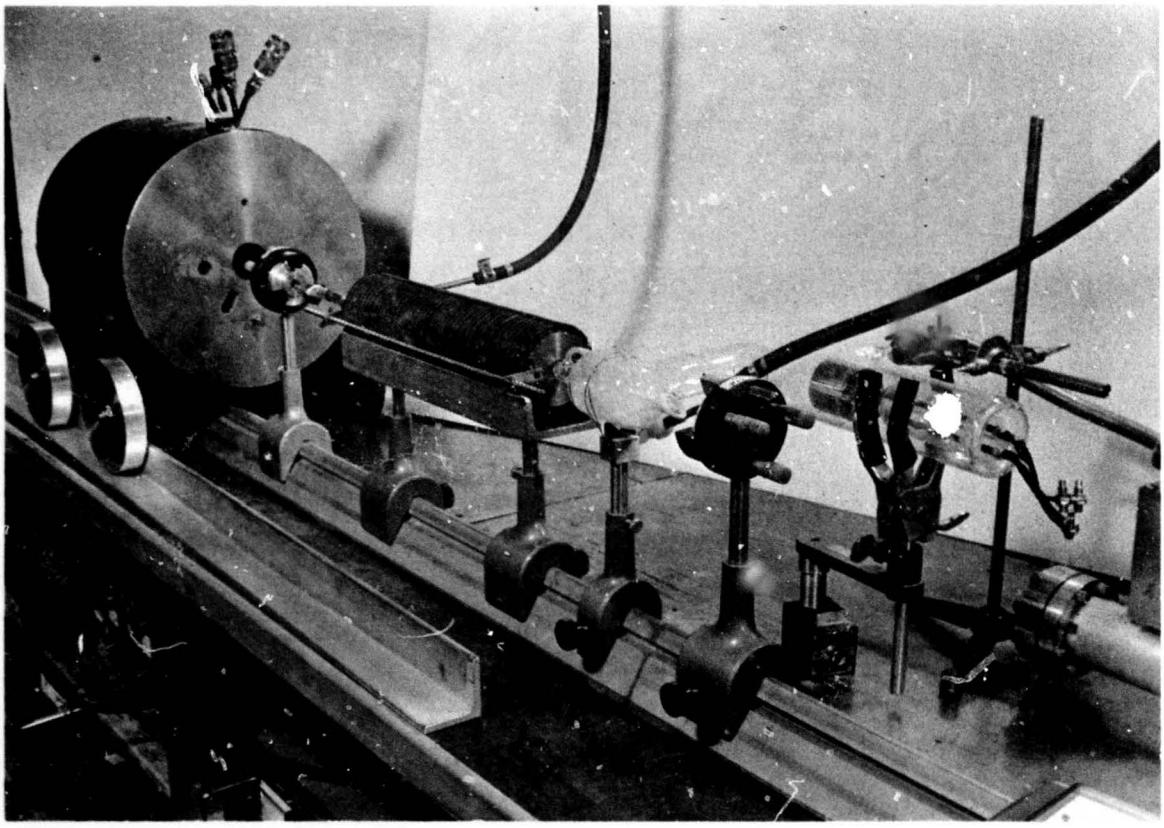

Fig. 71. View of solenoid and PPM laser system.

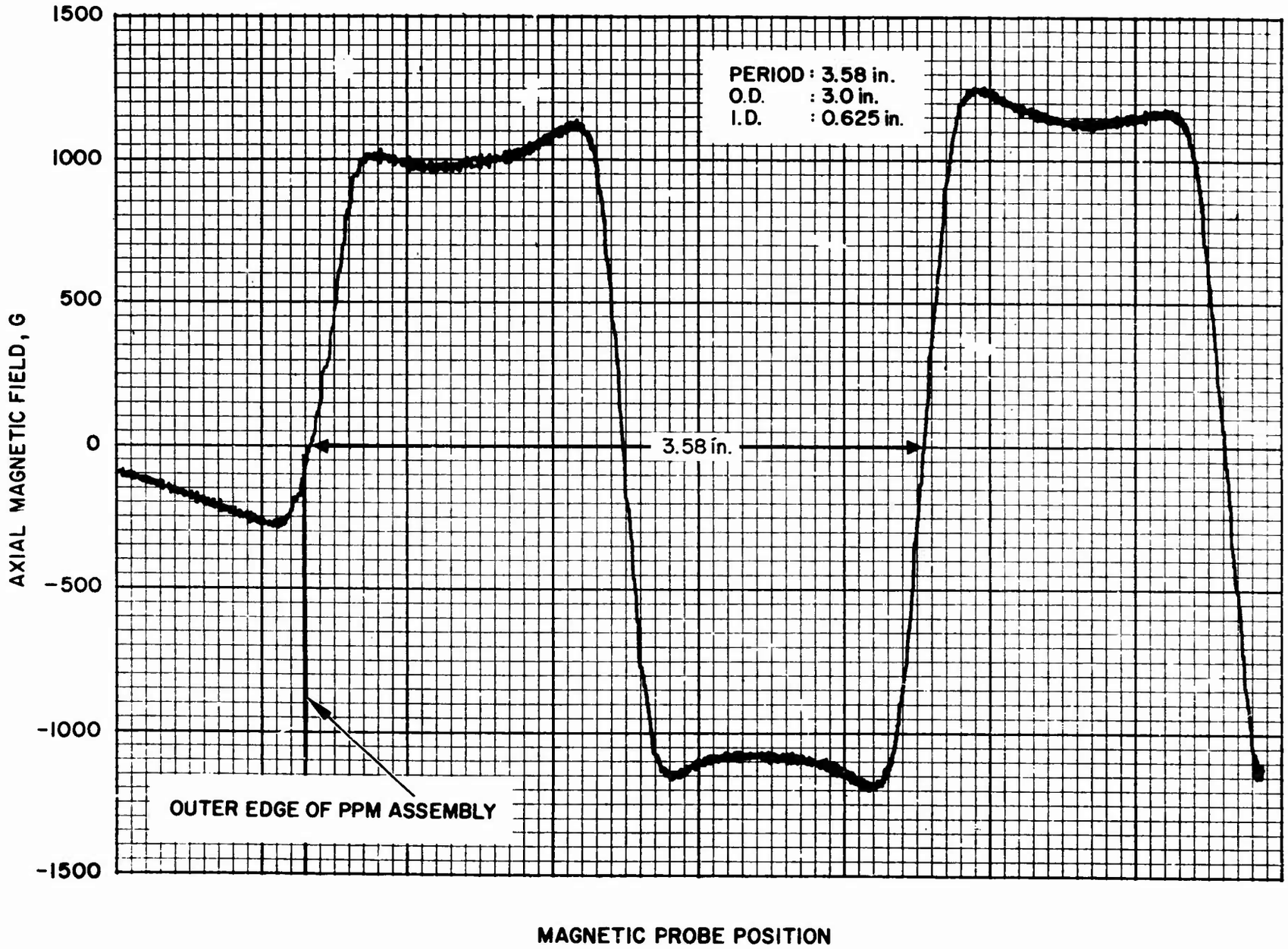

Fig. 72. Axial variation of PPM field. Period = 3.58 in.

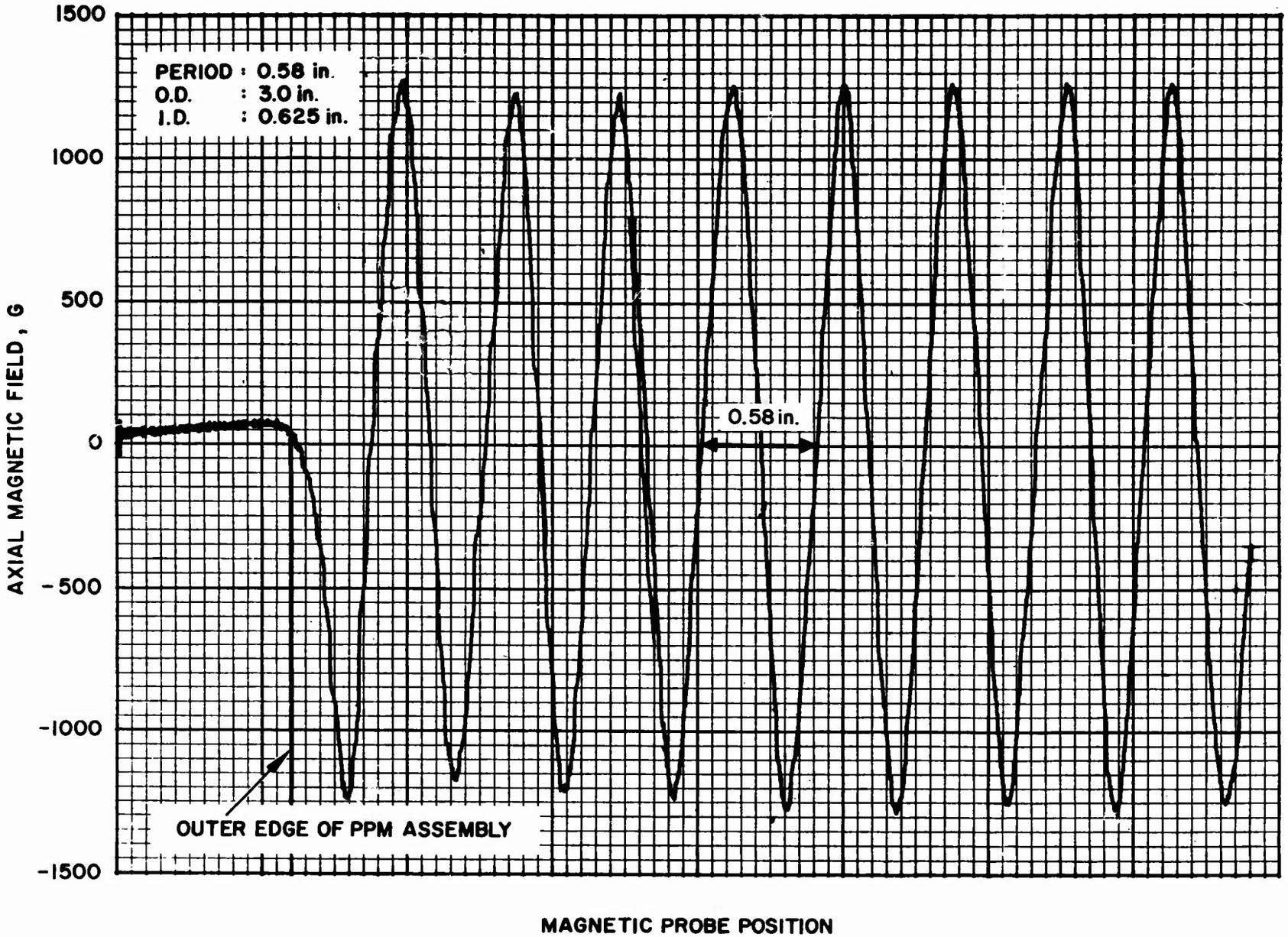

Fig. 73. Axial variation of PPM field. Period = 0.5 in.

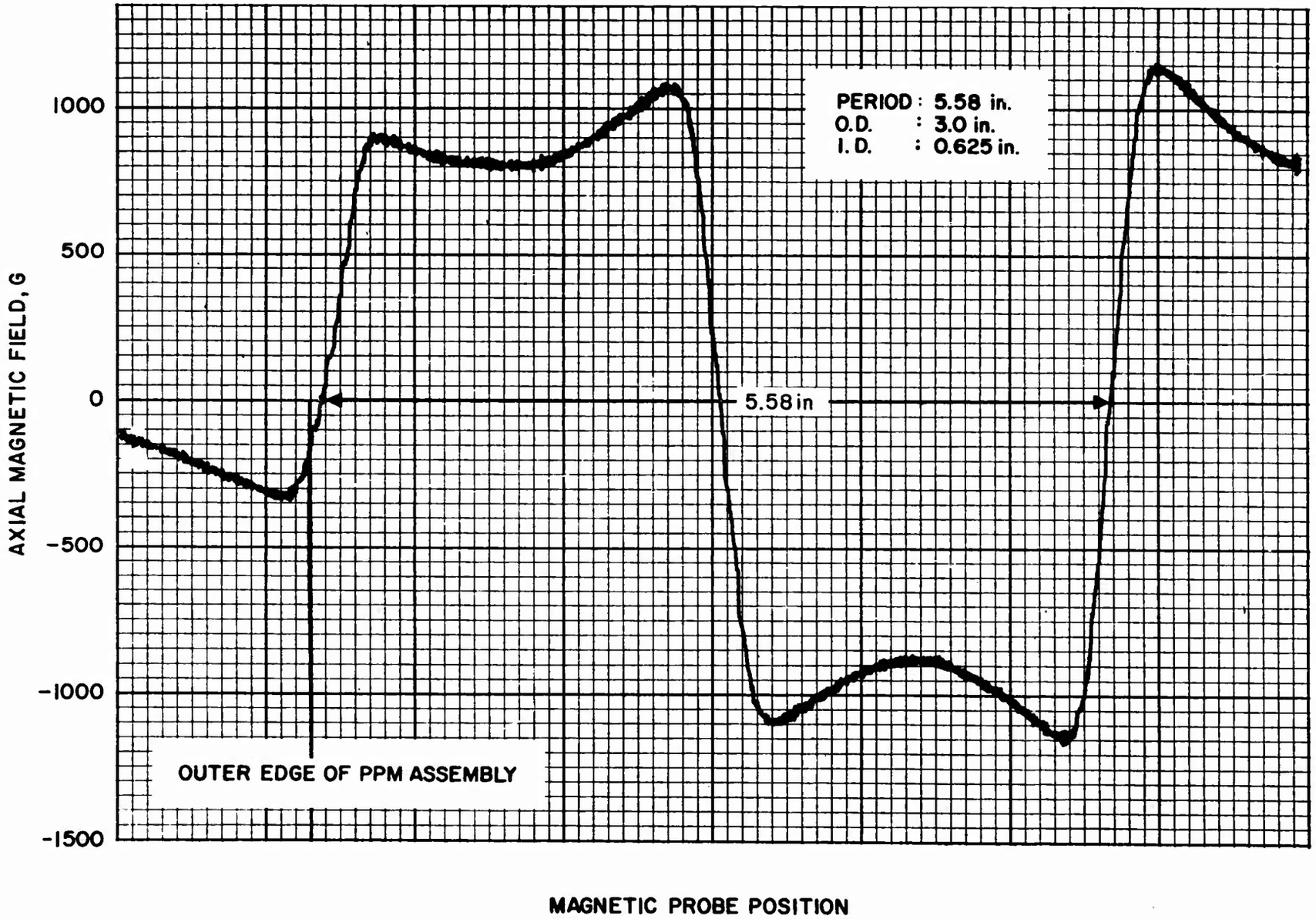

Fig. 74. Axial variation of PPM field. Period = 5.58 in.

At the left in Figure 71 is shown a 12 in. long magnet solenoid which could be rolled into position around the discharge tube to provide a uniform magnetic field.

3. Argon Laser Discharge Characteristics

The primary concern was to determine the change in the operating characteristics of the argon ion laser when the solenoid was replaced by a periodic permanent magnet assembly. It was first necessary to establish the optimum gas fill pressure and axial field strength using the 2 mm bore discharge tube with a conventional solenoidal magnetic field. Figures 75 and 76 show the variation of laser output power and tube voltage as a function of discharge current for cold filling pressures of 0.30, 0.33, and 0.36 Torr. The laser output power reached a maximum and was essentially independent of field strength for solenoid fields between 1.2 and 1.8 kG. Therefore, the optimum solenoid field strength was set at 1.5 kG. In accordance with the theory of the argon ion laser, somewhat above threshold the power output displays an I^4 dependence with current, whereas at higher current densities an I^2 behavior is observed. For higher gas fill pressures at a given value of discharge current, lower power output and higher tube voltages are observed. In the low pressure-high current domain the discharge becomes unstable at the anode.

The operational characteristics of the argon laser employing a periodic permanent magnet are also included in Figures 75 and 76 for comparison. A PPM stack with a 3.58 in. period and a 1.2 kG maximum axial field strength (see Figure 72) was selected to replace the solenoid. The discharge tube was filled to a cold pressure of 0.33 Torr. The power output displays the expected I^4 and I^2 dependence in the appropriate regions of operation. It is quite apparent in Figure 75 that for a given discharge current the power available is considerably higher when the PPM stack is employed. However, this is also accompanied by a higher tube voltage which results in comparable operational efficiencies for both tubes. Efficiencies of 0.045% and 0.041% were measured at a discharge current of 10 A for the PPM and solenoid operated tubes, respectively. This is a reasonable efficiency for this short tube at low power levels. It is interesting to note that in Figure 76 the current at which the tube voltage begins to increase is considerably lower than for solenoid fields. This is not fully understood, but may be indicative of an increased electron loss rate which is accompanied by an electron temperature elevation. Such behavior is often characteristic of the onset of an instability within the discharge.

A considerably more serious disadvantage associated with the use of a periodic magnetic field was the extreme bore erosion which occurred at the field reversals. This can be seen as discolored regions

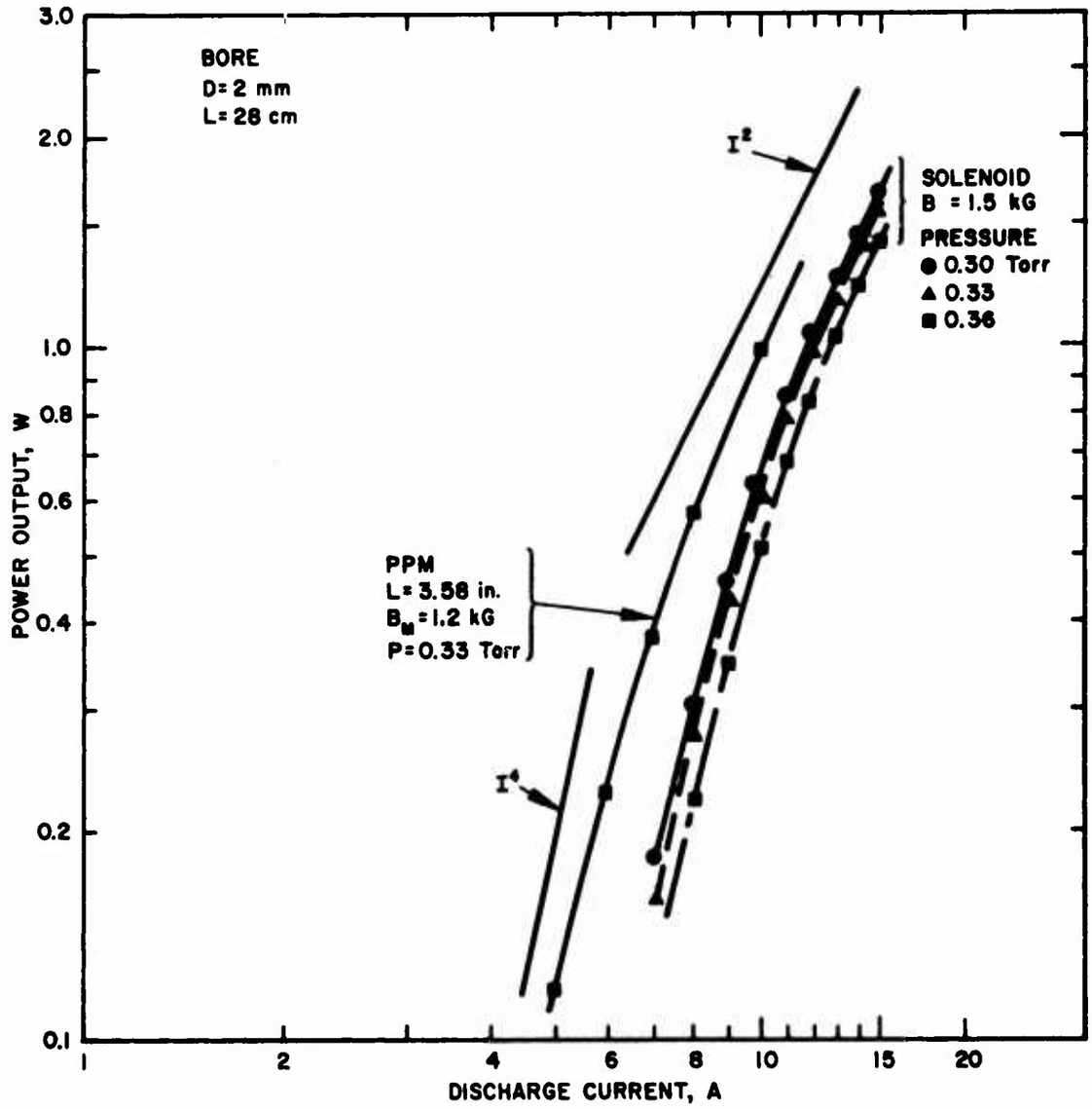

Fig. 75. Current dependence of the argon ion laser output power for a tube with PPM and solenoidal magnetic field confinement.

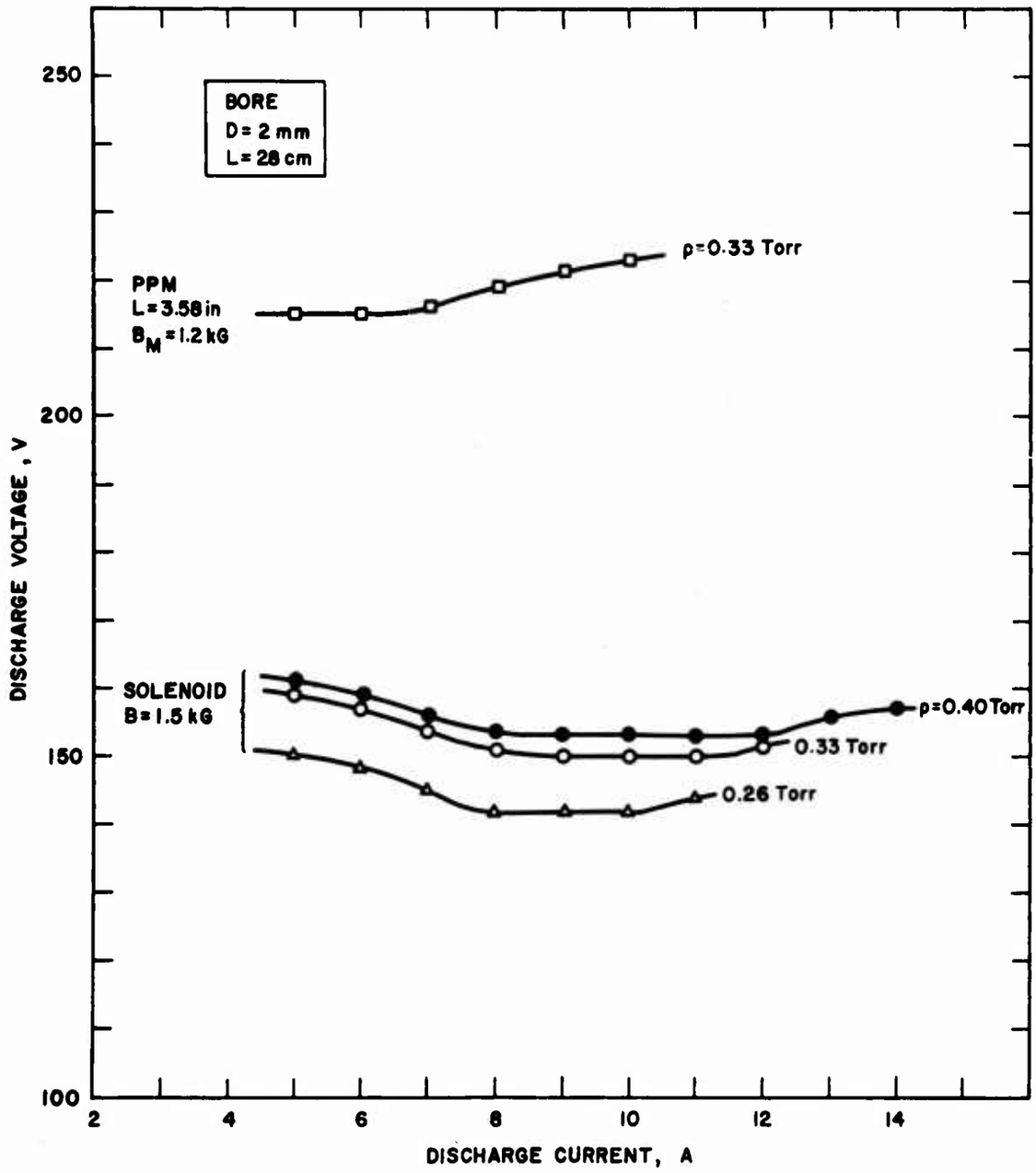

Fig. 76. Tube voltage versus discharge current.

evenly spaced along the bore in Figure 77. The localized tube damage is attributed to excessive ion bombardment resulting from charged particle losses in the vicinity of the magnetic field cusps. Enlarged cross sectional views of the undamaged and damaged regions of the tubes are shown in Figure 78. Figure 78(a) shows the uniform bore of an undamaged section of the precision bore quartz tubing. The damaged sections (Figure 78(b) and (c)) no longer have a circular bore cross section but appear to have an excess of quartz in some regions and a deficiency in others. The bore damage is noticeably more intense toward the cathode end of the discharge tube. The electrons in the vicinity of the throat constriction at the cathode are known to possess higher energies (see Section IV-H of Ref. 1). Since the electrons and ions are essentially guided into the wall at the field reversal, it is not unreasonable to find severe bore damage in these regions.

The bore damage shown in Figures 77 and 78 occurred during 15 min of operation at 10 A. In order to make PPM laser operation practical, the problem of bore damage must be eliminated. A possible solution may be to use a segmented bore designed such that a segment is located at each field reversal.

C. SUMMARY AND CONCLUSIONS

The possibility of employing a periodic permanent magnet assembly in place of a solenoid is attractive and was investigated. The PPM stack requires no external power supply, and a considerably lighter assembly produces an equivalent axial magnetic field.

The magnetic field along the axis of the periodic permanent magnet assembly is a function of the inner and outer radii of the magnet, the period of the magnetic sections, the shape of the pole pieces, and the demagnetization characteristics of the magnetic material. For larger axial field strengths, it is advisable to work with a magnetic material with a high coercive field strength H_c. Ceramic magnetic materials having the approximate composition $BaFe_{12}O_{19}$, such as Indox and Genox, are ideally suited for PPM applications.

Several basic problems arise in adapting a PPM structure to ion laser use. In an electron tube, the PPM structure provides strong magnetic fields across short gaps in the pole pieces; these periodic regions of strong field confine the beam by periodic focusing. In an ion laser, we desire a long region of uniform magnetic field to reduce the plasma diffusion rate. The field reversals, which provide the focusing action for an electron beam, are a hindrance.

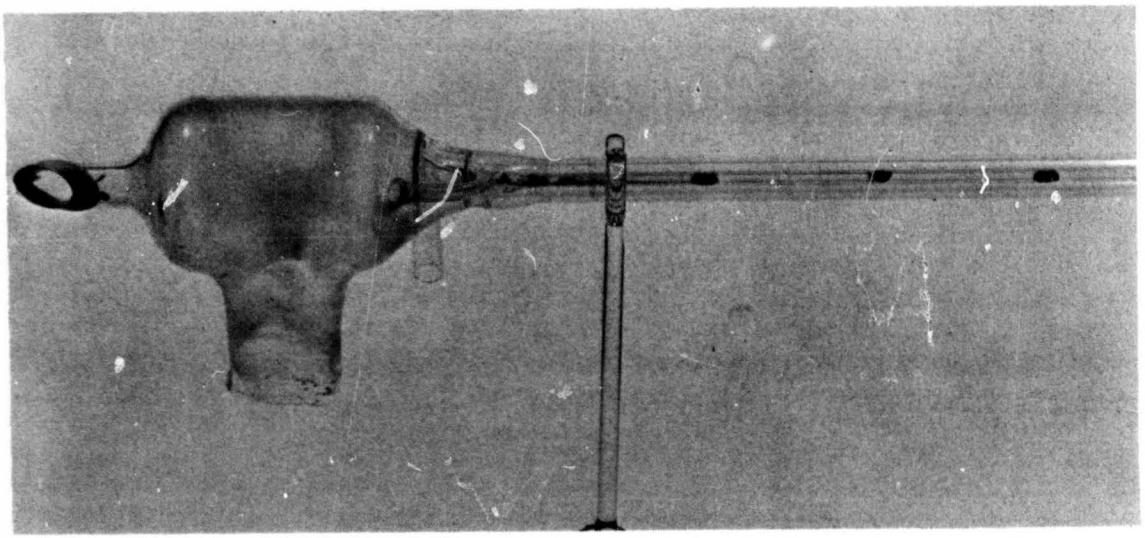

Fig. 77. Bore damage at the cathode end of the discharge tube.

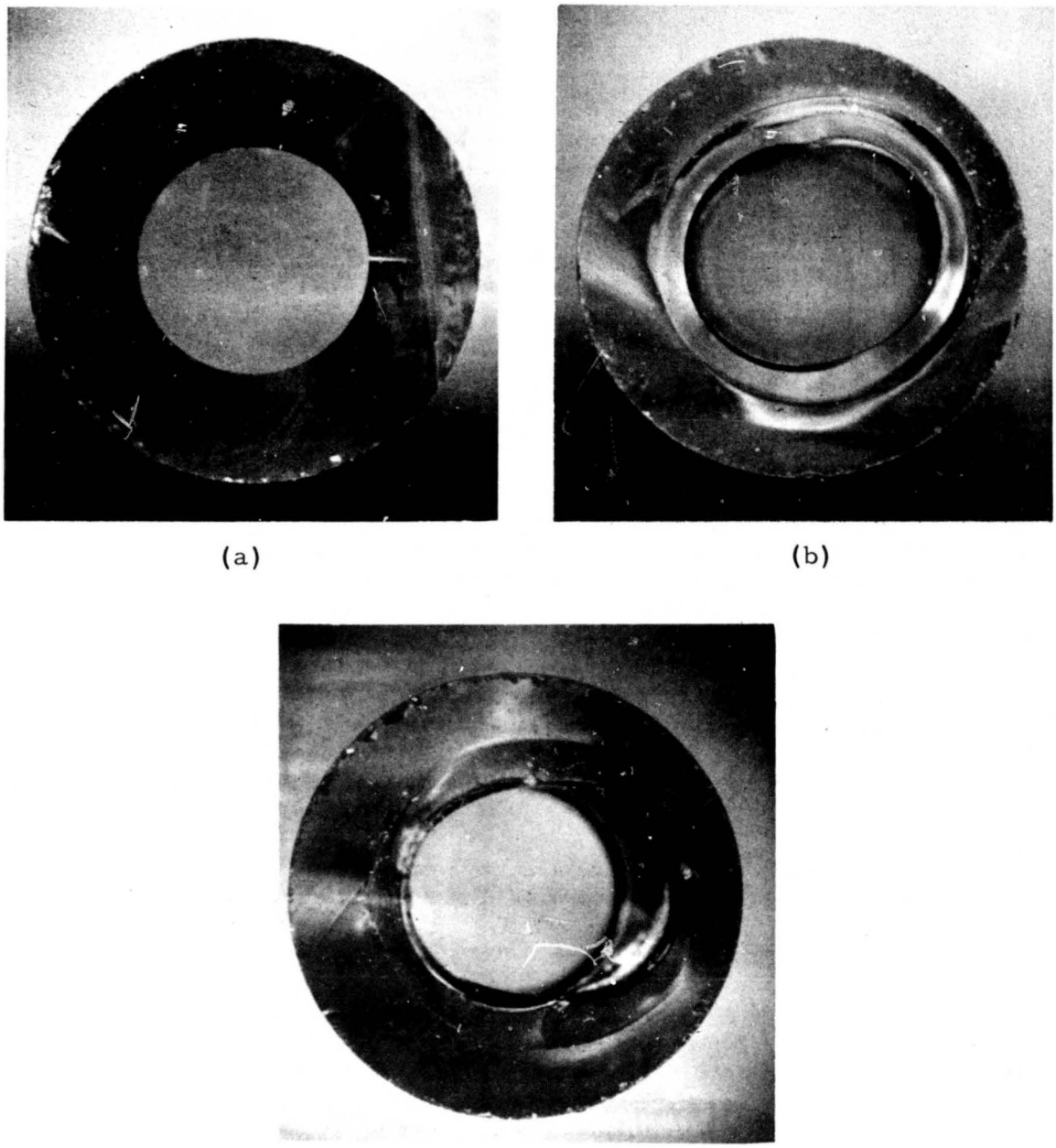

Fig. 78. Cross-sectional view of laser bore illustrating the damage which occurred at the field reversals. (a) Undamaged bore. (b) and (c) Damaged sections.

The peak axial magnetic field strength increases with decreasing magnet i.d. and shim separation. The inner radius is usually determined by the over-all diameter of the discharge tube. Increasing the o.d. of the magnets will increase the field strength, but at the expense of greater weight.

The number of field reversals in a given length of discharge may be reduced by increasing lengths of the magnet sections. However, this results in a decrease in the magnetic field strength and a more gradual field reversal.

Rapid field reversals are desired so that electrons will be trapped within the magnetic cusp and returned to the discharge before reaching the walls. In fact, such a trapping effect is extremely difficult to obtain because the wall of the discharge is generally several millimeters away from the pole pieces because of the coolant path. The field strength at the wall therefore is not much greater than that on-axis, and electrons are not trapped. In fact, the high magnetic field regions at the field reversals lie external to the plasma, and charged particles are guided to the walls.

A first solution to this problem would appear to be to introduce a bore segment of sputter-resistant material at positions in the tube where field reversals occur. However, this requires a larger tube diameter, which in turn will lower the axial field strength and reduce the abruptness of the field reversal.

Almost identical laser tube efficiencies were obtained from the laser using the PPM structure and a conventional solenoid. At a given discharge current, greater output power at a higher voltage was obtained using the PPM assembly. This indicates that the electron energy and the electron loss rate from the plasma column to the wall is higher when permanent magnetic confinement is used instead of a solenoid. Very severe wall damage occurred at each field reversal during operation with permanent magnets. Since bore erosion in argon ion lasers is currently a more critical problem than over-all laser efficiency, the use of a PPM structure to provide plasma confinement is not particularly attractive.

SECTION VI

GENERAL LASER DESIGN CONSIDERATIONS

Two topics relating to laser design improvements have been pursued briefly during the contract. These are (1) the design of internal gas return paths in segmented-bore tubes, and (2) the dependence of the localized power dissipation in the cathode throat on magnetic field strength and position in the magnet. Experiments and observations relating to these topics are discussed below.

A. GAS RETURN PATH DESIGN

One of the added advantages of the segmented or disk bore tube design is that off-axis holes may be drilled in the segments or disks to provide a gas return path. The design of a tube using such an internal gas return path (GRP) is generally simpler and more compact than when an external GRP from anode to cathode is used.

We have previously reported in detail on gas pumping mechanisms, pumping rates, and the design of the external GRP (Ref. 13). It was concluded from this study that an external path with a vacuum conductance (for viscous flow) at room temperature equal to the conductance of the bore was adequate to obtain maximum laser efficiency and discharge stability. Measurements were made on the effectiveness of internal gas return paths. It was found that very large areas must be allocated to gas return path holes in order to achieve an adequate internal gas return path conductance, larger than one might expect from a simple geometric comparison of GRP and bore conductance. This increase proved to be necessary because of the high gas temperature within the segmented bore structure. The increased viscosity of the higher temperature gas decreases the effective conductance of an internal GRP.

1. Description of the Experiment

Measurements were made on a metal-ceramic envelope tube having 0.750 in. diameter, 0.500 in. long PG bore segments. Each segment in this tube had three off-axis gas return path holes, each 2.7 mm in diameter, located symmetrically around the 3 mm bore as shown in Figure 79(a). The gas conductance for viscous flow through a cylinder of radius R varies as R^4. The three off-axis holes in the segment, each 88% of the bore diameter, should combine in parallel to provide a conductance which is 1.8 times that of the bore.

(a) (b)

Fig. 79.
Bore segments with (a) three-axis holes for gas flow, and (b) the same segment with six additional slots machined on the o.d.

A 3 mm i.d. external gas return path from the anode to the cathode was also provided on this tube. A stopcock located in the external GRP allowed this path to be opened or closed.

Initial measurements of laser output power were made with the external GRP both opened and closed. Only about one-half the power available with the external GRP open could be obtained with the GRP closed.

Before more complete data were taken, the segments were removed and the six additional grooves were machined in the outer diameter, as shown in Figure 79(b). These grooves were 0.062 in. wide and 0.092 in. deep. Calculations based on viscous conductance predict these six slots should combine in parallel to provide a conductance equal to the conductance of the bore at room temperature. Therefore, the combined conductance of the six off-axis slots and three holes was calculated to be 2.8 times that of the bore. The tube was reassembled with the external gas return path in place.

2. Experimental Results

The output power and tube voltage were measured as a function of discharge current and gas filling pressure (tube cold). Figure 80 is a plot of output power versus current at different filling pressures with the gas return path open and closed.

The curves with the external GRP open follow the usual pattern with the optimum pressure increasing as the current increases. Only the pertinent regions of the curve at each pressure are shown to avoid confusing the figure. The output power obtained at different current levels is typical of a 3 mm diameter segmented or continuous bore tube of this length with an external GRP.

Data taken with the GRP closed are shown with dotted lines in Figure 80. Two important effects are observed:

- At currents < 25 A, the output power is less when the GRP is closed than when it is open
- The optimum pressure for maximum power output is much lower when the external gas return path is closed.

We have previously shown (Ref. 13) that the net gas pumping rate decreases with increasing current for I > 5 A and eventually crosses through zero and reverses between 20 and 30 A in a 3 mm diameter tube. At this crossover point, there is no pressure difference across the tube and no gas return path is required. This apparently explains why the two sets of curves approach one another in the 25 A range.

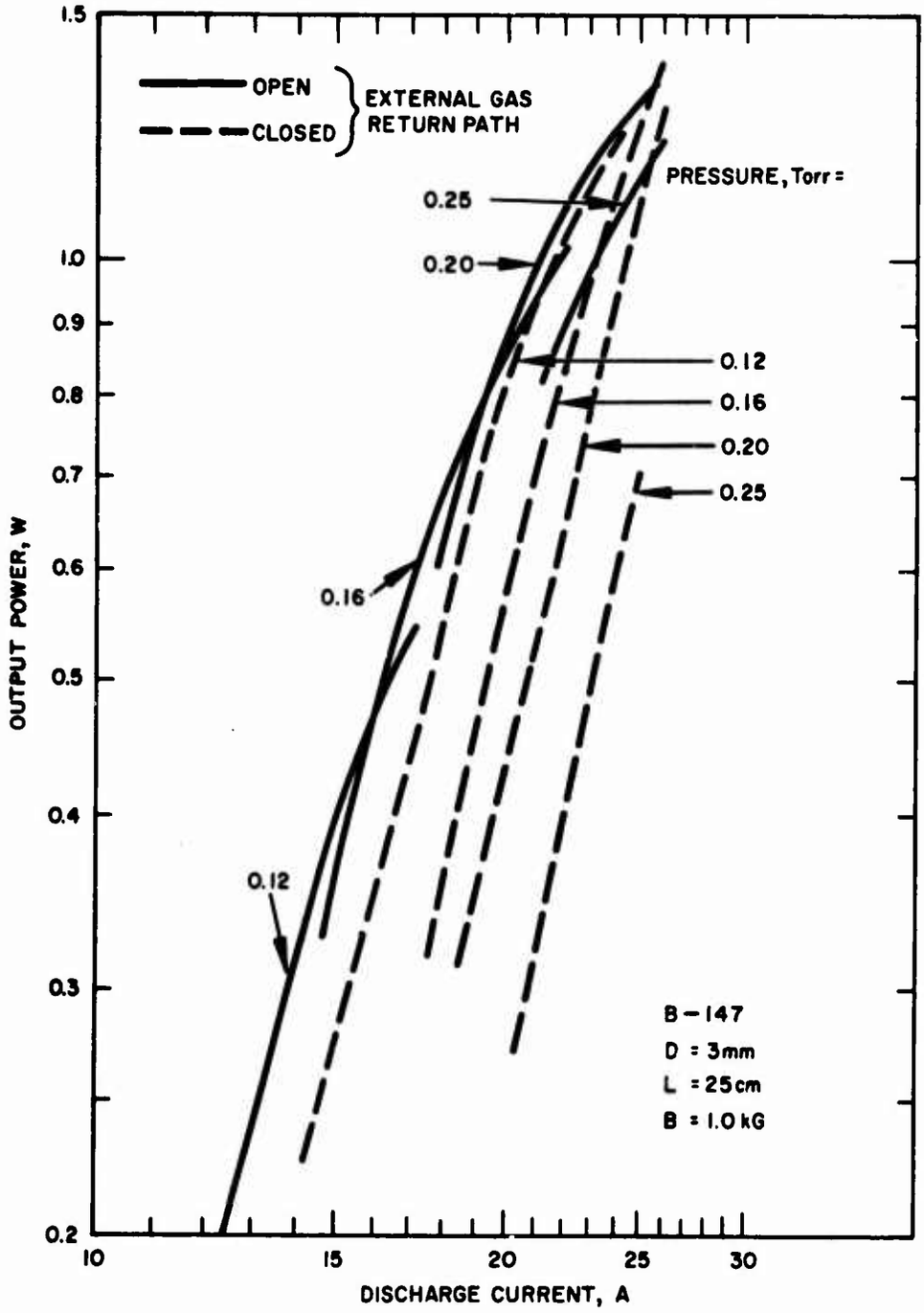

Fig. 80. Output power versus discharge current for different cold filling pressures and with the external gas return path open and closed.

3. Discussion

The ineffectiveness of the off-axis holes in providing an adequate gas return path is attributed to the high neutral gas temperature in the tube. The vacuum conductance for gas flow through a cylinder of radius R and length ℓ is given by the expression (Ref. 14)

$$C = \frac{\pi R^4}{8\eta\ell} p_{o_{avg}} ,$$

where η is the coefficient of viscosity of the gas and $p_{o_{avg}}$ is the average reduced pressure in the bore. The reduced pressure is the pressure of a gas at 0^oC with the same density as the gas at temperature T. In terms of the actual gas pressure p at absolute temperature T,

$$p_o = p\left(\frac{273^o}{T}\right) .$$

The coefficient of viscosity of the gas is also a function of temperature, and for the noble gases an approximate expression for the increase in η with absolute temperature is (Ref. 14)

$$\eta = \eta_o\left(\frac{T}{273^o}\right)^{3/4} .$$

Combining the above equations yields, for the temperature dependence of the conductance,

$$C = \frac{\pi R^4 p}{8\eta_o\ell}\left(\frac{273^o}{T}\right)^{7/4} .$$

From this expression we may calculate the ratio of the conductance at room temperature C to the conductance C_T when the gas in the bore is at a temperature T. The results of such a calculation are shown in Table VI.

TABLE VI

Variation of Gas Conductance with Gas Temperature

C_T/C	Temperature, °C
1.0	27
0.5	172
0.2	478
0.1	840
0.05	1400

The radiation-cooled bore segments typically operate in the temperature range from 950 to 1200°C. This is probably a reasonable estimate for the temperature of the gas flowing through the holes totally inside the segments. The gas flowing through the slots in the o.d. of the segments is undoubtedly cooler on the average as a result of contact with the water-cooled ceramic wall on one side.

Assuming a gas temperature of 1000°C, one can calculate that an internal GRP is only 1/13 as effective as an external GRP of the same dimensions in reducing the pressure difference across the tube. This situation makes it difficult to include internal gas return paths in small outside-diameter (< 1 in.) segmented tubes. For example, if GRP holes with 90% of the bore diameter are used (larger holes cannot be used without baffling, or the discharge will break down through these holes instead of the bore), then 20 holes are required to be as effective as an external path with the same diameter as the bore. Generally there is insufficient cross sectional area in a small diameter segment to allow this many holes and/or slots to be drilled, and an external path must be provided for maximum efficiency. If large diameter disks or segments are employed (> 1.5 in.), a large cross section is available and the use of internal gas return paths again becomes practical. (Of course, the magnet i.d., and hence the magnet weight, will be greater for these tubes.)

B. CATHODE THROAT STUDIES

The cathode-end bore constriction is observed to be the region of greatest bore erosion and power dissipation in continuous bore or segmented bore tubes. These conditions occur because of the existence

of a double sheath in the cathode throat which forms to equalize the random plasma electron currents passing between the large and small diameter regions of the bore (Ref. 15). Electrons accelerated through this double sheath from the cathode region raise the electron energy, ionization rate, and wall sheath height in the throat and bore region.

The bore erosion caused by high energy ions striking the walls near the throat region can be a serious problem, as discussed earlier. Previous experiments have shown that the sputtering rate and specific power dissipation in the throat region are affected by the throat shape and the position of the throat in the magnetic field (Ref. 16). Measurements were made during the present contract period to determine the dependence of throat conditions on magnetic field strength and the position of the throat with respect to the converging magnetic field.

1. Experimental Apparatus

Information on conditions in the throat may be obtained by measuring the temperature of bore segments in a radiation-cooled, segmented-bore tube. The apparatus constructed to monitor the temperature of the segments is illustrated in Figure 81. A 12-in. solenoid with a 6 in. i.d. was used for the experiments. The large i.d. simplified the observation of segment temperatures. A simple sliding periscope was fabricated to speed data-taking. This is an improvement over earlier apparatus which used a mirror taped on a rod and required two people to gather data. Pole pieces were used to shape the fields at each end of the tube. These were split in two halves so that the tube could be removed easily. The solenoid was mounted on wheels to allow variation in the position of the converging magnetic field with respect to the bore and throat.

2. Experimental Results

Before the discharge tube was mounted in the solenoid, a flux plot was taken with and without the pole pieces mounted on the solenoid. The variation in magnetic field along the axis of the tube for these two cases is shown in Figure 82. With the 0.875 in. i.d. pole pieces in place, the flux pattern resembles that of a small diameter solenoid.

The bore segment arrangement used inside the 0.5 in. i.d. quartz envelope is sketched at the top of Figure 83. The bore constriction was 1.8 in. long and consisted of one 0.375 in. long segment and seven 0.080 in. thick graphite disks spaced 0.125 in. apart. The 3 mm diameter uniform bore was constructed of five 0.080 in. thick graphite disks and 0.5 in. long segments, as shown. Thin graphite disks were used in the throat region instead of longer segments in order to observe temperature differences on a finer scale.

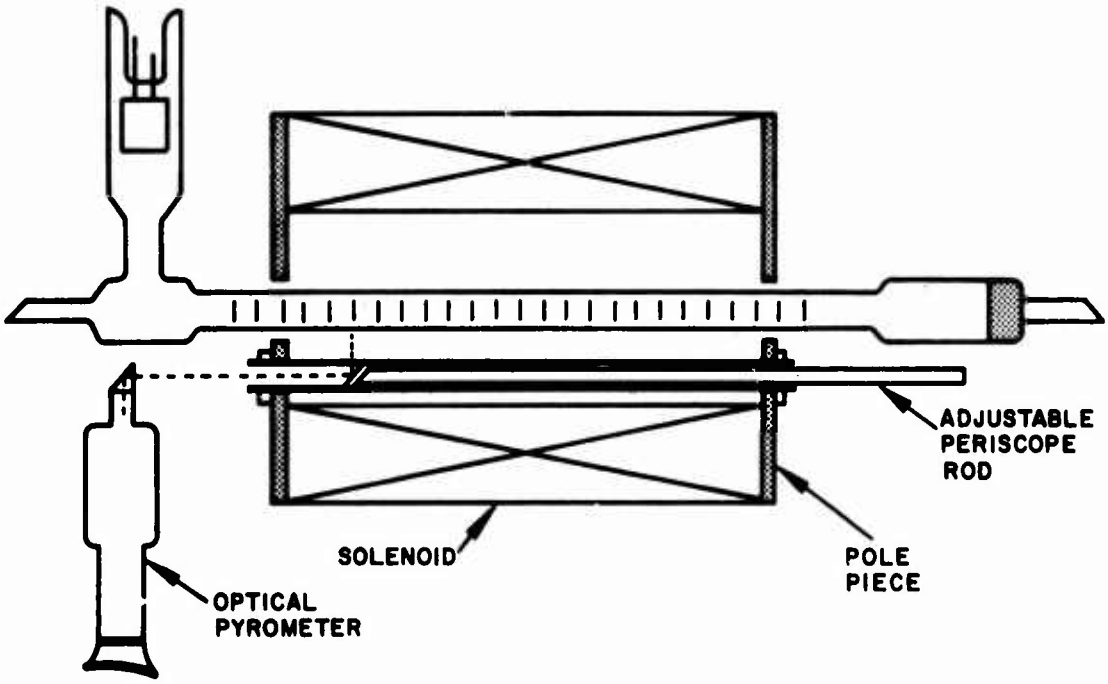

Fig. 81. Apparatus for measuring temperature of segments in a segmented-bore tube.

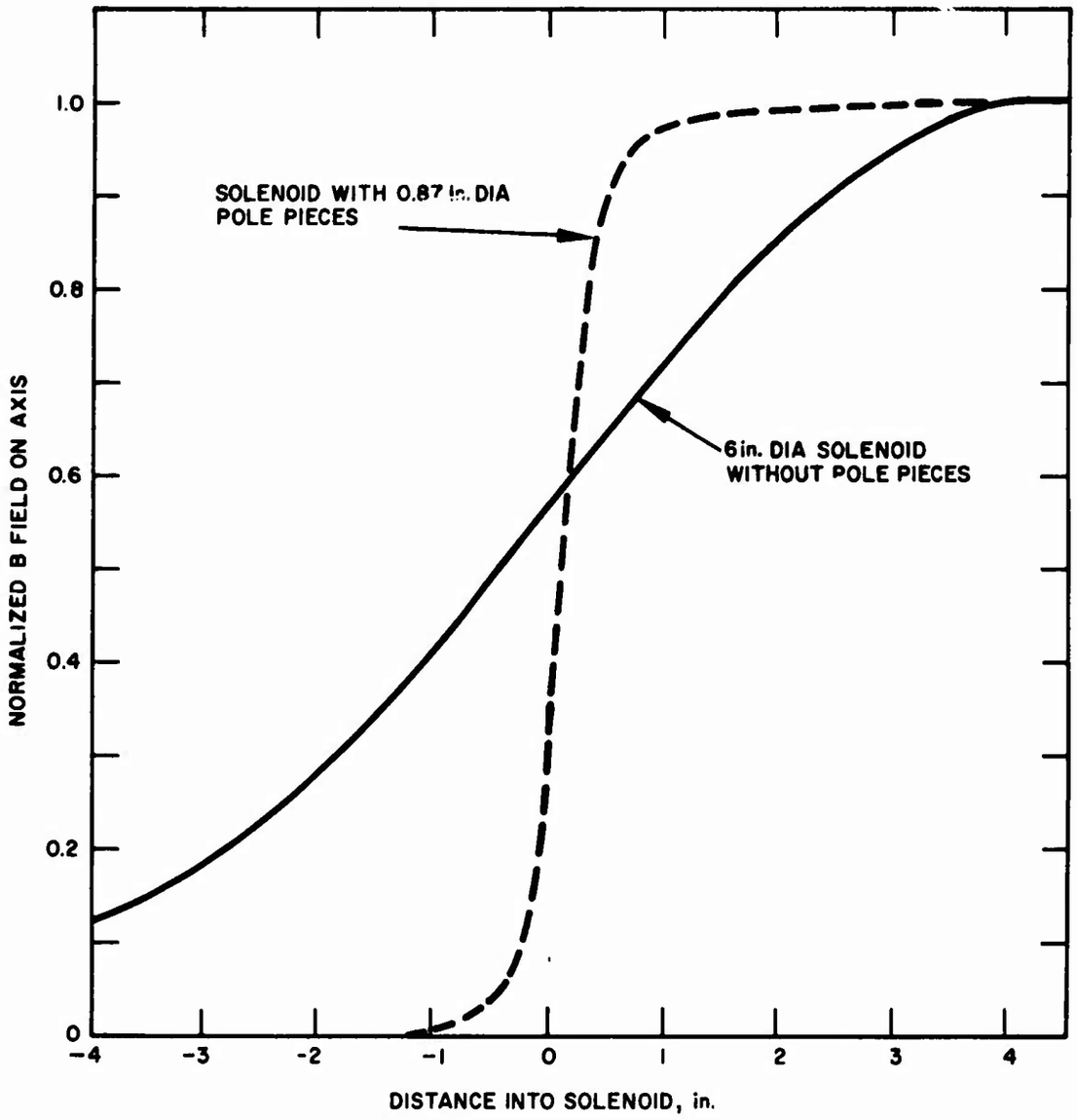

Fig. 82. Variation of magnetic field strength along the axis of the solenoid with and without pole pieces.

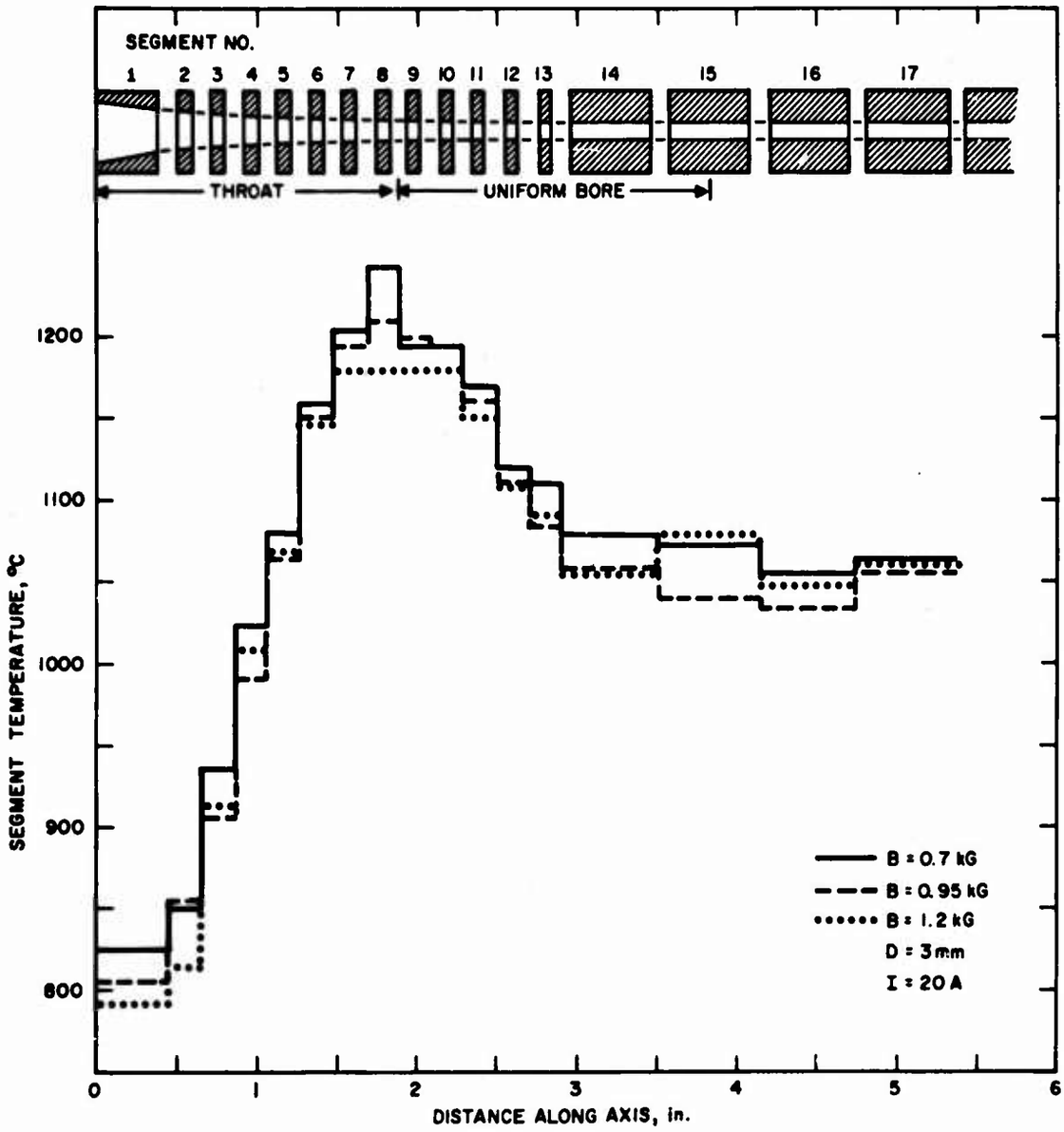

Fig. 83. Dependence of segment temperature on field strength. The bore constriction is drawn to scale at the top of the figure.

The dependence of segment temperature on magnetic field strength is shown in Figure 83. These measurements were taken with the first bore segment 0.25 in. outside the solenoid and flush with the outer surface of the pole piece. The figure is drawn to scale so that the temperature reading of a particular segment is plotted directly below that segment (e.g., segment No. 8 was the hottest segment). Two conclusions may be drawn from these data. First, power dissipation in the throat region is significantly greater than in the uniform bore region and is distributed very non-uniformly. Segment 8, the last tapered segment, operated at the highest temperature. At 1200°C, this segment radiates 50% more power per unit area than the segments at 1050°C. A second conclusion is that the amount and the distribution of the power dissipated along the segmented bore are relatively independent of field strength. Therefore, modifications in throat shape, throat position, and field curvature should be sought in order to reduce localized heating, rather than changes in field strength.

The change in the bore temperature distribution caused by shifting the position of the throat in the solenoid is illustrated in Figure 84. The greatest bore heating is observed to occur when the throat was farthest into the solenoid. As seen from Figure 82, the entire constriction is in a reasonably uniform field (< 7% variation) when the throat is in this position, i.e., 0.62 in. inside the solenoid. The tube voltage was 127 V for the tube in this position. Minimum heating occurred with the throat positioned outside the solenoid. The tube voltage in this case was 120 V. Obviously there is a strong interrelation between throat heating and position of the throat in the converging magnetic field.

3. Discussion

Measurements taken thus far show that localized throat heating is strongly dependent on the position of the throat with respect to the converging magnetic field. The distribution and magnitude of localized heating are not dependent on magnetic field strength to first order. Additional measurements using the same apparatus still must be made to determine the dependence of output power, efficiency, and throat temperature on the relative shaping of the bore and magnetic field constriction at the cathode end of the tube.

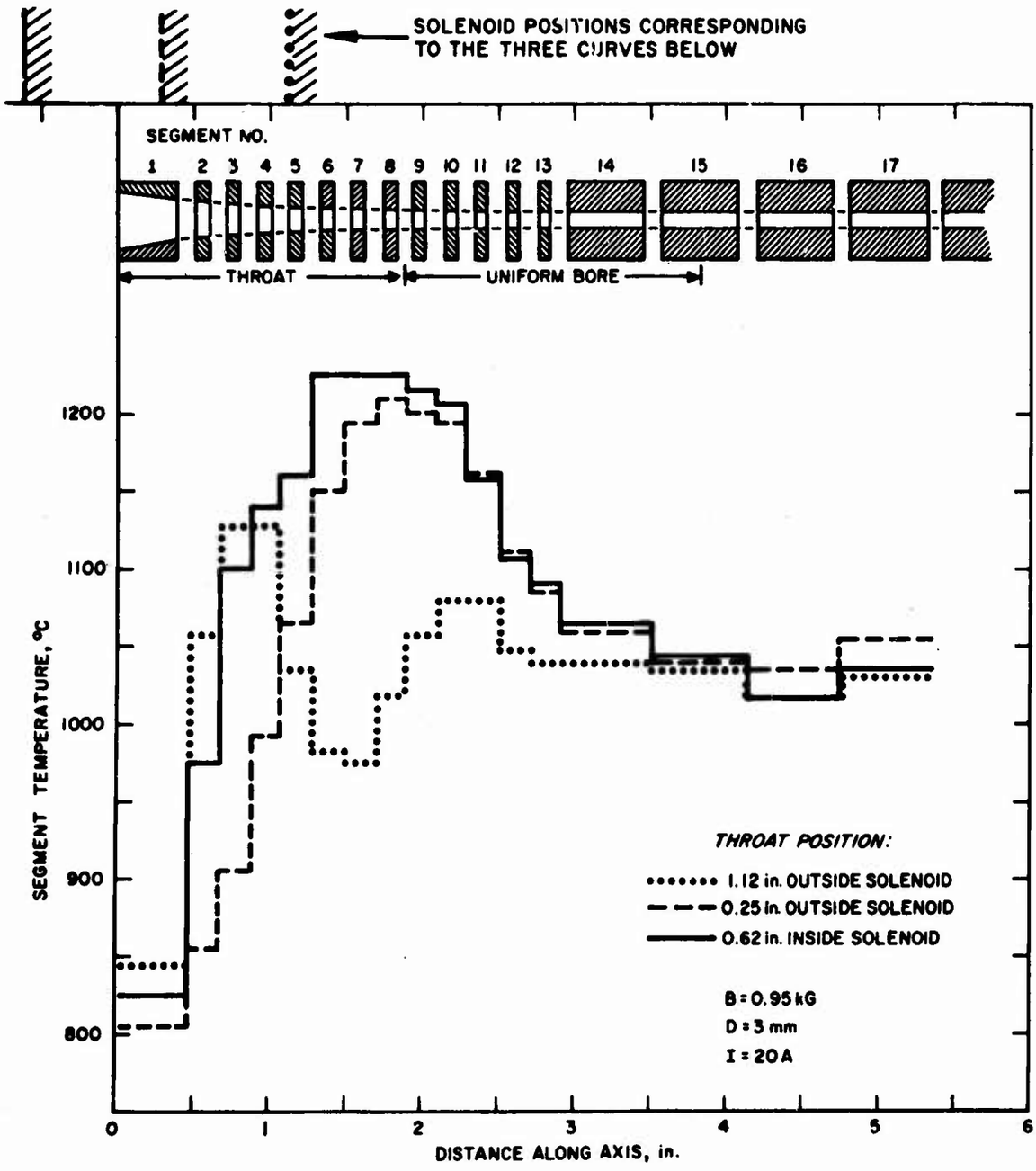

Fig. 84. Dependence of segment temperature on the position of the throat in the converging magnetic field.

SECTION VII

NOISE STUDIES

Once reasonable lifetimes are obtained, more subtle demands on laser performance characteristics can be expected. One of these second generation requirements already of some interest is to minimize the noise modulation on the emitted beam. This is the problem treated in this section.

Fluctuations in the power output of an ion laser may be caused by

1. ripple in the anode, solenoid, or filament power supplies
2. fluctuations in the active medium (the plasma) caused by instabilities in the discharge
3. changes in the optical cavity loss or cavity length caused by movement of the mirrors or variation of the index of refraction of the air
4. competition effects among different transverse modes or between adjacent cavity modes.

The goal of this study was to measure the noise contribution (amplitude and frequency spectrum) of each of the above mechanisms, and to minimize the noise modulation in the laser output. Measurements show that the total peak-to-peak (p-p) noise contribution from sources (2) through (4) above is $< 1\%$ of the dc level; the modulation introduced by power supply ripple may easily exceed 10% unless special care is taken.

A. POWER SUPPLY MODULATION OF THE LIGHT OUTPUT

1. Theory.

We wish to develop the transfer function which describes how power supply fluctuations couple to the light output. Power supply ripple will affect the laser output by modulating the excitation rate of the upper laser level population which, in turn, depends on the plasma density n_e and electron temperature T_e. The electron density and temperature interact with power supplies only through the discharge current I and the magnetic field B. Thus, we may write for the output power P

$$P(n_e, T_e) = P(I, B) . \tag{17}$$

The modulation of P is therefore given by the relation

$$\frac{dP}{dt} = \frac{\partial P}{\partial B}\frac{dB}{dt} + \frac{\partial P}{\partial I}\frac{dI}{dt} . \tag{18}$$

The first term on the right reflects the dependence of P on B at constant I; this dependence is illustrated in Figure 85. Near the optimum magnetic field B_{opt}, the dependence of P on B may be approximated by the expression

$$P = P_{opt} - C_1(B - B_{opt})^2 \tag{19}$$

where C_1 is a constant which gives the best fit of (18) to the curves of Figure 85 near B_{opt}. At 20 A for the curve shown, $P_{opt} = 3$ W, $B_{opt} = 1.05$ kG, and $C_1 \cong 2$ W/kG^2. For use in (18), we differentiate (19) to obtain

$$\frac{\partial P}{\partial B} = -2C_1(B - B_{opt}) . \tag{20}$$

In the second term of (18), we know from parametric study data that

$$P = C_2 I^n \tag{21}$$

where n = 2 at high power levels (fully saturated medium), and $n \geq 4$ at low power levels. For a 3 mm diameter tube 46 cm long at high powers, $C_2 = 0.005$ W/A^2.

The current ripple factor dI/dt in (18) must be expressed in a form which takes into account the power supply and circuit characteristics; we must also allow for the possibility that the discharge current can be modulated by the magnetic field. This latter dependence occurs because the tube voltage is a function of B. We therefore express dI/dt as

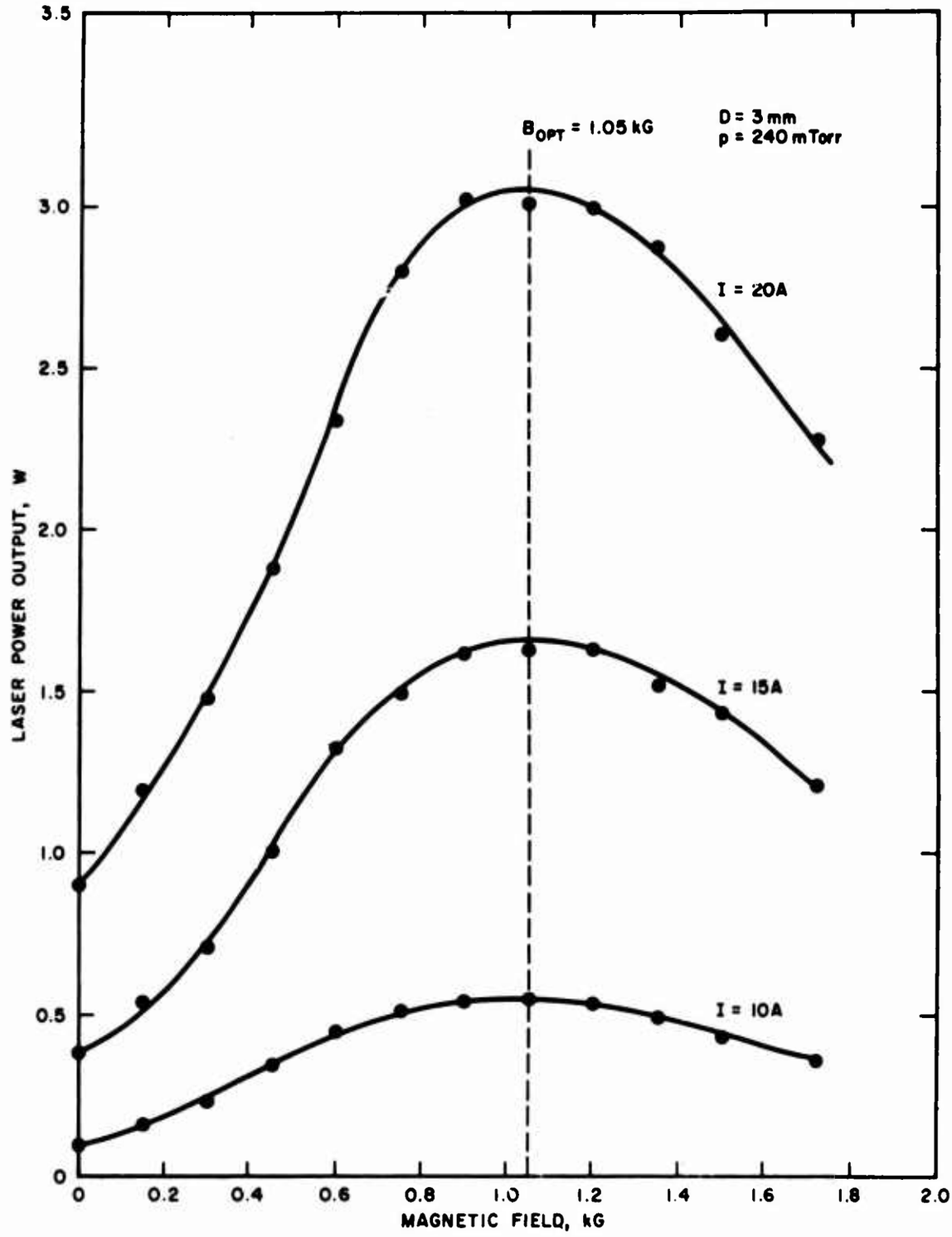

Fig. 85. Dependence of laser output power on magnetic field at constant discharge current.

$$\frac{dI}{dt} = \frac{\partial I}{\partial B}\frac{dB}{dt} + \frac{\partial I}{\partial V_s}\frac{dV_s}{dt} \tag{22}$$

where V_s is the supply voltage. Figure 86 shows the equivalent circuit for the anode power supply, ballast resistor R_B, and the tube which exhibits a current dependent resistance R_T. The internal resistance R_S of an ideal voltage supply is zero, while R_S for an ideal current regulated supply is infinite.

From Figure 86,

$$I(R_S + R_B) = V_s - V_T , \tag{23}$$

so that

$$\frac{\partial I}{\partial B} = -\frac{1}{R_S + R_B}\frac{\partial V_T}{\partial B} . \tag{24}$$

The variation of V_T with B in a 3 mm tube at 15 A and 20 A is shown in Figure 87. From these curves, $\partial V_T/\partial B = -30$ V/kG at 0.8 kG and -11 V/kG at 1.0 kG. From (24), for larger $(R_S + R_B)$, the current modulation resulting from the dependence of V_T on B will be smaller.

To express $\partial I/\partial V_S$ in (22) in the desired form, we differentiate (23) to obtain

$$\partial I(R_S + R_B) = \partial V_s - \frac{\partial V_T}{\partial I}\partial I . \tag{25}$$

We recognize $\partial V_T/\partial I$ as the dynamic resistance of the tube,

$$\frac{\partial V_T}{\partial I} = R_{Tac} . \tag{26}$$

Figure 88 illustrates the V_T versus I characteristics of a 4 mm tube. The slope of the curve at a given value of current is the low frequency dynamic resistance R_{Tac} at that particular value of current. For

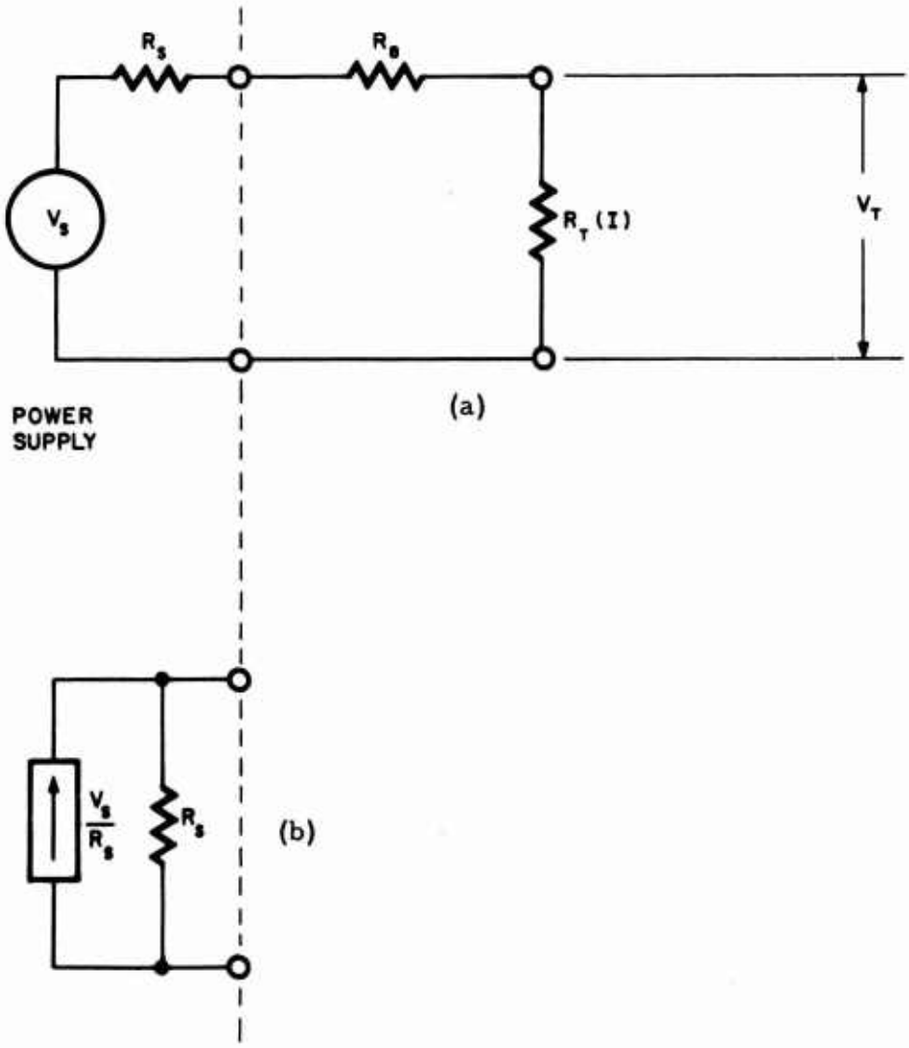

Fig. 86. (a) Equivalent circuit showing the relation of the power supply, ballast resistor, and discharge tube. (b) Equivalent circuit expressed as a current source. $R_s = 0$ for an ideal voltage source and $R_s = \infty$ for an ideal current source.

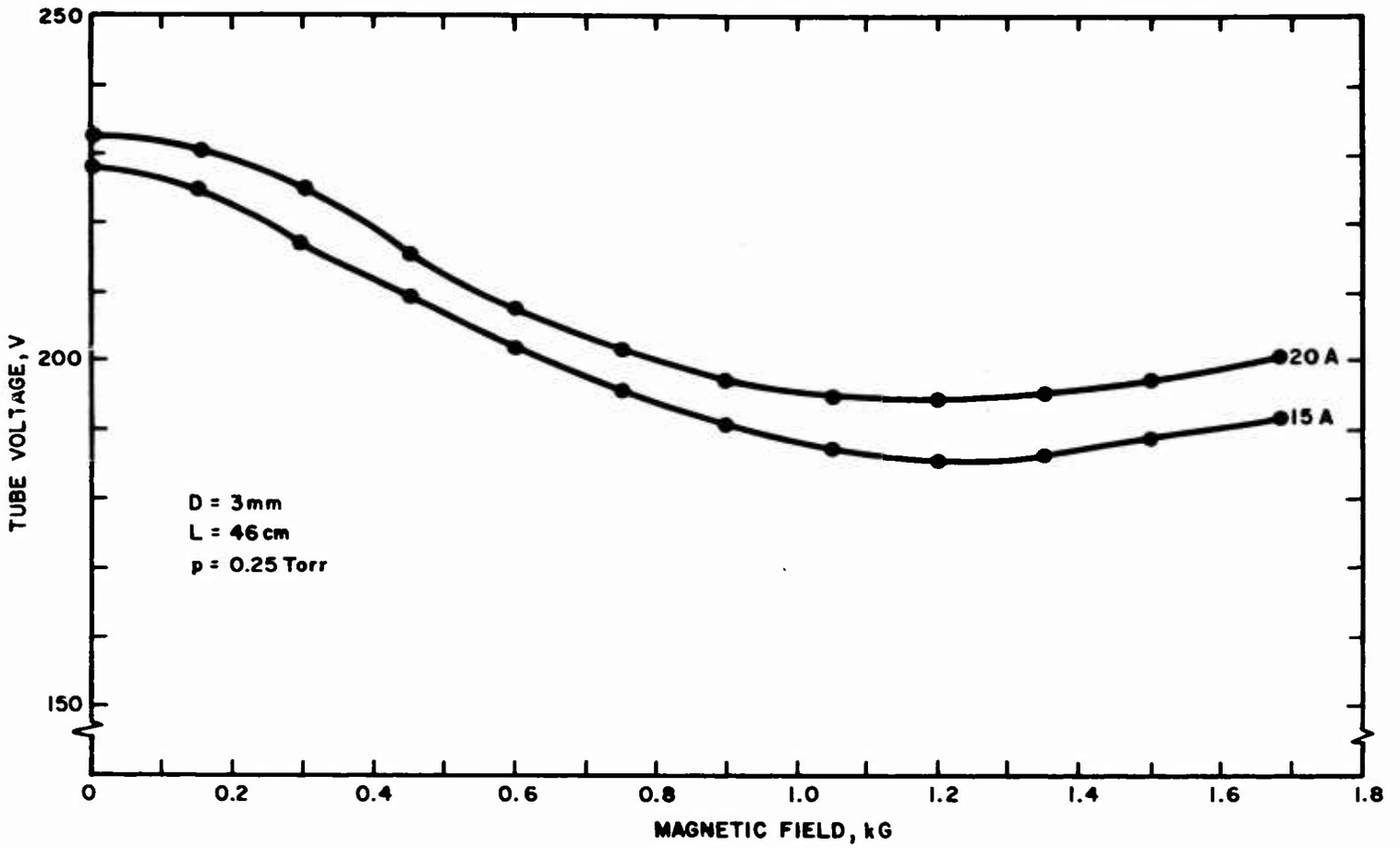

Fig. 87. Dependence of tube voltage V_T on magnetic field for two different values of discharge current.

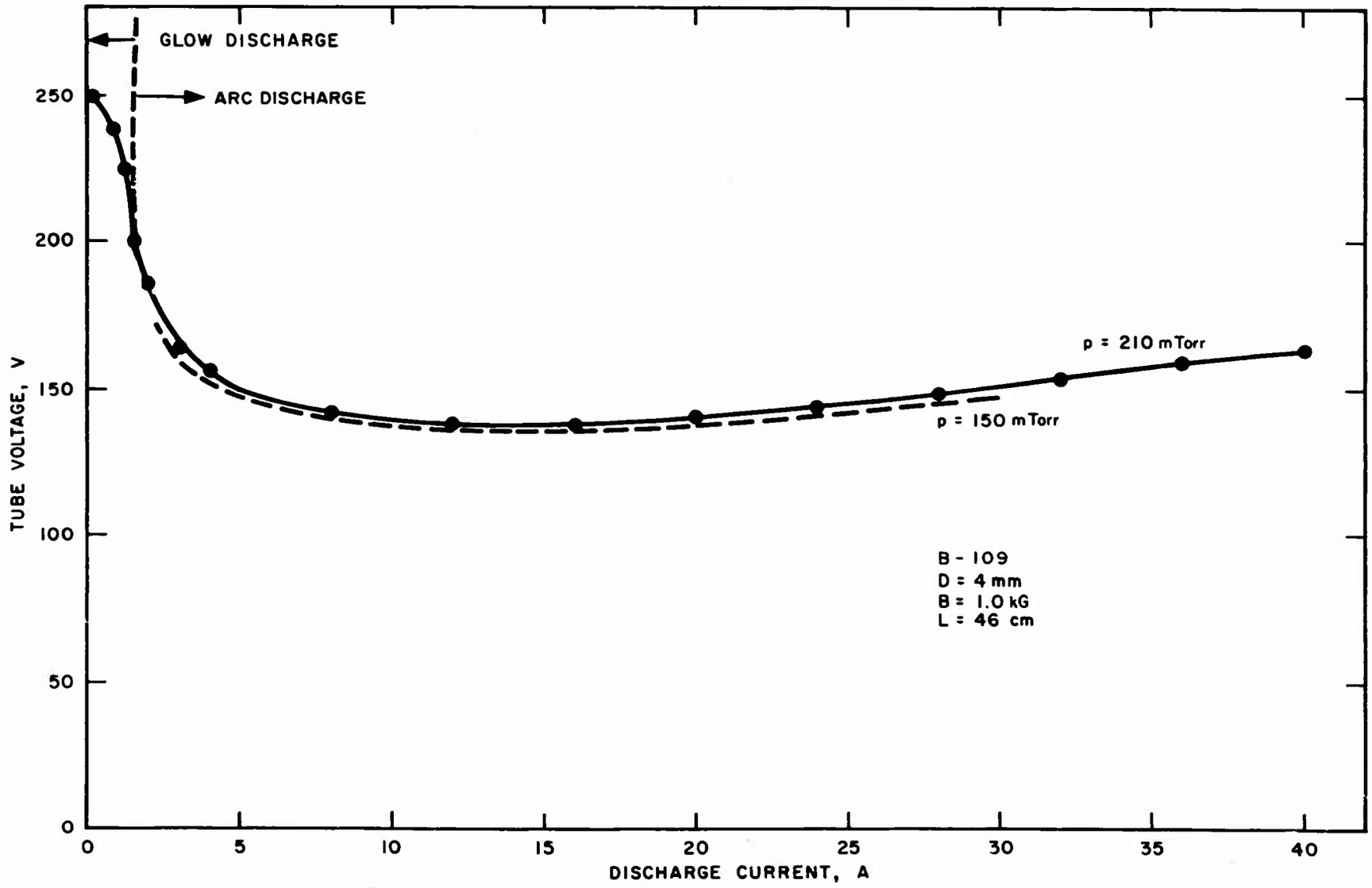

Fig. 88. Tube voltage versus discharge current at two different gas pressures for the 4 mm diameter tube.

$I > 20$ A in a 4 mm tube or $I > 12$ A in a 3 mm tube, $R_{Tac} \cong 1\Omega$. Substituting (26) into (25) and rearranging terms yields

$$\frac{\partial I}{\partial V_s} = \frac{1}{R_S + R_B + R_{Tac}} , \tag{27}$$

which may be conveniently written in the form

$$\frac{1}{I}\frac{\partial I}{\partial t} = \left[\frac{R_s + R_B + R_T}{R_S + R_B + R_{Tac}}\right] \frac{1}{V_s} \frac{\partial V_s}{\partial t} . \tag{28}$$

Finally, introducing (22), 24), and (27) into (18), we obtain

$$\frac{dP}{dt} = \left[\frac{\partial P}{\partial B} - \frac{1}{R_S + R_B}\frac{\partial P}{\partial I}\frac{\partial V_T}{\partial B}\right]\frac{dB}{dt} + \left[\frac{1}{R_S + R_B + R_{Tac}}\frac{\partial P}{\partial I}\right]\frac{dV_s}{dt} \tag{29}$$

which is the desired transfer function coupling power supply ripple to modulation of the output. Numerical values for the coefficients $\partial P/\partial B$, $\partial P/\partial I$, $\partial V_T/\partial B$, and R_{Tac} may be obtained from tube operating characteristics as discussed above.

2. Selection of Power Supplies

a. Current Regulated Supplies

Since the output power is a function only of discharge current and magnetic field, it is clear that beam modulation will be minimized when low ripple, current regulated supplies are used to drive the discharge and solenoid. If an output power P_o is obtained with a dc current I_o and a dc magnetic field B_o, then, from (21),

$$P = \frac{P_o}{I_o^n} I^n , \tag{30}$$

and

$$\left.\frac{\partial P}{\partial I}\right|_{I_o} = \frac{nP_o}{I_o} . \tag{31}$$

The fractional change in P_o caused by a ripple in B or I may be expressed by dividing (18) by P_o and introducing (31) to obtain

$$\frac{I}{P_o}\frac{dP}{dt} = \left(\frac{B_o}{P_o}\frac{\partial P}{\partial B}\right)\frac{1}{B_o}\frac{dB}{dt} + n\frac{1}{I_o}\frac{dI}{dt} . \tag{32}$$

From the second term of (32) it is evident that the peak-to-peak (p-p) beam modulation of a laser operating in the $P \sim I^n$ regime due to the ripple of a constant current anode supply will be n times the p-p anode power supply ripple. For high power lasers, n = 2.

A quick calculation of the quantity $(B_o/P_o)\ \partial P/\partial B$ in (16) from the data of Figure 85 shows that this coefficient is $\ll 1$ for B_o near B_{opt} and reaches a maximum of 0.7 at $B_o/B_{opt} = 0.6$. The ripple requirements on a current regulated solenoid supply are therefore much less stringent than on the anode supply.

Suitable current regulated SCR power supplies are available* which claim to have a maximum rms ripple of 0.15%. It should therefore be possible to maintain the rms ripple of the light beam at <0.4% with commercially available supplies. It is not possible to estimate the corresponding p-p ripple without knowledge of the current waveform. A 0.4% rms sinusoidal ripple corresponds to a 1.1% p-p ripple.

b. Voltage Regulated Supplies

Our typical laboratory ion laser power supplies are unregulated, low impedance units using diode rectifiers. Solenoid supplies employ a standard 3ϕ bridge circuit which should have a 4.2% rms and a 14% p-p ripple; we measure a 13% p-p ripple. Anode supplies utilize a 3ϕ transformer with a dual Δ- Y secondary connected for 6ϕ rectification. Capacitive filtering of the output reduces the ripple to 2% p-p. The high current, low impedance characteristics of the discharge make it difficult to reduce the ripple further by simple filtering.

*For example, H-P Model 6479A, or Rowan Model SCR 250-40.

We shall now consider the output modulation when such a low impedance voltage supply, with a p-p ripple of > 2% is used.

Introducing (31) into (27) and using the relation

$$V_s = I(R_S + R_B + R_T) , \tag{33}$$

the fractional change in power output caused by changes in B and V_s may be expressed as

$$\frac{I}{P_o}\frac{dP}{dt} = \left[\frac{B_o}{P_o}\frac{\partial P}{\partial B} - \frac{n B_o}{(R_S + R_B) I}\frac{\partial V_T}{\partial B}\right]\frac{1}{B_o}\frac{\partial B}{\partial t}$$

$$+ \left[\frac{n(R_S + R_B + R_T)}{R_S + R_B + R_{Tac}}\right]\frac{1}{V_s}\frac{dV_s}{dt} \tag{34}$$

Considering first the effect of fluctuations in V_s, we note that for a truly voltage regulated supply ($R_S = 0$) the modulation of the output is n times the ratio of the dc to ac resistance times the power supply ripple. Typical values of resistance used with simple low impedance voltage supplies are $R_S = 0.5\ \Omega$, $R_T = 10\ \Omega$ (in a 3 mm tube at 20 A), and $R_{Tac} = 1\ \Omega$, so that

$$\frac{R_S + R_B + R_T}{R_S + R_B + R_{Tac}} \cong \frac{10.5 + R_B}{1.5 + R_B} . \tag{35}$$

and nothing is gained by precision voltage regulation (i.e., making $R_S = 0$). Obviously, a large ballast resistor is required if ripple is to be minimized using a constant voltage supply. This is, of course, equivalent to adding a large series resistance to approximate a constant current supply. If we require that the ballast resistor dissipate no more power than is dissipated in the discharge, then $R_B = R_T \cong 10\ \Omega$. For this case, from (34) and (35), the output modulation will be n(20.5/11.5) = 1.8 n times the power supply ripple. This multiplication factor will be 3.6 at high powers.

The two terms which comprise the coefficient of the magnetic field ripple term may be evaluated from the data shown in Figures 85

and 87. The magnitudes of the two coefficients are compared in Table VI for the case of a 3 mm tube at 20 A; power was taken to vary as I^2. The relative sizes of the two terms will depend on the value of $(R_S + R_B)$; typically, the sum of these resistances is in the range of 3 Ω to 10 Ω. For example, if $B_o/B_{opt} = 0.8$, and $(R_S + R_B) = 10\ \Omega$, the magnetic field ripple coefficient would be $(0.4 + 1.9/10) = 0.6$ and the output beam would have 0.6 of the ripple of the solenoid supply.

For $B_o \approx B_{opt}$, we conclude that the ripple transferred from the magnetic field to the output beam is much less than that caused by fluctuations in V_s.

TABLE VI

Magnetic Field Ripple Coefficients in Eq. (34) for a 3 mm Tube at 20 A

B_o/B_{opt}	B_o (kG)	$\left[\frac{B_o}{P_o}\frac{\partial P}{\partial B}\right]$	$-\left[\frac{n B_o}{(R_S + R_B) I}\frac{\partial V_T}{\partial B}\right]$ with n = 2, I = 20 A
0.4	0.42	0.6	$2.6 \div (R_S + R_B)$
0.6	0.63	0.7	2.6 ÷ "
0.8	0.84	0.4	1.9 ÷ "
1.0	1.05	0	0.3 ÷ "
1.2	1.26	-0.2	-0.6 ÷ "
1.4	1.47	-1.0	-1.8 ÷ "

3. Experimental Results

The best way to verify the power supply ripple-output modulation relationships developed above would be to employ very low ripple supplies, and then introduce a known amount of ripple in B, I, or V_s and measure the resulting beam modulation. Unfortunately, low ripple solenoid, filament, and anode supplies were not available in our laboratory during this phase of the program. However, a suitable integrated power supply was available in an argon laser system built here over a

year ago and now installed at another HAC facility. Noise and ripple transfer measurement were made on this system. The major difficulty in carrying out the measurements was that the filament, solenoid, and anode supplies were integrated into a common 400 Hz supply with intricate interlocking logic. This made it rather difficult to monitor supply characteristics. The results reported below for the over-all supply performance are in agreement with predicted behavior, however.

The characteristics of the solid state, 400 Hz supply are as follows:

Filament Supply: 2.2 V dc at 25 A with a p-p modulation of 7%. The modulation consists of 10 μsec pulses at a 100 μsec prf.

Solenoid Supply: 120 V dc at 10 A ($B_o = B_{opt} = 1$ kG) with a 1.25% p-p ripple at 200 Hz.

Anode Supply: Current regulated, 20 A, with a 0.5% current ripple at 200 Hz when driving the discharge.

When the laser was operated at 18 A discharge current (2 W output), the modulation of the output was 1% p-p at 200 Hz. This is in agreement with the behavior predicted above when the magnetic field is near the optimum and the tube is operated at high powers.

The random noise modulation of the beam — that is, the modulation not clearly identified by frequency as fluctuations caused by power supply ripple — was 0.4%.

A 60 Hz, single phase solenoid supply with a 20% p-p ripple at 120 Hz was substituted for the low-ripple solenoid supply to observe the degree to which magnetic field ripple was transferred to the output beam. A 1% p-p modulation of the beam at 120 Hz was measured; this is a transfer of 0.05 of the B field ripple to the beam.

A 60 Hz ac filament power was applied to the directly heated oxide cathode. Low-ripple supplies were used for the solenoid and anode. The output beam had a 60 Hz, 29% p-p modulation at a discharge current of 15 A, and a 12% modulation at 18 A. This ripple is caused by the ac variation in the potential of the directly heated cathode mesh with respect to the anode, and not by a periodic change in the emission characteristics of the cathode. (This cathode temperature does not change that rapidly, and in addition such a change would occur at a 120 Hz rate, rather than an observed 60 Hz.)

The variation in cathode potential is equivalent to varying V_s. We would not expect this variation to modulate the output when a constant current supply is used. It is likely in this case that the response time of the anode supply is greater than 16 msec since a large output filter

capacitor (2000 μF) was used, in which case the supply behaves like a constant voltage source to a 60 Hz variation. A much faster regulator circuit could compensate for spurious ripples introduced into cathode or solenoid supplies.

One side of the cathode mesh is common to the negative lead of the anode supply. The other side varies over a range of $\pm 2.2\sqrt{2} = \pm 3.1$ V with respect to the negative side. If we consider that the average p-p variation in cathode potential is 3 V, which is the change in potential of a point midway between the cathode terminals, the ac circuit resistance which would allow a 29% to 12% modulation of the beam may be calculated. A 29% modulation of the beam at 15 A indicates a 14.5% modulation of the current, or a p-p ripple of 2.2 A. The ac circuit resistance at 15 A is therefore $3V/2.2A = 1.4\ \Omega$. The ac resistance at 18 A would be 1.5Ω, in good agreement with the value taken from Figure 88.

B. OTHER NOISE SOURCES

In addition to power supply induced ripple, we have studied laser output noise associated with the discharge plasma. The latter consists of two types: random noise fluctuations and modulation at discrete frequencies. By careful selection of operating conditions, we find that less than 1% peak-to-peak plasma-induced modulation of the light output can be obtained. However, other choices of operating conditions may result in noise modulation as high as 12% of the dc light level.

1. Description of the Experimental Apparatus

We have made general observations of the noise modulation of the laser output of continuous bore (quartz), segmented, and disk-bore tubes, and find that the peak-to-peak modulation level of these different tubes is approximately equal. Detailed measurements have been on a quartz-bore tube; the conclusions reached using this continuous bore tube will have to be checked later using tubes with different bore structures. This remains an area of great interest since disk bore tubes appear to offer the greatest promise for practical ion lasers.

The quartz discharge tube used for these studies has an active bore length of 46 cm and a 3 mm bore diameter. It was enclosed in a solenoid 50 cm long with an i.d. of 2 in.

The laser cavity used a 4.87 m high reflectance mirror and a flat 5% output mirror. At a discharge current of 20 A, the maximum power output of 2.5 W from this laser was obtained with a filling pressure of 250 m Torr and a longitudinal magnetic field of 1000 G.

The laser output was monitored with a silicon photodetector and an oscilloscope or a low frequency (200 Hz to 15 MHz) spectrum analyzer. We have varied the parameters of the detection circuit to determine that the frequency response of the system is not limited by the silicon detector or the associated circuitry. We have also observed the laser output through a spectrometer and photomultiplier. Photomultipliers have not proved suitable for these measurements because they add their own noise component to the observed laser signal.

2. Random Noise Modulation

The effect of random discharge noise on the laser output has been studied as a function of laser operating parameters. The amplitude-versus-frequency noise envelope has been observed over the frequency range from 200 Hz to 15 MHz. The effects of magnetic field and fill pressure have been studied separately, holding the laser output constant by slight variations in the discharge current.

At a fill pressure of 200 mTorr the discharge noise seen in the laser output increases with increasing magnetic field over the entire range observed. At higher pressures (360 mTorr) the opposite occurs, with minimum noise at maximum magnetic field. At intermediate pressures the noise is at a maximum at low and high fields, decreasing to a minimum for $B \approx 1000$ G. At all pressures the application of a magnetic field shifts the center of gravity of the noise envelope toward higher frequencies. Typically the noise amplitude is at a maximum at low frequency, decreasing monotonically with increasing frequency at frequencies less than 1 MHz. A typical frequency spectrum of the random modulation is shown in Figure 89.

The dependence of the noise spectrum on gas pressure is not so strong. At fields of 750 G and below, the noise increases slightly with increasing pressure. At high fields the reverse is true.

3. Modulation at Discrete Frequencies

Modulation is also observed at discrete frequencies — a fundamental frequency in the range from 150 to 220 kHz, plus as many as five harmonics. The frequency of the fundamental is dependent on tube filling pressure, magnetic field, and discharge current. The number of harmonics appearing is also dependent on these parameters. The modulation occurs only at magnetic fields above a critical value, and under some conditions it can be suppressed by still higher fields. Observations have been made at discharge currents up to 20 A, fill pressures from 200 to 360 mTorr, and fields from 250 to 1500 G.

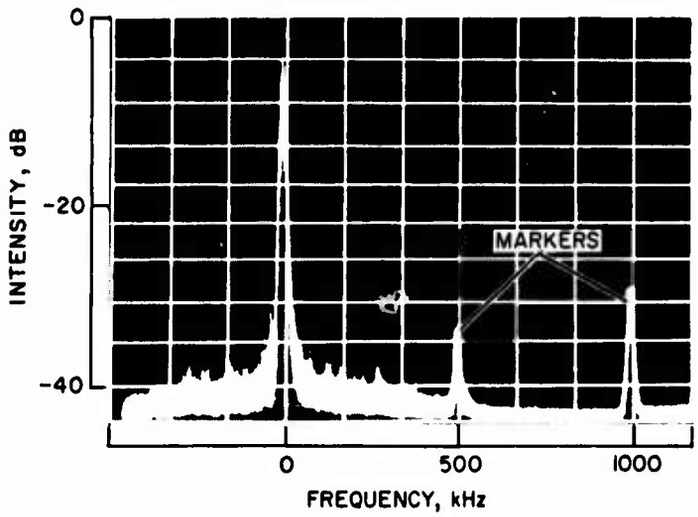

Fig. 89. Spectrum analyzer display of random fluctuation of laser output. The laser discharge current is 17 A, the fill pressure is 200 mTorr, and the magnetic field is 1.5 kG.

Figure 90 shows a typical spectrum analyzer display with the fundamental and two harmonics present, as well as the central zero-frequency pip. The peak-to-peak noise modulation has been observed to be as high as 12% of the dc laser output. This extreme case is observed only at low power levels, however.

The modulation also appears in spontaneous emission. It has been determined that the modulation is strongest in the cathode and cathode throat areas of the discharge. A silicon photodetector was used to scan along the discharge tube from cathode to anode. The spontaneous emission was observed on the spectrum analyzer. Modulations of the type shown in Figure 90 were prominent in the cathode and throat areas of the discharge, but not in the bore itself. This suggests that the modulation may be due to ion acoustic waves excited by oscillation of the double sheath in the throat region as observed by Crawford and Freeston (Ref. 17) and discussed in Ref. 1. However, this must remain as speculation pending further experiments.

The discrete modulation of the laser output may also be related to the Kadomtsev plasma instability studied by others under somewhat different discharge conditions. A rough calculation of the expected frequency of the Kadomtsev instability yields reasonable agreement with the observed values. Additional theoretical and experimental work would be necessary here also before a positive identification could be made, however.

There is, of course, very high frequency modulation of the beam at tens of megahertz and above, generated by mixing between different longitudinal and transverse modes. This modulation was not detected in our present experiments, indicating that these noise components are much weaker than the modulation reported here.

C. CONCLUSIONS

Modulation of the output of an ion laser may be several percent of the dc level. The greatest contribution to the modulation is normally ripple introduced by the power supplies. The coupling of ripple from the anode, solenoid, and heater supplies to the light output has been considered in detail, and experimental results have been given. Good power supply filtering and regulation can eliminate all of these contributions, however.

Measurements of the random noise fluctuations show the spectrum to extend out to about 300 kHz. Higher frequency components at tens of megahertz generated by mode competition have not been studied; however, contributions in the 0.5 to 30 MHz range are not observed to be significant compared with the amplitude of the 0 to 300 kHz spectrum.

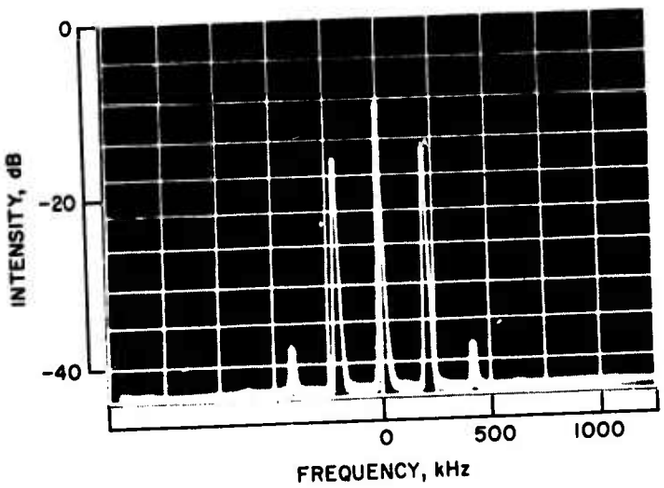

Fig. 90. Spectrum analyzer display of laser output spectrum, showing beam modulation at ≈ 200 kHz and two harmonics.

The random modulation of the beam has been measured to be < 1% peak-to-peak of the dc level in quartz-bore, segmented bore, and disk bore tubes. More detailed measurements on a 3 mm quartz-bore tube show that under certain operating conditions at higher-than-optimum magnetic fields, modulation at a discrete frequency in the 150 to 200 kHz range and at higher harmonics may appear. A peak-to-peak modulation of 10% of the output has been observed.

Targ and Yarborough (Ref. 18) have reported 20 to 30 dB of low frequency AM noise suppression in the 0 to 300 kHz range by FM or phase-locked operation of argon ion lasers. Quieting occurs when the longitudinal mode spectral components become locked together in amplitude and phase. However, this quieting reduces the peak-to-peak modulation to only the 1% level (Ref. 19). This is the level we observe in typical laser operation without phase-locking the modes. One might suppose that our measurement was made on a laser which was self-mode locked; self-mode locking has been observed recently by several investigators in high power argon ion lasers. However, we have measured this < 1% modulation level in such a variety of lasers at widely different operating conditions that self-locking does not appear likely. Additional measurements are required, and are being carried out.

SECTION VIII

CONCLUSIONS

Testing and evaluation of cathodes, bore materials, and tube design features were carried out under this program to improve the reliability and operating characteristics of cw ion lasers. The following conclusions may be drawn from this work:

- Oxide and impregnated tungsten cathodes have been tested and shown to provide discharge currents of tens of amperes for 2000 hours or more in high power ion lasers. Cathode processing and operating characteristics have been described. To achieve long life, care should be taken to compensate for cathode heating by the discharge.

- Bore material studies have shown pyrolytic graphite to be superior to normal graphite as a bore material in its resistance to powdering. Powdering may be completely eliminated in the bore by using tungsten-overcoated graphite. However, the tungsten overcoat (or solid tungsten) does exhibit erosion in the cathode throat constriction when "long" segments (i.e., 3/8 in.) are used. Beryllia also appears to exhibit good characteristics as a bore material. Unfortunately, sufficient time was not available for a thorough evaluation of this material.

- The operating characteristics, resistance to erosion, and large heat dissipation capability which have been demonstrated by tungsten disk-bore structures make this method of bore construction very attractive.

- Almost identical power output and efficiency could be obtained from a laser using either periodic permanent magnets to confine the discharge or a conventional solenoid. However, very severe wall damage occurred at each field reversal when the tube was used with permanent magnets. For this reason, the use of a PPM structure in high power lasers is not considered to be practical.

- To provide an adequate internal gas return path, very large areas in segmented tubes must be allocated to gas return path holes. A larger gas conductance than one might expect from a simple geometric area comparison of return path and bore conductances is required because of the high gas temperature within the bore structure.

- The peak-to-peak noise modulation of high power argon ion lasers can be made less than 1% of the dc level provided extreme care is taken to avoid power supply modulation of the output. The residual random noise spectrum extends out to approximately 300 kHz. Transfer of ripple from the filament, solenoid, or anode power supplies can easily introduce more than a 1% ripple in the output unless care is taken to filter the supplies; power supply ripple requirements have been treated in detail.

The state of the art in ion laser technology is now at a point where bore structures of several types (graphite, tungsten-disk, beryllia) can withstand high power operation (>200W/cm bore dissipation) for several hundred hours. Additional testing is still required with these different configurations to determine the ultimate power limiting processes of each (for example, thermal strain, bore erosion, gas pumpout from the bore region, etc.). Another important problem which has not been covered in this report is that of mode distortion and power limiting caused by losses in contaminating films deposited on the inside surface of windows or internal mirrors. This problem is at present the most critical problem impeding the construction of short (<1 m), high power (>10 W), small bore tubes; the requirement in such a tube to position windows within 6 in. of the bore and prevent the formation of films which will not cause distortion of the beam when exposed to flux densities of 5000 W/cm^2 is very difficult to satisfy in long-life tubes. Careful work in the selection of materials (bore, envelope, and cathode), tube processing, and contaminant analysis for different bore and cathode types is required before existing bore power dissipation capabilities can be fully utilized.

REFERENCES

1. W. B. Bridges and A. S. Halsted, "Gaseous Ion Laser Research," Technical Report No. AFAL-TR-67-89, Hughes Research Laboratories, Malibu, California, May 1967 (DDC Number AD 814 897).

2. G. A. Haas, "Thermionic Emission Sources," NRL Report 5657, U. S. Naval Research Laboratories, Washington, D. C., October 6, 1961.

3. G. A. Haas and J. T. Jensen, Jr., "Use of oxide cathodes in demountable vacuum systems," Rev. Sci. Instr. 28, 1007 (1957).

4. R. V. Stuart and G. K. Wehner, "Sputtering yields at very low bombarding energies," J. Appl. Phys. 33, 2345 (1962).

5. Bridges and Halsted, op. cit.

6. G. V. Jorgensen and G. K. Wehner, "Sputtering studies of insulators by means of Langmuir probes," J. Appl. Phys. 36, 2673 (1965).

7. J. Darrah, private communication.

8. N. I. Sax, Dangerous Properties of Industrial Materials (Reinhold, New York, 1963).

9. J. V. Parker, "Metal Aperture Lasers," Paper No. 14.1, International Electron Devices Meeting, Washington, D. C., October 18-20, 1967.

10. S. C. Brown, Basic Data of Plasma Physics (Wiley and Sons, New York, 1959).

11. F. C. Sterzer and W. W. Siekanowicz, "The design of periodic permanent magnets for focusing of electron beams," RCA Rev. 28 (1957).

12. H. Alfvén and C. Fälthammar, Cosmical Electrodynamics (Oxford Clarendon Press, London, 1963).

13. Bridges and Halsted, op. cit., Section VI.

14. S. Dushman, Vacuum Techniques (Wiley and Sons, New York, 1958).

15. Bridges and Halsted, op. cit., Section IV-A.

16. Ibid., Section V-D.

17. F. W. Crawford and I. L. Freeston, "The Double Sheath at a Discharge Constriction," Microwave Laboratory Report No. 1043, Stanford University, Stanford, California, June 1963.

18. R. Targ and J. M. Yarborough, "Mode-lock quieting of He-Ne and argon lasers," Appl. Phys. Letters 12, 31 (1968).

19. R. Targ, private communication.

APPENDIX I

HEAT TRANSFER CHARACTERISTICS OF A DISK-BORE TUBE

Consider a series of disks of diameter D with emissivity ϵ_1 each at an absolute temperature T_1 as shown in Figure 1-1. The cylindrical surface surrounding the disks has emissivity ϵ_2 and is at a temperature T_2. If the disks and wall are both black bodies, so that $\epsilon = 1$, the heat transfer to the wall from both sides of one disk, or equivalently, from the surface of two opposing disks, is given by

$$P_{1-2} = 2A_1F_{12}\sigma(T_1^4 - T_2^4) \qquad \text{(I-1)}$$

where σ is the Stefan-Boltzmann constant (5.67×10^{-12} W/cm^2 $^\circ$K^4). F_{12} is the configuration factor which takes into account the geometric arrangement of the two surfaces, and is defined as

$$F_{12} = \frac{\text{direct radiation from surface 1 to surface 2}}{\text{total radiation from surface 1}} \qquad \text{(I-2)}$$

The configuration factor F_{11} for heat transfer from one disk to the next is tabulated in the literature* as a function of the ratio D/L. Since the total radiation leaving surface 1 is made of fractional parts sent to each surrounding surface, it is clear that

$$F_{12} = 1 - F_{11}. \qquad \text{(I-3)}$$

The parameter F_{12} is plotted as a function of the ratio D/L in Figure I-2 from the tabulated values of F_{11}, and eq. (I-3). For small D/L, the disks are many diameters apart and $F_{12} \cong 1$ since almost all the radiation reaches the wall.

---

*H. C. Hottel, "Radiant heat transfer," Mech. Eng. 52, 699 (1930).

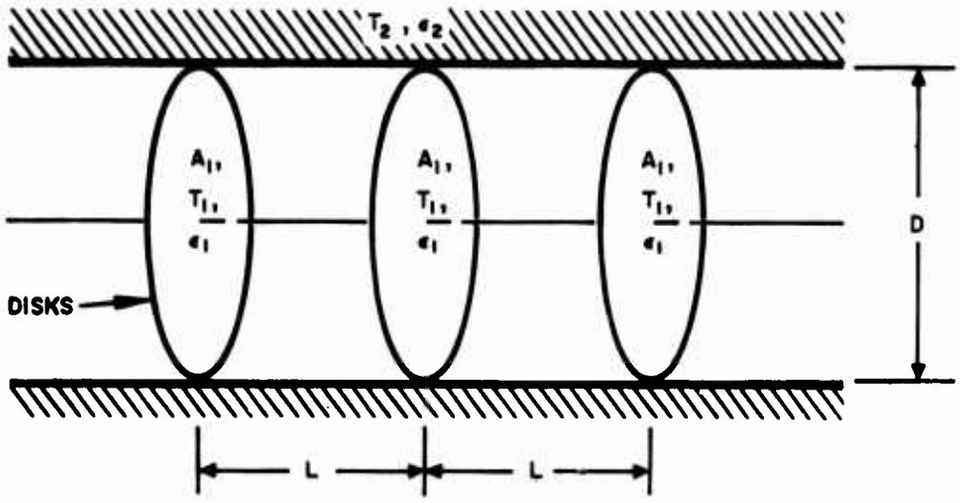

Fig. I-1. Schematic representation of a circular disk structure surrounded by an absorbing cylindrical surface.

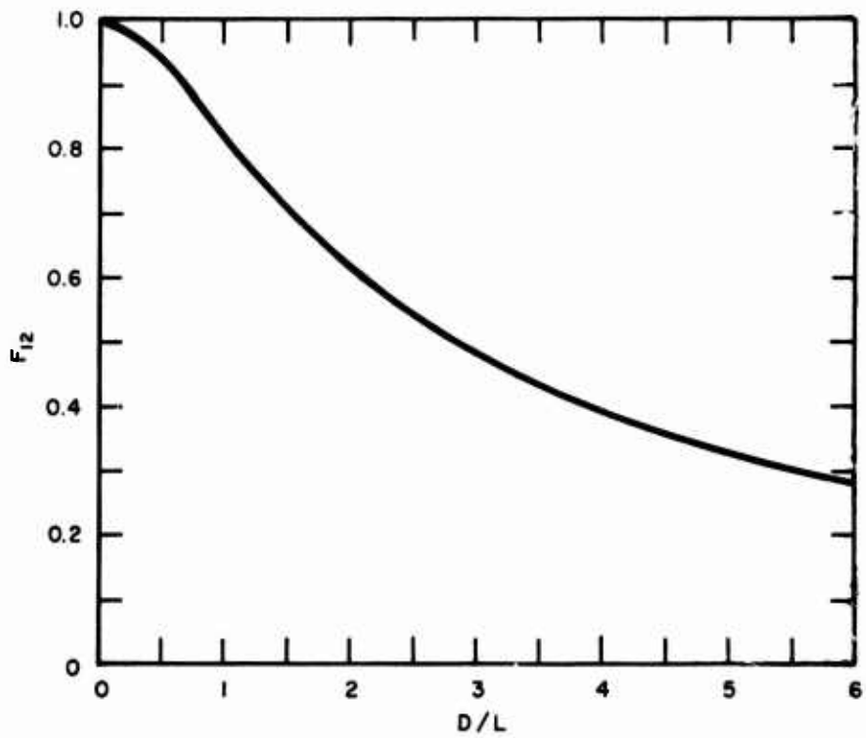

Fig. I-2. Dependence of the configuration factor F_{12} on the ratio of the diameter to the spacing of the disks. F_{12} is the fraction of the direction radiation from one side of a disk which reaches the wall.

In the arguments above, we have assumed that all surfaces act as black bodies. If surfaces 1 and 2 are gray bodies, a more general configuration factor $\overline{F}_{12}$ which takes into account the emissivities of the surfaces must be introduced. This factor is defined as

$$\overline{F}_{12} = \frac{1}{\frac{1}{F_{12}} + \left(\frac{1}{\epsilon_1} - 1\right) + \frac{A_1}{A_2}\left(\frac{1}{\epsilon_2} - 1\right)} \tag{1-4}$$

For the particular disk bore structure supported in a quartz water jacket to be analyzed, we make take the approximations

$$T_1 >> T_2,$$

$$\epsilon_2 = 1 . \tag{I-5}$$

In this case, eq. (I-1) becomes

$$P_{1-2} = 2A_1 \overline{F}_{12} \sigma T_1^4 , \tag{1-6}$$

where

$$\overline{F}_{12} = \frac{1}{\frac{1}{F_{12}} + \left(\frac{1}{\epsilon_1} - 1\right)} , \tag{I-7}$$

Note that for D/L small (the disks far apart), F_{12} approaches 1 and $\overline{F}_{12}$ becomes just ϵ_1 so that, as expected,

$$P_{1-2} = 2A_1 \epsilon_1 \sigma T_1^4 . \tag{1-8}$$

For our purpose, it is convenient to use (I-6) to define an equivalent emissivity ϵ_{eq} as the emissivity of a cylinder of diameter D which, at T_1, radiates the same power per unit length as a disk structure of the same diameter. By definition, then, the power radiated per unit length from a disk structure D is

$$P_{1-2} = (\pi D)\, \epsilon_{eq}\, \sigma\, T_1^4 \ . \qquad \text{(I-9)}$$

A disk structure with disk spacing L radiates, from (I-6), a power per unit length of

$$P = 2\left(\frac{\pi D^2}{4}\right) \overline{F}_{12}\, \sigma\, T_1^4/L \ . \qquad \text{(I-10)}$$

Equating (I-9) and (I-10) and solving for ϵ_{eq} yields

$$\epsilon_{eq} = \frac{D}{2L} \cdot \overline{F}_{12} = \frac{D}{2L} \cdot \frac{1}{\frac{1}{\overline{F}_{12}} + \left(\frac{1}{\epsilon_1} - 1\right)} \qquad \text{(I-11)}$$

This expression has been plotted in Figure I-3 for several different values of emissivity.

To make it clear how these data can be used, consider the following examples which correspond to conditions in the tungsten and graphite disk experimental tubes described in Section IV.

<u>Example 1</u>: What will be the operating temperature of the thin tungsten disks in a tube with D = 3 cm, L = 1 cm if the discharge diameter is 2.3 mm and the tube is operated at 20 A?

<u>Solution</u>: With D/L = 3, and assuming ϵ = 0.25 for sandblasted tungsten at 1250°C, $\epsilon_{eq} \cong 0.3$ from Figure I-3. Since ϵ_{eq} is $> \epsilon_1$, the disk structure runs slightly cooler than a solid tungsten cylinder of 3 cm diameter.

For a 2.3 mm bore at 20 A, the input power to the bore is (3.5 V/cm) (20 A) = 70 W/cm which must be radiated from the disk structure.

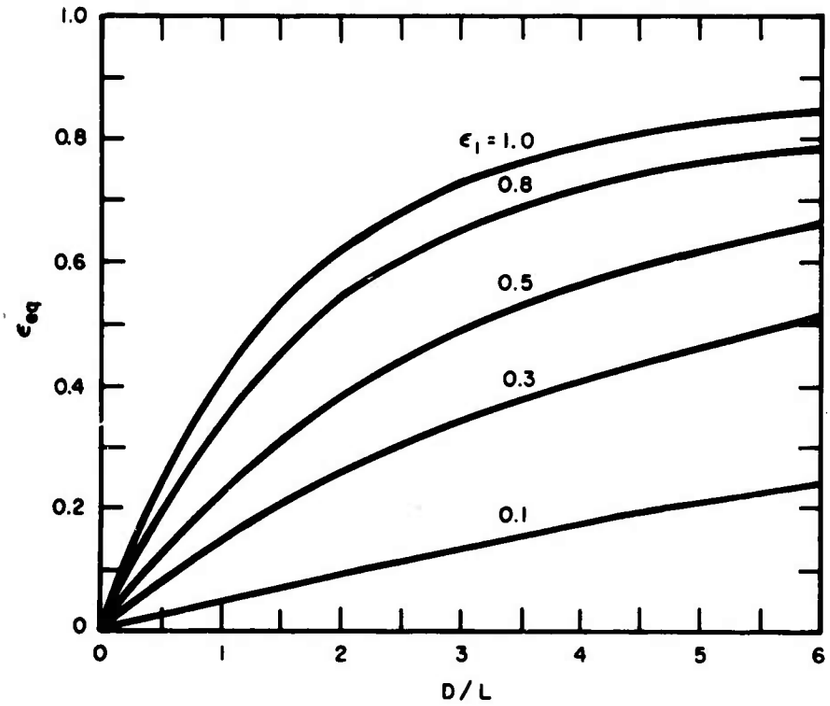

Fig. I-3. Dependence of the equivalent emissivity on the ratio of D/L for disks of emissivity ϵ_1. A cylinder of diameter D and emissivity ϵ_{eq} at T_1 radiates the same power per unit length as a disk structure at T_1.

From (I-9),

$$T_1 = \left[\frac{P}{\pi D \epsilon_{eq} \sigma}\right]^{1/4}$$

$$= \left[\frac{70}{(\pi)(3.0)(0.3)(5.67 \times 10^{-12})}\right]^{1/4} \qquad \text{(I-12)}$$

so

$$T_1 = 1445^{\circ}K, \text{ or } 1172^{\circ}C$$

The true operating temperature (i.e., the corrected brightness temperature) of the disks in the tungsten disk tube at 20 A was measured to be approximately 1150°C.

Example 2: In the experimental disk tube described in Section IV-A, which had L = 0.63 cm, D = 1.9 cm, and graphite segments ΔL = 0.32 cm thick, we actually measured the segment temperature at 20 A to be 1025°C. Does this agree with what one would expect from theory?

Solution: The power input to the bore was approximately (3.3 V/cm) (20 A) = 66 W/cm. Since segments are spaced every $(L + \Delta L)$ = 0.95 cm along the bore, the power input per segment was ~63 W/segment. Using ϵ_1 = 0.8 for graphite and D/L = 3, we find ϵ_{eq} = 0.66 from Figure I-3.

The total power radiated from one disk is the sum of the radiation from the sides and for outer cylindrical surface, so

$$P = (\pi D \Delta L)(\epsilon_1)\, \sigma T_1^4 + (\pi D L)(\epsilon_{eq})\, \sigma T_1^4$$

$$= \left[\Delta L \epsilon_1 + L \epsilon_{eq}\right] \pi D \sigma T_1^4 \,. \qquad \text{(I-13)}$$

Substituting $P = 63$ W and the appropriate values for ϵ_{eq} and the physical dimensions of the structure into (I-13) and solving for T_1, we find

$$T = 1017^{\circ}C$$

which is in good agreement with the measured temperature of $1025^{\circ}C$.

UNCLASSIFIED
Security Classification

DOCUMENT CONTROL DATA - R&D

(Security classification of title, body of abstract and indexing annotation must be entered when the overall report is classified)

1. ORIGINATING ACTIVITY *(Corporate author)* Hughes Research Laboratories 3011 Malibu Canyon Road Malibu, California 90265	2a. REPORT SECURITY CLASSIFICATION Unclassified 2b. GROUP N/A

3. REPORT TITLE

Gaseous Ion Laser Research

4. DESCRIPTIVE NOTES *(Type of report and inclusive dates)*

Final Report, Contract F33615-67-C-1435, Jan. 1967 through 30 June 1968

5. AUTHOR(S) *(First name, middle initial, last name)*

Halsted, A.S., Bridges, W.B., and Mercer, G.N.

6. REPORT DATE July 1968	7a. TOTAL NO. OF PAGES 176	7b. NO. OF REFS 20
8a. CONTRACT OR GRANT NO. Contract F33615-67-C-1435 b. PROJECT, TASK, WORK UNIT NOS. 5237-08-003 c. DOD ELEMENT d. DOD SUBELEMENT	9a. ORIGINATOR'S REPORT NUMBER(S) AFAL-TR-68-227 9b. OTHER REPORT NO(S) *(Any other numbers that may be assigned this report)*	

10. DISTRIBUTION STATEMENT This document is subject to special export controls and each transmittal to foreign governments or foreign nationals may be made only with prior approval of AF Avionics Laboratory (AVTL), Wright-Patterson AFB, Ohio 45433

11. SUPPLEMENTARY NOTES	12. SPONSORING MILITARY ACTIVITY Air Force Avionics Laboratory AF Systems Command, Wright-Patterson AFB, Ohio

13. ABSTRACT

The results of a program to improve the reliability and operating characteristics of argon ion lasers are reported. This work on laser technology is a continuation of the earlier studies on excitation mechanisms, scaling laws, plasma properties, and laser technology which was described in a previous final report of the same title.* Emphasis of the present work has been on life testing of cathodes and bore materials, evaluation of bore construction techniques (continuous, segmented, and disk bore structures), and improvement of operational characteristics. Both oxide and impregnated tungsten cathodes were evaluated under typical ion laser conditions in extended life tests. Extensive data were gathered on gas cleanup rate and on the amount of additional cathode heating which occurs when discharge current is drawn from the cathode. Promising laser bore materials were evaluated to determine resistance to ion sputtering, cleanliness as a vacuum material, gas cleanup properties, and thermal characteristics. Materials tested and reported upon are pyrolytic graphite, graphite overcoated with pyrolytic graphite, graphite overcoated with tungsten, tungsten, quartz, and beryllia. The characteristics of lasers having bores constructed of thin disks spaced many disk-thicknesses apart are described. The output power, efficiency, resistance to erosion, and large heat dissipation capability demonstrated by tungsten disk-bore structures make this method of bore construction very attractive. The operation of argon ion lasers using periodic permanent magnets (PPM) to replace the conventional solenoid magnet was investigated. A comparison is reported of the performance of a laser when operated in a solenoid and in a PPM assembly. Severe bore erosion occurred at the field reversals with PPM confinement. The theory of segmented bore lasers with internal gas return paths is considered. Very large areas in the bore segments or disks must be allocated to gas return path holes to provide an adequate gas return path because of the high gas temperature within the bore structure. Modulation of the output beam by power supply ripple and discharge fluctuations was investigated. The quantitative relationship between laser light modulation and the ripple amplitude of the several power supplies used to run a laser is given and was confirmed experimentally. Less than 1% total peak-to-peak beam modulation can be obtained. Characteristics are given of a discharge instability in the hundred kilohertz range which is present under certain discharge conditions and which increases the beam modulation level.

W. B. Bridges and A. S. Halsted, "Gaseous Ion Laser Research, Technical Report No. AFAL-TR-67-89, Hughes Research Laboratories, Malibu, California, May 1967 (DDC No. AD 814897).

DD FORM 1 NOV 65 1473

UNCLASSIFIED
Security Classification

14. KEY WORDS	LINK A ROLE	LINK A WT	LINK B ROLE	LINK B WT	LINK C ROLE	LINK C WT
Gas lasers						
Ion lasers						
Argon ion lasers						